

University of Windsor

Scholarship at UWindor

Electronic Theses and Dissertations

Theses, Dissertations, and Major Papers

2011

Analysis of W-Beam Guardrail Systems Subjected to Lateral Impact

Abdelmonaam Sassi
University of Windsor

Follow this and additional works at: <https://scholar.uwindsor.ca/etd>

Recommended Citation

Sassi, Abdelmonaam, "Analysis of W-Beam Guardrail Systems Subjected to Lateral Impact" (2011).
Electronic Theses and Dissertations. 409.
<https://scholar.uwindsor.ca/etd/409>

This online database contains the full-text of PhD dissertations and Masters' theses of University of Windsor students from 1954 forward. These documents are made available for personal study and research purposes only, in accordance with the Canadian Copyright Act and the Creative Commons license—CC BY-NC-ND (Attribution, Non-Commercial, No Derivative Works). Under this license, works must always be attributed to the copyright holder (original author), cannot be used for any commercial purposes, and may not be altered. Any other use would require the permission of the copyright holder. Students may inquire about withdrawing their dissertation and/or thesis from this database. For additional inquiries, please contact the repository administrator via email (scholarship@uwindsor.ca) or by telephone at 519-253-3000ext. 3208.

Analysis of W-Beam Guardrail Systems Subjected to Lateral Impact

by

Abdelmonaam Sassi

A Dissertation

Submitted to the Faculty of Graduate Studies

Through the Department of Civil and Environmental Engineering

in Partial Fulfillment of the Requirements for

the Degree of Doctor of Philosophy at the

University of Windsor

Windsor, Ontario, Canada

2011

© 2011 Abdelmonaam Sassi

Analysis of W-Beam Guardrail System Subjected to Lateral Impact

By

Abdelmonaam Sassi

APPROVED BY

Dr. K. Sennah
Department of Civil Engineering/ Ryerson University

Dr. N. Zamani
Department of Mechanical, Automotive and Materials Engineering

Dr. B. Budkowska
Department of Civil and Environmental Engineering

Dr. F. Ghrib, Advisor
Department of Civil and Environmental Engineering

Dr. S. Cheng
Department of Civil and Environmental Engineering

J. Sokolowski, Chair of Defence
Department of Mechanical, Automotive & Materials Engineering

30 June 2011

DECLARATION OF ORIGINALITY

I hereby certify that I am the sole author of this thesis and that no part of this thesis has been published or submitted for publication.

I certify that, to the best of my knowledge, my thesis does not infringe upon anyone's copyright nor violate any proprietary rights and that any ideas, techniques, quotations, or any other material from the work of other people included in my thesis, published or otherwise, are fully acknowledged in accordance with the standard referencing practices. Furthermore, to the extent that I have included copyrighted material that surpasses the bounds of fair dealing within the meaning of the Canada Copyright Act, I certify that I have obtained a written permission from the copyright owner(s) to include such material(s) in my thesis and have included copies of such copyright clearances to my appendix.

I declare that this is a true copy of my thesis, including any final revisions, as approved by my thesis committee and the Graduate Studies office, and that this thesis has not been submitted for a higher degree to any other University or Institution.

Abstract

The primary purpose of this work is to evaluate and to improve the response of guardrail system during a lateral impact. The problem was analyzed in the first step at the component level, which consists of a single post embedded in a cohesionless soil and laterally loaded by an impactor. The lateral post response was evaluated during static and dynamic loading using a theoretical formulation able to predict the lateral load in static and dynamic modes. An improved subgrade method for soil-post interaction which includes the stiffness, damping and inertia effect involved during the crash, was proposed in this thesis. The improved model serves to study the effect of different design parameters on the post response and to evaluate the interaction between these different parameters during the dynamic loading using a Design of Experiments (DoE) approach.

The results of parametric study and the Design of Experiment conducted on a single post were used to develop a new guardrail design that was implemented in a full-scale finite element model of a Chevrolet C1500 pick truck impacting a guardrail post. The new design consists of replacing the incompressible blockout by a crushable one. The results of the simulation show that the pickup truck was redirected safely with more reduced speed, less roll angle and plastic strain than those for the baseline configuration.

To My Parents

ACKNOWLEDGEMENTS

Thank you god for giving me the patience and the perseverance to finish this work.

I started this doctoral research in fall 2002 having in mind to finish it within a few years. The task was not as easy as I expected. I had to face more challenging technical problems and it was a very demanding in terms of time, health and work. Without the help, support and assistance from the surrounding people, I would not be able to achieve my goal. I would like to thank everybody who contributed to the development of this project and especially:

- my parents, they prayed day and night for my success. They were always for me a source of inspiration and guidance.
- my wife, children, brothers and sisters for their unconditional love, support and their enormous sacrifice during the last eight years.
- my advisor, Dr. Faouzi Ghrib, for his support, persistent supervision, sharp comments, knowledgeable advice, patience, understanding and suggestions.

I should be very thankful to my colleague Dr. S. Battachargee, whose comments helped me shaping especially the second and the third chapters of this dissertation.

I would like to thank the dissertation committees, Dr. K. Sennah, Dr. N. Zamani, Dr. B. Budkowska and Dr. S. Cheng for reviewing my work. Their suggestions and comments contributed to the improvement the quality of the work.

I extend my thanks to Dr. R. Changati, visiting scholar at Windsor University, who extended my knowledge in the word of Design of Experiment (DoE). He kindly introduced me to Qualitek 4 software for my runs and helped me to analyse the results.

I extend my thanks to my colleagues and friends who always give me the hands, especially Syed Imam for his finite element support, and El-Houssain Waled for reshaping the wording of my dissertation.

TABLE OF CONTENTS

DECLARATION OF ORIGINALITY.....	iii
ABSTRACT.....	iv
DEDICATION.....	v
ACKNOWLEDGEMENTS.....	vi
LIST OF TABLES.....	xi
LIST OF FIGURES.....	xiv
Chapter I: Introduction	1
1.1 Research Background	1
1.1.1 Weak post guardrail system	5
1.1.2 Strong post guardrail system.....	6
1.1.3 History of the crash test requirements for the guardrail system	8
1.1.4. Design requirements of the guardrail post.....	11
1.1.5. Full crash testing and simulations	11
1.2 Summary and Objective of the Study.....	17
1.3. Organization of the Dissertation.....	18
Chapter II: Behaviour of Guardrail Posts Subjected to Static Lateral Load	20
2.1. Introduction	20
2.2. Literature Survey	23
2.2.1. Linear elastic procedures	23
1) Soils having a uniform modulus, E_s	24
2) Soils with linearly increasing modulus	27
3) Illustrative example of Poulos' solution applied to a guardrail post	30
2.2.2. Method of subgrade reaction.....	31
2.2.3. The P-Y method.....	34
2.2.4. The ultimate capacity method	40
1) Method of Broms (1964)	43
2) Method of Meyerhof et al., (1981)	45
3) Method of Prasad & Chari (1999).....	48

2.2.5. Summary of the literature review	50
2.3. Proposed Method for the Ultimate Lateral Load Estimation	51
2.3.1. Guardrail post rigidity	51
2.3.2. Theoretical background	53
2.3.3. Determination of the rotation centre	58
2.3.4. Determination of k_p passive earth pressure in 3D.	59
2.4. Determination of the Force F	68
2.5. Relation of Static and Dynamic Tests	70
2.5.1. Dynamic loading	71
2.5.2. Results and interpretation.	72
2.6. Conclusions	73
Chapter III: Analysis of Laterally Impacted Guardrail Posts	75
3.1. Introduction	75
3.2. Baseline Dynamic Test	77
3.3. Continuum Approach	80
3.3.1. Post and impactor modeling.....	80
Material properties.....	81
Strain rate effect.....	82
3.3.2. Soil modeling	82
Soil constitutive model.....	83
Soil material models parameters	87
Geometry and boundary conditions	88
Mesh properties.....	88
3.3.3. Results of the continuum simulation.....	90
3.4. Improved Subgrade Method	95
3.4.1. Interpretation methods of soil-pile interaction under dynamic load	96
3.4.2. Proposed subgrade method of highway post embedded in cohesionless soil.....	100
3.4.3. Calculation of the spring stiffness	101
3.4.4. Evaluation of the lumped mass	104
3.4.5. Calculation of the damping factor	108
3.5. Analysis of the Upgraded Subgrade Method Results.....	110

3.6. Improved Subgrade Method for Cohesive Soil.....	115
3.6.1. The continuum Method.....	116
3.6.2. The subgrade method with the new approach.....	116
Calculation of the spring stiffness	117
Evaluation of the lumped mass.....	119
Evaluation of the damping factor	119
3.6.3. Analysis and results for the case of clay	120
3.7. Conclusions	122

Chapter IV: Parametric Study of the Post Guardrail Embedded in Soil

4.1. Introduction.....	123
4.2. Baseline Study.....	124
4.3. Parametric Study	125
4.3.1. Effect of the impactor speed.....	125
4.3.2. Effect of the embedment depth	131
4.3.3. Effect of sand friction angle	136
4.3.4. Effect of the impactor mass.....	142
4.3.5. Effect of crushable post blockout.....	146
4.3.6. Effect of the clay undrained shear strength	153
4.4. Summary of the Parametric Study	157
4.5. DoE and Taguchi Method Applied to the Problem of Guardrail Post.....	158
4.5.1. Phase 1: Planning of the DoE	161
4.5.2. Method of evaluation	163
Peak load:	164
Average Load:	164
Energy dissipation:	164
Post deflection:	164
4.5.3. Phase II: DOE Results	164
4.5.4. Analysis of the L16 DOE results:	164
4.5.5. Conclusion	171
4.6. L9 Orthogonal Array	171
4.6.1. Phase 1: Planning of the DOE.....	171

4.6.2. DOE results and discussion	173
4.7. Conclusion.....	180

Chapter V: Full-Scale Finite Element Model Development

and Analysis	182
5.1. Introduction.....	182
5.2. Finite Element Modeling	183
5.2.1. Guardrail modeling	183
5.2.2. Guardrail post modeling	185
5.2.3. Soil-post interaction.....	187
5.2.4. W beam rail to the post connections.....	188
5.2.5. Vehicle development.....	190
5.3. Validation of the Pickup Truck Model	193
5.3.1. Full frontal crash testing	193
5.3.2. Validation of the truck model in side crash	195
5.4. Impact of the Pickup with the Guardrail System: Baseline Model.....	200
5.4.1. Full Scale finite element model.....	200
5.4.2. Comparison between finite element simulation and full-scale crash test	201
5.4.3. Results of the base model and analysis	206
5.4.4. Results of the base model with crushable blockout	210
5.5. Conclusion.....	216

Chapter VI: Conclusions and Recommendations.....218

6.1. Introduction.....	218
6.2. Summary of the Research	218
6.3. Future Work.....	220

References.....223

VITA AUCTORIS.....	234
--------------------	-----

LIST OF TABLES

Table 1.1: Collisions and casualties in Canada from 1988 to 2007, Transport Canada (2010).	2
Table 1.2: Statistics of vehicle involved in fatal collision by vehicle event (Transport Canada 2001)	4
Table 1.3: Test Matrix for longitudinal barriers (Ross et al., 1993)	12
Table 2.1: Dynamic and static tests for post loaded laterally.....	22
Table 2.2: Proposed values of k_{v1} in tons/ft ³ for 1-ft square plate or 1ft wide beams resting on Sand (Terzaghi 1955)	32
Table 2.3: Values of the Constant of Horizontal Subgrade Reaction n_h in tons/ft ³ for a pile 1-ft Wide in sand (Terzaghi 1955).....	32
Table 2.4: Representative values of k (pci) (Reese et al., 1974).....	37
Table 2.5: W 152 x 13.5 beam properties	53
Table 2.6: Static tests conducted in sand by Bierman (1995)	58
Table 2.7: Static tests conducted in sand by Dewey (1982)	59
Table 2.8: K_{py} for different values of B/H and δ/ϕ after Škrabl and Macuh (2005)	63
Table 2.9: K_{py} for different values of B/H and δ/ϕ sorted by friction angle.....	64
Table 2.10: Values of the parameters of correlation.....	66
Table 2.11: k_p values for B/H = 0.1 for different friction angles	67
Table 2.12: Comparison of the predicted load maximum load with the maximum load of the static test.....	69
Table 2.13: Comparison of the predicted maximum load with the maximum load obtained from dynamic tests	74
Table 3.1: Dynamic test matrix of steel post embedded in soil conducted by Coon et al. (1999)	79
Table 3.2: Radioss material properties of the guardrail post, Engstrand (2000).....	81
Table 3.3: Soil properties for the cohesionless soil	90
Table 3.4: Comparison of the average force and maximum deflection between dynamic test and Finite Element simulation.....	91
Table 3.5: Comparison of the post reaction parameters for different threshold displacement.....	106

Table 3.6: Parameters of springs and dampers calculated for the Model with lumped mass for the test of Coon et al. (1999)	108
Table 3.7: Comparison of the average force and maximum deflection between dynamic test and simplified Finite Element simulation	111
Table 3.8: Simulation statistics for simulation of the different models	115
Table 3.9: Soil properties for the cohesive soil used by Bendidi (2002)	116
Table 3.10: Variation of undrained shear strength of the clay as function of the depth for the Dewey's test (1982).....	119
Table 3.11: Parameters of the springs-mass-dashpot system used to correlate the Dewey (1982) test	120
Table 4.1: Summary of the simulation results of impactor hitting the post embedded in the soil with different impact speeds.....	126
Table 4.2: Summary of the simulations results of the impactor with the post located at different depths embedment.	131
Table 4.3: Typical friction angle for different sand densities.....	136
Table 4.4: Typical values of lateral subgrade modulus for different sand density.....	141
Table 4.5: Impactor mass used in the literature	143
Table 4.6: Results of the energy dissipation with different mass impactor	143
Table 4.7: Properties of the Steel Material.....	147
Table 4.8: Results of the energy dissipation with different blockout design.....	150
Table 4.9: Consistency and undrained shear strength of the cohesive soils	155
Table 4.10: Summary of the simulations results of the impactor with the post embedded in different cohesive consistency.	155
Table 4.11: Factors and levels used in DoE layout	161
Table 4.12: L ₁₆ Orthogonal array of the current study	166
Table 4.13: Results of the DOE Study	165
Table 4.14: Analysis of Variation (ANOVA) for post displacement	167
Table 4.15: ANOVA of the different criteria the post loaded laterally.....	168
Table 4.16: Results of interaction factors of the different criteria.....	169
Table 4.17: Contribution of the different parameters	170
Table 4.18: parameters and steps of the current study	172
Table 4.19: L ₉ Orthogonal array of the current study.....	172
Table 4.20 Results of the DOE Study	173
Table 4.21: Contribution for the different parameters.....	176

Table 4.22: ANOVA of the different criteria for L9 DOE matrix.....	177
Table 4.23: Results of interaction factors of the different criteria for L9 DOE matrix.....	178
Table 5.1: Material properties for modeling guardrail steel (Plaxico, 2002)	184
Table 5.2: Material properties for modeling guardrail post steel.....	186
Table 5.3: Comparison of the C2500 between the NHTSA test and simulation model .	192
Table 5.4: Description of the impact of C2500 truck against the barrier concrete.....	197

LIST OF FIGURES

Figure 1.1: Weak post W beam guardrail (Ray and McGinnis 1997).....	6
Figure 1.2 Strong post W beam guardrail (Ray and McGinnis 1997)	7
Figure 2.1: (a) Stress acting on pile, (b) Soil adjacent to pile	23
Figure 2.2: I_{ph} Value of free head floating pile for a constant soil modulus (Poulos and Davis 1980)	25
Figure 2.3: I_{pM} and $I_{\theta h}$ Values of free head floating pile for a constant soil modulus (Poulos and Davis 1980).....	26
Figure 2.4: Yield displacement factor F_p of free head floating pile for a constant soil modulus F_p and P_y (Poulos and Davis 1980).....	26
Figure 2.5: Ultimate Lateral resistance of unrestrained rigid pile (Poulos and Davis 1980)	27
Figure 2.6: I'_{pM} and $I'_{\theta h}$ Value of free head floating pile for a linearly varying soil modulus (Poulos and Davis 1980).....	28
Figure 2.7: I'_{ph} Value of free head floating pile for a linearly varying soil modulus (Poulos and Davis 1980).....	29
Figure 2.8: Yield displacement factor F of free head floating pile for a constant soil modulus F'_p and P_y (Poulos and Davis 1980).....	29
Figure 2.9: Model for pile loaded laterally with p-y curves.....	35
Figure 2.10 P-y curve proposed by Reese et al., (1974).....	37
Figures 2.11: Resistance reduction coefficient A as function of relative depth after Mosher and Dawkins (2000)	39
Figure 2.12 Resistance reduction coefficient B as function of relative depth after Mosher and Dawkins (2000).....	40
Figure 2.13 Slip planes within the soil mass at mid plane of pile (2D approximation).....	41
Figure 2.14: Mohr's circle at rest, active and passive states	41
Figure 2.15: Mohr's circle at the failure envelope.....	42
Figure 2.16: Deflection load, shear and moment diagrams for a rigid pile in sand with unrestrained head displacement.....	44
Figure 2.17: Shape factors of laterally loaded pile in sand after Meyerhof & al., 1981 ...	47
Figure 2.18: Pressure diagrams and pressure distribution around the pile after Prasad and Chari (1999).....	49
Figure 2.19: a) Guardrail post in the soil. b) Guardrail post cross section.	52

Figure 2.20: Pressure diagrams and pressure distribution around the pile as proposed by Prasad and Chari (1999).....	54
Figure 2.21 a) View of the finite element model set for the static loading of the post in cohesionless soil, b) Details of the load mechanism system attached to the post	56
Figure 2.22 Vertical cross section of the soil mobilized during lateral loading of the post	57
Figure 2.23: Von-Mises stress distribution of the post embedded in the soil and subjected to lateral loading.	57
Figure 2.24 Fitting curve of the variation of Log(b/h) vs. Log(Kp).....	65
Figure 2.25: kp values for B/H = 0.1 for different friction angles.....	63
Figure 2.26 Relation of the maximum test load with the calculated test load for the static tests.....	70
Figure 2.27: View of the finite element model for the dynamic loading of the post in cohesionless soil	71
Figure 2.28: Load-deflection curve for static and dynamic cases.....	72
Figure 3.1: View of full-scale finite element model of guardrail system combining the subgrade with the continuum method (Kennedy et al., 2004).....	77
Figure 3.2: Schematic representation of the dynamic test set-up used by Coon et al., (1999).....	78
Figure 3.3 View of the finite element model of the post embedded in the soil.	80
Figure 3.4: Yield criterion in the plane of $\sqrt{J_2}$ and P.....	84
Figure 3.5 a) Horizontal cross section of finite element model of the soil and the post, b) Horizontal cross section of the finite element model of the inner soil and the post.	89
Figure 3.6: Comparison of load-deflection curve of dynamic test # 3 and that obtained using the continuum method.....	92
Figure 3.7 Dynamic loading simulation results of the continuum model at initial and deformed state.....	93
Figure 3.8: Variation of the impactor force as function of time obtained using the continuum method	94
Figure 3.9: View of the mass of soil mobilized at the top surface during impact obtained at 20 ms	95

Figure 3.10: Winkler beam in springs and dashpot foundation for laterally loaded dynamic pile (Novak, 1974)	96
Figure 3.11: Soil pile interaction for weakened soil around the pile circumference (Novak and Sheta, 1980)	97
Figure 3.12: Soil-post interaction model (El Nagggar and Bentley, 2000)	98
Figure 3.13: Configuration of soil-structure interaction (Tacioglu et al., 2006).....	99
Figure 3.14: Interaction of pile with soil represented by spring, mass and dampers Pacheco-Crosetti ,2007)	100
Figure 3.15: Proposed dynamic model for lateral post response	103
Figure 3.16: load deflection curve of the unidirectional spring calculated by Habibagahi and Langer approach for Coon et al (1999) test.....	103
Figure 3.17: View of the finite element model vertical cross-section of the soil mass mobilized during the impact at 20 ms.....	105
Figure 3.18: Comparison of dynamic test load-deflection curve for different displacement criteria.....	106
Figure 3.19: Approximate cross section of active mass at the ground level mobilized in the guardrail post test.	107
Figure 3.20: Variation of the impactor displacement as function of the time for different damping ratios.	109
Figure 3.21: Variation of the impactor load as function of the time for different damping ratios.....	110
Figure 3.22: Comparison of the dynamic test load-deflection curve obtained using both the subgrade and continuum methods.....	112
Figure 3.23: Post-soil model with initial interface gap	113
Figure 3.24: Comparison of the dynamic test load deflection curve obtained using the upgraded subgrade method with initial gap.....	113
Figure 3.25 Comparison of the impactor force as function of time for the base model and the base with lumped mass approach.....	114
Figure 3.26: Dynamic testing Set-up used by Dewey (1982)	118
Figure 3.27: Load deflection curves of the unidirectional springs calculated for the test (Dewey, 1982).	121
Figure 3.28: Comparison of the Dewey dynamic test load time history with the curve obtained using the improved subgrade method	121
Figure 4.1: Variation of the impactor load as function of time for different speed	126

Figure 4.2 Variation of the impactor displacement vs. time for different speed.....	127
Figure 4.3: Variation of the impactor displacement as function of the speed.....	127
Figure 4.4 Variation of the maximum impactor load and average load as function of the impact speed.	128
Figure 4.5 Plastic strain of the guardrail post at 80 ms and 160 ms.	130
Figure 4.6 Variation of the impactor load vs. time for different depth embedment.....	132
Figure 4.7 Variation of the impactor maximum load vs. post embedment	133
Figure 4.8: Variation of the impactor displacement as function of time for different depth embedment.....	134
Figure 4.9 Variation of the impactor maximum displacement as function of post embedment.....	134
Figure 4.10: Energy dissipation of the guardrail at different embedment.....	135
Figure 4.11: Variation of the impact load with time for different sand densities.	139
Figure 4.12: Variation of the impactor displacement as function of time for three sands densities of sand.....	139
Figure 4.13 Variation of the modification factor (MF) as function of the friction angle by different models	142
Figure 4.14: Effect of the impactor's mass on the load-deflection the guardrail post	144
Figure 4.15: Variation of the impactor displacement as function of time for mass impactor.....	145
Figure 4.16: Energy dissipation of the guardrail post for different mass impactor	145
Figure 4.17: Different blockout layout to absorb energy during the impact.....	148
Figure 4.18: Internal energy dissipation as function of time for the blockout design.....	151
Figure 4.19: Variation of the Impactor load as function of time for different crushable blockout systems.	151
Figure 4.20: Behaviour of the crushable system as function of time	153
Figure 4.21: Variation of impact load as function of time for different cohesive consistency.....	156
Figure 4.22 Variation of impact displacement as function of the time for different cohesive consistency.....	156
Figure 4.23: Steps involved in the use of Taguchi methodology	160
Figure 4.24: Crushable and non crushable blockout post	162
Figure 4.25: Variation reduction plot for smaller post deflection.....	179
Figure 5.1: Guardrail cross-section of the W beam after AASHTO (1998)	184

Figure 5.2: Finite element meshing of the W-beam.....	185
Figure 5.3: Finite Element meshing of the post guardrail	187
Figure 5.4: Subgrade modelling of the post-soil interaction.....	189
Figure 5.5: Details finite element model of pickup C2500	192
Figure 5.6: Load cell force time histories at front barrier of the NHTSA test and the Finite element simulation.....	194
Figure 5.7.Engine deceleration time histories for NHTSA test and the finite element simulation	195
Figure 5.8 Comparison of the vehicle C2500 after crash for the NHTSA test and the finite element simulation.....	196
Figure 5.9 Sequential overhead of impact event of NHTSA test and finite element simulation.	198
Figure 5.10 Sequential frontal view of impact event of NHTSA test and finite element simulation.	199
Figure 5.11: Finite element model of pickup truck impacting guardrail system.....	200
Figure 5.12: Velocity time-history at the C.G. of the vehicle for the dynamic test and the finite element analysis.	202
Figure 5.13: Roll angle displacement-time history at the C.G of the vehicle for the dynamic test and the finite element analysis.....	203
Figure 5.14: Sequential frontal view of impact event of NHTSA test and finite element simulation.	204
Figure 5.15 Sequential overhead of impact event of dynamic test and finite element simulation.	205
Figure 5.16: Post deflections of the guardrail system in the longitudinal axis (X) during the pickup impact.....	207
Figure 5.17 Post deflections of the guardrail system in the transversal axis (Y) during the pickup.	208
Figure 5.18 Speed of the posts in the longitudinal and transversal axis during the pickup	208
Figure 5.19 a) Side view of post # 13 at 80 ms. b) Top view of the post #13 at 80 ms..	209
Figure 5.20: Force applied on the posts during the crash event of the full scale crush test.	209
Figure 5.21 Sequential frontal and side views of the finite element simulation of the C2500 impacting the guardrail system with crushable blockout.	212

Figure 5.22: Velocity time-history at the C.G. of the vehicle for the dynamic test and the finite element analysis for crushable un-crushable blackout.....	213
Figure 5.23: Roll angle as function of time history at the C.G of the vehicle for the dynamic test and the finite element analysis for crushable and non-crushable blackout.....	213
Figure 5.24: Crushable blackout of the post 12 to 15 during the impact.....	214
Figure 5.25: Deflection of the Posts 13 and 14 in the transversal axis (X) during the pickup impact for base and the crushable models.....	214
Figure 5.26 Deflection of the Posts 13 and 14 in the transversal axis (Y) during the pickup impact base and the crushable models.....	215
Figure 5.27: Plastic strain of the guardrail at 100 ms for the baseline model.....	215
Figure 5.28: Plastic strain of the guardrail at 100 ms for the baseline with crushable blackout	216

Chapter I

Introduction

1.1 Research background

Canadians are among the most mobile people in the world. Statistics show that 74% of citizens aged 16 years or older own a motor vehicle and travelled an average of 16,000 kilometres on Canada's roadways during the year 2004, Transport Canada, (2006). The number of licensed drivers jumped from 17.1 million in 1988 to over 22.5 million in 2005, Transport Canada (2010). This level of mobility comes with a price. In fact, Statistics Canada shows that the number of accidents, though decreased during the last decade, still remains high as illustrated in Table 1.1. The number of fatalities decreased from 4154 in 1988 to 2767 in 2007 whereas the number of serious accidents decreased from 28031 in 1988 to 13723 in 2007. The cost of the reported accidents in 2004 was approximately \$63 billion Vodden et al., (2007). Because of the deaths and injuries, traffic collisions continue to be the major transportation safety problem in Canada and remain one of the leading contributors to years of lost life among Canadians, due in large part to deaths among young people, Transport Canada (2006). In the United States, Baker and Krueger (1992) reported that in 1985 motor vehicle accident injuries cost \$49 billion dollars in hospital spending, therapy and indirect costs.

The vehicles are subjected to different kinds of collision: full front, rear impact, side impact, rear angular impact, rollover etc... Accidents can happen in the city, at low speeds, or on the highways at higher speeds. In order to improve the vehicle performance and reduce the motor vehicle injuries and fatalities, government organizations issue regulations and safety standards. The reduction of injuries can be achieved either by enhancing the traffic regulation or by implementing more active safety features or by improving passive safety performance of the vehicle.

Table 1.1: Collisions and casualties ⁽¹⁾ in Canada from 1988 to 2007

Transport Canada (2010)

Year	COLLISIONS		VICTIMS		
	Fatal ⁽²⁾	Personal Injury ⁽³⁾	Fatalities ⁽⁴⁾	Serious Injuries ⁽⁵⁾	Injuries ⁽⁶⁾ (Total)
1988	3610	190094	4154	28031	278820
1989	3651	192595	4238	27422	285178
1990	3445	178515	3963	25183	262680
1991	3228	170693	3690	26035	249217
1992	3073	169640	3501	25521	249823
1993	3121	168106	3615	23902	247593
1994	2837	164642	3230	22830	241899
1995	2817	161950	3313	21494	238458
1996	2679	153966	3062	18737	227320
1997	2617	147538	3033	17294	217403
1998	2576	145612	2911	16409	213304
1999	2635	148660	2984	16186	218437
2000	2569	153273	2927	15579	222830
2001	2432	148961	2776	15282	216441
2002	2594	153850	2932	15906	222706
2003	2486	150473	2768	15104	216089
2004	2430	145256	2722	15605	206232
2005	2558	145604	2905	15812	204751
2006	2610	142508	2895	15861	199966
2007	2469	138470	2767	13723	194177

⁽¹⁾ "Collisions and casualties" were revised from 1996 to 2006 based on submissions from one jurisdiction

⁽²⁾ "Fatal collisions" include all reported motor vehicle crashes that resulted in at least one death, where death occurred within 30 days of the collision, except in Quebec (8 days)

⁽³⁾ "Personal injury collision" include all reported motor vehicle crashes that resulted in at least one injury, but not death, within 30 days of the collision, except in Quebec (8 days)

⁽⁴⁾ "Fatalities" include all those who died as result of a reported traffic collision within 30 days of its occurrence, except in Quebec (8 days)

⁽⁵⁾ "Serious injuries" include persons admitted to the hospital for treatment or observation. Serious injuries were estimated from 1988 to 2006 because several jurisdictions underreported these numbers

⁽⁶⁾ "Total injuries" include all reported severities if injuries ranging from minimal to serious.

In Canada, the Ministry of Transportation is the official entity that regulates vehicle safety. The Transportation Development Centre (TDC) is Transport Canada's central research and development branch, under the Policy Group's Transportation Technology and Innovation directorate. As Transport Canada's centre of expertise for research and development, it manages a multimodal R&D program aimed at improving the safety, security, energy efficiency, and accessibility of the Canadian transportation system, while protecting the environment. Its mandate is to enhance the department's technological capability, to address the department's strategic objectives and federal government priorities, and to promote innovation in transportation.

Many studies have been conducted to investigate the safety effect of guardrails on accidents and the cause of harm in crashes involving guardrail contact. Transport Canada provides national leadership with the collection of traffic accident, the data analysis and the development of programs to reduce traffic accidents. Many programs and initiatives have been introduced for this matter, such as the drinking and driving laws in 1969, the mandatory seat belt usage laws and public education campaigns helped to decrease the annual traffic deaths, Transport Canada (2006).

One part of the overall strategy for reducing the fatalities and improving the roadside safety has been the use of roadside safety appurtenances such as guardrails and median barriers in highways, (Ray and McGinnis 1997). The guardrails are one the common basic roadside devices used in Canadian highways. The main goal of the guardrail is to prevent the errant vehicle from leaving the roadside. The data of Table 1.2 shows that the number of fatalities in accidents involving vehicles impacting the guardrail is higher than the number of fatalities of vehicles that run off the roadways, Transport Canada (2001).

Table 1.2: Statistics of vehicle involved in fatal collision by vehicle event (Transport Canada 2001)

Event/Year	1988	1989	1990	1991	1992	1993	1994	1995	1996	1997
Other/Unknown event	5049	5064	4993	4552	4314	4540	4198	4111	3853	3770
Hit other vehicle	2974	3293	3087	2717	2683	2876	2677	2607	2332	2324
Ran off the roadway	857	702	731	672	670	715	556	590	495	498
Overturned	599	591	555	542	493	480	417	441	342	394
Hit pedestrian	562	476	562	472	432	456	378	407	436	371
Hit ditch, earth bank	552	422	428	386	397	408	358	375	316	352
skidding sliding	421	483	404	400	412	428	384	378	349	388
Hit rigid posts, pole	300	257	245	221	207	188	197	194	205	184
Hit low rigid obstacle	174	160	130	120	120	116	120	98	111	86
Hit guardrail, median	169	150	144	122	126	108	107	103	101	87
Hit tree	128	119	100	132	126	126	99	109	99	111
Hit bicycle	111	67	69	65	50	65	47	41	36	43
Hit other object	96	99	99	107	89	87	63	87	75	74
hit wall, road structure	94	74	61	53	59	50	46	42	46	45
Fire, explosion	77	53	45	46	48	53	52	47	36	45
Other non-collisions event	77	76	68	49	63	49	73	57	62	51
Hit other vehicle type	74	94	85	84	56	55	82	59	53	63
Hit barricade, fence	55	48	29	29	26	25	24	26	18	16
Hot rock face	43	33	36	33	32	25	38	24	31	14
Hit rail vehicle	42	62	38	46	52	32	39	27	53	26
Submersion	39	29	37	35	37	33	43	43	28	36
Hit snow bank, drift	20	34	20	14	16	23	3	25	25	26
Hit tree, bush	19	21	17	18	17	16	14	24	15	14
jack-knife	16	13	7	13	11	9	9	15	10	9
Hit animal	12	11	22	20	18	22	18	26	24	11
Hit other moving object	10	8	5	5	2	5	3	4	3	1
Hit crash cushion	3	4	9	1	2	5	10	6	7	4

In general, the best designs cannot eliminate all serious injuries and all fatalities. The guardrails are installed when the risk of striking an object on the highway is judged more

serious than striking the guardrails. The guardrail system is composed of a post embedded in the soil to hold the rail that is mounted at the top of the post. The post material is in generally made of wood with a circular or rectangular cross section or steel W shape beam. Other types of guardrail could be found in the highways, such as concrete barriers used as median barriers to prevent median crossover accidents. These barriers could be installed easily in narrow spaces and remain very effective in keeping vehicles from crossing into opposite lanes. Two main guardrail systems are implemented in Canadian and American highways: the weak-post barrier system and the strong-post barrier system. A very good summary of the advantages and disadvantages of each system was presented by Ray and McGinnis (1997)

1.1.1 Weak-post guardrail system

The weak-post guardrail consists of a post embedded in the soil to a certain depth and holding directly the W guardrail beam or tension cables as shown in Figure 1.1. The spacing between the posts is specified to be 5000 mm for the guardrail cable and 3810 mm for the W beam. The primary objective of the weak-post guardrail is to gradually redirect the errant vehicle by dissipating the energy in stretching the cables and bending the posts. The deflection of the cables could reach 4 m which requires that free space should be available behind the barrier fence. The main advantages of the weak-post systems are (i) the relatively low cost of installation, (ii) the relatively good crashworthiness performance and (iii) no accumulation of the snow on the roadways in the cable type. However, the main disadvantages are (i) the relatively high repair cost in high-traffic highways, (ii) the restricted application to low volume traffic and (iii) the need to re-tension the cable periodically to keep the guardrail system functional. The W beam weak-posts are also relatively inexpensive to install but remain limited to roadways with a low traffic volume. The main disadvantage of this type of guardrail is the poor crashworthiness performance noticed during the impact with vans and pickup trucks. The weak-post passed the requirement of level 2 (TL2) of the report 350 (Ross et al., 1993) but failed the higher test level 3 (TL3). To perform per design, the post should separate from the beam guardrail during the impact by failing the bolt attaching the beam to the post. By separating the post from the rail, the vehicle continues to interact with the rail and to be redirected. This failure mechanism can occur also when the snow

and ice are plowed against the barrier causing the rail to fall down which requires an immediate repair. When the rail is mounted on wood posts, the failure mechanism is not usually successful and the post can pull the guardrail to the ground during the impact which can result in the vehicle overriding the guardrail system. For this reason, the weak wood post is not recommended. In general, the poor performance of this system in full crash testing during the impact with a pickup truck raised a concern about the use of this system on highways.

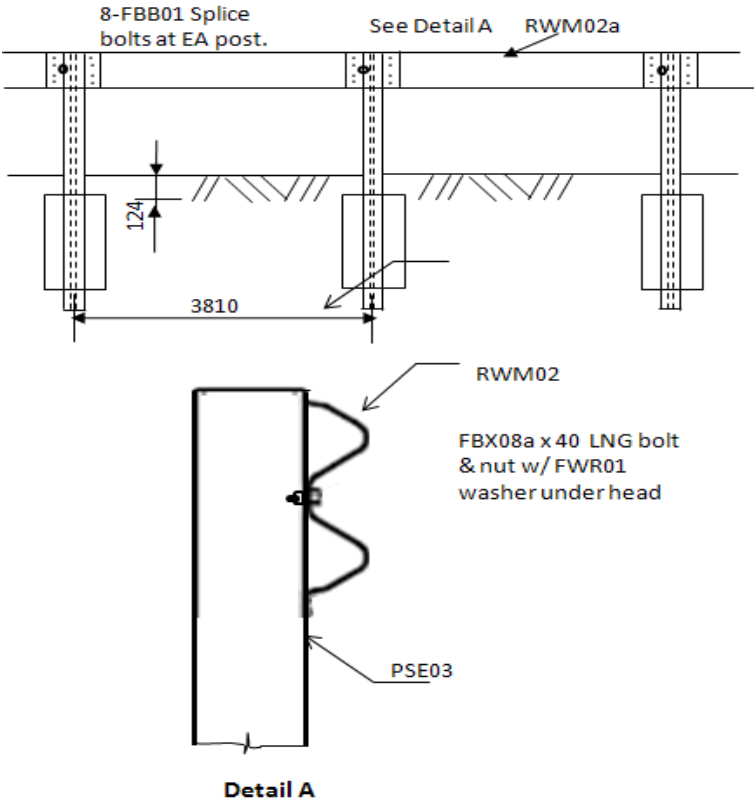


Figure 1.1: Weak-post W beam guardrail (Ray and McGinnis 1997)

1.1.2 Strong-post guardrail system

The strong-post guardrail system consists of a W beam or wood post embedded in the soil to a specific depth and holding a guardrail fence separated from the post by a separator called blockout. This blockout is either a W-shape beam or could be of wood

with a rectangular cross section as shown in Figure 1.2. M14 bolt attaches the post to the guardrail. A variety of posts and blockouts for the strong-post W beam are being used in Canada and in the USA. However, the most common posts are the W 150x12.6 steel beams and the rectangular wood of 140 x 190 mm cross-section. The posts are spaced by 1905 mm and the height of the post above the ground is 730 mm. The strong-post W beam has become the most popular guardrail system because of its relatively low cost. They could be implemented when very limited room is available.

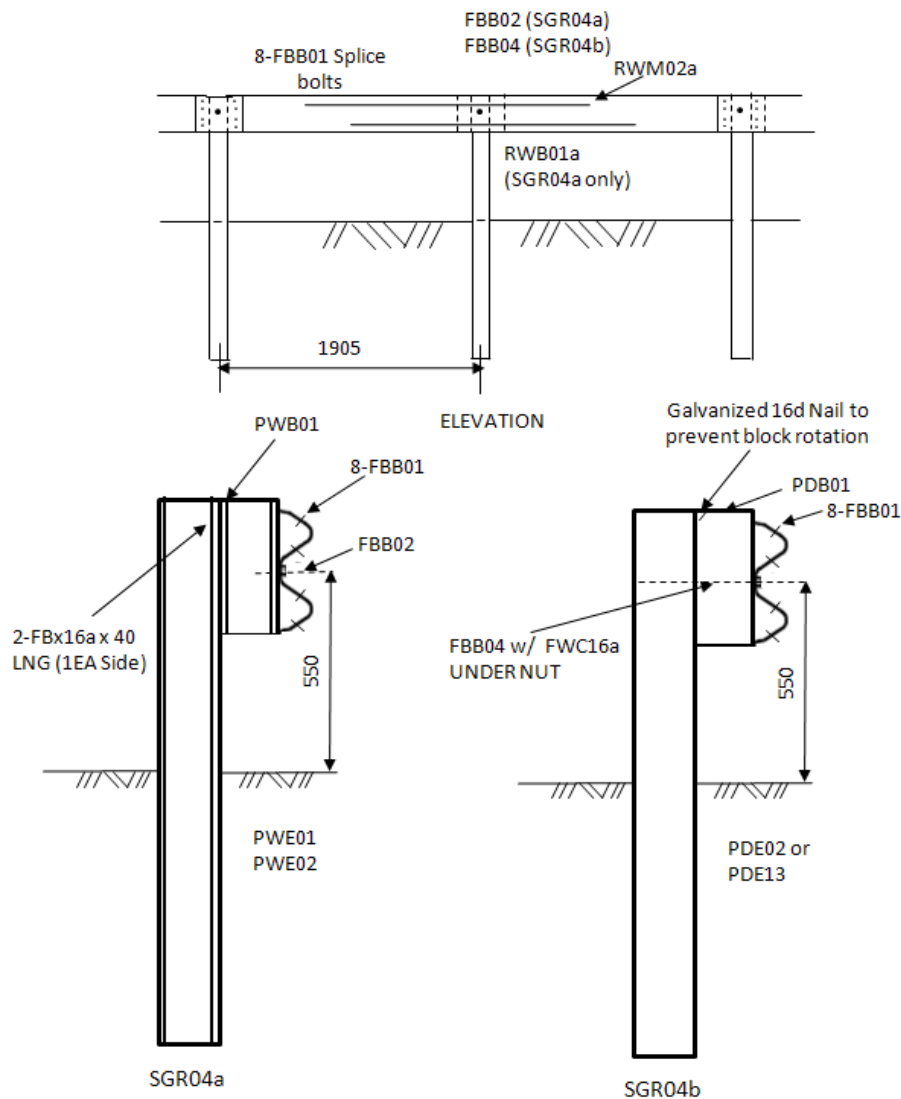


Figure 1.2: Strong-post W beam guardrail (Ray and McGinnis 1997)

Many full crash tests have been conducted to evaluate the crashworthiness of the strong-post with different options. One major concern that was noticed in most of the tests is the snagging of the wheel with the post that causes a severe damage to the front tire and the suspension of the impacted side. The test reported by Mak and Menges (1994) shows that a pickup truck rolls over after wheel snagging and the barrier did not meet the level TL3 of service. The failure mechanism of the W beam occurs because of the twisting of the post around the vertical axis then bending to the ground. In other tests, the wood blockout failed during the impact and the guardrail impacted directly the edge of the post which caused the complete shear and the failure of the guardrail. As a result, the pickup truck passed through the guardrail system. For the case of the wood post, tests show that posts rotated in the soil surrounding the post pushing the soil in the front of the post causing the soil failure. If the soil is dense, the post could fracture under ground level at the location of maximum bending moment. The soil conditions are very important factors and any variation on these parameters results in different post reactions. Patzner et al., (1999) found that the maximum guardrail deflection was relatively high for soils with a lower effective unit weight and as the effective unit weight of the soil initially increased, the maximum deflection decreased.

The strong-post should be installed with enough length to protect the vehicles from localized hazardous situations (trees, culverts, etc). If they are short, the guardrail systems could not offer adequate resistance and can become even more hazardous themselves. In fact, full scale tests conducted by the State of California showed that the unanchored guardrail less than 19 m long was ineffective to redirect a 2000 kg large passenger vehicle travelling at 100 km/h and 25° angle of impact (Ray and McGinnis, 1997).

1.1.3 History of the crash test requirements for the guardrail system

Since the installation of guardrails in the early fifties of the last century, the guardrail installation and testing procedures are constantly re-evaluated to accommodate the change in vehicle fleet and operating conditions. In 1958, California and General Motors conducted a series of full crash tests to assess the performance of the existing guardrail.

These tests put the first stone for the procedures of the full-scale vehicle crash testing of guardrails that was first published in 1962 (Highway Research Circular 482). This procedure was a one-page document where the vehicle mass, impact speed, and approach angle for the crash tests were specified. *Circular 482* made the first step to measure the barrier performance and standardize the testing procedures.

In 1974, National Cooperative Highway Research Program (NCHRP) published the second report entitled "Recommended Procedures for Vehicle Crash Testing of Highway Appurtenances," to address the gaps that were not covered in *Circular 482*. The 16-page report, called Report 153, was based on technical input from individuals and agencies. In 1987, the American Association of State Highway and Transportation Officials (AASHTO) recommended to update *Report 230* (Michie, 1981) AASHTO recognized the drastic changes in the vehicle fleet, the emergence of many new barrier designs in service at highways, the promulgation of new policies requiring the use of safety belts, the increasing interest in matching safety performance to levels of roadway utilization and the huge advances in computer simulation and other evaluation methods. *NCHRP Report 350* (Ross et al., 1993) was published to present a comprehensive update and revision of the procedures for safety performance evaluation. It recognized that the larger passenger sedan is not present in the vehicle population. As reported in Report 350, the changes implemented with regards to Report 230 are as follows:

1. The report adopted the metric units in anticipation of the U.S. conversion to SI units of measurement. Hard conversions were made in the update process, which will alter the mass, speeds, and tolerances used in testing.
2. It provides a wider range of test procedure to permit safety performance evaluations for a wider range of barriers, terminals, crash cushions, breakaway support structures and utility poles, truck-mounted attenuators, and work zone traffic control devices.
3. It uses a 3/4-ton pickup truck as the standard test vehicle in place of the 4500-lb passenger car to reflect the fact that almost one-quarter of the passenger vehicles on U.S. roads are in the "light truck" category. This change was made recognizing the

differences in wheel bases, bumper heights, body stiffness and structure, front overhang, and other vehicular design factors.

4. Report 350 defines other supplemental test vehicles including a mini-compact passenger car (700 kg), single-unit cargo trucks (8000 kg), and tractor-trailer vehicles (36,000 kg) to provide the basis for optional testing to meet higher performance levels.

5. Report 350 includes a broader range of tests for each category of safety feature to provide a uniform basis for establishing warrants for the application of roadside safety hardware that consider the levels of use of the roadway facility. Six basic test levels are defined for the various classes of roadside safety features, and a number of optional test levels are defined to provide the basis for safety evaluations to support more or less stringent performance criteria.

6. The report includes guidelines for the selection of the critical impact point for crash tests on redirecting-type safety hardware.

7. It provides information related to enhanced measurement techniques related to occupant risk and it incorporates guidelines for device installation and test instrumentation.

8. The three basic evaluation criteria categories remain the same and are defined as:

a- The occupant risk criterion retains the use of the flail space model, but defines preferred and maximum levels of occupant impact velocity and acceleration.

b- The lateral occupant impact velocity limits were altered to be equivalent to longitudinal limits to reflect recent research findings.

c- The redirection criteria were altered to incorporate a limiting 12 m/s vehicular velocity change requirement in the longitudinal direction.

9. Report 350 reflects a critical review of methods and technologies for safety-performance evaluation, such as surrogate test vehicles and computer simulations, and incorporates state-of-the-art methods in the procedures.

10. Report 350 provides optional criteria, established by others, for side impact testing.

1.1.4. Design requirements of the guardrail post

Strong-post used in longitudinal traffic barriers could be designed and tested for one of six "test levels" as defined in Report 350 guidelines. A test level is defined by impact conditions (speed and angle of approach) and the type of test vehicle (ranging in size from a small car to a fully loaded tractor-trailer truck). In general the lower test levels are used to evaluate the feature designed and implemented on a low service level roadway such as a rural collector or local road while the higher test levels are applicable to evaluate the features used on higher service level roadways or at locations that require a special high-performance barrier (Ross et al., 1993). Test level 3 (TL-3) represents the basic level to which most existing hardware is designed to that level.

As shown in Table 1.3, Test level 3 TL-3, recommends two tests for the evaluation of the guardrail system, Test 3-10 and Test 3-11. Test 3-10 consists of 820 kg passenger vehicle travelling at a nominal speed of 100 km/h and impacting the guardrail barrier at an angle of 20° while Test TL 3-11, consists of 2000 kg, pickup truck, travelling at a speed of 100 km/h and impacting the guardrail barrier at angle of 25°. The two tests cover the impact of most of the vehicle fleet with the guardrail system. The tests recommended are based on past experience and accidents data. It is obvious that TL3-11 is harder to achieve because of the level of energy involved and the higher center of gravity of the vehicle.

1.1.5. Full crash testing and simulations

The objective of roadside safety engineers is to design the safest economical hardware able to absorb large amounts of energy and safely contain the impacted vehicle. Analyzing such system is complex because it involves dynamic loading, very large deformations, material failure and nonlinear elastic material. For all these conditions, it is impossible to derive the solution of the problem in a closed form. To solve the problem of designing roadside hardware, two established methods are often utilized: component or full scale testing and the nonlinear explicit finite element method (Bendidi, 2002)

Table 1.3: Test matrix for longitudinal barriers (Ross et al., 1993)

Test Level	Barrier Section	Test Designation	Impact Conditions ^c			Impact Point
			Vehicle	Nominal Speed (km/h)	Nominal Angle, θ (deg)	
1	Length of Need	1-10 S1-10 ^a 1-11	820C 700C 2000P	50 50 50	20 20 25	(b) (b) (b)
	Transition	1-20 ^d S1-20 ^a 1-21	820C 700C 2000P	50 50 50	20 20 25	(b) (b) (b)
2	Length of Need	2-10 S2-10 ^a 2-11	820C 700C 2000P	70 70 70	20 20 25	(b) (b) (b)
	Transition	2-20 ^d S2-20 ^a 2-21	820C 700C 2000P	70 70 70	20 20 25	(b) (b) (b)
3 Basic Level	Length of Need	3-10 S3-10 ^a 3-11	820C 700C 2000P	100 100 100	20 20 25	(b) (b) (b)
	Transition	3-20 ^d S3-20 ^a 3-21	820C 700C 2000P	100 100 100	20 20 25	(b) (b) (b)
4	Length of Need	4-10 S4-10 ^a 4-11 ^d 4-12	820C 700C 2000P 8000S	100 100 100 80	20 20 25 15	(b) (b) (b) (b)
	Transition	4-20 ^d S4-20 ^a 4-21 ^d 4-22	820C 700C 2000P 8000S	100 100 100 80	20 20 25 15	(b) (b) (b) (b)
5	Length of Need	5-10 S5-10 ^a 5-11 ^d 5-12	820C 700C 2000P 36000V	100 100 100 80	20 20 25 15	(b) (b) (b) (b)
	Transition	5-20 ^d S5-20 ^a 5-21 ^d 5-22	820C 700C 2000P 36000V	100 100 100 80	20 20 25 15	(b) (b) (b) (b)
6	Length of Need	6-10 S6-10 ^a 6-11 ^d 6-12	820C 700C 2000P 36000T	100 100 100 80	20 20 25 15	(b) (b) (b) (b)
	Transition	6-20 ^d S6-20 ^a 6-21 ^d 6-22	820C 700C 2000P 36000T	100 100 100 80	20 20 25 15	(b) (b) (b) (b)

The full scale and the component method remains the traditional design method that has been used for decades. It is an expensive method that needs extensive instrumentation and careful handling if dummies are incorporated. The main drawback of this method is that many parameters cannot be controlled before and during the test. These include the point of the impact, the contact between the post and the soil, the speed and angle of impact, failure of the wiring, bad channels...etc

The literature dealing with the highway guardrail impact is very rich and diversified. The following review is a survey of the test conducted in the roadside safety area.

Bronstad and Burket (1971) described five full-scale crash tests performed in 1968 for the Ohio Department of Highways with a timber weak-post W-beam system. The purpose of these tests was to determine whether the system met the then-current crash test requirements. This system used timber posts connected to W-beam a guardrail. A full-size, 2000-kg, four-door sedan, impacted the system at a speed of 110 km/h and an impact angle of 25°. The post-rail connection in the test consisted of a 7.94 mm diameter bolt with front and rear washers and a nut behind the post. The connection was supposed to fail due to shearing the bolt but the bolt and rear washer were instead pulled through the post material. Even though the vehicle was redirected, loss of rail height and lack of sufficient post strength allowed it to straddle the rail which contributed to multiple rollovers.

Ivey et al., (1986) performed full-scale crash tests with conventional W-beam and thrie-beam guardrail systems that were impacted by heavy vehicles. Two crash tests were conduct with a bus at different speeds, 89.5 km/hr and 96.0 km/h and an impact angle of 13.5° and 15.0° respectively. The bus weight was kept equal to 9081 kg for both tests. It was concluded that the two tests failed: the first test resulted in 90° roll over and the second test resulted in a penetration into the guardrail. Few countermeasures were introduced to the guardrail design consisting in raising the height of the barrier, increasing the blockout depth to 360 mm, increasing the depth of the post embedment and changing the rail to a thrie-beam guardrail. The modified guardrail was retested under the same loading condition and the results were considered satisfactory and no snagging was observed.

Elvik (1995) reported the results of the analysis of 32 evaluation studies that have qualified the effect of guardrails and crash cushions on the probability and severity of accidents. His analysis showed that the guardrails reduce the number of accident fatality and their severity. This result applies both to new installations and to replacements. Results showed that the guardrails reduce the chance of sustaining a fatal injury by about 45%.

Rosson et. al., (1996) assessed guardrail strengthening techniques by conducting crash tests on W-beam guardrails strengthened by nesting the W-beam and reducing the post spacing by half. The test results found that nesting the W-beam provided little benefit, whereas reducing the post spacing increased the guardrail performance considerably. Similar results were obtained in the crash tests performed in Japan by Seo et al., (1995). The authors modified the existing guardrails, to reduce the injury severity in high-speed collisions. They observed that the installed guardrails resulted in high injury severity due to the increased mileage of the national expressways and the increased speed limits adopted on these highways. The guardrails were modified by strengthening the posts, replacing the weak-posts by strong-posts and reducing the post spacing. The modified guardrails were found to perform well and respond favourably in high-speed impact collisions.

Wright and Ray (1996) described the techniques for modeling steel materials in LS-DYNA3D (Hallquist, 2006) software used to simulate guardrail materials. To validate the finite element model, quasi static laboratory tension tests were performed on guardrail steel coupons and compared to the results of finite element solutions. Two different material models were retained for modeling the guardrail steel, the kinematic/isotropic elastic-plastic material model (Type 3) and the rate-dependent tabular isotropic elastic-plastic material model (Type 24). The authors came to the conclusion that “material Types 3 and 24 are not adequate for modeling strain rate effects for AASHTO M-180 guardrail” and therefore, they did not include strain-rate effects in the models.

Shukla (1997) investigated the quasi-static tension test for roadside hardware material using LS_DYNA3D and compared with the standard laboratory tests. The author simulated the soil with different material models. He showed that the material “Piecewise-linear-plasticity” model 24 is the most computationally but the most accurate as comparable to the test data.

Plaxico et al., (1998) investigated the post-soil interaction. They discussed the finite element modeling of wooden guardrail posts and the interaction with the soil during impact events using the nonlinear finite element program LS-DYNA3D. They found that

their finite element results are comparable to pendulum tests. The post-soil interaction was modeled using the subgrade reaction approach which involves an array of nonlinear springs attached along the length of the post below grade.

Kilareski and al., (1999) reported the results of three full-scale crash tests with the G2-system performed in 1998 by the Pennsylvania Transportation Institute. These tests were at NCHRP Report 350 test level-3 conditions (i.e., a 2000-kg pickup truck, 100 km/h, and 25°) The objective of the tests was to determine whether the weak-post W-beam guardrail system meet the Report 350 level-3 requirements. The first two tests did not conform to test level-3 since the impact speed was much lower than the required 100 km/h. The third test, however, did conform to test level-3 conditions. The test vehicle impacted the system between post 5 and 6. The rail ruptured at the splice at post 7 and the vehicle penetrated the barrier. The system performance was poor with a rail splice rupture occurring at the splice on post 7. The rupture occurred approximately 0.228s after impact and occurred when the right front corner of the test vehicle was between post 8 and 9. The maximum deflection was 1.5 m just before panel rupture.

Reid (1999) developed a new post design of mailbox using nonlinear finite element analysis. The new breakaway concept consisted of modifying the existing anchor bolt configuration to include bolts fabricated from high strength and a lower percentage elongation. A Honda Civic full car model was used to impact the system. The soil was assumed to be rigid.

Bendidi (2002) evaluated the crash performance of G4-1S guardrail system with two different designs: post with routed and non-routed blockout. He developed a finite element model including the post, the soil, the W-beam and the impactor. The model was validated in the component level against available static and dynamic tests of a single I-beam embedded in gray clay soil. The full model was impacted by a pickup truck traveling at 100 km/h with 25° impact angle. LS-DYNA (Hallquist, 2006) was used as finite element code to perform the simulation. He showed that roll angles are greater for the guardrail system with non-routed than with the routed blockout.

Kennedy et al., (2004) evaluated the performance of new post and W beam system under impact conditions consistent with report 350 using finite element simulation. A finite element model of the guardrail was developed and the non-linear finite element program LS-DYNA was used to impact a 2000-kg pickup truck into the system. The soil was modeled in the analysis using the horizontal subgrade modulus approach in which the horizontal subgrade modulus was used to determine the properties of the nonlinear springs that simulate the soil resistance. The results of their analysis indicated that the system would safely contain and redirect the vehicle.

Faller et al., (2004) conducted a full crash test for the development of the Midwest Guardrail System in order to provide increased safety for higher center-of-mass vehicles, provide reasonable barrier height tolerances, and reduce the potential for W-beam rupture. They evaluated guardrail stiffening and determined appropriate guardrail placement guidelines for shielding rigid hazards using full-, half-, and quarter-post spacing designs. They developed a guardrail-to-curb barrier combination that provides increased hydraulic capacity and placement farther in front of the rail face to reduce the frequency of snow plow damage to guardrails. All development and testing of the Midwest Guardrail System was conducted in accordance with Test Level 3 (TL-3) safety performance criteria set forth in NCHRP (Ross et al., 1993). The research study also included dynamic bogie testing on steel posts placed at various embedment depths and computer simulation modeling, using BARRIER VII software program, to analyze and predict dynamic guardrail performance. Recommendations for the placement of the original Midwest Guardrail System as well as its stiffened variations were also made.

Wu and Thompson (2007): investigated the interaction of gravel and post through experiments and computer simulations. In the experimental research, the force applied directly to the post was measured to obtain the strength of the single post anchored in gravel. Two corridors were formed from the measured data of the quasi-static and dynamic tests. When a test was repeated using an identical post, the measured resistance force showed some differences probably because the degree of compaction of gravel around the post was not exactly the same. A parametric study was subsequently conducted to investigate the influence of the gravel stiffness on the soil–

post interaction through computer simulations using LS-DYNA. The numerical results showed that the LS-DYNA soil and concrete model and the Cowper–Symonds steel model effectively captured the soil–post interaction since the calculated strength of the post agreed with the range of the test data. The input parameters for the soil and concrete material model were recommended for roadside gravel in crash analyses.

1.2 Summary and objectives of the current study

From the literature study it was found that many static tests have been conducted on posts embedded in the soil. The loading was in general very slow to assume that lateral loading was static. However, no correlation has been established between the static and the dynamic load as function of the soil stiffness and no study has been conducted to evaluate the maximum static load as function of the soil parameters and to develop a theoretical formulation for laterally loaded posts embedded in either cohesionless or cohesive soil under static conditions.

The literature review shows increasing use of the finite element method. In fact, the impact simulation using the explicit nonlinear finite element code is becoming an effective tool in the stages of design and validation in the roadside area. The prediction accuracy of these models depends upon the inputs. Some work has been performed to study the interaction of the soil with the guardrail post on component and full scale levels. However, the model developed presented many limitations such as the absence of the soil inertia and soil damping when the subgrade model is used.

To contribute to fill these gaps, the major contribution of this dissertation research is expected to help engineers in the roadside safety area to:

- Understand the interaction of the guardrail post with the surrounding soil during static dynamic load.
- Develop theoretical formulation for laterally loaded posts embedded in cohesionless soil under static condition.

- Develop a finite element model that encompasses all the soil parameters namely: stiffness, damping and inertia effects and able to predict accurately the dynamic tests.
- To perform finite element simulation to understand the contribution of the different parameters in the post response.
- To use the results of the parametric studies to develop a guardrail system, using crushable spacer offering better performance during the impact with a vehicle.

1.3. Organization of the dissertation

The following outlines the organization of this dissertation.

Chapter I: **Introduction** provided a brief description on the importance of research on the area of roadside safety, a summary of the procedure and a description of different guardrail implemented in the highways in Canada and in USA. It also summarizes the literature review that les to the objectives of this thesis.

Chapter II: **Behaviour of Guardrail posts subjected to static lateral load.** This chapter summarizes the computation of the ultimate load for different methods available in the geotechnical field. A new method based on the evaluation of the passive lateral earth pressure in 3D is developed and compared to field tests.

Chapter III: **Analysis of laterally impacted guardrail posts.** In this chapter, a new model for guardrail posts embedded in soil and impacted dynamically was developed including all relevant soil components such as the soil stiffness, the soil damping and the soil mass involved in the dynamic impact. The two conventional methods for simulating the guardrail post were analyzed. The mass of the soil and the damping effect were introduced in the subgrade method to simulate more accurately the load deflection curve of the impactor. The approach developed initially for cohesionless soil was applied to the case of cohesive soil

Chapter IV: **Parametric study of the post guardrail embedded in soil.** In this chapter, the effects of the different test parameters on the interaction of the post and soil were evaluated. Five parameters were evaluated and analyzed, namely,: impactor speed, impactor mass, the post embedment depth, the blockout crushability and the soil density. A finite element model of a guardrail post was used to conduct the study which suggested design guidelines to improve the soil-post interaction for the full-scale crash test. Design of Experiment (DoE), a powerful statistical technique for the study of multiple variables simultaneously, was conducted to investigate the interaction between the different parameters and the contribution of each parameter to the guardrail post reaction. Taguchi method, extensively applied in industry, was selected among the various DoE methods available in practice to study the effects of experimental parameters.

Chapter V: **Full-Scale finite element model development and analysis.** The main objective of this chapter was to implement the conclusions and recommendations of chapter III and the parametric and the design of experiment study to build a full-crash test model of a vehicle travelling at 100 km/h and impacting the guardrail with an angle of 25° as defined by NCHRP Report 350. A finite element model of the C1500 Chevrolet pickup truck was built and correlated dynamic frontal crash test conducted by NHTSA (National Highway Transport Safety Administration).

Chapter VI: **Conclusions and recommendations.** This chapter discussed the conclusions of the present research and presented recommendations for future work.

Chapter II

Behavior of Guardrail Posts Subjected to Static Lateral Load

2.1. Introduction

To understand the interaction between the guardrail post and the soil, researchers conducted experimental tests and computer simulations for both quasi-static and dynamic loading cases. These tests measured different parameters, such as the impact force and the post displacement. Many impact tests have been conducted on the guardrail system to determine its efficiency. It was found that the energy dissipation of the system and the ability to redirect an errant vehicle are influenced primarily by the soil-post interaction (Dewey, 1982). The post of the guardrail system embedded in the soil and impacted laterally by an impactor could be analyzed as a conventional problem of a pile embedded in the soil and loaded laterally. During the last decades, numerous methods have been proposed to analyze the problem of laterally loaded piles. These methods include simple approaches, using design charts, to more complex and sophisticated models. Such methods are very diverse but could be grouped into the following categories:

- 1- Linear elastic procedure
- 2- The subgrade method
- 3- The P-Y method
- 4- Limit analysis
- 5- The Finite element method

Most of these methods have been developed for the geotechnical problems where the failure criteria occur for small deformations. In the Canadian engineering practice, three failure modes of the vertical pile loaded horizontally could be defined (Canadian Geotechnical Society 2006), namely:

- 1- The capacity of the soil may be exceeded, resulting in a large horizontal movement of the piles and failure of the foundation.

- 2- The bending moment and/or shear may generate excessive bending or shear stresses in the pile material, resulting in a structural failure of the piles and
- 3- The deflections of the pile heads may be too large to be compatible with the superstructure.

These conditions of failure are apparently not applicable to the case of the guardrail post loaded laterally where the post is not designed to hold a structure. The failure criteria are not related to the maximum displacement of the pile/post or to the capacity of the soil but to the capacity of the guardrail system to redirect errant vehicles. The problem of the post embedded in the soil is not similar to the conventional problem of the pile. Two types of posts are commonly used in highways namely: the circular wood post and the W152x13.5 steel beam. The wood post has an approximate diameter of 180 mm, an overall length of 1750 mm and an embedment length of 965 mm. The W beam has a length of 1830 mm and an embedment length of 1100 mm.

Despite the abundant work conducted to evaluate the soil-pile interaction in the static and dynamic domain, very limited work has been conducted to study the guardrail post-soil interaction with the conventional geotechnical method or to develop new analytical models for the laterally loaded post. In this Chapter, different conventional methods available in the literature to calculate the ultimate load of a horizontally loaded pile are reviewed and discussed to identify their limitations when applied to the special case of guardrail post. As a second step, a new analytical model is developed to analyze the guardrail post subjected to lateral load. The new model, based on the Rankine passive earth pressure, assumes a simplified soil pressure distribution along the post length. It takes into account the three-dimensional (3D) analyses of passive earth pressure, which is more suitable for the case of the guardrail post embedded in soil. The results are compared to data collected from the literature.

In order to review such conventional methods, results of static and dynamic tests of the soil-post interaction for a cohesionless soil were collected from the literature and summarized in Table 2.1. The embedment of the post, the height of the applied load, the speed of the impactor and the maximum lateral load are collected for the tests. For static tests, the post is pulled laterally with very low speed.

Table 2.1: Dynamic and static tests for post loaded laterally

Reference	Post	Width (mm)	Type	Speed m/s	Embedment (mm)	Height of load (mm)	Soil Friction angle (°)	Soil density kN/m ³	Load kN
Eggers and Hirsch. (1986)	Wood	177.8	static		457	533	55	18	3.1
Eggers and Hirsch. (1986)	Wood	177.8	static		610	533	55	18	5.8
Eggers and Hirsch. (1986)	Wood	177.8	static		762	533	55	18	10.2
Eggers and Hirsch. (1986)	Wood	177.8	static		965	533	55	18	17.8
Dewey (1982) test 1	Wood	100.00	static		965	533	45	19.2	14.2
Dewey (1982) test 1	Steel	100	static		965	533	45	19	14.7
Dewey (1982) test 3	Steel	100	static		1118	533	45	19	17.3
Wu and Thomson (2007)	Steel	100	static		1000	550	40	21	15.4
Bronstad et al., (1988)	Wood	304.8	dynamic	6.1	914	711	40	18	99.2
Bronstad et al., (1988)	Wood	254	dynamic	6.1	914	711	40	18	73.0
Bronstad et al., (1988)	Wood	203.2	dynamic	6.1	914	711	40	18	55.2
Bronstad et al., (1988)	Steel	100	dynamic	6.1	1118	711	40	18	59.6
Bronstad et al., (1988)	Steel	100	dynamic	6.1	1118	711	40	18	64.1
Coon et al., (1999)	Steel	100	dynamic	4.6	1118	550	35	20	64.0
Coon et al., (1999)	Steel	100	dynamic	5.4	1118	550	35	20	66.9
Coon et al., (1999)	Steel	100	dynamic	5.9	1118	550	35	21	67.0
Coon et al., (1999)	Wood	150	dynamic	4.9	1118	550	35	21	36.3
Coon et al., (1999)	Wood	150	dynamic	4.8	1118	550	35	20	38.8
Coon et al., (1999)	Wood	150	dynamic	9.6	1118	550	35	20	77.8
Holloway et al., (1996)	Wood	151	dynamic	9.1	1118	533	35	19	35.6
Dewey (1982) test 2	Steel	100	dynamic	7.9	965	533	45	19	99.6
Polivka et al., (2004)	Steel	100	dynamic	8.9	1092	632	40	19	45.5
Polivka et al., (2004)	Steel	100	dynamic	9.3	1016	632	40	19	52.6
Polivka et al., (2004)	Steel	100	dynamic	9.0	940	632	40	19	60.7
Wu and Thomson (2007)	Steel	100	dynamic	5.0	1000	550	40	21	16.4

2.2.Literature Survey

2.2.1. Linear elastic procedure

Poulos (1971, 1974) published a general solution for a single pile loaded laterally within an elastic continuum. The pile is assumed to be a thin vertical strip of width d , length L and a constant flexibility $E_p I_p$. The pile is divided into $(n+1)$ elements as shown in Figure 2.1. The soil is assumed to be homogeneous, isotropic, incompressible and elastic, and applying a constant, uniform pressure on the pile. The Poisson's ratio, ν_s , was 0.5 and it was assumed to have relatively little influence on the solution. Poulos (1971) published the solution for two cases namely: (i) the uniform soil, where the Young's modulus, E_s , is constant and (ii) the non-uniform soil, where Young's modulus linearly increases with the depth. In the analysis, soil and pile displacements are evaluated and equated at the elements' centers except for the two extreme elements, for which displacements are calculated at the top and the tip of the pile.

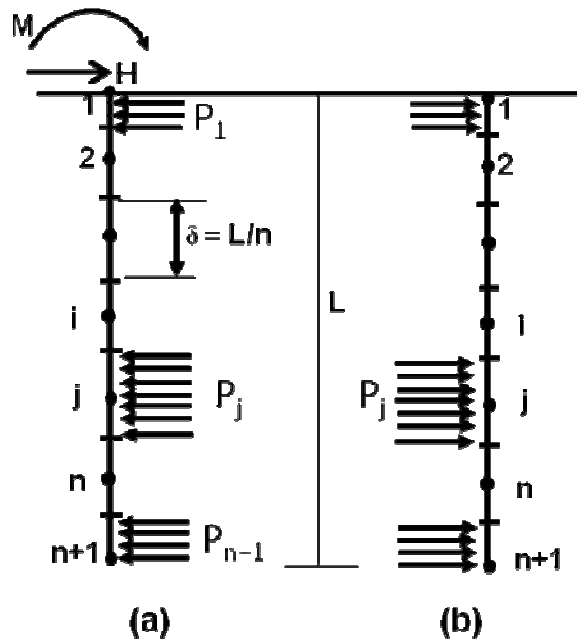


Figure 2.1: (a) Stress acting on pile, (b) Soil adjacent to pile

The soil displacements along the post may be expressed as:

$$\{y_s\} = \frac{d}{E_s} [I_s] \{p\} \quad (2.1)$$

where $\{y_s\}$ and $\{p\}$ are $n+1$ column vectors of the horizontal soil displacement and horizontal loading between soil and pile, respectively; $[I_s]$ is an $(n+1) \times (n+1)$ matrix of soil displacement-influence factors and d is the width pile.

For the free-head or unrestrained pile, the displacement of the pile is calculated based on the differential equation for bending of a thin beam and the appropriate boundary conditions at the top and the tip of the pile. Poulos (1971) derived the following equation for the pile displacement at the centre of the element:

$$-\{p\} = \frac{E_p I_p n^4}{d L^4} [D] \{y_p\} + \frac{E_p I_p}{d L^4} \{A\} \quad (2.2)$$

where $\{y_p\}$ is a column vector of pile displacement, $[D]$ is matrix of finite difference coefficients, $\{A\}$ is a vector of vertical load, E_p is the modulus of elasticity of the pile, I_p is the moment of inertia of the pile, L is the length of the pile and d is the pile width.

By equating the soil horizontal displacement, y_s , and the pile displacements, y_p , at each of these points and using appropriate equations of equilibrium, the horizontal displacement could be determined at each element as a function of the pile and soil properties.

1) Soils having a uniform modulus, E_s

Poulos published the solution for the case of free-head floating pile, loaded horizontally by a force H at distance e . The soil is assumed uniform. The groundline displacement, y , is expressed as:

$$y = \frac{\left(\frac{H}{E_s L} I_{pH} + \frac{e}{L} I_{pM} \right)}{F_p} \quad (2.3)$$

where H is the applied horizontal load, e is the load eccentricity (i.e.: height of the load above the ground), I_{pH} and I_{pM} are the elastic influence factors for a displacement caused by the horizontal load and the moment, respectively. For a constant E_s , they are

determined from Figures 2.2 and 2.3. F_p is the yield displacement factor determined by Figure 2.4 as function of H/H_u where H_u is the ultimate horizontal loading.

The elastic influence factors, I_{pH} and I_{pM} defined in Equation (2.3), are functions of the ratio e/L and the pile flexibility factor, k_R , defined as:

$$k_R = \frac{E_p I_p}{E_s L^4} \quad (2.4)$$

The ultimate load is calculated as a function of the two expressions the ratio e/L and $H_u/(P_u d L)$ as shown in Figure 2.5 where P_u was defined previously as the ultimate horizontal load, P_u is the ultimate soil resistance at the tip of the pile and e is the height above the ground level where the force is applied.

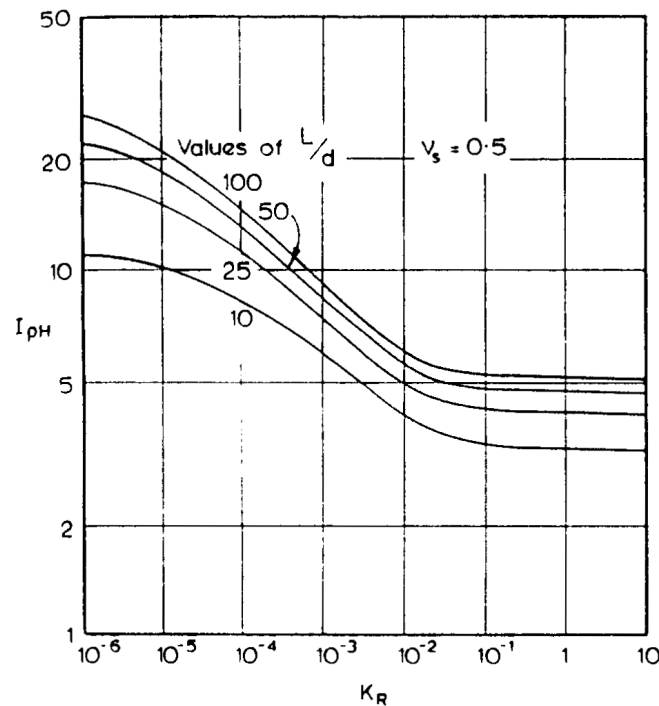


Figure 2.2: I_{pH} Value of free head floating pile for a constant soil modulus (Poulos and Davis 1980)

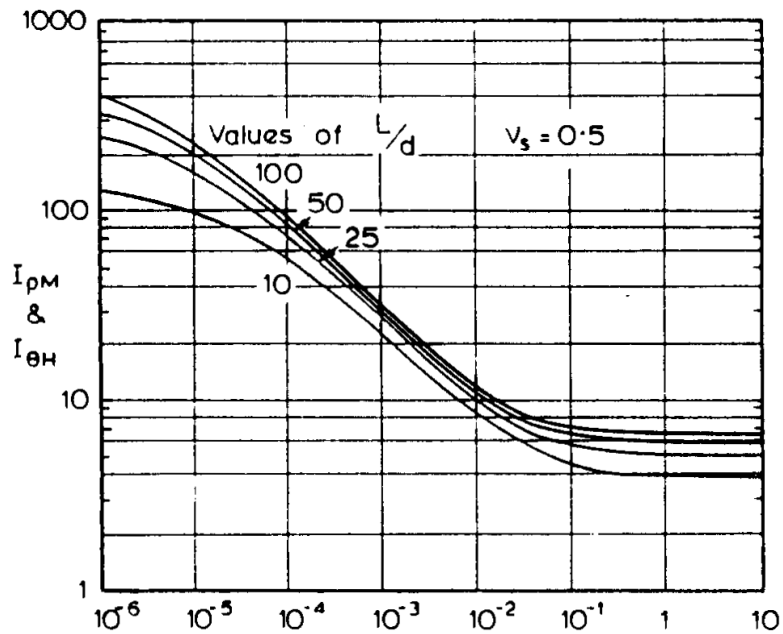


Figure 2.3: I_{pM} and $I_{\theta H}$ Values of free head floating pile for a constant soil modulus (Poulos and Davis 1980)

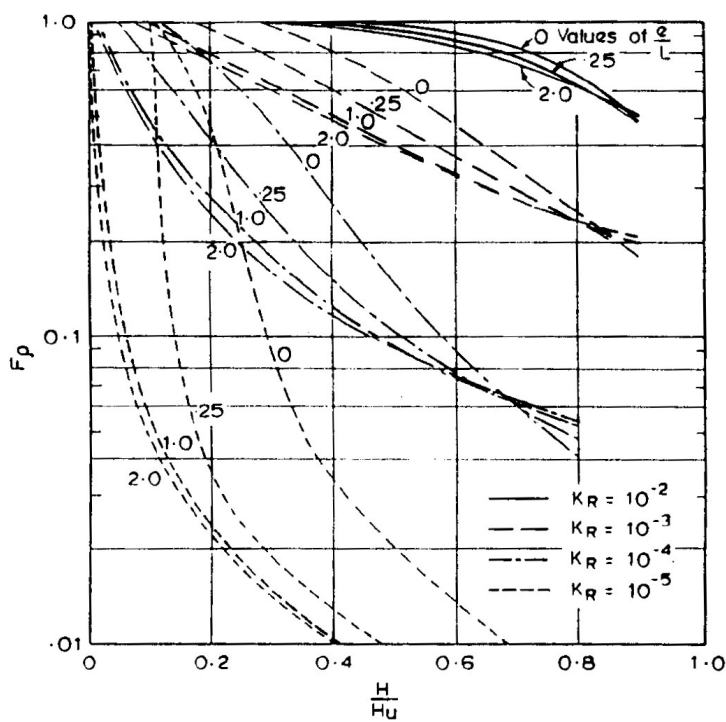


Figure 2.4: Yield displacement factor F_p of free head floating pile for a constant soil modulus F_p and P_y (Poulos and Davis 1980)

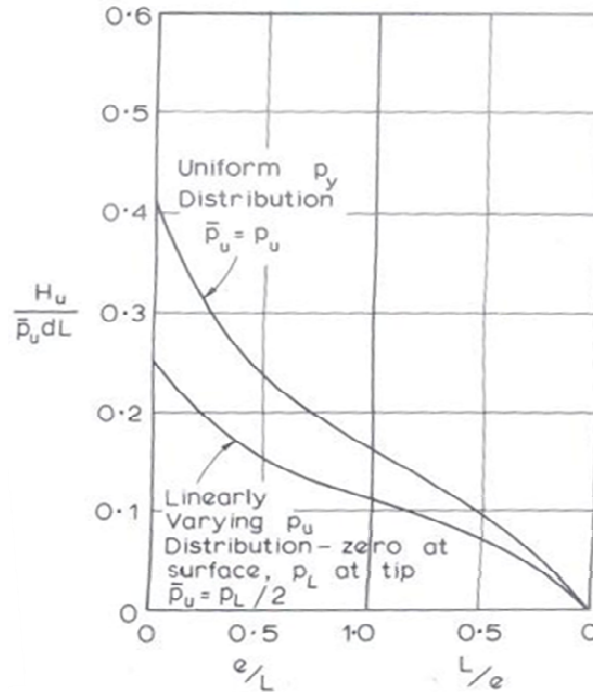


Figure 2.5: Ultimate Lateral resistance of unrestrained rigid pile
(Poulos and Davis 1980)

2) Soils with linearly increasing modulus

Poulos (1974) published a similar solution for the free-head pile when the modulus of elasticity increases as function of depth. The deflection at the groundline is defined by:

$$y = \frac{H}{N_h L^2} \frac{\left(I'_{\rho H} + \frac{e}{L} I'_{\rho M} \right)}{F'_\rho} \quad (2.5)$$

where H is the applied horizontal load, e is the height of the load above the ground, $I'_{\rho H}$ and $I'_{\rho M}$ are the elastic influence factors for a displacement caused by the horizontal load and the moment, respectively. For a varying modulus, E_s , they are defined from Figures 2.6 and 2.7. F'_ρ is the yield displacement factor determined by Figure 2.8. The rate of increase of E_s with depth is denoted N_h .

The elastic influence factors are functions of the ratio e/L and the pile flexibility factor, K_N , defined as:

$$K_N = \frac{E_p I_p}{N_h L^5} \quad (2.6)$$

The ultimate load is calculated as a function of the expression $H_u/(P_u d L)$ and the ratio e/L as shown in Figure 2.5.

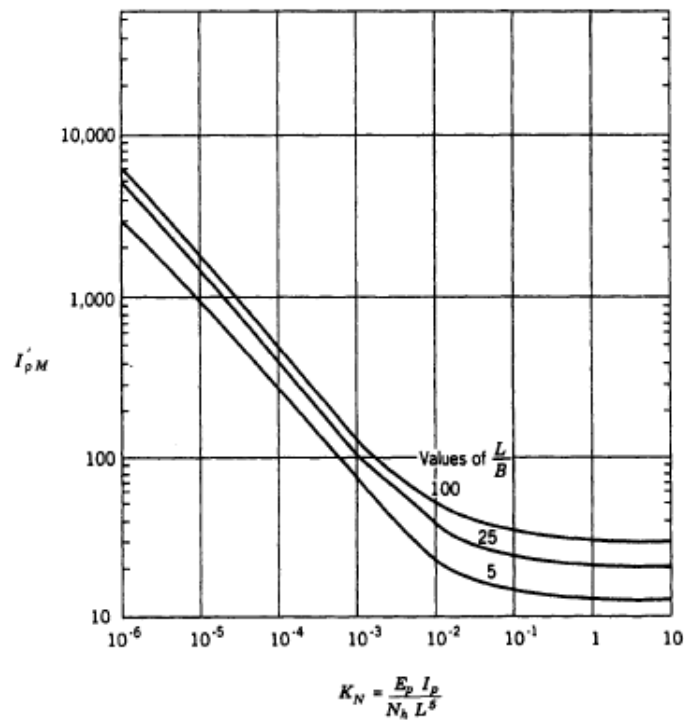


Figure 2.6: I'_{pM} and I'_{eh} Value of free head floating pile for a linearly varying soil modulus (Poulos and Davis 1980)

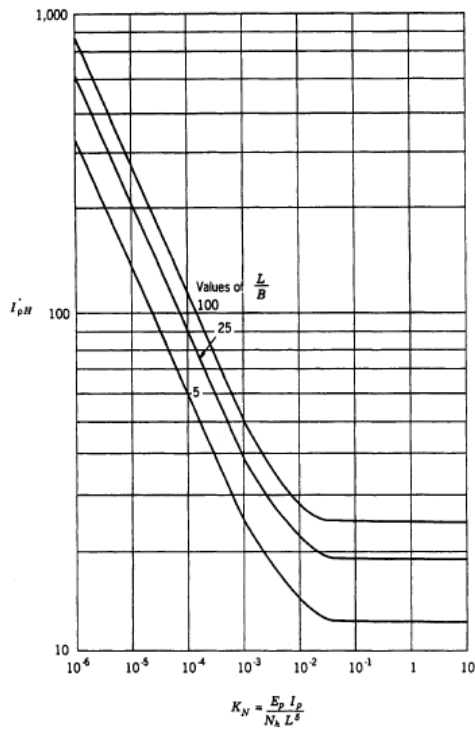


Figure 2.7: $i_{\rho H}$ Value of free head floting pile for a linearly varying soil modulus (Poulos and Davis 1980)

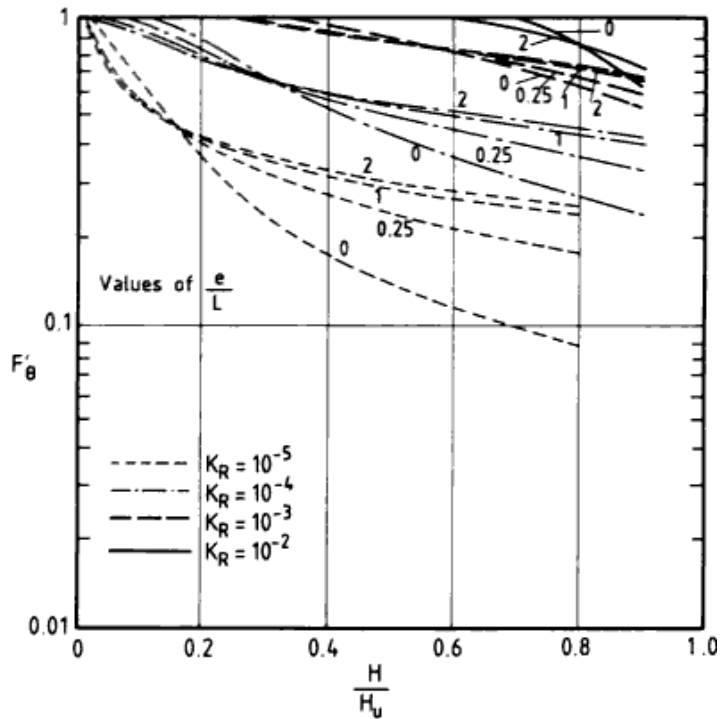


Figure 2.8: Yield displacment factor F of free head floting pile for a constant soil modulus F'_{ρ} and P_y (Poulos and Davis 1980)

3) Illustrative example of Poulos' solution applied to a guardrail post

Dewey (1982) conducted a static test with a post embedded 1117 mm in sand. The force applied to the post at a height of 533.4 mm above the ground level. The sand is assumed to have no cohesion $c' = 0$ and a friction angle $\phi = 45^\circ$. The density of the soil is 19.2 kg/m^3 . The static test recorded a maximum load of 17.2 kN as shown in Table 2.1. For the cohesionless soil, the Young modulus, E_s , is assumed to vary linearly with depth. N_h is equal to 17500 kN/m^3 (56 tons/ft³)

The moment of inertia I of the W 152x13.5 post is $685.5 \cdot 10^{-8} \text{ m}^4$

The Young modulus E_p of the steel post is approximately 210 GPa.

The flexural rigidity of the post is $EI = 1.438 \times 10^6 \text{ Nm}^2$

From Equation 2.6, the flexibility factor of the post $k_N = 1.438 \times 10^6 / 1.75 \cdot 10^8 \times (1.117)^5$

$$k_N = 0.047$$

$$L/d = 1.117 / 0.100 = 11.17$$

$$e/L = 0.533 / 1.117 = 0.477$$

$I'_{\rho H}$ and $I'_{\rho M}$ can be determined from Figure 2.6 and Figure 2.7 and are found to be

$$I'_{\rho H} = 15, \quad I'_{\rho M} = 20$$

From Figure 2.5 one can find that

$$\frac{H_u}{P_u dL} = 0.15$$

P_u is calculated as suggested by the Broms' method, $P_u = 3k_p \sigma'_v$ (Broms, 1964)

$$P_u = 3 \times \tan^2(45 + 45 / 2) \times 0.558 \times 19.2 = 187 \text{ kN/m}^2$$

The ultimate force would be $H_u = 0.15 \times 187 \times 0.1 \times 1.117 = 3.13 \text{ kN}$

The results show a significant discrepancy between the actual static test result (17.2 kN) and the prediction (3.13 kN) from the elastic method. In fact, this method seems to have the advantage of taking into account the soil continuity. However, it has many disadvantages. One basic disadvantage is that it cannot be easily extended to a stratified soil medium. The soil is assumed to be homogeneous and isotropic, which is

not the case most of the time. The method has considered a linearly varying modulus of elasticity which shows large discrepancy. Moreover, the case of the guardrail embedded in the soil presents very large deflections, which makes unrealistic assumption of the linear elastic behavior of the soil.

2.2.2. Method of subgrade reaction

The theory of the subgrade reaction was expanded by Terzaghi (1955) where the problem of a pile embedded in the soil is simulated as a one dimensional beam having a bending stiffness EI and a length L and resting on a flexible foundation. The determination of the modulus of subgrade reaction is generally carried out by one the following methods (Poulos and Davis, 1980):

- 1-Full-scale lateral-loading on a pile
- 2- Plate loading tests
- 3- Empirical correlations with other soil properties

The use of an instrumented laterally loaded pile is the most direct and straightforward method to measure the pressure applied to pile and its deflection. This method is precise but expensive and time-consuming. The use of the plate loading test is an alternative of the full-scale testing which consists of loading plate then the load deflection curve is determined from the test result. This method has been discussed by Terzaghi (1955) which outlined that the main problem with this method is the extrapolation of the result of a plate to a pile. Terzaghi noticed that the value of the subgrade modulus depends only on the elastic properties of the soil and on the dimensions of the contact area. He suggested the following expression for the vertical subgrade coefficient:

$$k_s = k_{v1} \left(\frac{B+1}{2B} \right)^2 \quad (2.7)$$

where k_{v1} is the coefficient of the vertical reaction for a square plate having a width of 30.48 cm (1 ft) as presented in Table 2.2 for different sand types and B is width of the pile.

Table 2.2: Proposed values of k_{v1} in tons/ft³ for 1-ft square plate or 1-ft wide beams resting on sand (Terzaghi, 1955)

Relative Density of sand	Loose	Medium	Dense
Dry or moist sand	40	130	500
Submerged sand	20	80	300

The coefficient of the vertical subgrade reaction, K_s , is related to the horizontal subgrade K_v . Terzaghi (1955) assumed that the modulus of elasticity depends only on the overburden pressure and the density of the sand and showed that:

$$n_h = \frac{A \gamma}{1.35} \quad (2.8)$$

where γ is the soil density and A is a factor shown in the Table 2.3

The coefficient of the horizontal subgrade reaction, k_h , for a pile embedded in cohesionless media is found to be proportional to the depth, z , the constant of horizontal subgrade reaction, n_h , on the width of the pile, B , and on the effective unit weight of the sand (Terzaghi, 1955). Typical values of the horizontal subgrade reaction are shown in Table 2.3.

$$k_h = n_h \frac{z}{B} \quad (2.9)$$

Table 2.3: Values of the Constant of Horizontal Subgrade Reaction, n_h , in tons/ft³ for a pile 1-ft Wide in sand (Terzaghi, 1955)

Relative Density of sand	Loose	Medium	Dense
Adopted value of A	200	600	1500
n_h for dry or moist sand	7	21	56
n_h for submerged sand	4	14	34

The determination of the subgrade modulus is used to solve the differential equation of the beam deflection expressed as:

$$E_p I_p \frac{d^4 y}{d^4 x} = p \quad (2.10)$$

where y is the lateral displacement of the beam, E_p is the Young modulus of the beam, I_p is the moment of inertia of the beam, x is the distance along the beam, and p is the soil reaction force per unit length of the beam.

The soil subgrade modulus, k_h , is such that:

$$p = -k_h y \quad (2.11)$$

Combining Equations (2.10) and (2.11), the differential equation of the beam deflection curve is expressed as:

$$E_p I_p \frac{d^4 y}{d^4 x} + k_h y = 0 \quad (2.12)$$

The solution of Equation (2.12) can be obtained either analytically or numerically. The analytical solution is available for the case of constant k_h along the pile. For other k_h distributions, solutions are conveniently obtained by the finite difference method. Several distributions have been employed. The most widely used was developed by Palmer and Thompson (1948) and has the form:

$$k_h = k_T \left(\frac{z}{L} \right)^n \quad (2.13)$$

where k_T is the value of k_h at the pile tip and n is a positive empirical index.

The coefficient n is zero for the clay, i.e. the subgrade modulus is constant along the depth of the pile whereas for cohesionless soil, $n = 1$, that is, the subgrade modulus increases linearly with the depth (Poulos and Davis, 1980). No convenient closed form

solution is available for the cohesionless soil. However, Barber (1953) presented an approximate solution for a rigid pile as follows:

$$y = \frac{18F \left(1 + 1.33 \frac{e}{L} \right)}{L^2 n_h} \quad (2.14)$$

Or the force could be derived from Equation 2.14 a

$$F = \frac{y L^2 n_h}{18 \left(1 + 1.33 \frac{e}{L} \right)} \quad (2.15)$$

Illustrative example

The example used with the elastic approach to calculate the maximum load is reconsidered with the subgrade method. The test was conducted by Dewey (1982) using static load and the post was embedded 1117.6 mm in sand. The force applied at the top is 533.4 mm above ground level. The sand had $c' = 0$ and $\phi' = 45^\circ$. The density of the soil was 19.2 kN/m^3 and the maximum load recorded was 17.3 kN.

As presented before, the critical parameters are:

$$e/L = 0.477$$

$$n_h = 56 \text{ tons/ft}^3$$

$$L = 1.117 \text{ m}$$

Equation (2. 15) is applicable in the linear portion of the load deflection curve where the pile head deflection is small. For a deflection of 10 mm, the force applied is therefore:

$$F = \frac{(1.117/0.3048)^2}{18(1+1.33 \cdot 0.477)} 56 \cdot 0.01/0.3048 = 0.84 \text{ tons} = 8.35 \text{ kN}.$$

The results show that static test result (17.2 kN) is 2 times higher than the predicted force (8.35 kN) calculated for a displacement of 10 cm, considered to be above the elastic domain.

2.2.3. The P-Y method

When a pile or a post is loaded laterally, the soil surrounding the pile resists the applied force. The reaction depends on the soil parameters such as the friction angle, the

cohesion, in the case of the cohesionless soil; or the undrained shear strength, in the case of clay. The relationship between the soil pressure p and the deflection y is nonlinear. Taking into account this nonlinearity, McClland and Focht (1958) developed the first p-y model based on the results of 0.609 m (24 in) pipe pile driven into the soil. The soil is modeled as a series of non-linear springs and a load deflection curve is defined for each spring. This method is a clear improvement over the previous model where the springs are considered linear.

Figure 2.9 shows the concept of p-y curves. It is assumed that the pile is perfectly straight before the lateral loading. When the pile is driven by a lateral load with a displacement y , the soil reaction could be calculated by integrating the pressure around it. Once the set of springs is determined, the pile deflection, rotation, bending moment, shear and soil reaction could be determined by solving the beam equation.

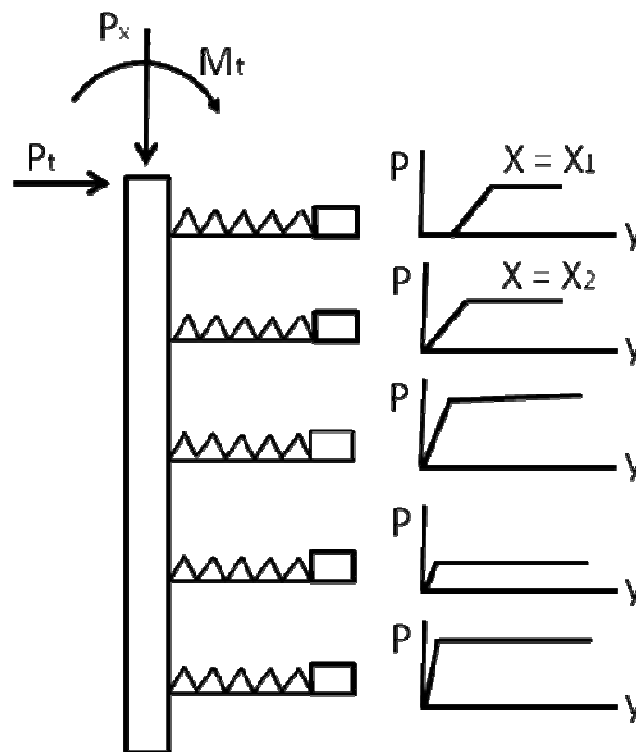


Figure 2.9: Model for pile loaded laterally with p-y curves

Figure 2.9 implies that the behavior of the soil at a particular depth is independent of the soil behavior at other locations. Although this assumption is not strictly true, Reese and

Matlock (1956) stated that the experiments indicate that it is sufficiently true for practical purposes. The p - y curves are obtained, in general, experimentally by conducting full tests of piles subjected to lateral load. The pile should be instrumented with strain gauges that measure the strains of the pile during the test. Knowing the pile stiffness and pile curvature during the test, the bending moment along the pile could be calculated. The soil reaction curve is obtained by double differentiating the bending moment diagrams. The p - y curves could be determined for any combination of external load applied to the pile as an axial compression, lateral load or bending moment, thus the curves are fully nonlinear with respect to the distance x .

The spring stiffness in the p - y curves is not defined only by the soil properties. It was found that the p - y curves are influenced by other factors, such as the pile cross-sectional shape and dimensions, the pile bending stiffness and pile head conditions. In fact, Ashour and Norris (2000), studied analytically the influence of some of these factors on p - y curves and found that the pile with square cross section in loose sand, dense sand or clay exhibited a soil-pile resistance higher than that of the circular cross section. Several p - y methods have been proposed in the literature to calculate the ultimate load. Most of these methods are derived from the tests conducted in the field on instrumented laterally loaded piles. Most of these methods are developed for monotonically increasing static load. Among the different available methods, the method of Reese et al., (1974) is presented for the sand in the next section.

Calculations for piles in sand: (Reese et al., 1974)

A series of static and cyclic lateral load tests were performed on pipe piles driven in sands. The p - y curve consists of four segments. The first portion of the curve is a linear segment from 0 to a defining the limit of the elastic portion. The second portion is an exponential variation of p with y from a to b where b is point located at $1/60$ of the relative displacement of u/b . The third portion is a second linear range from b to c , while the last part is a constant resistance for displacements beyond c where c defines the limit of the second linear portion as shown in Figure 2.10.

To build the p - y curves of a pile, the pile is divided into multiple segments. For each segment located at a depth z ., the steps for constructing the p - y curve are as follows:

- 1- Determine the slope of the initial linear portion of the curve from the linear relation $P = k z$ where k is the linear stiffness of the soil obtained from Table 2.4

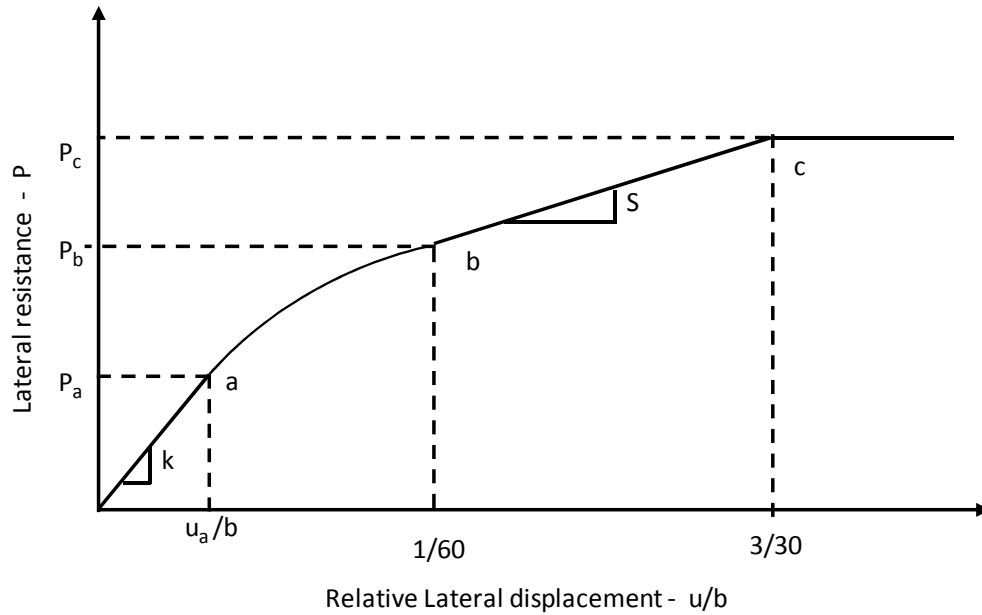


Figure 2.10: P-y curve proposed by Reese et al., (1974)

Table 2.4 Representative values of k (pci) (Reese et al., 1974)

Relative Density of sand	Loose	Medium	Dense
Dry or moist sand	20	60	125
Submerged sand	25	90	225

- 2- Determine the ultimate load as the smaller of the following equations:
For the wedge failure:

$$p_{\max} = (C_1 z + C_2 b) \gamma' z \quad (2.16)$$

For the flow failure at depth z :

$$P_{\max} = C_3 b \gamma' z \quad (2.17)$$

where the three constants C_1 , C_2 and C_3 are defined as:

$$C_1 = \frac{K \tan \phi \sin \beta}{\tan(\beta - \phi) \cos(\phi / 2)} + \frac{\tan^2 \beta \sin \phi / 2}{\tan(\beta - \phi)} + K_e \tan \beta (\tan \phi \sin \beta - \tan(\phi / 2)) \quad (2.18)$$

$$C_2 = \frac{\tan \beta}{\tan(\beta - \phi)} - \tan^2 (45 - \phi / 2) \quad (2.19)$$

$$C_3 = K \tan \phi \tan^4 \beta + \tan^2 (45 - \phi / 2) (\tan^8 \beta - 1) \quad (2.20)$$

Where z is the depth below the ground, γ' is the effective unit weight of the sand, K_e is the horizontal earth pressure coefficient chosen as 0.4 to reflect the fact that the surfaces of the assumed failure model are not planar, ϕ is the angle of internal friction, b is the width of the pile perpendicular to the loading direction and β is equal $45 + \phi / 2$

- 3- Compute the lateral resistance for the transition points c and b on the curve of Figure 2.10 from:

$$P_b = A P_{\max} \quad (2.21)$$

$$P_c = B P_{\max} \quad (2.22)$$

where P_{\max} is defined from Equations (2.16) and (2.17).

A and B are reduction coefficients from Figures 2.11 and 2.12, respectively, for the appropriate static or cyclic loading condition. The second straight line segment of the curve, from b to c , is established by the resistances P_b and P_c and the prescribed displacements of $u = b/60$ and $3b/30$. The slope of the segment is given by

$$s = \frac{40(P_c - P_b)}{b} \quad (2.23)$$

4 – Determine the exponential curve from a to b , defined by:

$$P = C y^{\frac{1}{n}} \quad (2.24)$$

The parameters C , n , p_a and u_a of Figure 2.10 are obtained by assuming the continuity of the curve of the lateral resistance as a function of the relative displacement (Figure 2.10).

The p - y curves are based on the assumption that the lateral resistance p at any point on the pile is a function only of the lateral displacement y at that point. But since the displacement y must be known before the lateral resistance P can be evaluated, numerical iterative solutions to solve the discretized model are required. The solution proceeds as a succession of trials and corrections until forces and displacements are compatible at every node, Mosher and Dawkins (2000)

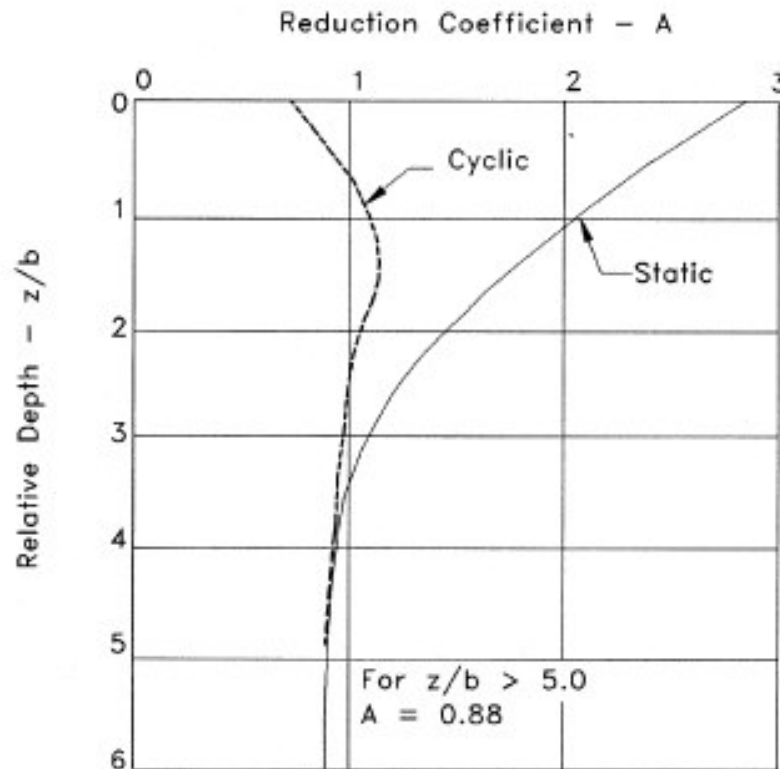


Figure 2.11: Resistance reduction coefficient A as function of relative depth after Mosher and Dawkins (2000)

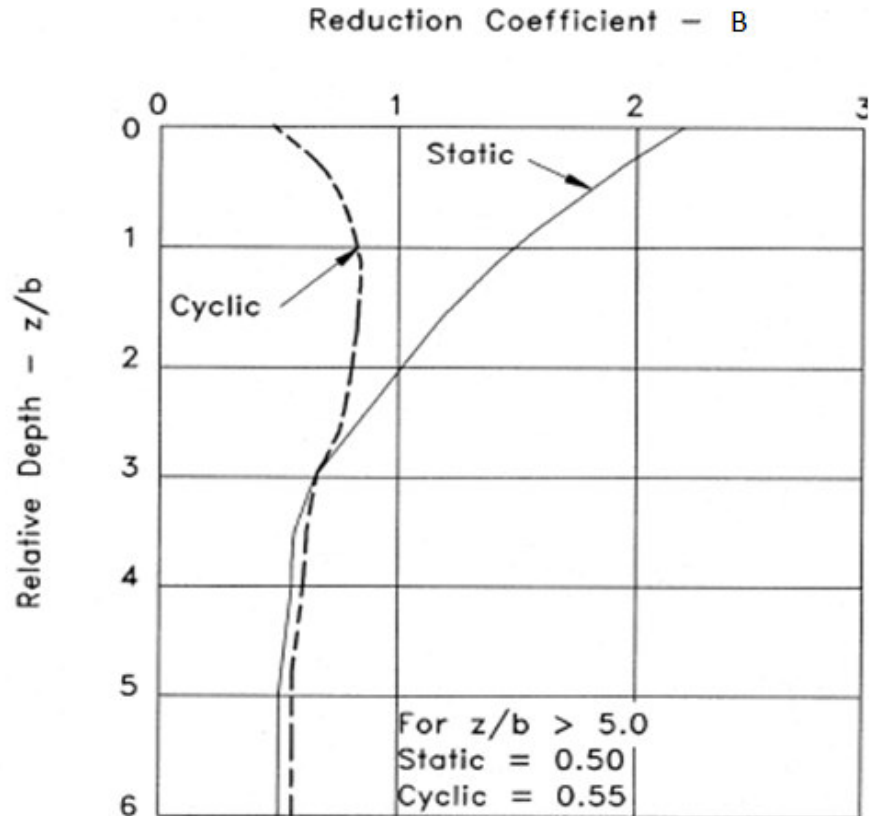


Figure 2.12: Resistance reduction coefficient B as function of relative depth after Mosher and Dawkins (2000)

2.2.4. The ultimate capacity method

The ultimate lateral capacity method focuses on the computation of the ultimate load applied to a laterally loaded pile. The method assumes that the soil around the pile reaches the state of plastic equilibrium. Thus, little or no additional load is required to produce more deformation in the soil and deflection of the pile.

When the pile is moved towards the soil, the vertical stress in points A and B as shown in Figure 2.13 remains the same, however the lateral stress increases in point A and decreases in point B . The two points where the state of the stress was represented by the same Mohr circle have two different circles as shown in Figure 2.14.

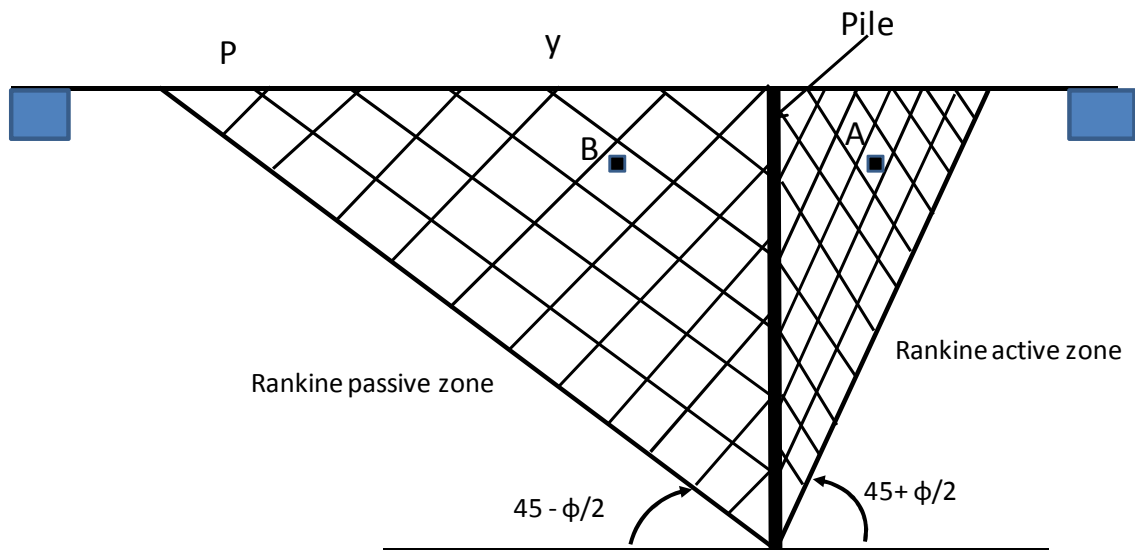


Figure 2.13: Slip planes within the soil mass at mid plane of pile (2D approximation)

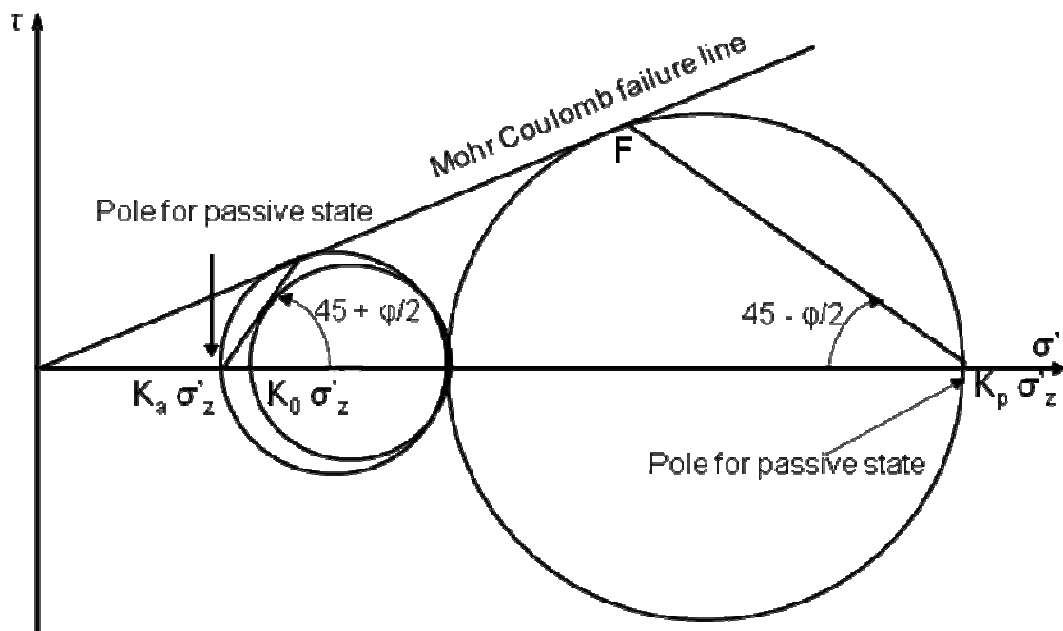


Figure 2.14: Mohr's circles at rest, active and passive states

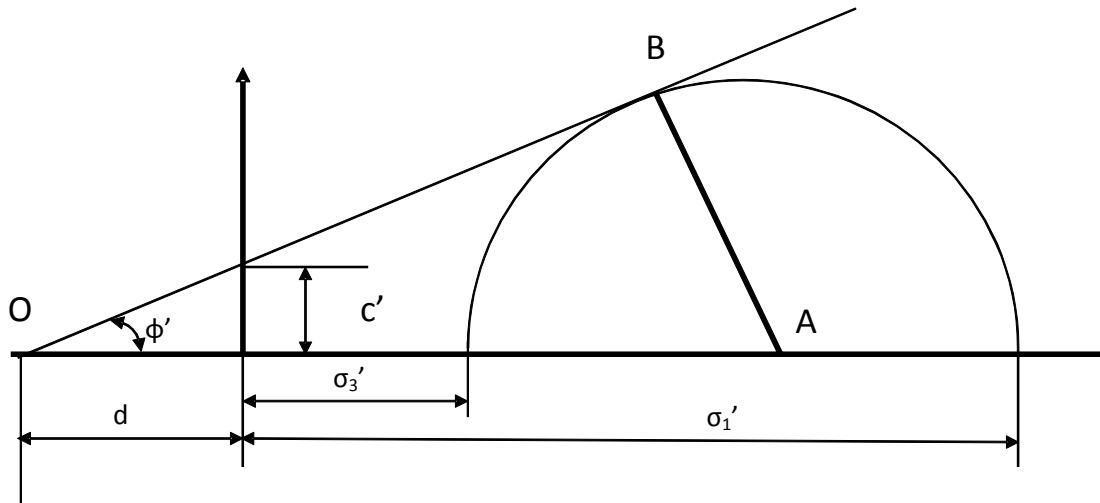


Figure 2.15: Mohr's circle of the failure envelope

The condition for failure occurs when the stress reaches the failure envelope. The major and minor principal stresses shown in Figure 2.15 are defined as follows:

$$\sigma_1' + d = OA + AB = OA(1 + \sin \phi') \quad (2.25)$$

$$\sigma_3' + d = OA - AB = OA(1 - \sin \phi') \quad (2.26)$$

This leads to:

$$\sigma_1' = \sigma_3' \frac{1 + \sin \phi'}{1 - \sin \phi'} + d \left(\frac{1 + \sin \phi'}{1 - \sin \phi'} - 1 \right) \quad (2.27)$$

Since d can be defined as:

$$d = c' \frac{\cos \phi'}{\sin \phi'}, \quad (2.28)$$

then

$$\sigma_1' = \sigma_3' \frac{1 + \sin \phi'}{1 - \sin \phi'} + 2c' \sqrt{\frac{1 + \sin \phi'}{1 - \sin \phi'}} \quad (2.29)$$

or :

$$\sigma_1' = \sigma_3' \tan^2 \left(45^\circ + \frac{\phi'}{2} \right) + 2c' \tan \left(45^\circ + \frac{\phi'}{2} \right) \quad (2.30)$$

If the cohesion c is null, the ratio of the lateral effective stress to the vertical effective stress is defined as:

$$K_a = \frac{\sigma_3'}{\sigma_1'} = \frac{1 - \sin \phi'}{1 + \sin \phi'} = \tan^2 \left(45^\circ - \frac{\phi'}{2} \right) \quad (2.31)$$

K_a is also called the active lateral earth pressure coefficient.

The passive earth pressure coefficient, K_p , and is such that:

$$K_a = \frac{1}{K_p} \quad (2.32)$$

1) Method of Broms (1964)

Broms (1964) developed a method for short and long piles in cohesionless soil based on Rankine passive earth pressure. Broms' method assumes that a short pile rotates about a centre point located close to the lower end of the pile. Within this approach the pile is assumed to deflect laterally, mobilizing the full passive resistance along the entire pile and reach failure. For short piles such as the case of highway posts, the post rotates as shown in Figure 2.16. The ultimate soil capacity is defined by

$$P_u = C_\phi \gamma z B K_p \quad (2.33)$$

where γ is the unit density of the soil, z is the depth of soil, K_p is the Rankine passive pressure coefficient defined as a function of the friction angle, $K_p = \tan^2(45^\circ + \phi/2)$ and

φ is the angle of friction. C_φ is a coefficient to account for the three dimensional effect of the failure wedge in the front of the pile. Broms assumed that $C_\varphi = 3$.

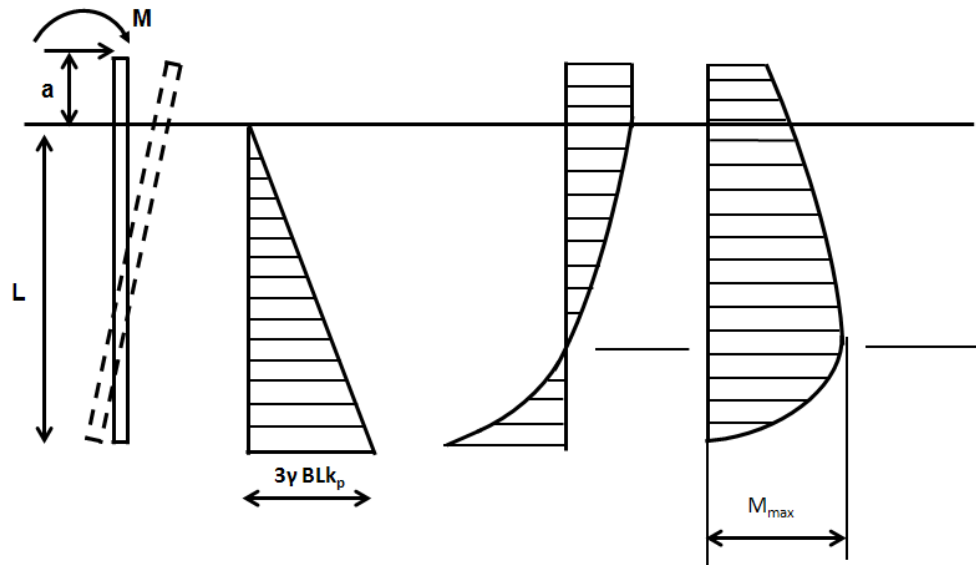


Figure 2.16: Deflection load, shear and moment diagrams for a rigid pile in sand with unrestrained head displacement

The curve describing the soil interaction with the post is shown in Figure 2.16. The equilibrium of the moments at the bottom of the pile is expressed as:

$$P_u(e+L) = (3\gamma B K_p L) \frac{L}{2} \frac{L}{3} \quad (2.34)$$

The value of the ultimate force P_u is determined as:

$$P_u = \frac{\gamma B K_p L^3}{2(e+L)} \quad (2.35)$$

Where e is the height at which the force is applied to the post above the ground.

Illustrative example

The same example used for the cohesionless soil conducted by Dewey (1982) is considered again:

- The load height is $e = 533.4$ mm
- The total embedment of the pile is $L = 1117.6$ mm
- The friction angle is $\phi' = 45^\circ$
- The soil density is $\gamma = 19.2$ kN/m³
- The max load of the test is $P_u = 17.3$ kN.

The value of the passive earth pressure coefficient k_p is

$$k_p = \tan^2(45^\circ + 45/2) = 5.828$$

Based on Equation (2.35), the ultimate load is calculated as follows:

$$P_u = \frac{19.2 \times 0.10 \times 5.828 \times 1.117^3}{2(0.533 + 1.117)} = 4.72 \text{ kN}$$

The ultimate load calculated by Broms' method is low compared to the 17.2 kN experimental static ultimate load.

2) Method of Meyerhof et al., (1981)

When a rigid wall or a pile with a free head is partially embedded in layered soil and subjected to a horizontal load at the top, (Meyerhof et al., 1981) assumed that a passive earth pressure is developed initially at the front face above the point of rotation and an active earth pressure is developed at the opposite side of the wall. Below the point of rotation, the lateral distribution is reversed and has approximately triangular pressure. This method, developed for a rigid wall by Meyerhof et al., (1981), has been extended to lateral rigid piles loaded laterally. The ultimate lateral resistance per unit width of rigid pile is greater than that of a corresponding wall due to the shearing resistance on the vertical sides of the failure wedges in the soil. To account for the three dimensional effect for the pile, a shape factor S is introduced. This factor is not constant, as assumed by Broms, but varies with the depth and the friction angle of the sand. It can be defined as:

$$S_b = 1 + \sin \phi \frac{z}{B} \leq \frac{K_o N_q}{K_b} \quad (2.36)$$

where: B is the pile diameter, K_o is the lateral earth pressure coefficient at rest, N_q is the bearing capacity factor for a strip footing and k_b is the net earth pressure coefficient for the pile defined as:

$$k_b = \tan^2 \left(45^\circ + \frac{\phi}{2} \right) - \tan^2 \left(45^\circ - \frac{\phi}{2} \right) \quad (2.37)$$

The ultimate lateral load resistance of the rigid pile is estimated for one homogenous sand layer by:

$$Q_u = \left(\gamma D^2 K_{b2} F_b r_b S_{bu} + c_2 D K_{c2} F_c r_c S_{cu} \right) B \quad (2.38)$$

where B is the pile diameter, D is the total pile embedment, F_b is the lateral resistance factor for the weight, F_c is the lateral resistance factor for the cohesion, K_c is the earth pressure coefficient due to the cohesion and K_b is the net earth pressure coefficient defined by Equation (2.37). The coefficient r_b is a reduction factor defined by:

$$r_b = \frac{1}{\left(1 + 1.4 \frac{e}{D} \right)} \quad (2.39)$$

When the cohesion is null, Equation 2.38 becomes:

$$Q_u = \left(\gamma D^2 K_{b2} F_b r_b S_b \right) B \quad (2.40)$$

The shape factor S_{bu} is defined from Figure 2.17:

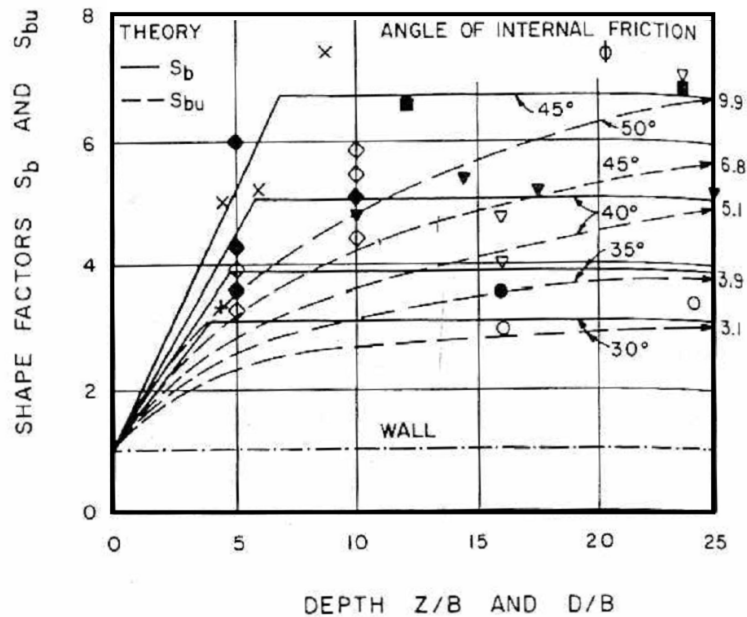


Figure 2.17: Shape factors of laterally loaded pile in sand after Meyerhof et al., (1981)

Illustrative example

The example used for the cohesionless soil conducted by Dewey (1982) is considered again:

- The load height is 533.4 mm
- The total embedment of the pile D is 1117.6 mm
- The friction angle is $\phi' = 45^\circ$
- The soil density is $\gamma = 19.2 \text{ kN/m}^3$
- The max load of the test, P_u , is 17.3 kN.

The value of the passive earth pressure coefficient k_p is

$$k_b = \tan^2(45^\circ + 45/2) - \tan^2(45^\circ - 45/2) = 5.657$$

$$\text{From equation (2. 39), } r_b = \frac{1}{1 + 1.4(0.533/1.11)} = 0.6.$$

From Figure 2.17, $S_b = 0.12$ for $D/B = 10$

$$\text{The ultimate load is } P_u = 19.2 \times (1.11)^2 \times (0.12) \times (0.6) \times (5.657) \times (4.8) = 4.62 \text{ kN}$$

The ultimate load calculated by the Meyerhof method is low compared to 17.2 kN the ultimate load obtained from the static test.

3) Method of Prasad and Chari (1999)

Prasad and Chari (1999) conducted a series of fifteen laboratory tests on fully instrumented rigid model piles buried in sand with different embedment ratios defined as a ratio of the embedded length of the pile to the pile diameter. The tests were conducted for various soil conditions and the soil was assumed to be uniform and homogenous for each test. Prasad and Chari found from the laboratory tests that the maximum earth pressure is located at a distance of approximately between 0.55 to 0.65 times the depths of the rotation point with an average of 0.6 (Figure 2.18 a). The stress distribution at any depth z was assumed to have a parabolic shape as shown in Figure 2.18b.

Based on their results, they proposed new idealized stress distribution profile along the pile as shown in Figure 2.18a. The soil pressure is assumed to be zero at the ground and at the point of pile rotation. The maximum lateral pressure is located at $0.6D$, where D is the distance from the ground to the point of rotation. The pressure profile has a triangular shape distribution. It increases linearly from zero at the ground to the depth of $0.6D$ then drops to zero at the point of rotation. The pressure continues to increase linearly from the other side of pile to reach 1.7 times the pressure at $0.6D$ at the tip of the pile as shown in Figure 2.18 a.

The maximum pressure P_d at this depth is:

$$P_d = S k_p \gamma d \quad (2.41)$$

where S : is a shape factor

γ is the soil density

d is the diameter of the pile and

k_p is the Rankine passive earth pressure coefficient, defined as:

$$k_p = \frac{1 + \sin \phi'}{1 - \sin \phi'} = \tan^2 \left(45^\circ + \frac{\phi'}{2} \right) \quad (2.42)$$

Prasad and Chari established a relationship between the shape factor S and the Rankine passive earth pressure with the friction angle defined as:

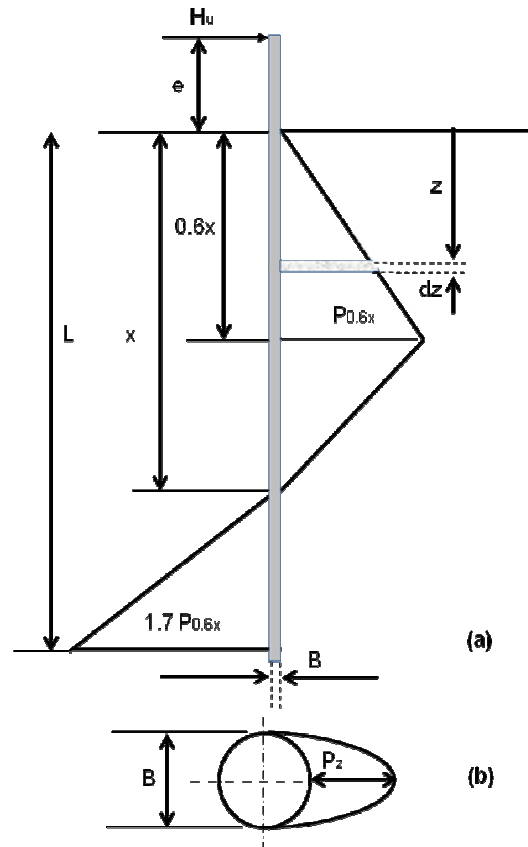


Figure 2.18: Pressure diagrams and pressure distribution around the pile after Prasad and Chari (1999)

$$S k_p = 10^{(1.3 \tan \phi' + 0.3)} \quad (2.43)$$

The ultimate lateral load F is defined as:

$$F = 0.24 \cdot 10^{(1.3 \tan \phi' + 0.3)} \gamma x B (2.7x - 1.7L) \quad (2.44)$$

The distance x is calculated as:

$$x = \frac{-(0.567L + 2.7e) + (5.307L^2 + 7.29e^2 + 10.541eL)^{0.5}}{2.1996} \quad (2.45)$$

where e is the eccentricity of the load and L is the embedment of the load in the ground.

Illustrative example

For the same example described before:

$$L = 1.117 \text{ m}$$

$$e = 0.533 \text{ m}$$

Equation (2.45) yields $x = 0.81 \text{ m}$

The value of P_u is defined from Equation (2.44)

$$P = 4.28 \text{ kN}$$

The ultimate load calculated by the method of Prasad and Chari is low compared to the 17.2 kN ultimate load obtained from the static test.

2.2.5. Summary of the literature review

Different conventional methods, used to calculate the lateral load of piles, have been applied to the case of the guardrail post. The review of these methods indicated that most of them are not able to predict accurately the ultimate force. In fact, these methods are used mainly in the geotechnical field to calculate the ultimate force F used in the design of the pile with a safety factor to avoid reaching the ultimate load or deforming the pile above the tolerance limit.

Although researchers developed different solutions for a variety of soil profiles and loading conditions, the use of these methods for real conditions is not straightforward. For the case of a highway post laterally loaded, the deflections are very large, which makes the problem highly nonlinear, thus, the assumption of linear soil behavior is not valid and any method making that assumption is not accurate.

The values of the ultimate load calculated from all the different methods: Meyerhof, Broms or Terzaghi are under-predicting the ultimate capacity value as obtained from the static test as shown in the previous examples.

Most of the solutions and methods using the lateral earth pressure concept consider the problem of the post loaded laterally as a 2-D problem of passive earth pressure. The

shape factors used by such researchers as Broms (1964) and Meyerhof et al., (1981) to account for this effect are shown to be not appropriate. In the case of a guardrail post, the area $B \times H$ is approximately $0.1 \text{ m} \times 1 \text{ m}$, which clearly makes the problem a 3-D passive earth pressure problem and it is well known that the 3-D configuration has the effect of increasing the passive earth pressure exerted on the post (Škrabl and Macuh 2005).

2.3 Proposed Method for the Ultimate Lateral Load

Estimation

The goal of this approach is to develop a simple but accurate method for the analysis and the design of the post in the highway guardrail subjected to a lateral load in static conditions. To the best knowledge of the author, no simple method has been developed in the literature to assist engineers in calculating the force applied on the guardrail post based on the soil parameters. Dewey (1982) developed an iterative method to determine the lateral force and the moment assuming the height of the lateral load is known and constant. The post was divided in segments and three components of force were calculated on each segment namely: the resultant of the lateral earth pressure, the resultant of the horizontal shear stress around the perimeter of the shaft and the drag force exerted by the soil as the shaft segment rapidly moves through the soil.

2.3.1. Guardrail post rigidity

Posts used in the highway side hardware consist of the w-beam W152x13.5 steel cross section shown in Figure 2.19. They have a length embedded in the soil of approximately 1.1 m. Piles are considered short if the applied lateral load at the head force the tip of the pile to rotate or translate. According to the definition of a short pile as defined by the US Corps of Engineers Manual (1991), the pile is considered to be short if $L/T \leq 2$ where L is the length of the pile embedded in the soil and T is defined as:

$$T = \sqrt[5]{\frac{EI}{n_h}} \quad (2.46)$$

where EI is the bending capacity of the beam and n_h is the modulus of horizontal subgrade reaction increasing linearly with depth.

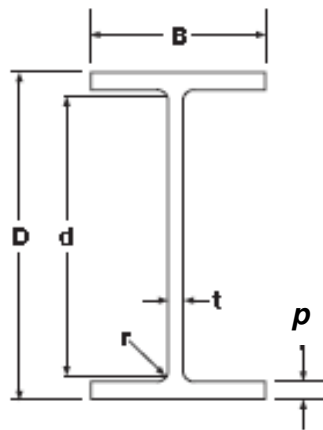


Figure 2.19: a) Guardrail post in the soil. b) Guardrail post cross section

For a cohesionless soil, $n_h = 56 \text{ lb/in}^3$ (17.5 N/cm^3) and 21 lb/in^3 (6.72 N/cm^3) for dense and medium sand, respectively, according to Table 2.3. Since the guardrail post is made out of steel, its Young modulus E is approximately $E = 210 \text{ GPa}$ and the moment of inertia I_x is 685.5 cm^4 for W152x13.5 as shown in Table 2.5.

For the medium sand, Equation (2.46) gives $T = 2.92 \text{ m}$ and $L/T = 1.1/2.92 = 0.38 < 2$.

For the dense sand, Equation (2.46) gives $T = 0.61 \text{ m}$ and $L/T = 1.1/0.61 = 1.8 < 2$.

Accordingly, the posts used in highway barriers are considered short and rigid.

Table 2.5: W 152 x 13.5 beam properties

Dimensions					Moment of Inertia		Section Modulus	
Depth D mm	Width B mm	Web Thickness mm	Section area cm ²	Weight Kg/m	I _x cm ⁴	I _y cm ⁴	S _x cm ³	S _y cm ³
150	100	4.3	17.3	13.5	685.5	91.8	91.4	18.4

2.3.2. Theoretical background

The proposed method is based on the ultimate capacity method where the post is embedded in the soil and subjected to a horizontal load at the top. In this case, a passive earth pressure is developed at the front face of the post above the point of rotation. At the same time, an active earth pressure is developed in the opposite side of the post below the centre of rotation. This assumption is similar to the approach of many researchers such as Meyerhof et al., (1981) and Prasad and Chari (1999) however the author proposed different pressure distribution. During the lateral loading, the post is acting as a rigid body and experiencing mainly a rotation around a point located under the ground. Almost no deformation on the post can be observed as has been noticed in many static tests (Dewey 1982).

The method developed in the current study is inspired from the approach proposed by Prasad and Chari. The soil is assumed to be isotropic and homogeneous. The soil friction angle and the soil-structure friction interface δ are assumed to remain constant. When the post embedded in cohesionless soil at depth L is subjected to lateral loading at height H above the ground level, a passive earth pressure is developed in the front face of the wall above the point of rotation. The net pressure distribution can be assumed to be linear. Figure 2.20 shows the earth pressure distribution applied to the post. The pressure increases linearly from zero at the ground to the depth $0.6a$, where a is the distance from the ground to the point of rotation. The soil pressure drops after to zero at the point of rotation. The pressure continues to increase linearly on the other side of the pile to reach approximately the pressure at $0.6a$ at the tip of the pile as shown in

Figure 2.20. For Prasad and Chari, the pressure at the tip of the pile was assumed to be 1.7 the soil pressure at 0.6 a depth.

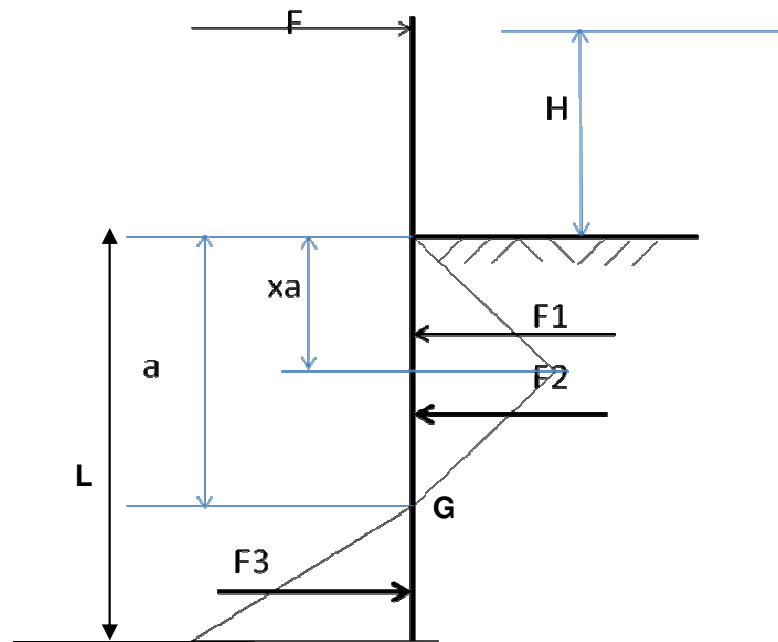


Figure 2.20: Pressure diagrams and pressure distribution around the pile as proposed by Prasad and Chari (1999)

To validate the assumption of the pressure distribution, a finite element model was built with Radioss software (Mecalog 2005) and was used for the same Dewey's test discussed previously. A guardrail post is embedded in the soil at depth of 1100 mm and an imposed displacement is applied to the post at the point of force contact located at 550 mm above the ground. The loading mechanism consisted of two springs with very high stiffness to minimize the springs' elongations and attached to the post in each side. The springs are connected to a rigid body which is connected to a third spring with very high stiffness as shown in Figure 2.21. The horizontal force is calculated at the end of the spring for each displacement applied and a load deflection curve is determined for the prescribed displacement. The soil was modeled as cylindrical block using 8 node hexahedron elements where the post was embedded in the center of the block. The guardrail post is formed by 2020 shell elements and 2142 nodes. The block has a diameter of 2700 mm and a height of 2100 mm and the nodes located at lateral

perimeter of the block were constrained from displacement on the three directions whereas their rotation were unrestrained. The nodes at the base of the soil block were constrained only on the vertical direction z. Details of the model will be presented and discussed in the next section. The results of the finite element model are used just to confirm the validity of the assumptions used in this section.

Figure 2.22 shows that the contour of displacement of the nodes after the force being applied to the post. It can be noted that the shape of the contour defined a cone with an apex located at a depth of 810 mm representing the center of rotation for the post. Figure 2.23, which represents the Von Mises stress distribution in cross section plane, shows that soil reaches the failure in front face of the post at the top and at rear face of the post at the tip. This stress distribution confirms the validity of the assumption used in the study.

Based on the proposed pressure distribution which is different from Chari and Prasad's, the forces applied to the post for the current study (Figure 2.20) could be calculated as:

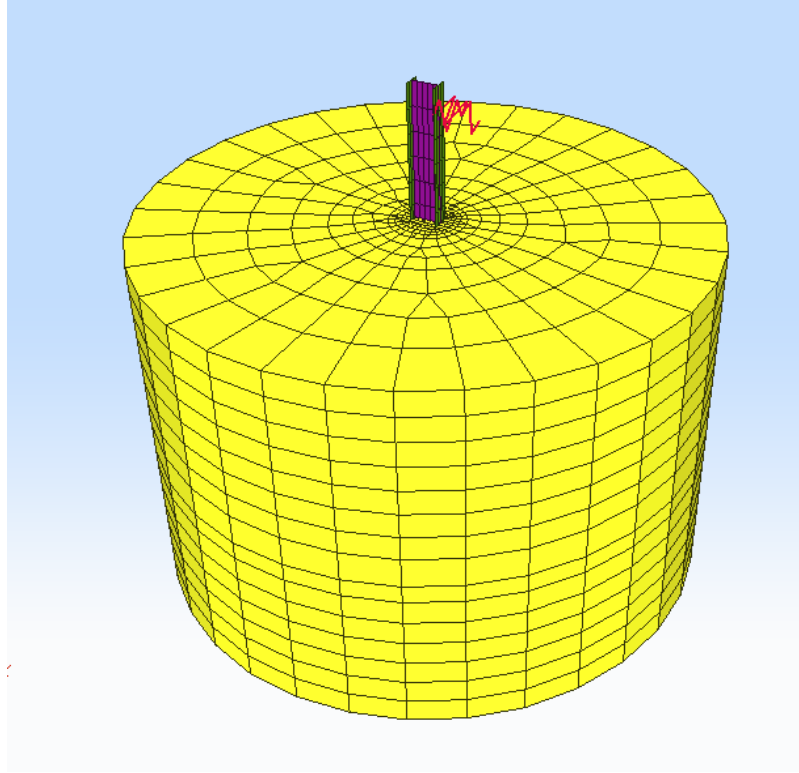
$$F_1 = B \gamma k_p \frac{(ax)^2}{2} \quad (2.47)$$

$$F_2 = B \gamma k_p \frac{x(1-x) a^2}{2} \quad (2.48)$$

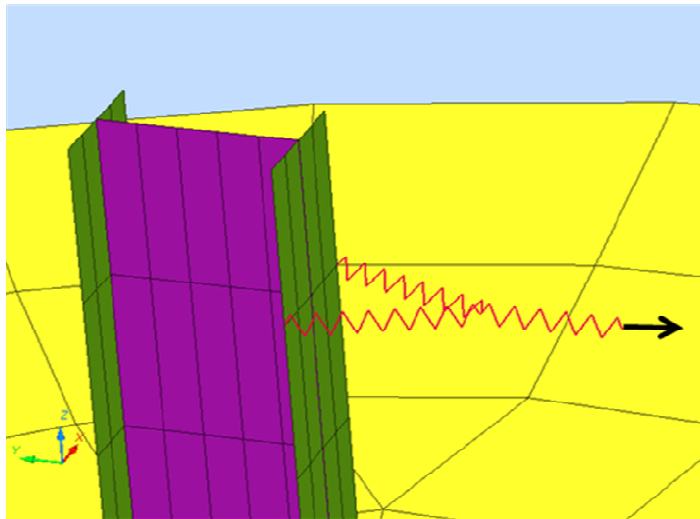
$$F_3 = B \gamma k_p \frac{(xa)(L-x)}{2} \quad (2.49)$$

The resultant of the two forces F_1 and F_2 represents the passive earth pressure acting above the centre of rotation on the front face of the pile while F_3 is the passive force developed below the point of rotation. The moment equilibrium expressed at the centre of rotation G leads to:

$$F(H+a) = F_1 \left(\frac{1}{3} xa + (1-x)a \right) + F_2 \left((1-x)a \frac{2}{3} \right) + F_3 \left((L-a) \frac{2}{3} \right) \quad (2.50)$$



(a)



(b)

Figure 2.21: a) View of the finite element model set for the static loading of the post in cohesionless soil, b) Details of the load mechanism system attached to the post

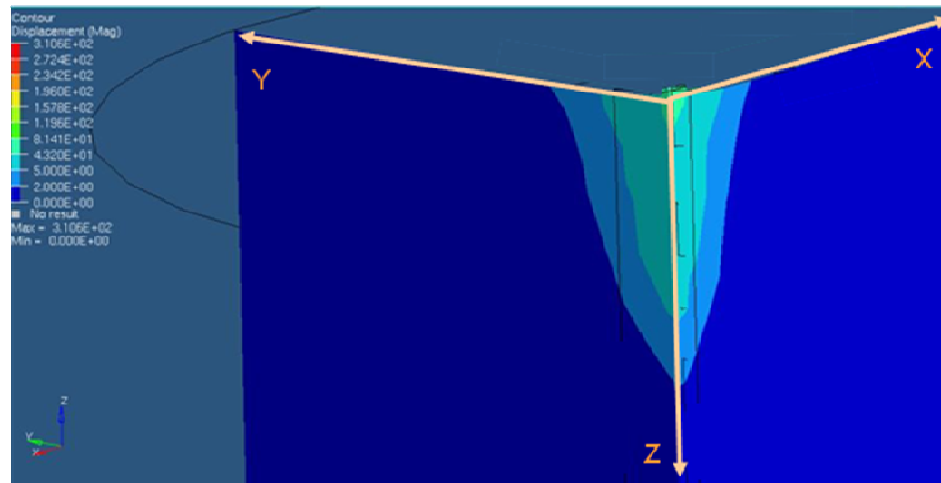


Figure 2.22: Vertical cross section of the soil mobilized during lateral loading of the post

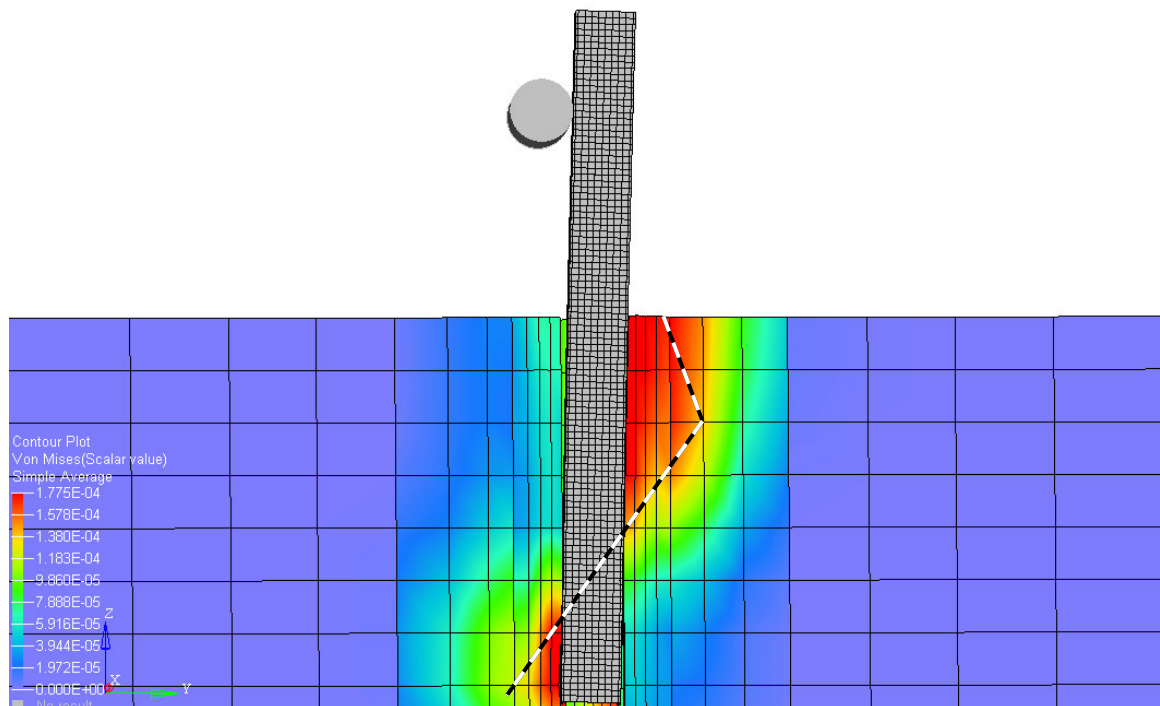


Figure 2.23: Von-Mises stress distribution of the post embedded in the soil and subjected to lateral loading

If Equations (2.47), (2.48) and (2.49) are combined with (2.50), we obtain:

$$F(H+a) = \eta B \gamma k_p \frac{(ax)}{2} \left(xa^2 \left(1 - \frac{2}{3}x \right) + \left(\frac{2}{3}(1-x)^2 a^2 \right) + \frac{2}{3}(L-a)^2 \right) \quad (2.51)$$

Equation (2.51) shows that the current method has three unknowns namely: the value of a representing the centre of rotation; the value of k_p , representing the lateral earth pressure calculated in 3-D, and the force F applied to the post.

The equilibrium of force could be considered to reduce the number of unknown in Equation 2.51. However this approach will lead to solve a polynomial equation higher degree.

2.3.3. Determination of the rotation centre

Many results in the literature show that the centre of rotation is located around 60% to 70% of the length of embedment. Based on eight tests conducted by Bierman (1995), it was found that the ratio of the depth of rotation point to the embedment depth ranges from 0.62 to 0.72 with an average of 0.66 as shown in Table 2.6.

Table 2.6: Static tests conducted in sand by Bierman (1995)

Post Test (PT)	Post Number	Point of Rotation (in)	Post Embedment (in)	Ratio to the Embedment Depth
1.1	12	29	44	66%
1.2	13	31	44.25	70%
5.1	20	30	44	68%
5.2	21	30	44	68%
6.2	10	28	44.5	62%
7.1	11	30	50.5	60%
10.1	18	27	44.5	61%
10.2	19	32	44.5	72%

Plaxico et al., (1998) reported that in their simulation, the post began to rotate at approximately 812 mm below grade for a total embedment of 1118 mm, which gave a ratio to the embedment depth equal to 0.73.

Dewey (1982) conducted three static tests in the sand as shown in Table 2.7. The ratio of the rotation point to the post embedment depth is approximately 73%.

Table 2.7: Static tests conducted in sand by Dewey (1982)

Post Test (PT)	Post type	Point of Rotation (in)	Post Embedment(in)	Ratio to the Embedment Depth
1	Wood	28	39	73%
2	Steel	28	39	73%
3	Steel	32	44	72%

Based on these data, it is assumed that the centre of rotation is located at 0.7 of the total embedment of the post. Therefore, it can be assumed for the new approach that:

$$a = 0.7 L \quad (2.52)$$

2.3.4. Determination of k_p passive earth pressure in 3D

Most of the solutions discussed earlier considered the problem of the post loaded laterally as a 2-D problem of the passive earth pressure. As mentioned previously in section (2.2.4), many approaches have been adopted to take into account the 3D effect. Broms (1964) used a coefficient equal to 3 for the pressure distribution. Meyerhof et al., (1981) used a coefficient that depends on the friction angle and depth. In reality, the dimensions B x H of 100 mm x 1100 mm, (B= post width and H=height) make the problem a 3-D mainly because the plane strain assumption is not valid. It is well known that the 3-D configuration has the favorable effect of increasing the passive earth pressure exerted on the post (Škrabl and Macuh, 2005). Few results are presented in the literature for the 3D problem (Blum, 1932 and Soubra and Regenass, 2000).

Horn (1972) proposed a linear relationship between the $K_{p\gamma(2D)}$ and $K_{p\gamma(3D)}$

$$k_{p\gamma(3D)} = k_{p\gamma(2D)} A \left(1 + C \frac{h}{b} \right) \quad (2.53)$$

Where A is a scale factor equal to 2.5 for $h = 0.10$ m and 0.75 for $h = 1.5$ m. Factor C is function of the soil friction angle φ as:

$$C = 2.50 \tan^2 \varphi - 0.48 \tan \varphi + 0.27 \quad (2.54)$$

where the soil friction angle φ is in degrees.

This method is a simplified form and assumed a linear relationship between k_p with B/H which is shown to be invalid. In fact Škrabl and Macuh (2005) presented a novel approach to the determination of passive soil pressures. They used the upper-bound method within the framework of the limit analysis theory. The method considered a three-dimensional, kinematically admissible failure mechanism for the calculation of the admissible solution. The failure mechanism is composed of a central and two lateral bodies that are connected by a common velocity field. This approach is similar to two-dimensional stability analyses. Their solution is based on many hypotheses and limitations, such as:

- 1- The pile is assumed to be vertical with an area of $B \times H$
- 2- The backfill is homogeneous, the soil is isotropic and considered as a Coulomb material.
- 3- The resulting value of passive earth pressure P_p is defined by

$$p_p = k_{p\gamma} \gamma \frac{h^2}{2} + k_{pc} c h b + k_{pq} q h b \quad (2.55)$$

where $K_{p\gamma}$ is the coefficient of passive earth pressure due to soil weight, K_{pc} is the coefficient of passive earth pressure due to cohesion, K_{pq} is the coefficient of

passive earth pressure due to the surcharge loading, c is the soil cohesion, γ is soil density and q is the surcharge loading.

- 4- The rotational failure mechanism is bounded by the log spiral in the region of the retaining wall and by the hyperbolic surfaces defined by the envelope of the connected hyperbolic half cones at the lateral sides.

Škrabl and Macuh gave the coefficients K_{py} for 2D and 3D cases for different shear angles and friction quotients between the retaining structure and the backfill. Table 2.8 shows that the value of k_{py} increases when the ratio B/H decreases. In fact, if one considers the case of cohesionless soil with a soil's friction angle of 40° and a friction angle δ between the post and the soil = 0 so $\delta/\varphi = 0$, the value of k_{py} can range from 7.155 for a $B/H = 10$ to 43.9 for $B/H = 0.25$. For the case of a highway post guardrail, B/H is approximately 0.1 (post embedment is generally 1100 mm and the post width is 100 mm). The value of K_{py} for this ratio is not available from Table 2.8 and no data is available in the literature for this ratio of $B/H = 0.1$.

In order to calculate the value of lateral earth pressure coefficient for $H/B = 11$, a method is developed for the current study by the author based on the extrapolation of the Table 2.8 results. The first step is to sort Table 2.8 based on the same friction angle and variable B/H instead of constant B/H and variable friction angle as shown in Table 2.9. The second step is to plot $\log(k_p)$ as a function of $\log(b/h)$ for each friction angle and φ and a relative friction angle and δ . A second degree equation is found to give a good correlation between the log of k_p and the log of B/H and the R^2 indicating the degree of correlation close to 1. The final step is use the second degree equation to determine the value of k_p for $B/H = 0.1$. The relationship between k_p and B/H could be expressed as:

$$\log(k_p) = a \left(\log \frac{B}{H} \right)^2 + b \log \frac{B}{H} + c \quad (2.56)$$

Table 2.9 shows that for any friction angle, the value of coefficient of lateral earth pressure k_p increases with the mobilized friction between the soil and the pile (δ/φ)

where δ is the friction angle at the soil–structure interface and decreases with the value of B/H . For the same B/H , k_p increases with the increase of the soil friction angle.

As illustrative example, the curve of the variation of $\text{Log}(B/H)$ vs. $\text{Log}(K_p)$ is plotted in Figure 2.24 for the case of the friction angle of 15° and $\delta/\varphi = 1$. The curve is a second degree equation with R^2 equal to 0.99. Table 2.10 summarizes the coefficients of the second degree equation of each case of a friction angle and δ/φ . All the data show very good correlation and an R^2 very close to 1.

For $B/H = 0.1$, k_p is extrapolated for each friction angle φ and δ/φ and summarized in Table 2.11. It can be noticed that for the same friction angle φ , the value of k_p increases with the ratio δ/φ . For a friction angle of 15° to 25° , k_p varies approximately linearly with δ/φ . However, the K_p is not linear when the friction angle is higher than 25° . For the same value of δ/φ , the value of K_p increases with the increase of the friction angle. The rate of increase is higher when the value δ/φ approaches the value of unity.

Table 2.8: K_{py} for different values of B/Hand δ/φ after Škrabl and Macuh (2005)

φ	b/h	δ/φ				
		0	0.33	0.5	0.67	1
15	0.25	3.630	4.170	4.463	4.775	5.358
20	0.25	5.327	6.563	7.220	7.926	9.476
25	0.25	7.982	10.337	11.785	13.424	17.286
30	0.25	11.865	16.490	19.637	23.429	33.115
35	0.25	20.043	28.317	34.907	43.591	68.659
40	0.25	43.954	59.403	72.807	92.674	160.035
45	0.25	121.518	157.946	190.263	240.399	437.890
15	0.5	2.672	3.048	3.241	3.438	3.835
20	0.5	3.736	4.494	4.920	5.372	6.351
25	0.5	5.229	6.727	7.630	8.641	10.985
30	0.5	7.443	10.254	12.188	14.452	20.134
35	0.5	11.983	16.906	20.779	25.849	40.135
40	0.5	25.084	33.912	41.546	52.802	90.357
45	0.5	66.766	86.835	104.658	132.186	239.688
15	1	2.189	2.477	2.622	2.768	3.060
20	1	2.887	3.452	3.759	4.082	4.769
25	1	3.850	4.913	5.540	6.232	7.809
30	1	5.222	7.150	8.451	9.944	13.614
35	1	7.954	11.199	13.799	16.944	25.839
40	1	15.650	21.166	25.917	32.858	55.480
45	1	39.386	51.278	61.825	78.099	140.857
15	2	1.949	2.186	2.306	2.423	2.663
20	2	2.465	2.925	3.171	3.427	3.964
25	2	3.159	3.999	4.484	5.014	6.200
30	2	4.111	5.614	6.569	7.670	10.323
35	2	5.938	8.342	10.166	12.477	18.658
40	2	10.931	14.793	18.101	22.878	38.000
45	2	25.691	33.496	40.418	51.056	91.352
15	5	1.798	2.009	2.113	2.217	2.418
20	5	2.211	2.605	2.812	3.027	3.470
25	5	2.743	3.343	3.842	4.272	5.217
30	5	3.444	4.670	5.426	6.288	8.621
35	5	4.730	6.626	8.034	9.782	14.332
40	5	8.099	10.970	13.410	16.875	27.463
45	5	17.4663	22.8226	25.5741	34.8296	61.6482
15	10	1.749	1.949	2.048	2.146	2.336
20	10	2.126	2.497	2.691	2.891	3.303
25	10	2.604	3.258	3.625	4.021	4.885
30	10	3.222	4.352	5.041	5.821	7.643
35	10	4.327	6.053	7.320	8.879	12.857
40	10	7.155	9.695	11.845	14.876	23.929
45	10	14.7205	19.2635	23.2928	29.4204	51.7471
15	2D	1.698	1.889	1.982	2.074	2.252
20	2D	2.040	2.388	2.569	2.754	3.133
25	2D	2.464	3.070	3.407	3.767	4.548
30	2D	3.000	4.032	4.653	5.349	6.959
35	2D	3.690	5.445	6.599	7.972	11.387
40	2D	4.599	7.622	9.835	12.661	20.308
45	2D	5.8284	11.1974	15.6822	21.9144	40.6109

Table 2.9: K_{py} for different values of B/H and δ/φ after Škrabl and Macuh (2005) sorted by friction angle

φ	b/h	δ/φ				
		0	0.33	0.5	0.67	1
	0.1					
15	0.25	3.630	4.170	4.463	4.775	5.358
15	0.5	2.672	3.048	3.241	3.438	3.835
15	1	2.189	2.477	2.622	2.768	3.060
15	2	1.949	2.186	2.306	2.423	2.663
15	5	1.798	2.009	2.113	2.217	2.418
15	10	1.749	1.949	2.048	2.146	2.336
15	2D	1.698	1.889	1.982	2.074	2.252
20	0.25	5.327	6.563	7.220	7.926	9.476
20	0.5	3.736	4.494	4.920	5.372	6.351
20	1	2.887	3.452	3.759	4.082	4.769
20	2	2.465	2.925	3.171	3.427	3.964
20	5	2.211	2.605	2.812	3.027	3.470
20	10	2.126	2.497	2.691	2.891	3.303
20	2D	2.040	2.388	2.569	2.754	3.133
25	0.25	7.982	10.337	11.785	13.424	17.286
25	0.5	5.229	6.727	7.630	8.641	10.985
25	1	3.850	4.913	5.540	6.232	7.809
25	2	3.159	3.999	4.484	5.014	6.200
25	5	2.743	3.343	3.842	4.272	5.217
25	10	2.604	3.258	3.625	4.021	4.885
25	2D	2.464	3.070	3.407	3.767	4.548
30	0.25	11.865	16.490	19.637	23.429	33.115
30	0.5	7.443	10.254	12.188	14.452	20.134
30	1	5.222	7.150	8.451	9.944	13.614
30	2	4.111	5.614	6.569	7.670	10.323
30	5	3.444	4.670	5.426	6.288	8.621
30	10	3.222	4.352	5.041	5.821	7.643
30	2D	3.000	4.032	4.653	5.349	6.959
35	0.25	20.043	28.317	34.907	43.591	68.659
35	0.5	11.983	16.906	20.779	25.849	40.135
35	1	7.954	11.199	13.799	16.944	25.839
35	2	5.938	8.342	10.166	12.477	18.658
35	5	4.730	6.626	8.034	9.782	14.332
35	10	4.327	6.053	7.320	8.879	12.857
35	2D	3.690	5.445	6.599	7.972	11.387
40	0.25	43.954	59.403	72.807	92.674	160.035
40	0.5	25.084	33.912	41.546	52.802	90.357
40	1	15.650	21.166	25.917	32.858	55.480
40	2	10.931	14.793	18.101	22.878	38.000
40	5	8.099	10.970	13.410	16.875	27.463
40	10	7.155	9.695	11.845	14.876	23.929
40	2D	4.599	7.622	9.835	12.661	20.308
45	0.25	121.518	157.946	190.263	240.399	437.890
45	0.5	66.766	86.835	104.658	132.186	239.688
45	1	39.386	51.278	61.825	78.099	140.857
45	2	25.691	33.496	40.418	51.056	91.352
45	5	17.4663	22.8226	25.5741	34.8296	61.6482
45	10	14.7205	19.2635	23.2928	29.4204	51.7471
45	2D	5.8284	11.1974	15.6822	21.9144	40.6109

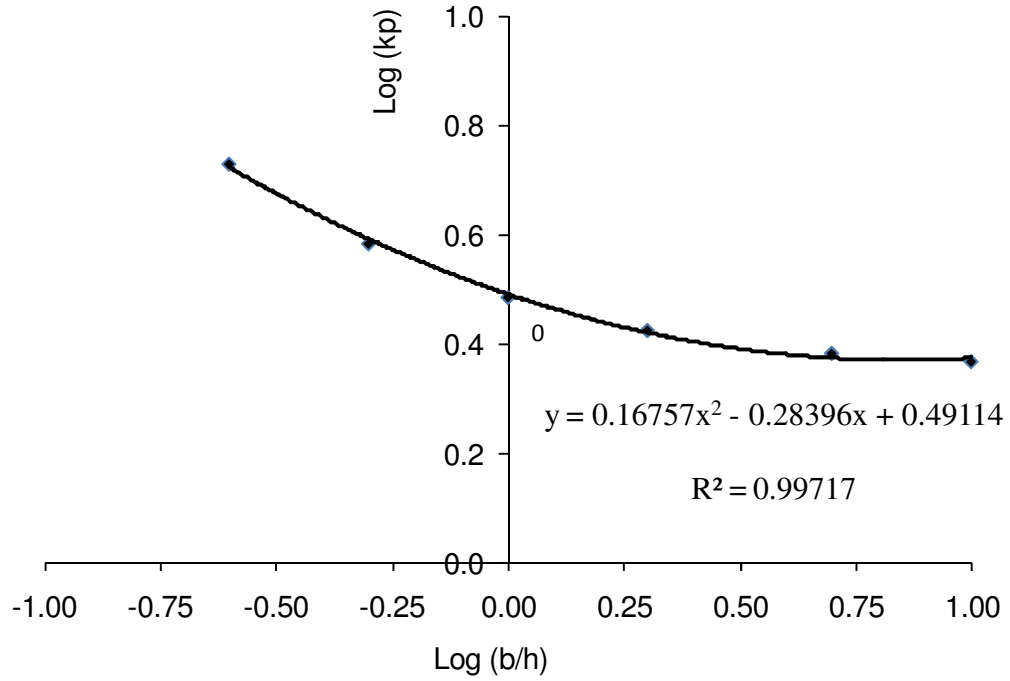


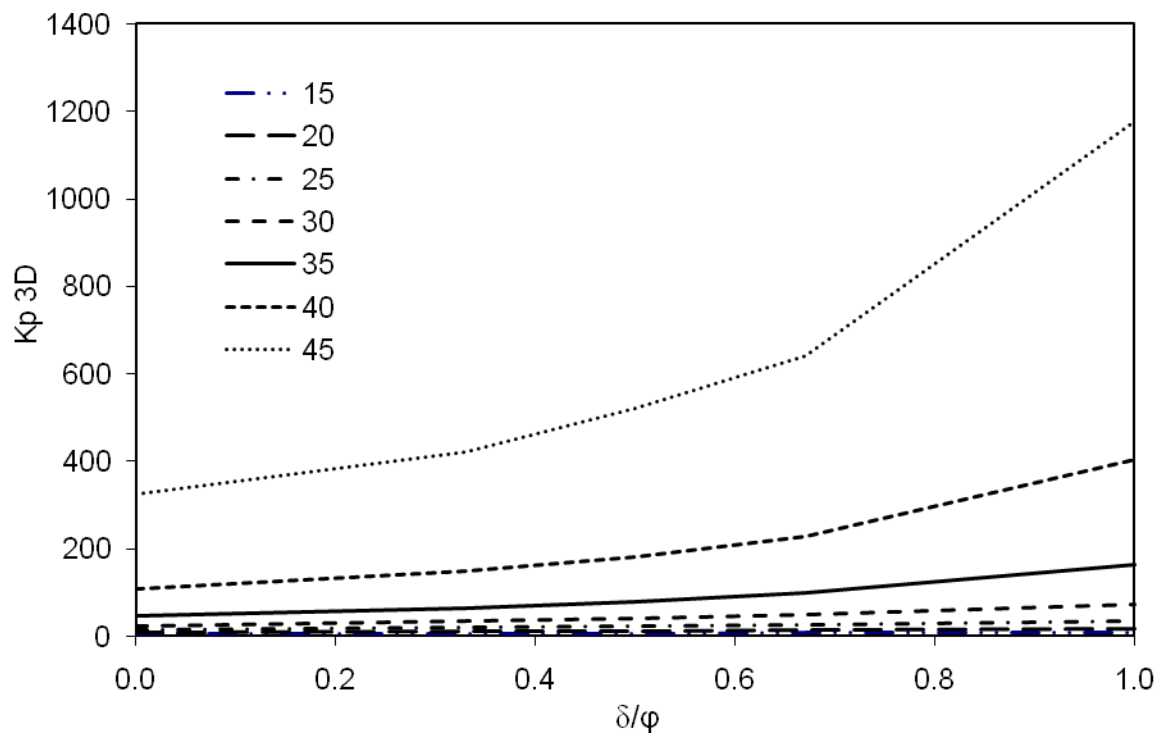
Figure 2.24: Fitting curve of the variation of Log(b/h) vs. Log(K_p)

Table 2.10: Values of the parameters of correlation

φ		δ/φ				
		0	0.33	0.5	0.67	1
15	A	0.15436	0.15807	0.16084	0.16514	0.16757
	B	-0.25119	-0.26115	-0.2672	-0.2744	-0.284
	C	0.34601	0.399652	0.42405	0.44736	0.49114
	R²	0.9959	0.9965	0.9966	0.9966	0.99717
20	A	0.18147	0.18956	0.19158	0.19378	0.19857
	B	-0.31436	-0.32951	-0.336	-0.3428	-0.3574
	C	0.46657	0.54388	0.58083	0.61655	0.68395
	R²	0.9981	0.9978	0.9979	0.9981	0.9984
25	A	0.21089	0.21481	0.21444	0.2165	0.2212
	B	-0.38018	-0.39508	-0.3981	-0.4064	-0.4245
	C	0.59219	0.69489	0.74896	0.79999	0.8976
	R²	0.9986	0.99946	0.99889	0.999	0.9992
30	A	0.22928	0.23123	0.23104	0.23268	0.23439
	B	-0.43864	-0.44688	-0.4555	-0.465	-0.482
	C	0.72304	0.85999	0.93168	1.00211	1.14049
	R²	0.9992	0.9992	0.9994	0.9995	0.9984
35	A	0.245	0.24497	0.24325	0.24533	0.24721
	B	-0.50931	-0.51208	-0.5171	-0.526	-0.5503
	C	0.904411	1.05294	1.14164	1.23236	1.41501
	R²	0.9997	0.9997	0.9998	0.9998	0.99989
40	A	0.25188	0.25198	0.25187	0.25136	0.24965
	B	-0.59167	0.59127	0.59211	-0.5958	-0.6151
	C	1.19601	1.32718	1.4151	1.5118	1.74186
	R²	0.99955	0.9999	0.9999	0.9999	0.9999
45	A	0.24508	0.24563	0.25115	0.24601	0.24435
	B	-0.67295	-0.67127	-0.6817	-0.6704	-0.6796
	C	1.59409	1.7087	1.78488	1.89148	2.1472
	R²	0.9999	0.9999	0.9986	0.9999	0.9999

Table 2.11: k_p values for $B/H= 0.1$ for different friction angles

φ	δ/φ				
	0	0.33	0.5	0.67	1
15	5.644	6.590	7.113	7.707	8.763
20	9.171	11.560	12.835	14.229	17.374
25	15.250	20.173	22.985	26.476	34.940
30	24.601	34.522	41.517	50.093	71.927
35	45.574	64.564	79.794	100.849	163.136
40	109.537	148.057	181.585	228.518	404.250
45	325.177	422.280	522.084	642.584	1178.013

Figure 2.25: k_p values for $B/H= 0.1$ for different friction angles

2.4 Determination of the Force F

Combining Equations (2.51) and (2.52) leads to:

$$F(H + 0.7L) = 0.0861 B \gamma K_p L^3 \quad (2.57)$$

Equation 2.57 defines the relation between the force applied to the post and the embedment required. The solution to determine the embedment L can be found by solving a third degree equation. For a known embedment, the maximum force F could be determined as:

$$F = \frac{0.0861 B \gamma K_p L^3}{(H + 0.7L)} \quad (2.58)$$

Example of Force Calculation

If we assume that:

$$B = 0.10 \text{ m}$$

$$\gamma = 19.2 \text{ kN/m}^3$$

$$\varphi = 40^\circ$$

$$H = 0.5\text{m}$$

From Table 2.11, K_p is equal to 109.5 for $\delta/\varphi = 0$ and to 404.2 for $\delta/\varphi = 1$. Therefore, the force F is found to be 12.4 kN for the first case ($\delta/\varphi = 0$) and 45.9 kN for the second case ($\delta/\varphi = 1$). According to the data published by NAVFAC (1982), the friction angle δ between the steel with the soil could range from 20° to 75% of the friction angle φ of the soil. This can lead to a value of δ ranging from 20° to 30° . If one considers a value of δ equal to $2/3 \varphi$, F is found to be 22.9 kN.

Table 2.12 summarizes the prediction for the static tests of Table 2.1 using the same methodology presented previously.

Table 2.12: Comparison of the predicted maximum load with the maximum load of the static test

Reference	Type of post	Post embedment (mm)	Height of load (mm)	Test load P kN	Predicted P kN
Eggers and Hirsch (1986) test 1	Wood	457	533	3.11	3.13
Eggers and Hirsch (1986) test 2	Wood	610	533	5.78	6.59
Eggers and Hirsch (1986) test 3	Wood	762	533	10.23	11.58
Eggers and Hirsch. (1986) test 4	Wood	965	533	17.79	20.77
Dewey (1982) test 1	Wood	965	533	14.23	12.46
Dewey (1982) test 2	Steel	965	533	14.68	12.33
Dewey (1982) test 3	Steel	1118	533	17.35	17.59
Wu and Thomson (2007)	Steel	1000	550	15.40	14.66

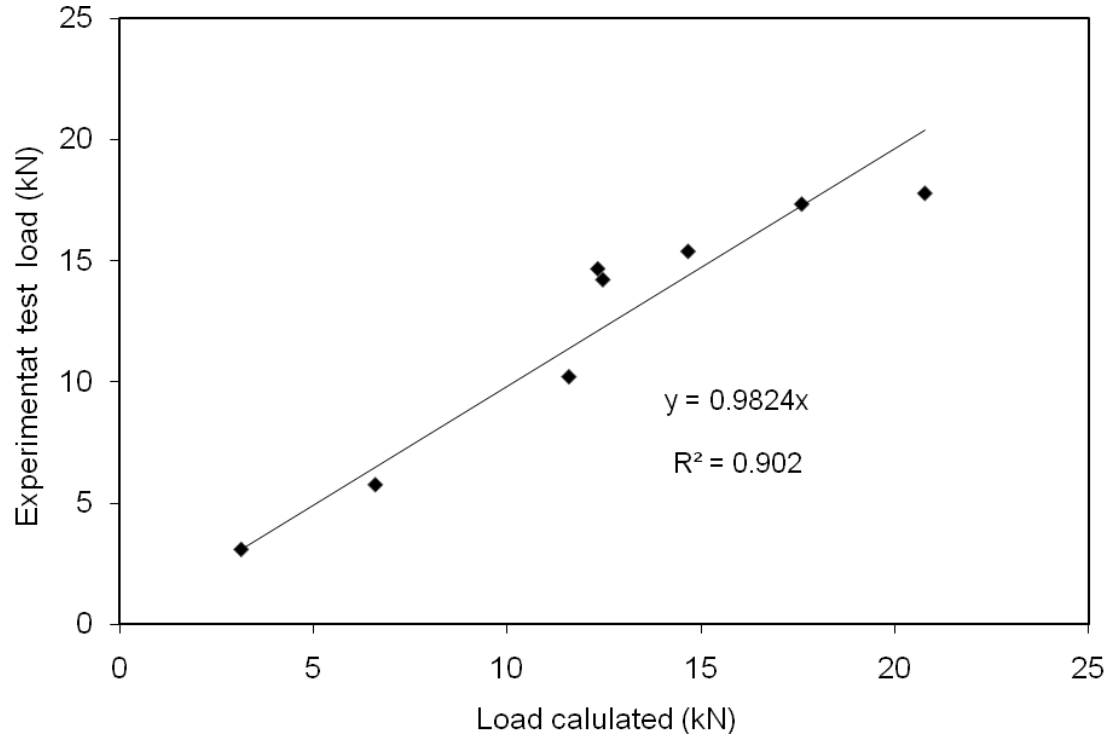


Figure 2.26: Relation of the maximum test load with the calculated test load for the static tests

The maximum loads of static test are plotted as functions of the predicted ultimate loads in Figure 2.26, which shows very good agreement.

2.5 Relation of Static and Dynamic Tests

To establish a relationship between the peak load in the dynamic test and ultimate load in the static test, the Finite Element Method is used to calculate the lateral load for both cases and estimate the ratio between them. The static model was briefly presented previously in the section 2.3.2 and more details are available in Chapter III.

2.5.1 Dynamic loading

For the dynamic tests, a rigid nose consisting of cylindrical shape is used to apply the dynamic lateral load on the post. Radioss software of Altair engineering (Mecalog, 2005) is used. The nose is normally attached to a rigid cart to minimize the energy dissipated in deforming or crushing. The soil and the post were modeled as described previously for the static condition. The displacement of the post was measured at the load application point by measuring the displacement of the rigid nose and the force is calculated at the interface of the post and the impactor. The complete finite element model is illustrated in Figure 2.27. The impact speed was 7.0 m/s. The data collected was filtered with CFC60 filter and the load-deflection curve is determined and plotted in Figure 2.28 with the results of the static loading. Further description and explanation of model used in the dynamic condition are presented in the Chapter III.

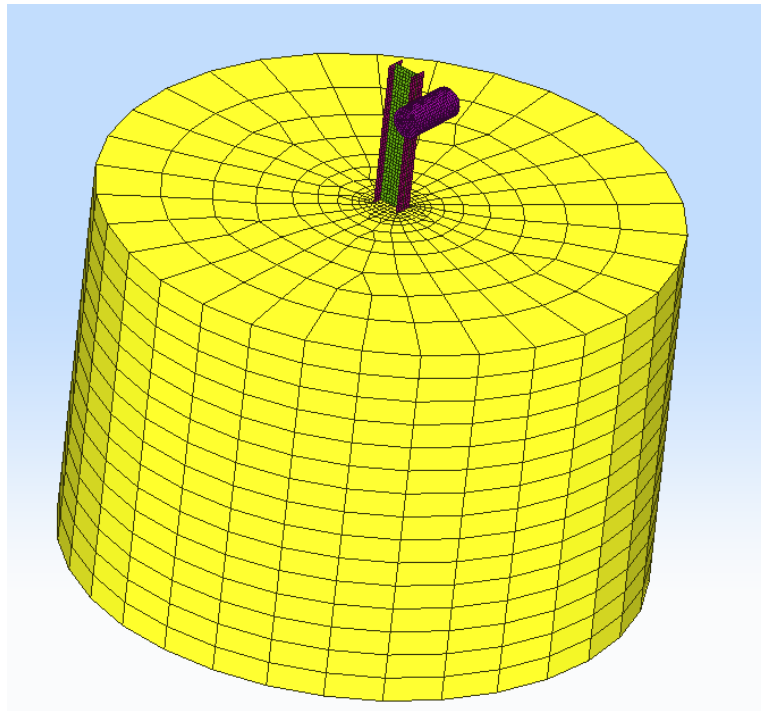


Figure 2.27: View of the finite element model for the dynamic loading of the post in cohesionless soil

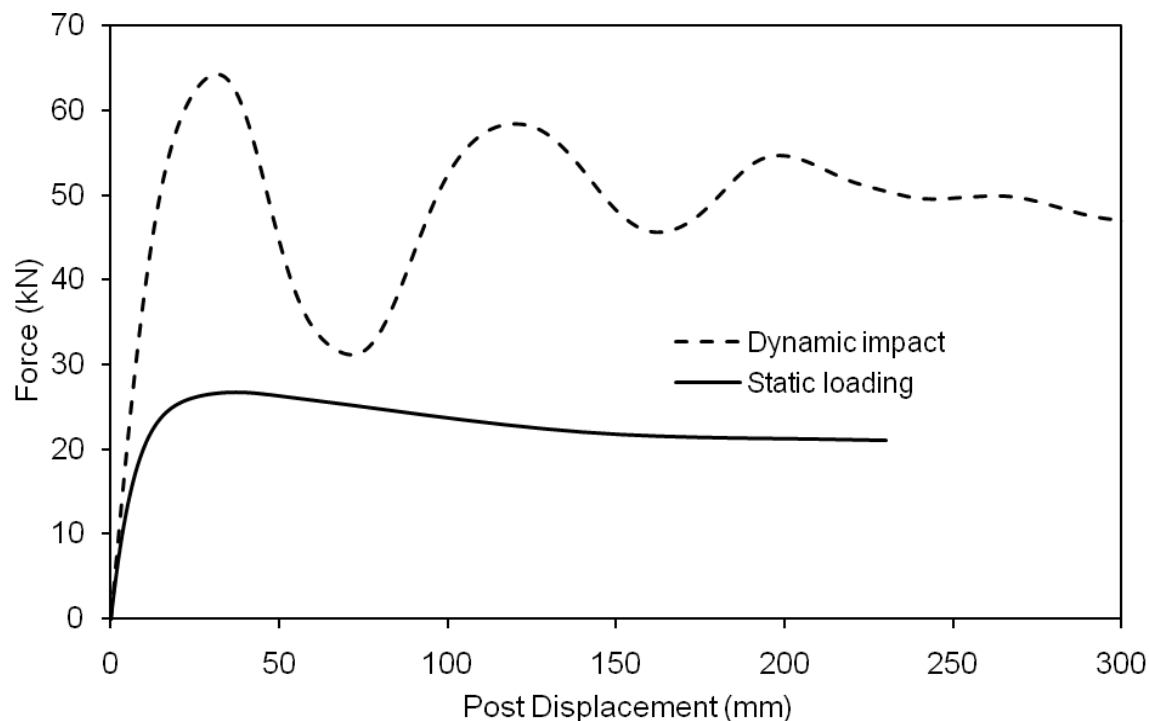


Figure 2.28: Load-deflection curve for static and dynamic cases

2.5.2. Results and interpretation

A finite element method was conducted to study the load deflection curve under the quasi-static and dynamic conditions. The curve of the static loading shows no peak developed and the maximum load reached was approximately 26.7 kN. The maximum dynamic force was about 64.1 kN which is 2.4 times the measured maximum quasi-static force for a same type of post embedded in the gravel. The maximum force was measured at the peak developed in the early stage of loading. The strain rate effects of the steel and the soil density were not considered in the study and need further investigation. The factor of 2.4 between the dynamic load and the static load is close to the factor of 2 found by Wu and Thompson (2007). In their field testing on post with Sigma (Σ) cross section shape, the measured maximum dynamic force was about twice the measured maximum quasi-static force for the same type of post embedded in gravel. To improve the prediction of the static load, the factor of 2.4 is applied to the Table 2.1 only for the dynamic tests and the results of the dynamic tests and the prediction is illustrated in Table 2.13.

The results show that a net improvement in load prediction from the load predicted without a scale factor. However a discrepancy between the prediction and the test conducted in-situ is still present. The difference could be explained by the different parameters involved in the test such as soil confinement, test speed, soil friction angle, the height of load...etc. Another source of discrepancy is the test variability for both the static and dynamic tests. Wu and Thompson conducted repeated static loading tests under the same test conditions and identical steel post. They noticed that a corridor was formed from the measured data of the quasi-static tests. This could be explained by the fact that when a test was repeated using an identical post, the measured resistance force showed some differences probably because the degree of compaction of gravel around the post was not exactly the same. (Wu and Thompson 2007)

2.6 Conclusions

The ultimate lateral resistance of rigid vertical posts in homogenous soil has been calculated based on a simplified lateral earth pressure distribution. The computation of the ultimate load for the tests collected in the literature is based on the determination of the passive lateral earth pressure k_p which is a function of the friction angle. However, many static and dynamic tests found in the literature did not conduct any geotechnical investigation to determine the soil properties including the friction angle, the density and the gradation and the geotechnical parameters have been estimated based on the technical properties of these materials.

Table 2.13: Comparison of the predicted maximum load and the maximum load obtained from dynamic tests

Reference	Embedment (mm)	Test load kN	Predicted load kN
Bronstad et al., (1988)	914	99.2	65.02
Bronstad et al., (1988)	914	73.0	54.19
Bronstad et al., (1988)	914	55.2	43.35
Bronstad et al., (1988)	1118	59.6	35.24
Bronstad et al., (1988)	1118	64.1	35.24
Coon et al., (1999)	1118	64.0	43.93
Coon et al., (1999)	1118	66.9	43.93
Coon et al., (1999)	1118	67.0	46.13
Coon et al., (1999)	1118	36.3	69.19
Coon et al., (1999)	1118	38.8	65.90
Coon et al., (1999)	1118	77.8	65.90
Hollooway et al., (1996)	1118	35.6	63.83
Jeyapalan at al., (1983) test 2	965	99.6	29.60
Polivka et al., (2004)	1092	45.5	37.11
Polivka et al., (2004)	1016	52.6	31.08
Polivka et al., (2004)	940	60.7	25.63
Wu and Thomson (2007)	1000	16.4	35.19

Chapter III

Analysis of Laterally Impacted Guardrail Posts

3.1. Introduction

To evaluate the performance of roadside safety devices, engineers employ destructive full-scale crash testing. These tests are not only very expensive but also require an extensive setup, instrumentation, and destruction of a test vehicle. Moreover, conducting full-crash tests is not always possible, such as when concrete piers are found near the roadway shoulder (Polivka et al., 2004). In this case, other alternative approaches, such as the Finite Element method, could be applied to optimize the design. Finite Element Analysis has rapidly become a fundamental tool of the analysis and design of roadside safety hardware systems. This method is reliable and relatively not expensive. It provides valuable information during the impact event, such as the stress in the barrier and the vehicle, the strain and the energy dissipated. The method is capable of dealing with the highly nonlinear material behaviour, large deformations, and strain rate effects (Plaxico 2002). Finite Element method has been used extensively to study the vehicle interaction with a guardrail barrier and to study the vehicle impact with roadside hardware. Another advantage of the FEM is that it is easy to vary the parameters of the impact and conduct analysis to determine the integrity of the guardrail or to study the vehicle kinematics. This aspect is very important, especially when an iterative process is needed to study the effect of the parameters' variation on the system response. Finite Element simulations must be validated to ensure that the predictions are realistic (Plaxico, 2002).

The first step in analyzing a full crash test is to study a subcomponent level model consisting of one guardrail post being impacted by a bogie vehicle. The analysis serves to understand the dynamic interaction between the post and the soil. Two types of approaches are used to simulate the soil namely: the subgrade modulus approach and the continuum model. The subgrade approach consists of representing the soil by a series of non-linear springs. To identify the spring stiffness, Habibagahi and Langer (1984) used the concept of the bearing capacity and established a linear relation between the soil reaction and the lateral bearing capacity. The method is computationally efficient. However, it cannot capture the effect of the soil inertia

consisting of the first spike seen in the force time-history plots of the dynamic tests. The soil was treated as a massless medium although the soil inertia plays a major role, especially in the initial contact of the post-soil during the impact (Kennedy et al., 2004). Most of the studies conducted in the area of roadside impact do not consider the effect of the soil mass and the energy dissipation through damping in the soil.

The second approach in modeling the soil in the Finite Element method is to represent it as continuum. This technique considers the soil as solid elements obeying a given constitutive law. The approach is more accurate than the subgrade model but computationally expensive. It automatically captures the soil-structure interaction and allows the analyst to study the effects of the backfilling and compaction. The accuracy of this method depends on many factors, the most important of which being the selection of the appropriate soil material model and its parameters. The soil behaviour is, in general, non-isotropic and nonlinear material and the soil properties can vary with the water content, degree of compaction and grain size, which makes the selection of the material model and its parameters more complicated. Drucker and Prager model is the simplest accurate constitutive law capable of simulating the main soil behaviour.

A combination of the two methods, the subgrade method and the continuum method, has been used by Kennedy et al., (2004) in a full-scale model of a vehicle impacting a highway guardrail. The soil stiffness was modeled by nonlinear springs determined by the Habibagahi and Langer method. To introduce the effect of soil inertia, Kennedy et al., introduced the soil continuum model only in the impact region as shown in Figure 3.1. The material parameters are determined such that the soil has the correct mass with a very low stiffness. Thus, in the impact area, the model includes the nonlinear springs to account for the soil stiffness and the soil block to account for the soil mass.

In this chapter, an improvement of the subgrade model is developed and validated with the dynamic test conducted in sand by Coon et al., (1999). The proposed approach accounts for the stiffness of the soil and the inertial effect generated by the soil mass. The soil reaction is modeled as a system of springs and dampers attached to concentrated masses. The soil mass surrounding the post is added as lumped mass and connected to the post to simulate the effect of the soil inertia. A Finite Element model is developed using the continuum approach and validated using the dynamic test

conducted by Coon et al., These tests covered various ranges of impactor speeds with different types of post material and geometry and were used by other researchers. Therefore, the soil properties and test conditions for both modeling approaches are documented. The continuum method serves to determine different parameters of the new subgrade model. This approach, developed initially for the cohesionless soil, is then extended to clay.

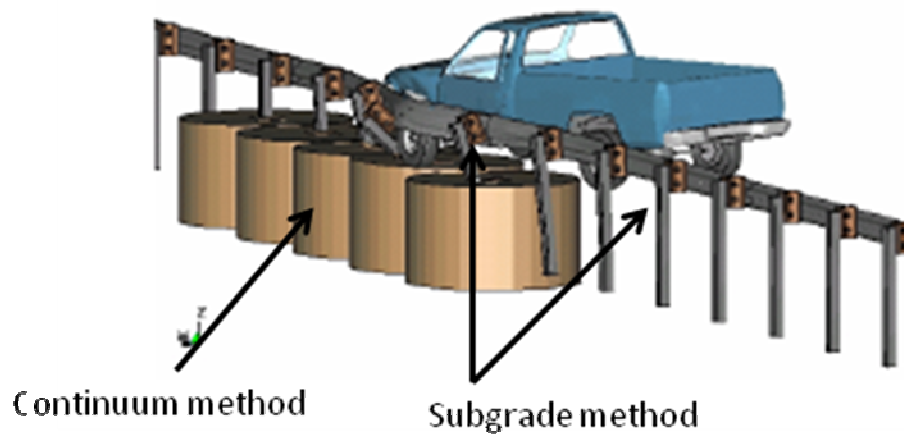


Figure 3.1: View of full-scale finite element model of guardrail system combining the subgrade with the continuum method (Kennedy et al., 2004)

This chapter is organized as follows. Section 3.2 describes the baseline dynamic tests used to calibrate the finite element simulations. Section 3.3 describes the continuum model used to define parameters for the subgrade model. Section 3.4 describes the proposed simplified model for cohesionless soil whereas Section 3.5 is an application of this model to cohesive soil.

3.2. Baseline Dynamic Test

Coon et al., (1999) conducted a series of 17 dynamic tests with different size of post and impactor speeds to evaluate the load capacity of guardrail posts. The Midwest Roadside

Safety Facility (MwRSF) was used to conduct these dynamic load tests. The cart consisted of a rigid nose bogie vehicle with a mass of 946 kg, instrumented with an accelerometer to measure the lateral deceleration during the impact. Four tests were conducted with W 152mmx13.5mm beam cross section. The speeds of the tests were 4.6, 5.4, 5.9 and 8.9 m/s. The soil density ranged from 1980 kg/m³ to 2240 kg/m³ with no moisture content in any of the four tests. The length of the post was 1830 mm with an embedment in the ground of 1100 mm. The point of impact of the bogie with the post was located at 550 mm above the ground level as illustrated in Figure 3.2. The results of these tests are presented in Table 3.1. Based on the response, it is clear that for speeds ranging from 4.6 m/s to 5.9 m/s, the impactor rebounds back. However, for the higher speed of 8.9 m/s the impactor overrides the post. Table 3.1 shows that the lateral travelling distance of the impactor and the lateral peak force increased with the speed.

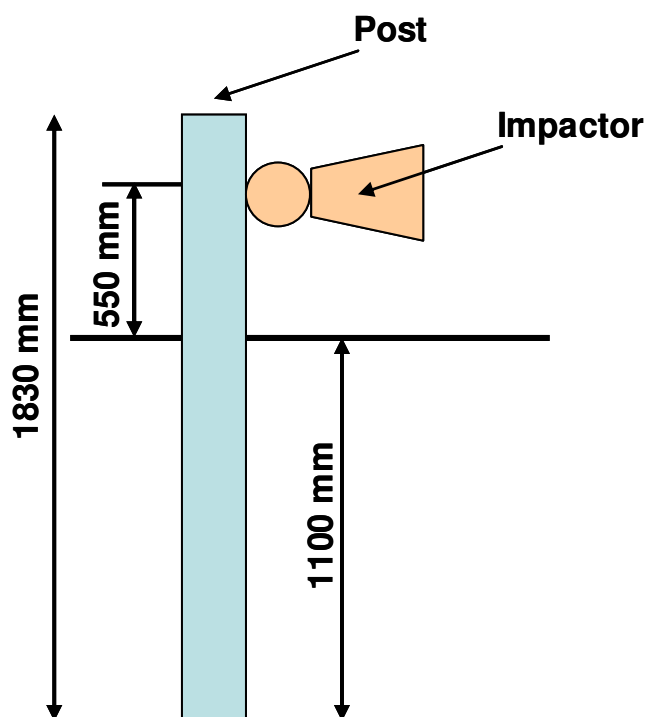


Figure 3.2: Schematic representation of the dynamic test set-up used by Coon et al., (1999)

Table 3.1: Dynamic test matrix of steel post embedded in soil conducted by Coon et al., (1999)

Test #	Soil Density kg/m ³	Moisture Content	Speed m/s	Post Deflection mm	Average Load kN	Peak Load kN
1	1980	Dry	4.6	234	42.8	64.0
2	2110	Dry	5.4	314	43.9	66.9
3	2240	Dry	5.9	348	47.3	67.0
4	NA	Dry	8.8	Override	NA	104.7

All the models in the current analysis were developed using the HYPERMESH and HyperCrash pre-processor software packages from Altair Engineering. The explicit code Radioss was used for the analysis. The post-processing analysis was performed using the Hyperview and Hypergraph software packages from Altair engineering.

3.3. Continuum Approach

3.3.1. Post and impactor modeling

The posts used in the guardrail system are of a W150x13.5 structural shape. The length of the post is 1830 mm, its width is 150 mm and the embedment depth is 1100 mm. The continuum model consists of a post embedded in a soil block as shown in Figure 3.3.

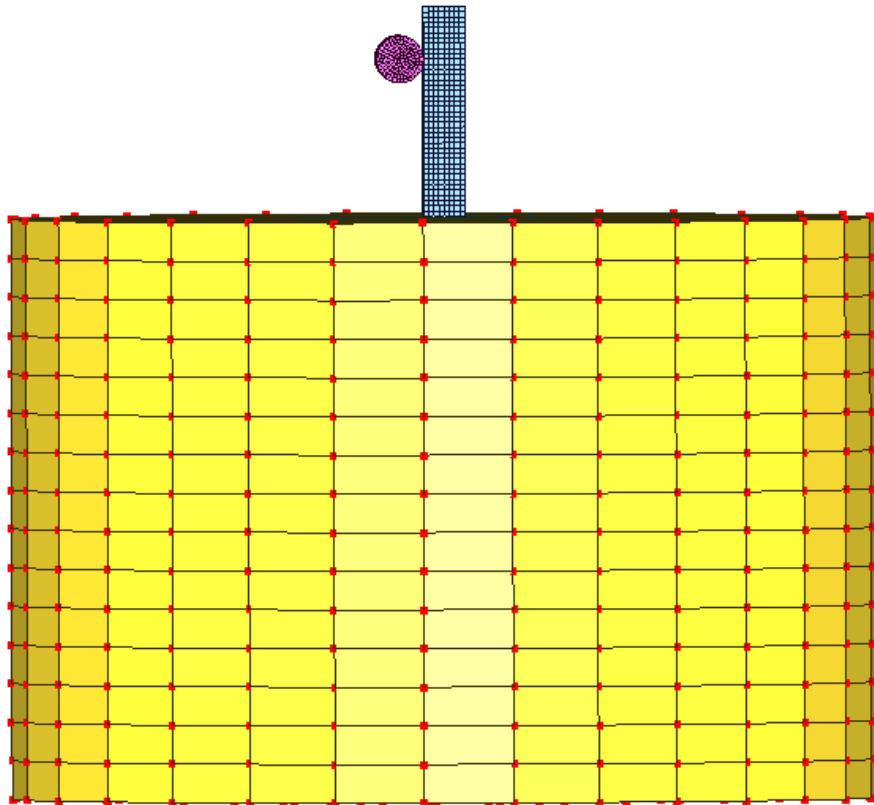


Figure 3.3 View of the finite element model of the post embedded in the soil

Material properties

The material of the W150x13.5 beam is classified as AASHTO M-183 (AASHTA 1998). The W shapes rolled in Canada and most mills supplying the Canadian market have essentially parallel flanges. Furthermore, the web-to-flange fillet radius may vary slightly from mill to mill (Canadian Institute of Steel Construction 1991). The fillet radius has been ignored in the current model and the steel post has been modeled with 4-nodes shell elements. The model of the steel post (W152x 13.5) as shown in Figure 3.3 is formed by 2020 shell elements and 5720 nodes. The post was meshed with four-nodes using QEPH shell formulation (type 24) in Radioss, which is an improved formulation of Belyshko-Leviathan formulation because of their computation efficiency and their control of the hourglass (Mecalog, 2005). The Gauss quadrature numerical integration was used with five integration points through the thickness of the element. The material properties of the post are considered elasto-plastic material and include the strain rate effect (type 44) in Radioss software (Mecalog 2005). The input data for the material is presented in Table 3.2 as been used by Plaxico (2002), Wright and Ray (1996) and Engstrand (2000). These material properties are typical and not very different from those used by Karlson (2000) or used by Atahan (2002) where the yield stress ranges from 350 to 450 MPa and Poisson's ratio ranges from 0.29 to 0.33.

Table 3.2: Radioss material properties of the guardrail post, Engstrand (2000)

Properties	Value
Young's Modulus (GPa)	210
Poisson's Ratio	0.3
Density (kg/mm ³)	7.8 E-06
Yield Stress (GPa)	415

Strain rate effect

The plastic behaviour of some materials such as steel is sensitive to the strain rate which is known as material strain rate sensitivity or visco-plasticity (Jones, 1989). This phenomenon is encountered in many practical engineering problems, such as the guardrail post. The material strain rate sensitivity is independent of the structure and manifests itself as a strengthening effect in the structure and influences its response (Jones, 1989). To include the effect of the strain rate in analysis, many constitutive equations have been proposed. Cowper and Symonds (1957) suggested the following equation for the uniaxial case:

$$\frac{\sigma'}{\sigma} = \left(1 + \left(\frac{\dot{\epsilon}}{D} \right)^{\frac{1}{q}} \right) \quad (3.1)$$

where σ and σ' are the quasi-static and dynamic stress, respectively, and $\dot{\epsilon}$ is the strain rate; q and D are the Cowper and Symonds' coefficients. For steel, the Cowper and Symonds' coefficients, q and D , are estimated to be 5 and 40.4, respectively (Jones, 1989).

The impactor has been modeled as a cylinder as shown in Figure 3.3 using 8-node hexahedron elements attached to a rigid body to eliminate the energy dissipated through the impactor. The cart used by Coon et al., consisted of thick steel cylinder filled with concrete which minimizes the energy absorbed by the impactor. An added mass was distributed on the impactor nodes to simulate the 946 kg cart mass used in the dynamic test.

3.3.2. Soil modeling

The soil surrounding the post is modeled as a cylinder block in which the post is embedded in its center as shown in Figure 3.3. A convergence study with various diameters has been conducted to determine the soil model size. The dimensions of the block are chosen such that the outer boundaries have minimum effects on the simulation results. The accuracy of the Finite Element model results depends on an adequate selection of the soil material parameters. The soil material can be modeled with solid element with different material laws.

Soil constitutive model

The most common engineering classification system groups the soils in three major groups: (1) coarse-grained soils (e.g. sand and gravel); (2) fine-grained soils (e.g. silts and clays); and (3) highly organic soils. Cohesive soils are characterized by the tendency of the particles to stick together because of their particle attraction or adhesion. Cohesionless soils are composed of gravel and sand, and the typical particle size of sand ranges from 0.06 mm to 2.0 mm and from 2 mm to 60.0 mm for gravel. For the cohesive soil, the particle sizes are, in general, less than 0.002 mm (Canadian Geotechnical Society, 2006). The fine-grained soils are not classified by grain size but according to their plasticity and compressibility.

The soil recommended in roadside installations is the cohesionless soil formed by crushed limestone road base material. The soil should be well-graded and contains a maximum aggregate size between 25 mm and 50 mm (Bligh et al., 2004). Report 350 (Ross et al., 1993) recommended that the standard soil meets AASHTO standard specifications (AASHTO 1990). The soil should be compacted in accordance with AASHTO Guide Specifications for Highway Construction. It is not easy to conduct traditional geotechnical tests on coarse soil such as triaxial tests or direct shear tests to determine the geotechnical soil parameters and, in particular, the friction angle and the cohesion property of the soil. To determine the friction angle, engineers use predefined correlations between the friction angle and geotechnical parameters such as the relative density, the gradation, and overburden pressure that could be measured on these soils. The simplest and most commonly used models in the area of geotechnical engineering are the Mohr-Coulomb and Drucker-Prager failure criteria. Mohr-Coulomb, where the failure occurs when the shear stress reaches a value under a normal stress σ , defines a hexagon. This failure criterion has a corner on the hexagon, which is not mathematically convenient and does not lend itself well to numerical solutions.

The base for soil modeling for Radioss (Macalog, 2005) and Ls_Dyna3D (Hallquist, 2006) is the work conducted by Krieg (1972) developed for cellular concrete and extended to the soil and rocks. Krieg proposed a cap model for cellular concrete based on Drucker and Prager failure criteria. The model is based on the assumption that for small strains, both in tension and compression, cellular concrete is linear elastic but as the strain s become larger, nonlinear stress-strain behaviour is noted and permanent set

occurs. The failure of the cell cavities in compression, however, is accompanied by development of cohesive strength so that finite shear strength remains while cells are being crushed and this shear strength grows as the pressure increases. This behaviour can be modeled with a yield surface in principal stress space which is a surface of revolution centered on the hydrostat and increasing in radius with increasing pressure. This behaviour is extended to rocks and soils and defined as Law 21 in Radioss and shown in Figure 3.4.

Krieg (1972) expressed the stress state applied at a point of the continuum medium in terms of the Cauchy' stress tensor σ_{ij} written as:

$$\sigma_{ij} = S_{ij} + P \delta_{ij} \quad (3.2)$$

Where i and j are indices varying between 1 and 3, and S_{ij} is the stress deviator tensor representing the state of pure shear; δ_{ij} is the Kronecker delta tensor, and p is the hydrostatic stress tensor or spherical stress tensor, defined as:

$$P = \frac{1}{3} \sigma_{ij} \delta_{ij} \quad (3.3)$$

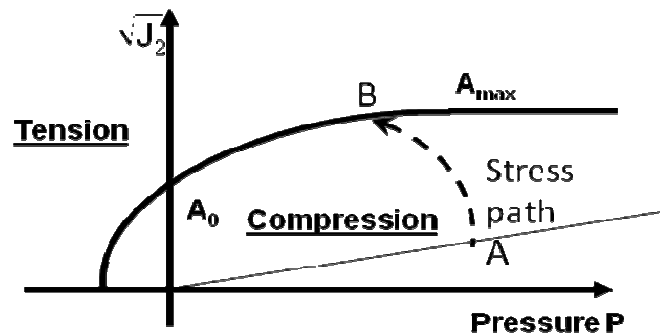


Figure 3.4: Yield criterion in the plane of $\sqrt{J_2}$ and P

The hydrostatic stress causes volume change whereas the deviatoric stress causes the change of shape. The general functional form of failure criteria may be written as a function of σ_1 , σ_2 and σ_3 . However, an alternative convenient way of describing the failure is to utilize combinations of the stress invariants. Experimental data showed that

the failure criteria for the cohesionless soil depend only on the hydrostatic state of stress. The simple parameter I_1 defined as the sum of the principal stresses describes a cylinder centered on the hydrostatic line. For the pressure-dependant material, the deviatoric cross section of the failure surface along the hydrostatic axis is different in size and is assumed to be similar in shape.

The surface is capped by a plane that is normal to the hydrostatic line and moves outward only. The yield surface defined by Krieg(1972) is expressed as:

$$\phi = (P - f) \left(J_2 - (a_0 + a_1 P + a_2 P^2) \right) = 0 \quad (3.4)$$

Where P is the pressure in the medium, f is a function of the mean total strain, J_2 is the second invariant of the stress deviator and a_0 , a_1 and a_2 are constants.

Krieg (1972) expressed the yield stress by two functions, one describing a paraboloid and the other describing the plane normal to the hydrostatic line:

$$\phi_p = (P - f) \quad (3.5)$$

$$\phi_s = J_2 - (a_0 + a_1 P + a_2 P^2) \quad (3.6)$$

ϕ_s is a function describing the paraboloid

ϕ_p is the surface perpendicular to the hydrostatic line.

To ensure that the stress state remains inside the yield surface, the tensile fracture should not occur, that is:

$$P \geq h \quad (3.7)$$

where h is a constant defining the minimum cut-off pressure..

The second step is to determine ϕ_p .

If

$$\phi_p = 0 \quad \text{and} \quad \dot{\phi}_p = 0 \quad (3.8)$$

then volumetric plasticity occurs. Krieg (1972) showed that the integration of Equation 3.8 leads to an elastic response.

For the deviatoric tensor, the conventional plasticity theory is used. If

$$\phi_s < 0 \quad \text{or} \quad \phi_s = 0 \quad \text{and} \quad \dot{\phi}_s < 0 \quad (3.9)$$

then the loading is considered to behave elastically in the deviatoric mode. In this case:

$$\dot{S}_{ij} = 2G \dot{\epsilon}_{ij} \quad (3.10)$$

where \dot{S}_{ij} is the deviatoric stress rate.

$\dot{\epsilon}_{ij}$ is the elastic strain rate component

If the yield surface is reached and the loading conditions are applied:

$$\phi_s = 0 \quad \text{and} \quad \frac{\partial \phi_s}{\partial S_{ij}} S_{ij} \geq 0 \quad (3.11)$$

then, a deviatoric plasticity is taking place. The total strain rate could be decomposed into elastic (recoverable) and plastic (irrecoverable) components:

$$\dot{\epsilon}_{ij} = \dot{\epsilon}_{ij}^e + \dot{\epsilon}_{ij}^p \quad (3.12)$$

where $\dot{\epsilon}_{ij}^p$ represents the plastic strain rate component and $\dot{\epsilon}_{ij}^e$ the elastic component.

The elastic component is defined as:

$$\dot{\epsilon}_{ij}^e = \frac{\dot{S}_{ij}}{2G} \quad (3.13)$$

The plastic strain rate is assumed to lie in a direction normal to the yield surface in the case of associative plasticity. This can be expressed as

$$\dot{\epsilon}_{ij}^p = \lambda \frac{\partial \phi_s}{\partial S_{ij}} \quad (3.14)$$

where λ is a positive scalar. Krieg (1972) showed that λ is determined by:

$$\lambda = \frac{S_{ij} \dot{\epsilon}_{ij} - (a_1 + 2a_2 p) \frac{\dot{p}}{2G}}{S_{ij} S_{ij}} \quad (3.15)$$

The deviatoric stress rate could then be calculated as:

$$\dot{S}_{ij} = 2G \dot{\epsilon}_{ij} - \left[2G \frac{S_{ij} \dot{\epsilon}_{ij}}{S_{ij} S_{ij}} - \frac{(a_1 + 2a_2 p) \dot{p}}{S_{ij} S_{ij}} \right] S_{ij} \quad (3.16)$$

Soil material models parameters

Considering the triaxial axial compression test under undrained condition, the initial stress state of triaxial compression test under undrained condition consists in applying uniform pressure ($\sigma_v = \sigma_h$). From this initial condition, the confining pressure is held constant and the axial loading is increased till the failure, defined by the maximum principal stress difference, occurs. At this point of failure, the values of I_1 and J_2 could be calculated:

$$J_2 = \frac{2}{3} (\sigma_1 - \sigma_3)_f^2 \quad (3.17)$$

$$I_2 = \frac{1}{3} (\sigma_1 + 2\sigma_3)_f \quad (3.18)$$

Three triaxial tests with different compression pressure will define the curve of J_2 as function of I_1 and the coefficient a_1 , a_2 and a_3 could be determined from the curve.

Another approach to determine the a_1 , a_2 and a_3 coefficient is to conduct unconfined compression test. In this case $a_1 = a_2 = 0$ and $a_0 = \sigma_y^2 / 3$.

Geometry and boundary conditions

The size of the soil block used in the Finite Element model varies in the literature. The diameter varies from 1.5 m (Bligh et al., 2004) to 4.0 m (Wu and Thomson, 2007). Bendidi (2002) and Bligh et al., (2004) used an intermediate diameter of 2.7 m. The depth of the block ranged from 1.0 m (Wu and Thomson 2007) where they set the depth the same as the embedment length of the post, to 2.02m (Bendidi 2002). Bligh et al., (2004) used an intermediate depth of 1.6 m and considered this depth enough to provide ample depth of material below the post. The post embedment depth in the soil was 1118 mm for Bendidi (2002) and Bligh et al., (2004). For all these models, the outer boundaries of the soil block are constrained with no-reflecting boundary around the outer face of the cylinder. The possible effect of stress wave reflection from outer boundaries was not considered in those previous studies. For the current study, the block has a diameter of 2700 mm and a height of 2100 mm.

Mesh properties

The soil is modeled using 8-node hexahedron elements which have been used by many researchers, such as Marzoughi et al., (2001), Bendidi (2002), Whitworth et al., (2004) and Mohan et al., (2005). The geometry of the soil mass interacting with the post is modeled as a cylinder with a post embedded at the center. The soil was divided into three coaxial cylindrical blocks having different mesh sizes. The mesh size of the soil was finer at the vicinity of the post to capture the soil deformation and coarser at the outer portion of the cylindrical block. Figure 3.5 illustrates the cross section of the soil blocks and steel post. The solid element formulation could have one integration to eight integration points or even higher with or without Corotational formulation. For this study, the inner soil block was selected to have a Corotational formulation with eight integration points. The middle and outer soil blocks are modeled with a Corotational formulation with one point of integration to optimize the computing time.

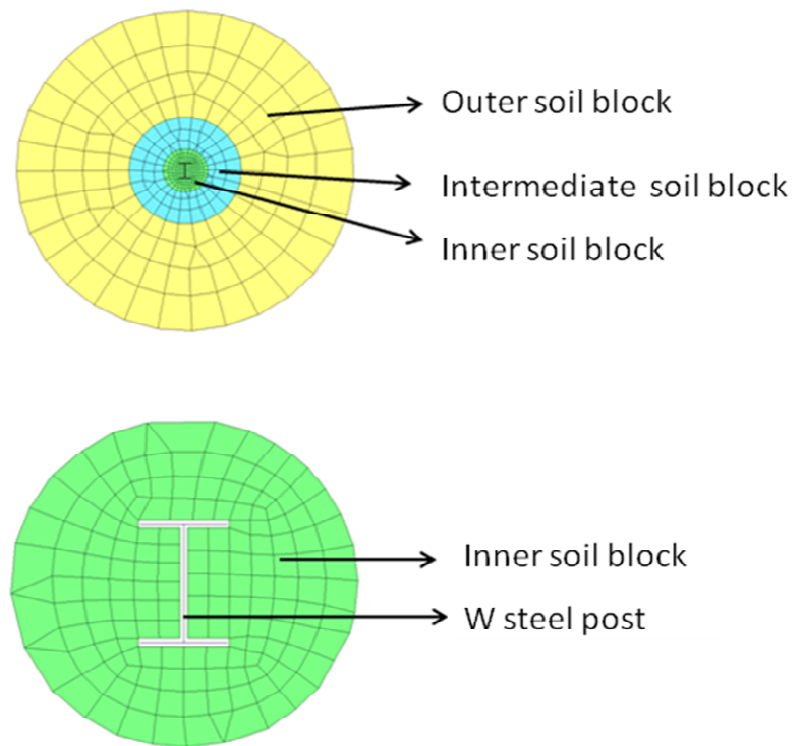


Figure 3.5: a) Horizontal cross section of finite element model of the soil and the post, b) Horizontal cross section of the finite element model of the inner soil and the post

The formulation using one point of integration despite its efficiency can generate zero energy hourglass modes. A check of the hourglass energy generated in the model was conducted at the end of each simulation to assure that the hourglass energy was low with no affect on the results. To prevent the effect of stress wave reflection, a silent boundary condition is introduced at the outer surface of the soil cylinders.

The soil-post interaction was simulated by an element-based surface to surface interface contact pair with a frictional contact (master-slave relationship). As the master surface (post) moved in contact with the slave surface (soil block), the normal and the shear forces were computed. The friction formulation is based on the Coulomb criterion. The nodes of the master surface are checked for penetration and if the penetration occurs, a force proportional to the penetration is applied on the node to push it back. A kinematic contact algorithm was used to enforce the contact constraints at the interfaces between the two surfaces. To prevent the intrusion between the thin edge of the post and the soil

mass, an edge to edge contact interface (type 11) is also used in the model. This type of interface is computationally demanding but unavoidable to prevent any penetration. Other interfaces were used in the model as the self impact interface for the soil and self impact interface for the post. These interfaces ensure that the elements of each part, soil and post, are not penetrating themselves during the crash (Radioss, 2005).

The nodes located at the outer block were kinematically constrained in the three directions whereas their rotation remained unrestrained. The nodes at the base of the soil block were constrained only in the vertical direction z . The parameters of the Drucker and Prager model were determined from a literature (Wu, 2000) and are presented in Table 3.3.

Table 3.3: Soil properties for the cohesionless soil

Parameters	Value
Young Modulus (MPa)	0.997
Poisson ratio	0.35
a_0	1.58 e -07
a_1	0.00012
a_2	0.024
a_{\max}	0.024
P_{\min} Cutoff pressure (MPa)	55 e -06

3.3.3. Results of the continuum simulation

The finite element simulation was conducted up to 200 ms and the results are summarized in Table 3.4 for the Finite Element simulation and the dynamic test for the different speeds. The load deflection curves obtained from the Finite Element simulation and the dynamic test show a good agreement. In fact, for the speed of 5.9 m/s for the

test #3, the average force was approximately 47 kN and the post displacement was 350 mm for both the simulation and the dynamic test (Figure 3.6). These results indicate that the continuum method correlated well to the dynamic test in terms of peak force, average force and in post displacement.

A review of the continuum model animation results shows that the displacement and the rotation in the direction of loading were dominant during the test as illustrated in Figure 3.7. The centre of rotation is located at around 810 mm under the ground level. It is interesting to note that the soil elements located at the vicinity of the post were significantly deformed and distorted and the element located at the outer border are not deformed. The impactor decelerated until it stopped completely (reached a speed 0 m/s); rebounded back at the time of 112 ms.

Table 3.4: Comparison of the average force and maximum deflection between dynamic test and Finite Element simulation

	Maximum Deflection (mm)		Average Force (kN)		Peak Force (kN)	
	Test	Model	Test	Model	Test	Model
Test #1	234	240	42.8	41.1	64.0	53.1
Test #2	314	321	43.9	42.5	66.9	57.8
Test #3	348	353	47.3	46.3	67.0	64.3
Test #4*	Override	Override	NA	55.3	104.7	97.2

* The post used in test 4 is W150x23.5 instead of W150x13.5

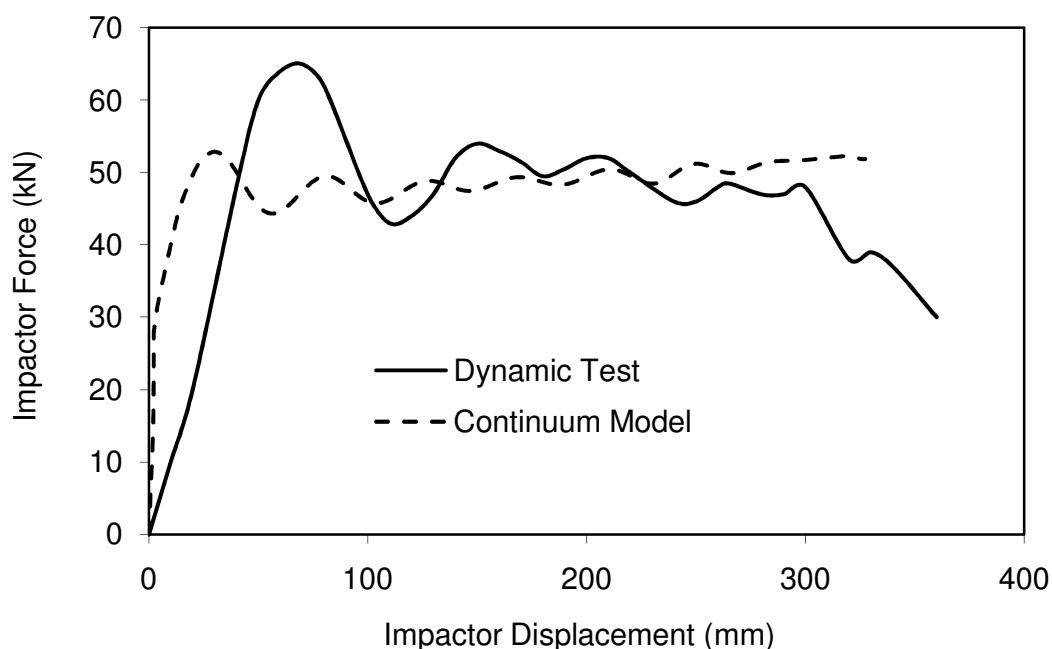


Figure 3.6: Comparison of load-deflection curve of dynamic test # 3 and that obtained using the continuum method

Figure 3.6 shows that the initial stiffness of the load deflection for the dynamic test is lower than that for simulation curve which explains the shift of approximately 15 mm between the two curves. The difference between the two curves could be explained by two possible reasons. The first explanation is the fact that the soil in contact with the post was not compacted enough in the test to load the post early, which results in less resistance to the post at the early stage of loading. In fact, to install the post in the cohesionless soil, an auger is used to dig a hole in the ground. After the soil is installed, the hole is backfilled and compacted. It is difficult to compact the area close to the post because of the risk to hit the post. Therefore, a slack is created in the system and the soil around the post showed less resistance. The second reason is the imperfection of the post's straightness as noticed by Reid et al., (2009) in wood posts. They suggested that these imperfections created a gap that allowed the post to rotate with the fixture when the force is applied. Reid et al., (2009) concluded that these geometric imperfections cannot be easily modeled and the gap is added between the soil and the post. Several iterations were conducted in the current study to examine the effect of the gap on the results. In the present finite simulation study, the soil reacts to the post

movement instantaneously because of the small gap between the soil block and the post. This gap could also explain the difference of the initial stiffness observed between the finite element model and the dynamic test. The maximum load is reached approximately after 40 mm of impactor displacement for the FEA simulation and 75 mm in the dynamic tests as shown in Figure 3.6.

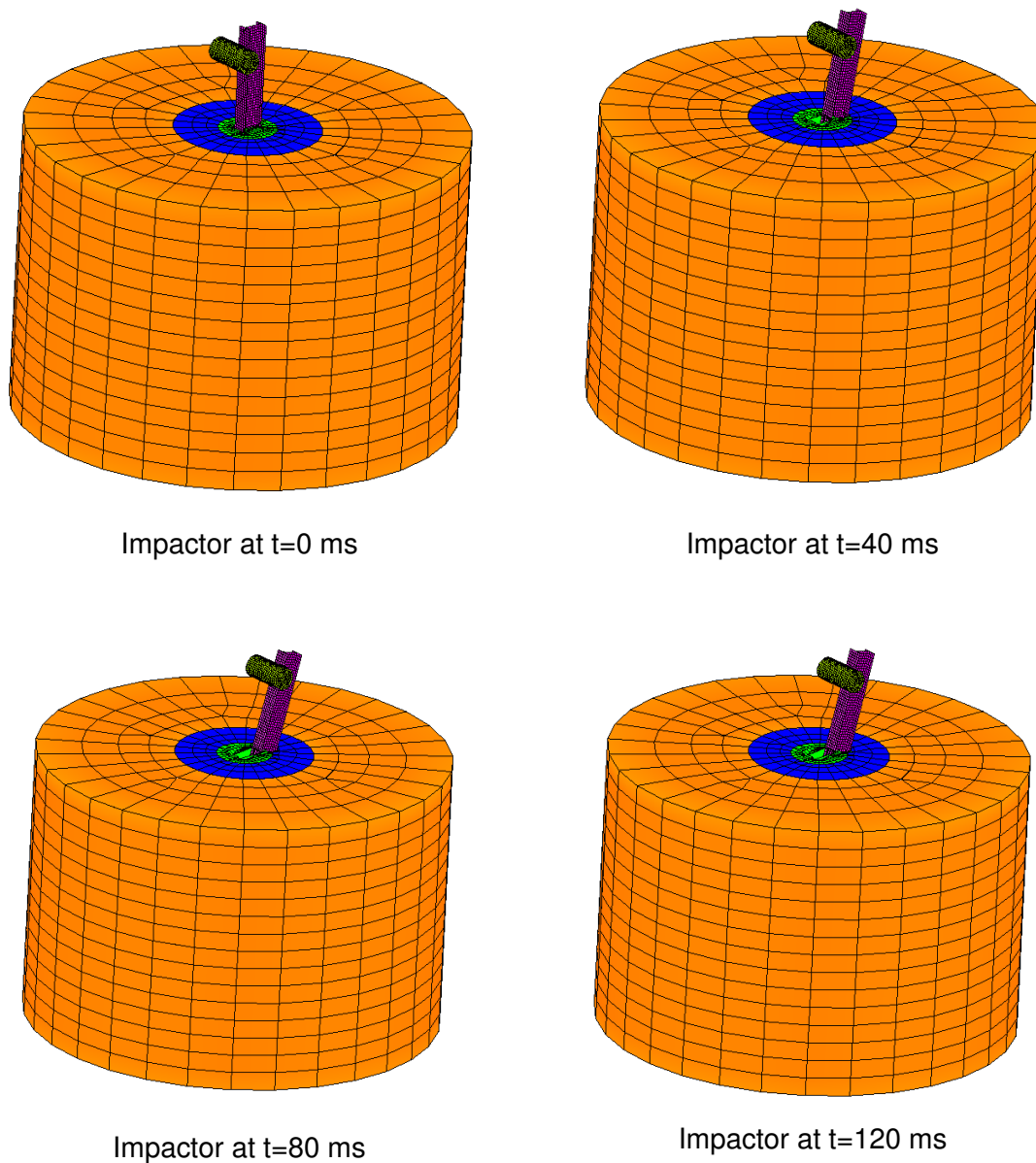


Figure 3.7: Dynamic loading simulation results of the continuum model at initial and deformed state

Figure 3.8 shows the variation of the impactor force as a function of time for the finite element model simulation. It can be seen that the first peak is reached at 8.5 ms and the average load is maintained constant up to approximately 110 ms then the post started to rebound.

Figure 3.9 shows the mass of the soil mobilized in the front of the post at 20 ms using contours representing the nodal displacement. The displacement of the soil mass ranges from appreciatively 160 mm at the vicinity of the post to 0 mm at the extremity of the soil block where the nodes are constrained to move. The shape of the soil mobilized for each displacement appeared as elliptical in shape with a maximum disturbed area at the ground level and zero at the center of rotation located at 810 mm under the ground level.

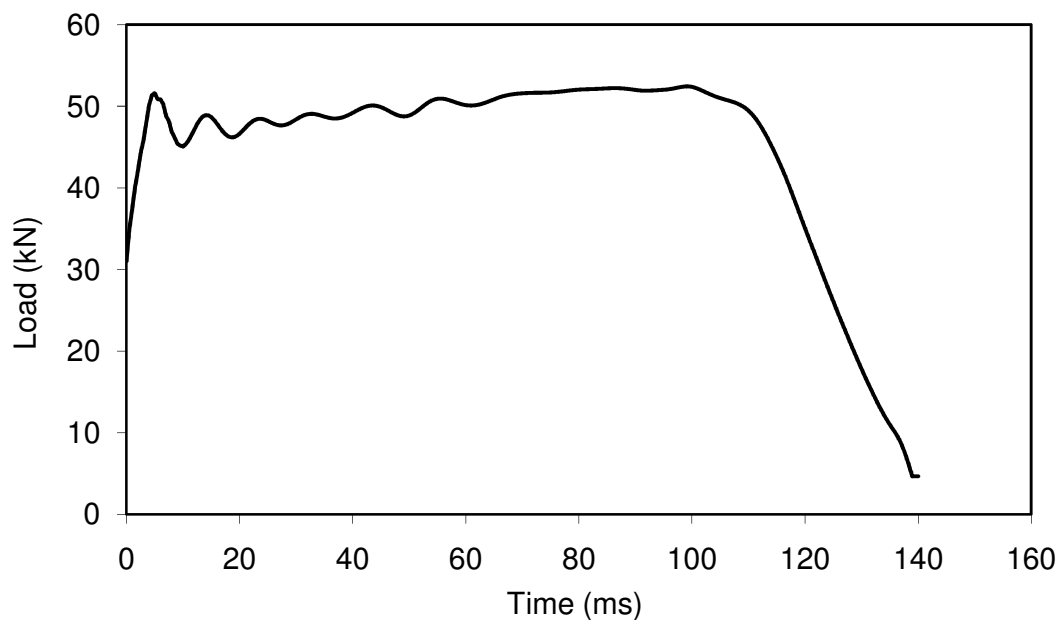


Figure 3.8: Variation of the impactor force as function of time obtained using the continuum method

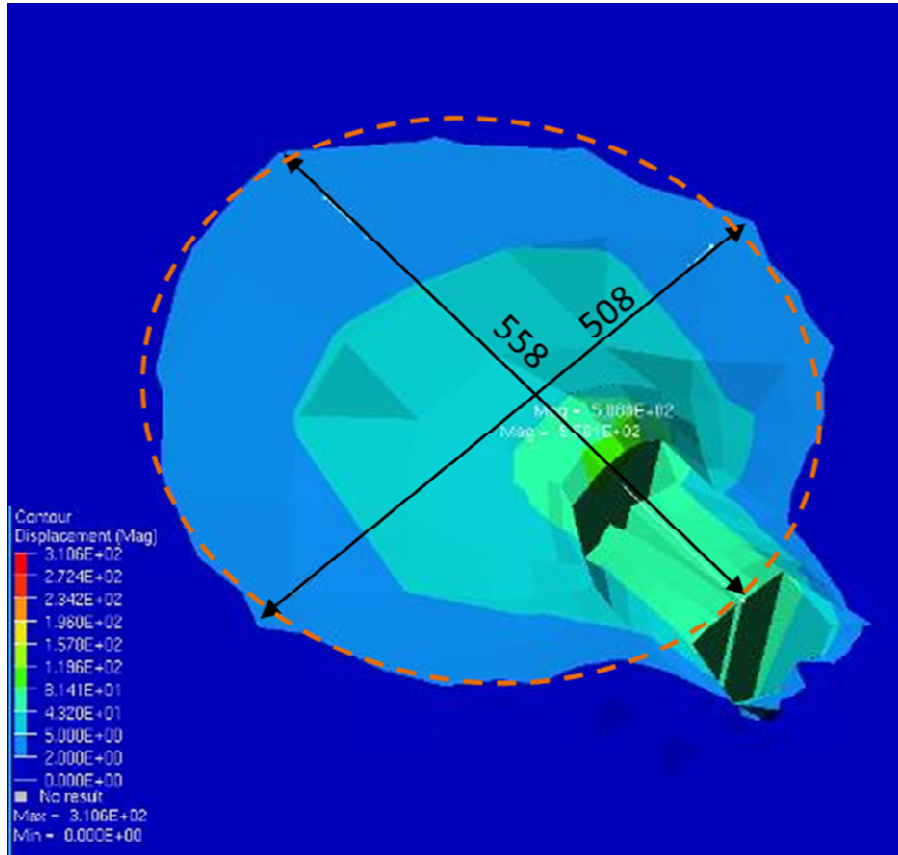


Figure 3.9: View of the mass of soil mobilized at the top surface during impact obtained at 20 ms

3.4. Improved Subgrade Method

The method of horizontal subgrade has been used extensively in the area of geotechnical engineering to calculate the soil lateral resistance in presence of buried structures as explained previously in section 2.2. The lateral loading of piles embedded in soil subjected to lateral load or seismic excitation is a typical example of this application. The method consists of substituting the soil surrounding the structure by a set of springs attached to the post. The pile embedded in the soil is simulated as a one dimensional beam having a bending stiffness EI and a length L and resting on a flexible foundation. The springs are non-linear and the load deflection curves for springs are defined to match the pile reaction. This method is a clear improvement over the previous model where the springs are considered linear.

3.4.1. Interpretation methods of soil-pile interaction under dynamic load

The finite element model of a post embedded in the soil and subjected to a dynamic load could be considered as a single vertical pile loaded under horizontally dynamic excitation. Different models in geotechnical engineering were investigated by geotechnical engineers to study the case of a pile subjected to dynamic load induced by seismic loading. Different models, including the effect of soil damping and soil stiffness, have been proposed.

In 1974, Novak simulated the soil-pile interaction for laterally loaded piles by independent-discrete elastic springs and viscous dashpots as illustrated in Figure 3.10.

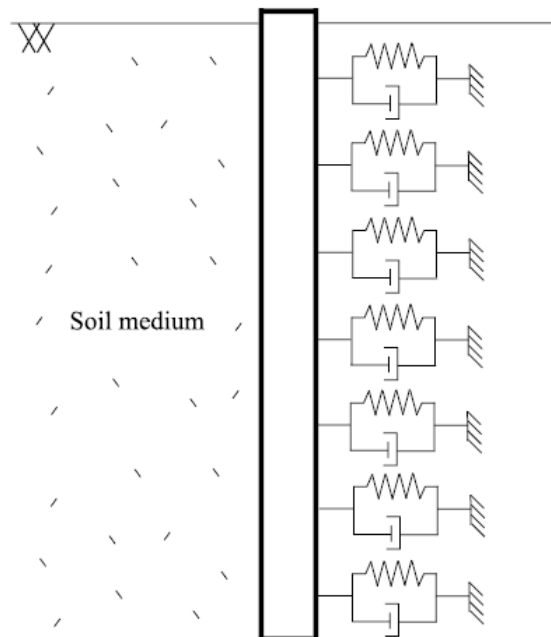


Figure 3.10: Winkler beam in springs and dashpot foundation for laterally loaded dynamic pile (Novak, 1974)

The approach accounts for the energy dissipation inherent to material damping behaviour. Novak concluded that the soil-pile system response is controlled by four dimensionless parameters namely: (a) the mass ratio, ρ/ρ_p , where ρ and ρ_p are the specific mass of the soil and the specific mass of the pile respectively, (b) the ratio of speed V_s/v_c where V_s is the shear wave velocity of the soil and v_c is the longitudinal

wave velocity of the pile, (c) slenderness ratio, L/r_0 , where L is the length of the pile L and r_0 is the pile radius and (d) the frequency of the load, ω , expressed as a dimensionless parameter defined as:

$$a_0 = \frac{r_0 \omega \rho}{G} \quad (3.19)$$

where G is the shear modulus of the soil.

Novak and Sheta (1980) developed a model that takes into account the nonlinear dynamic behaviour of the soil-pile interaction by dividing the soil medium into two regions namely: the inner and the outer field regions (Figure 3.11). The near field region in the vicinity of the pile shaft, where strong nonlinear soil response occurs, is represented by a set of nonlinear springs and dashpots. The soil around the pile is naturally weakened by the installation process and an imperfect bond between the soil and the pile interface takes place. The far field region, where the behaviour is primarily linear elastic, is represented by a series of springs and dashpots. A simpler model based on this approach was proposed by El Naggar and Novak (1995, 1996) and used by Mostafa and El Naggar (2002), consisting of a series of non-linear springs and dashpots for the inner field, and a series of linear springs and dashpots for the far field. They also included a lumped mass of the soil where the mass of the inner field is distributed among the two nodes of the inner field element but its value was not addressed in the aforementioned papers (Figure 3.12).

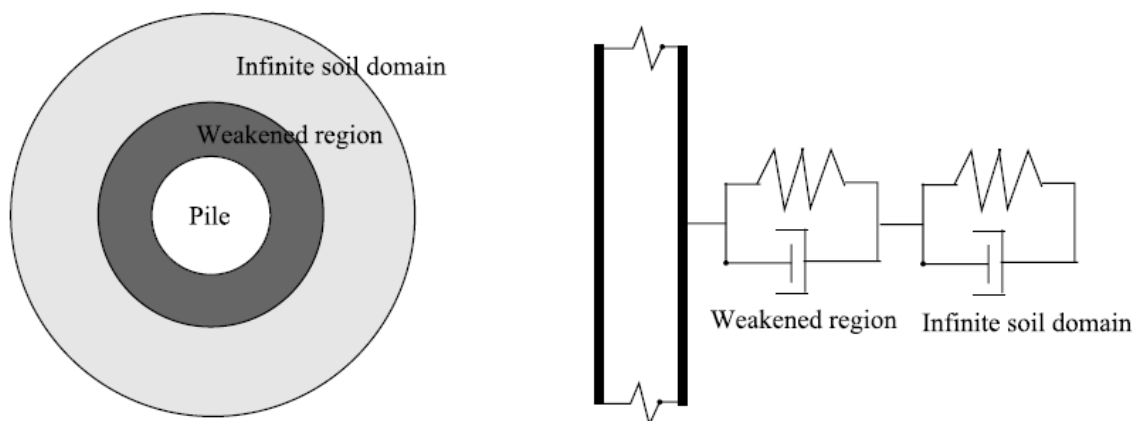


Figure 3.11: Soil pile interaction for weakened soil around the pile circumference (Novak and Sheta, 1980)

A new Single degree of freedom (SDOF) interaction (macro-) element has been developed by Taciroglu et al., (2006). The model incorporates frictional forces and formation of gaps at the soil–pile interface as well as the damping behavior of the soil. The macro-element is an assembly of various basic elements, each of which incorporating a particular aspect of the soil–pile interaction. The assembly includes (1) a drag element to account for the friction between the pile and the soil, (2) a gap element to account for the gapping between the pile and the soil, and (3) an elastoplastic p - y element to account for the hysteretic response of the soil (Figure 3.13). Although the model accounts for the gap between the pile and the soil, it assumes the soil to be massless.

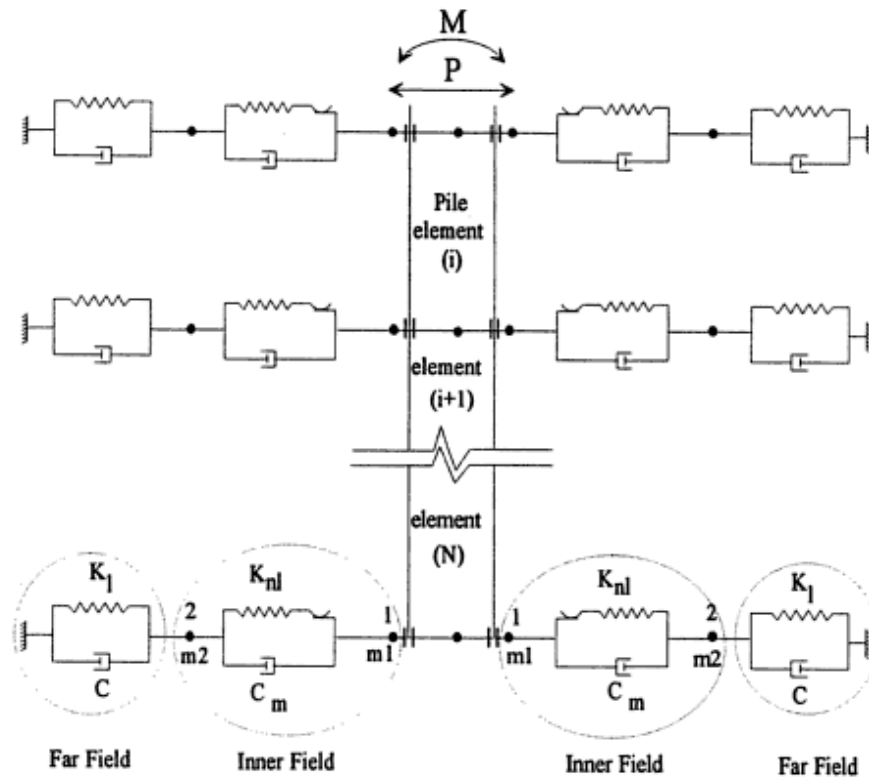


Figure 3.12: Soil-pile interaction model (El Naggar and Bentley 2000)

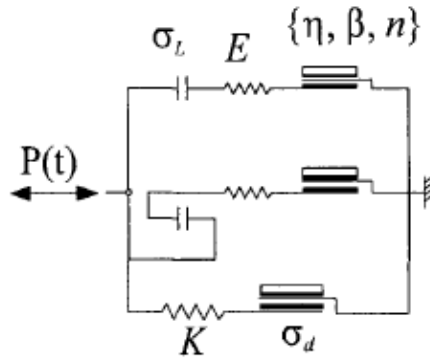


Figure 3.13: Configuration of soil-structure interaction (Tacioglu et al., 2006)

A simplified lumped model, consistent with the Winkler hypothesis, was proposed by Pacheco-Crosetti (2007), where the pile-soil interaction is taken into account through three independent elements namely: a spring with stiffness k_a , a mass m_a , and a dashpot with a coefficient c_a (Figure 3.14). The spring-mass-dashpot coefficients k_a , m_a , and c_a that represent the soil can be obtained by means of simple equations. The approach has the advantage of including all soil components, stiffness, damping and inertia, but it assumes that the components remain constant along the pile depth.

In conclusion, the literature review treating the subject of the pile-soil interaction under lateral loading shows that most of the widely used models consisting of modeling the pile as a series of beam elements and the soil as a group of unconnected, concentrated springs perpendicular to the pile. Some models considered the soil as a combination of dashpots and springs. The soil stiffness and damping properties are the only parameters included in the dynamic analysis but the effect of soil mass is generally ignored.

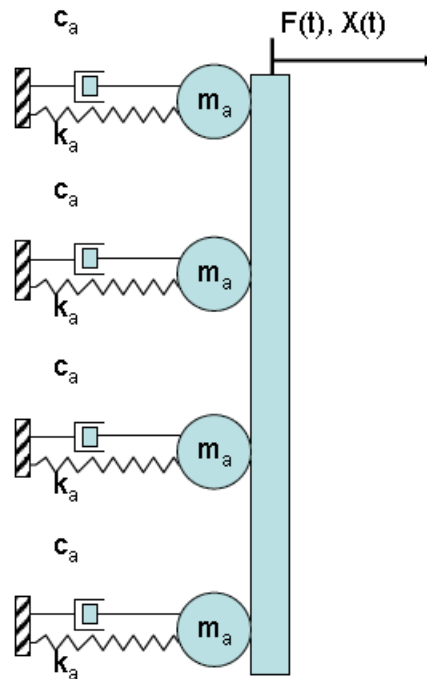


Figure 3.14: Interaction of pile with soil represented by spring, mass and dampers (Pacheco-Crosetti, 2007)

3.4.2. Proposed subgrade method of highway post embedded in cohesionless soil

Different empirical expressions are available in the literature for the modulus of subgrade reaction of different types of soil (Terzaghi 1955, Menard 1962 and Reese et al. 1974). Most of the relations are based on curve fitting of field load tests results and are, in general, conservative when the deflection is small. The method to calculate the modulus of subgrade reaction used in the current study refers to the work of Habibagahi and Langer (1984). The method is based on the bearing capacity concept and does not assume a constant horizontal subgrade reaction, k_h . In fact the coefficient k_h increases with depth and decreases with the increase of deflection as it has been demonstrated by load test data. This method was used by many researchers in the area of roadside safety engineering (Plaxico et al., 1998, Atahan 2002, Atahan and Cansiz 2005 and Kennedy et al., 2004) and correlated well with dynamic testing after the initial loading.

Most of the methods proposed in the area of roadside safety do not account for the soil damping or for the mass of the soil in front of the post. Plaxico (2002) and Kennedy et al., (2004) noticed that the dynamic test shows an initial peak recorded in the load deflection curve. They explained the absence of the initial peak loading in the Finite Element simulation by the absence of the inertial effect as in the real dynamic test.

To include the effects of the stiffness, damping and inertia, a new model of the subgrade method is developed where the soil block is modeled as a system of spring-mass with a damper or dashpot as shown in Figure 3.15. The model is an upgrade of the traditional subgrade approach and it accounts for the nonlinearity of the soil and the lumped mass and the damping properties vary with the depth. The model is also an extension over Pacheco-Crosetti's model (2007). The lumped mass represents the mass of the soil being involved during the dynamic impact. The springs store the elastic energy and, hence, cause vibrations. The damper dissipates the energy and damps the mechanical system. Since the soil parameters vary with depth and in order to improve the accuracy of the simulation, the soil mass has been divided into thinner layers of 100 mm where the soil parameters are assumed to remain constant for each layer. This layer size of 100 mm is inline with the tests instrumentation conducted by Rhode et al., (1999) in cohesionless and cohesive soils. Ten pressure transducers were mounted on steel and wood post with construction adhesive and spaced between 102 mm to 127mm. The post and the soil are represented by a post attached to a series of spring-mass-damper systems at every 100 mm interval where the soil mass/stiffness and damping factors are lumped at the interconnecting nodes of the post model. To describe the model, three parameters have to be defined: the stiffness of the spring, the damping factor and the lumped mass. The soil parameters dependent on the soil depth and density and take into account the separation of the soil-pile.

3.4.3. Calculation of the spring stiffness

The method used to calculate the stiffness of the spring in this study was proposed by Habibaghi and Langer (1984). For a cohesionless soil, the coefficient of subgrade reaction k_n was found to increase with the depth and decrease with the deflection, Habibaghi and Langer (1984) proposed a simple relationship for the calculation of k_n in kN/m^3 based on the bearing capacity concept as follows:

$$k_h = N_q \frac{\sigma'}{y} \quad (3.20)$$

where N_q is the lateral bearing capacity factor, y is the post lateral deflection and σ' is the effective overburden pressure defined as:

$$\sigma' = \sum_{i=1}^n \gamma z \quad (3.21)$$

where γ is the soil density, z is the soil depth and N_q depends on the deflection y and the depth z and is defined as:

$$N_q = A + \sqrt{\frac{z}{B}} \quad (3.22)$$

where B is the width of the post (100 mm) and A is a constant that depends on the post deflection and the soil internal friction angle.

Using test data from the field, Habibaghi and Langer (1984) recommended the value of A to be 5, 9, 12 and 15 for deflections of 2.54, 6.35, 12.7 and 25.4 mm, respectively.

Plaxico et al., (1998) extrapolated the value of A above the limit of 25.4 mm proposed by Habibaghi and Langer (1984) to use it for the large deformation of the post during the component testing. A relationship between A and the lateral deflection y based on the method of least squares was proposed. The relationship shows that A has a maximum value of 15.27 when the deflection became significant. A is defined as:

$$A = 15.276 - 14.09 e^{-(0.1245y)} \quad (3.23)$$

To calculate the stiffness of the springs along the post, the post is divided into layers of 100 mm; the effective overburden pressure is calculated for each layer. The value of A is determined by Equation 3.23 and the lateral bearing capacity N_q is determined by Equation 3.22. Figure 3.16 shows certain spring stiffnesses at different depth for the post configuration studied before by Coon et al., (1999).

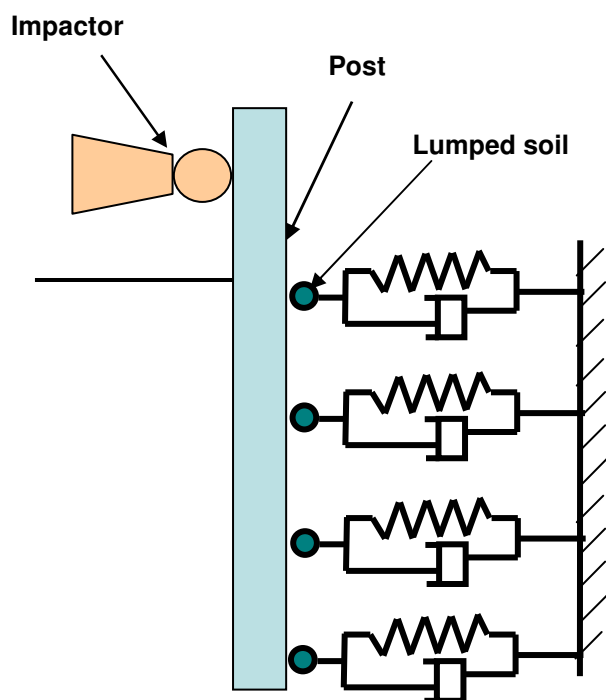


Figure 3.15: Proposed dynamic model for lateral post response

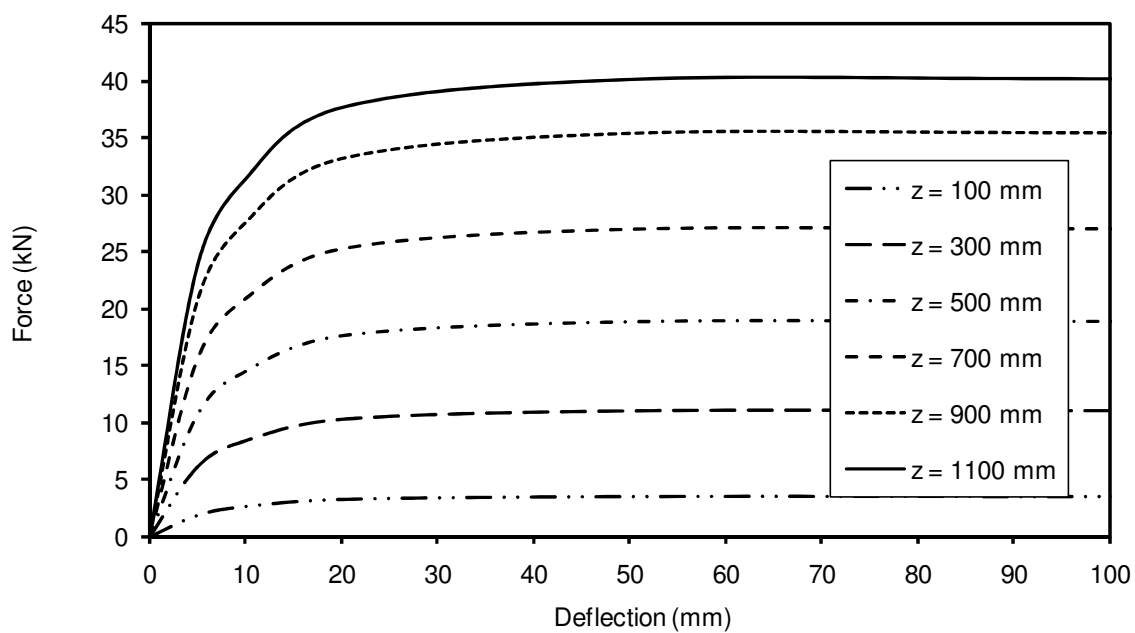


Figure 3.16: load deflection curve of the unidirectional spring calculated by Habibagahi and Langer approach for Coon et al., (1999) test

3.4.4. Evaluation of the lumped mass

The lumped mass of each mass-spring system is the mass per layer involved during the impact which is not known *a priori*. Pacheco-Crosetti (2007) defined the lumped mass to be uniform along the pile and defined by:

$$m_a = \pi r_0^2 \rho \alpha_m \quad (3.24)$$

where r_0 is the diameter of the pile, ρ is the soil density and α_m is a factor defined as function of the Poisson's coefficient.

The lumped mass defined by Equation (3.24) is not realistic since it assumes that the inertia effect is constant for a guardrail post. In fact, the deflection post is large especially close to the ground level and in consequence, the effect of the inertial force developed along the post is not constant.

In the current study, it is proposed to use the results of the continuum method to determine the size of the mass block involved during the impact. The displacement contours of the nodes of the soil block are shown in Figure 3.9. A cross section of the soil block shows that the iso-displacement defined a cone with an apex located at the centre of rotation and the base at the ground level as shown in Figure 3.17. As a first approximation, a displacement (d) is assumed to represent the criterion to determine the lumped mass: any soil mass with a displacement higher than d is involved in the inertial force and could be called "active mass". Any mass with a lower displacement is assumed to be too far from the post to have any effect in inertial force. This cone is divided into layers of 100 mm, representing the space between the springs. The mass of each layer is then assessed and lumped to the system of mass-spring.

A parametric study was conducted to define the displacement threshold to be used. The results of this parametric study show that using a very small displacement of 0.25 mm results in a large active soil mass added to the spring-damper system. In the opposite, if the displacement threshold is increased to 10 mm, the active mass became smaller which reduced the peak load and the inertia effect. Figure 3.18 shows the variation of the impactor load as a function of time for different displacement limits. It can be seen that the peak load increased to 105 kN in the first 10 ms for a mass associated to a

displacement of 0.25 mm. However, for the criterion of 10 mm displacement, the peak load disappears from the post response which is equivalent to no inertia effect. Table 3.5 summarizes the results of the different criteria. The results of simulation show that increasing the lumped mass has a small effect on the impactor displacement and a major effect on the peak load. Based on the parametric study, a displacement of 2 mm was found to give the best results and correlation to the dynamic tests of Coon et al., (1999) in terms of average load, impactor displacement and peak load.

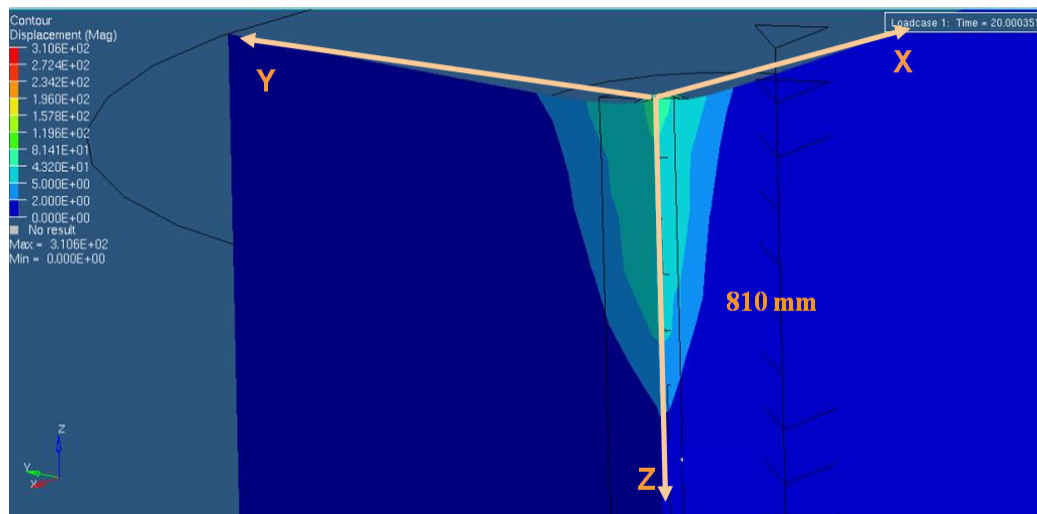


Figure 3.17: View of the finite element model vertical cross-section of the soil mass mobilized during the impact at 20 ms

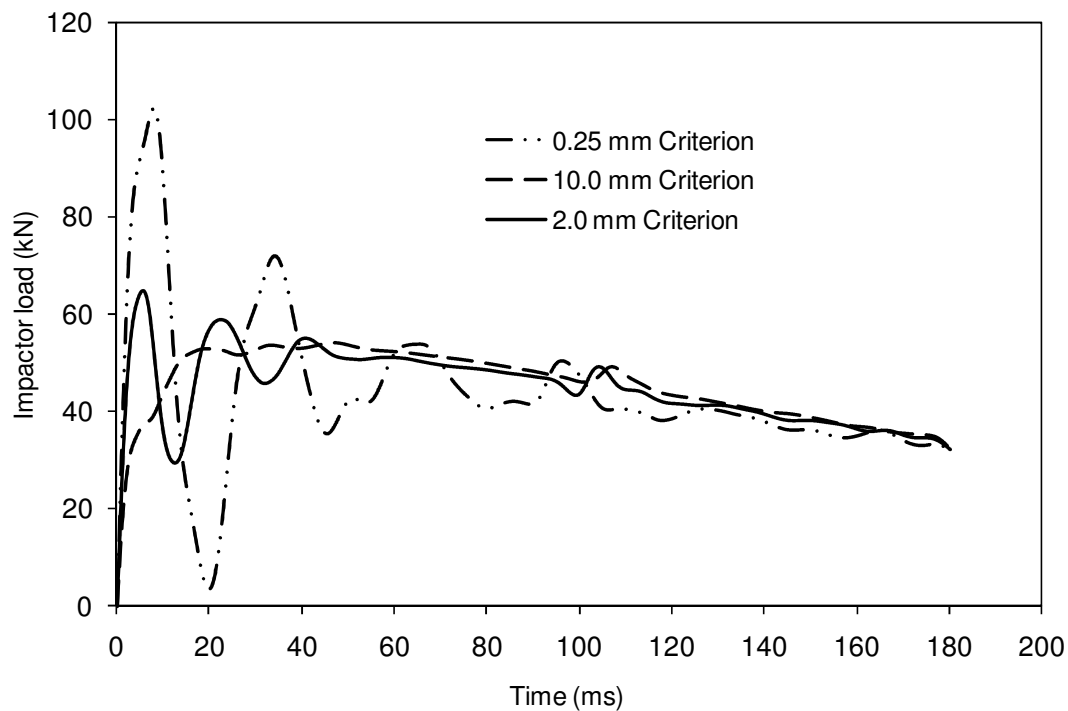


Figure 3.18: Comparison of dynamic test load-deflection curve for different displacement criteria

Table 3.5: Comparison of the post reaction parameters for different threshold displacement

Displacement threshold (mm)	Energy dissipated(kJ)	Max load (kN)	Max displacement (mm)	Average load (kN)
0.25	12.29	53.9	330	49.3
2.0	12.63	66.5	336	44.8
10.0	13.34	105.4	340	43.6
Dynamic test	--	67.0	348	47.3

Figure 3.9 presents the ground plan of the mass involved in the calculation. It was approximated by an ellipse with dimensions of the top area approximately 580 mm by 502 mm which represents approximately 5.8 B and 5.0 B where B is the width of the

post. The depth of 810 mm represents 73.6 % of the total embedment of 1100 mm. The size of the mass involved is normally related to the friction angle of the soil. In fact, the higher the friction angle the larger the soil mass involved in the calculation and the higher is the spike of the deflection curve. No data is available to correlate the active mass and the friction angle. A simple but approximate method to determine the active mass for post loaded laterally could start by assuming that the active mass defines a cone with its apex located at a depth of $0.7 D$ where D is the total embedment of the post in the soil. The base at the ground level is defined by an ellipse where the major and minor radii are $3B$ and $2.5 B$, respectively, where B is the width of the post.

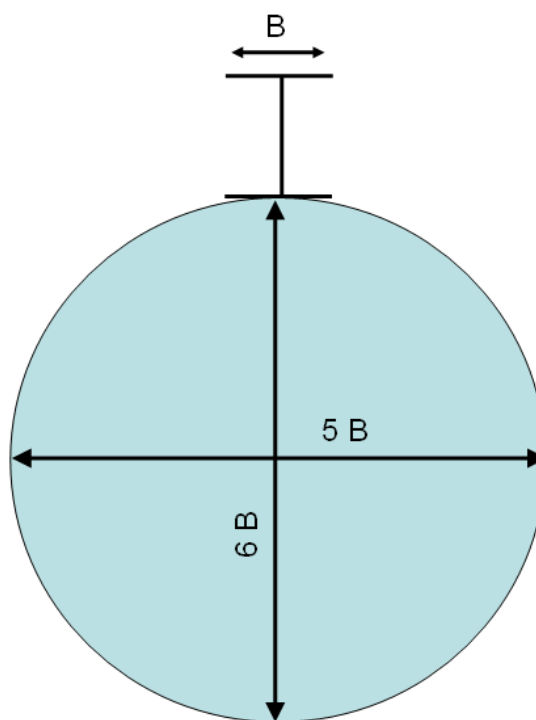


Figure 3.19: Approximate cross section of active mass at the ground level mobilized in the guardrail post test

Table 3.6 shows the mass calculation and the damping coefficients for each layer calculated for three damping factor. The column # 4 containing the value of C_c , critical damping ratio, is obtained as $2\sqrt{m.k}$. The mass distribution along the post is clearly not

uniform. It can be seen that most of the active mass is located at the first 300 mm close to the ground surface and the smallest is close to rotation center.

Table 3.6 Parameters of springs and dampers calculated for the Model with lumped mass for the test of Coon et al., (1999)

Z	Mass	K	C _c	5% C _c	20% C _c	12% C _c
Mm	kg	kN/mm	N/s			
100	34.08	2.39	18.05	1.81	2.71	2.26
200	25.61	2.39	15.65	1.56	2.35	1.96
300	18.35	4.95	19.06	1.91	2.86	2.38
400	12.30	7.62	19.36	1.94	2.90	2.42
500	7.46	10.37	17.59	1.76	2.64	2.20
600	3.83	13.13	14.19	1.42	2.13	1.77
700	1.41	16.09	9.53	0.95	1.43	1.19
800	0.20	19.04	3.92	0.39	0.59	0.49
900	0.65	22.12	9.38	0.76	1.13	0.95

3.4.5. Calculation of the damping factor

The damping of the soil is, in general, the result of the friction of solid particles against each other within the skeleton and also the result of relative motion between the solid skeleton and the pore fluid (Karl et al., 2006). The soil damping ratio has been determined for different type of soils. Karla et al., used the Seismic Cone Penetration Testing to determine the soil damping ratio from time histories measurement. The values calculated are in the range of 0 to 20% with an average value for the sand of 9.6% and 7% for sandy silt. No experimental data is available for the case of Coon et al., tests to calibrate the subgrade model. Therefore, a parametric study was conducted to determine the proper level of damping for the model. The criterion was to measure the

energy absorption for each damping ratio and compare it with the energy absorbed during the actual dynamic test. In fact, the damper is the element responsible for the energy dissipation and any change in the damping parameter should be reflected in the energy absorption.

In the current study, the soil is assumed homogeneous and has one damping ratio, ξ for the entire soil block and, by consequence, for all the subsystems, the damping ratio, expressed in terms of critical damping, c_c , is defined by:

$$\xi = \frac{c}{c_c} \quad (3.25)$$

Figure 3.20 shows the predicted impactor displacement time histories for different damping level assumptions. The curves show that the model with a high damping ratio had less impactor displacement. Using the test results of the peak impactor displacement equal to 348 mm, the appropriate damping level comes out to be 12% of the critical value.

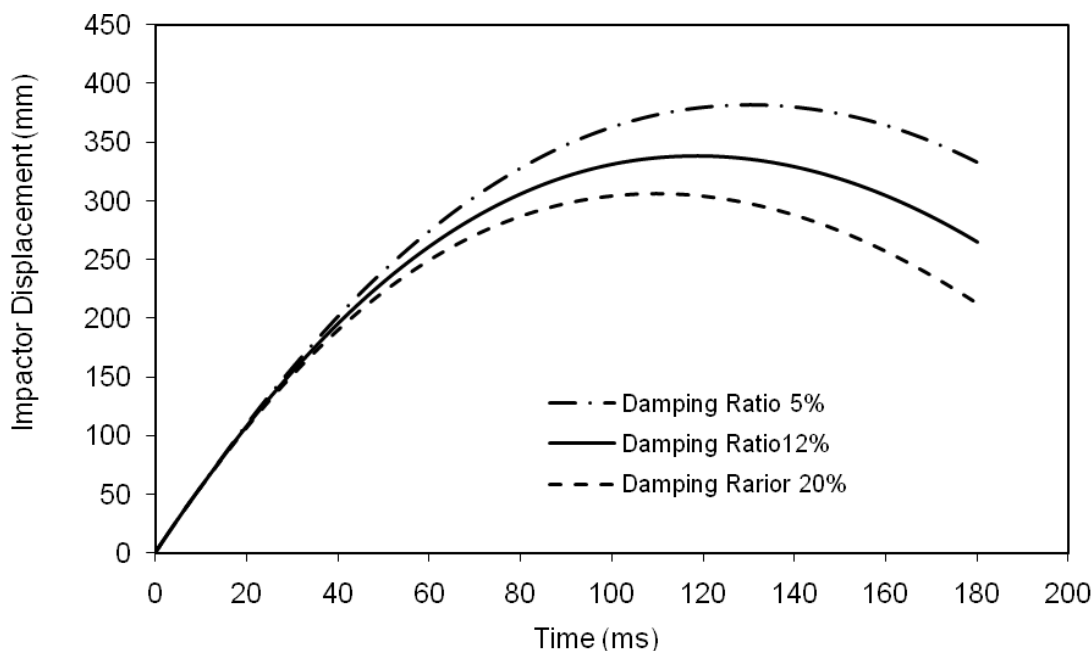


Figure 3.20: Variation of the Impactor displacement as function of the time for different damping ratio

The results of the simulation also show that a damping factor, ξ , of 20% has an average load of 44.1 kN (Figure 3.21) and an energy absorption of 11.79 kJ whereas a damping factor of 5% shows an average load of 42.2 kN and an energy absorption of 14.47 kJ.

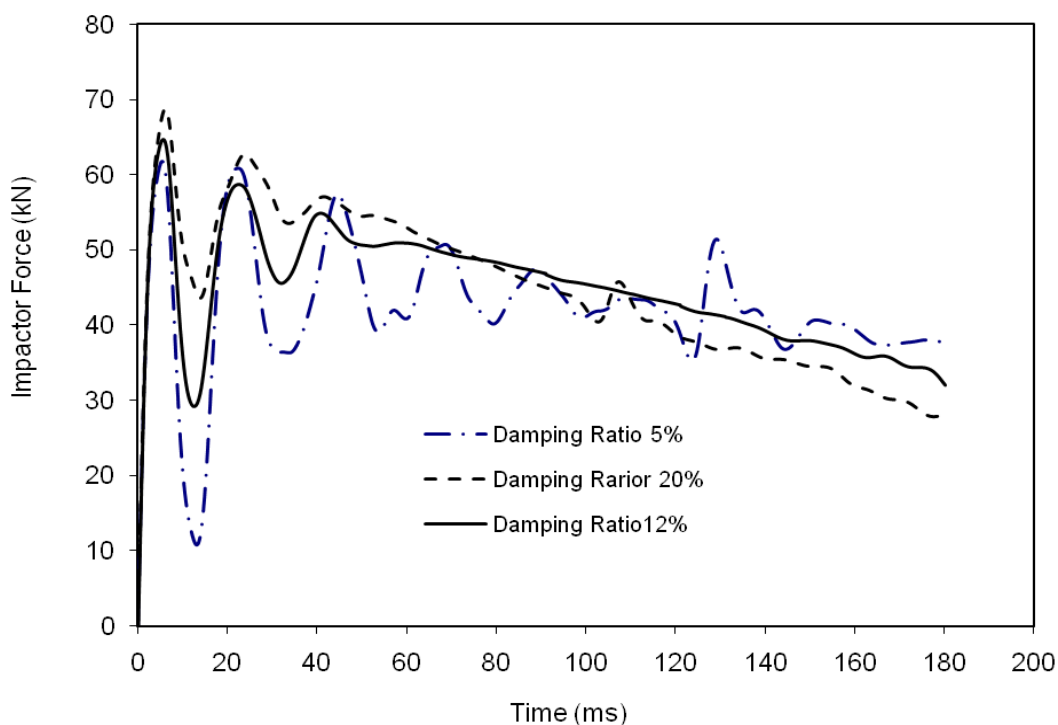


Figure 3.21: Variation of the impactor load as function of the time for different damping ratios

3.5. Analysis of the Upgraded Subgrade Method Results

The results of the subgrade model for the impact speed of 5.9 m/s show that the steel post did not bend or twist during the impact, which is similar to the behaviour of the post in the continuum model and the dynamic test. The post shows a combination of lateral displacement and the rotation at the point located around 830 mm under the ground level similar to what was observed in the continuum model and the dynamic test. The

impactor decelerated with time until it reached zero speed then rebounded back at the time of 110 ms. The results of the simulation show that the impact recorded a peak load value of 64 kN, an average force of 47.3 kN and a maximum impactor displacement of almost 338 mm before the rebound of the impactor. Table 3.7 compares the Finite Element simulation and the dynamic test results. The results show that the upgraded subgrade method has comparable results to the dynamic tests in the term of peak force, average force and post displacement. This indicates that the upgraded subgrade method correlated well with the dynamic test. Figure 3.22 shows that the load deflection curves of both the continuum and the upgraded subgrade models, presenting very close results.

In Table 3.6, the value of the damping ratio decreases with the depth. These results are inline with the tests of Kokusho (1980) which showed that the confining stress has the tendency to decrease the damping ratio. The model of the soil-post in the new approach was calibrated with results of corresponding speed of 5.9 m/s. Coon et al., (1999) conducted in the same site three dynamic tests with different speeds of 4.6 m/s, 5.4 m/s and 8.9 m/s. The subgrade model developed was then validated for these three dynamic tests. Table 3.7 summarizes the results of the simulations of the different speeds compared to dynamic test results. A good agreement can be seen between the dynamic test and the simulation. These results prove that the new subgrade model, developed with the incorporation of the active mass and damper effects, predicts accurately the behaviour of the post during impact.

Table 3.7: Comparison of the average force and maximum deflection between dynamic test and the simplified Finite Element simulation

	Maximum Deflection (mm)		Average Force (kN)		Peak Force (kN)	
	Test	Model	Test	Model	Test	Model
Test #1	234	233	42.8	43.0	64.0	53.1
Test #2	314	296	43.9	45.9	66.9	57.8
Test #3	348	338	47.3	47.9	67.0	64.3
Test #4*	Override	Override	NA	56.3	104.7	97.2

* The post used in test #4 is W150x23.5 instead of W150x13.5

The initial stiffness of the load deflection curves (Figure 3.22) for the two simulations, continuum and simplified models, is higher than the initial stiffness of the dynamic test. This can be explained by the fact that the soil just in contact with the post was not compacted enough to load the post early, which result in less resistance to the post at the early stage of loading in the dynamic test. However, in the Finite Element simulation (continuum approach), the soil is considered homogenous with a small gap (2.1 mm) between the soil mass and the post, which implies that it reacts to the post movement instantaneously. In the subgrade model, the spring is attached to the post. Consequently, the spring/mass reaction is instantaneous. To improve the correlation of the load deflection relationship for the last case between the subgrade simulation and the dynamic test, the effect of mass was delayed by introducing a gap between the springs and the post. In this case, the two parts, the post and spring, are not sharing the same nodes. Therefore, a contact interface is defined between the springs and the post as illustrated in Figure 3.23. The response of the dynamic test and the spring model with a gap of 15 mm is presented in Figure 3.24. The introduction of the initial gap improved the prediction of the initial stiffness of the system and a good agreement between the simulation and the test results is obtained.

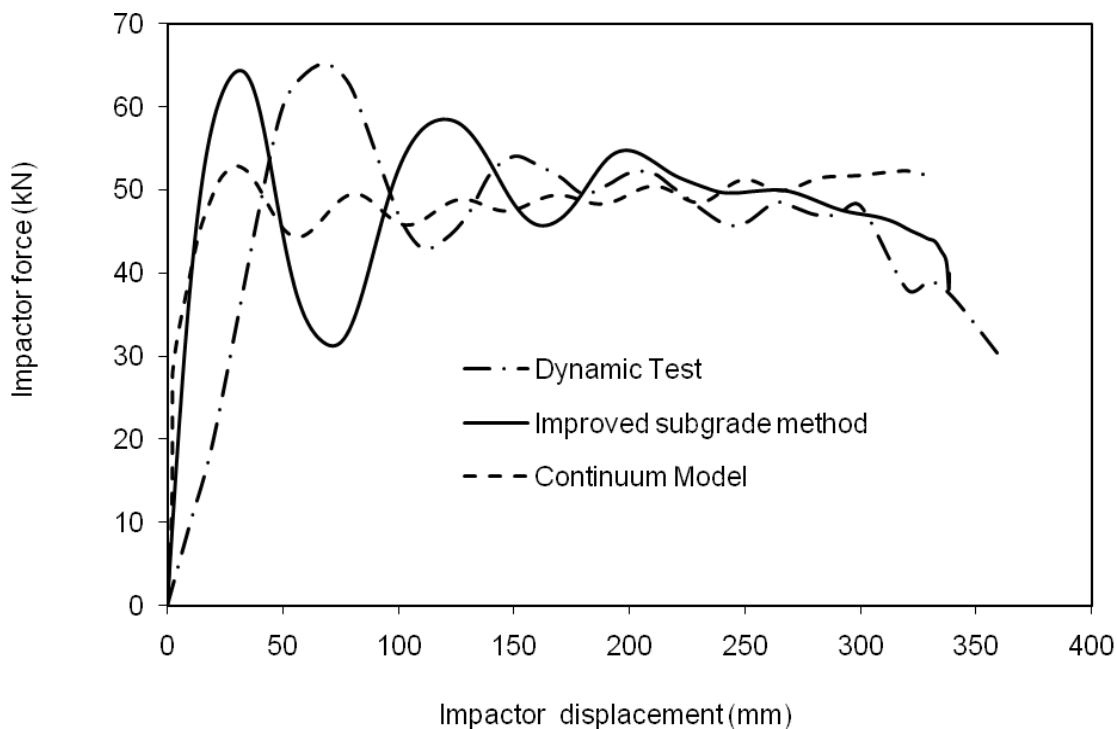


Figure 3.22: Comparison of the dynamic test load-deflection curve obtained using both the subgrade and continuum methods

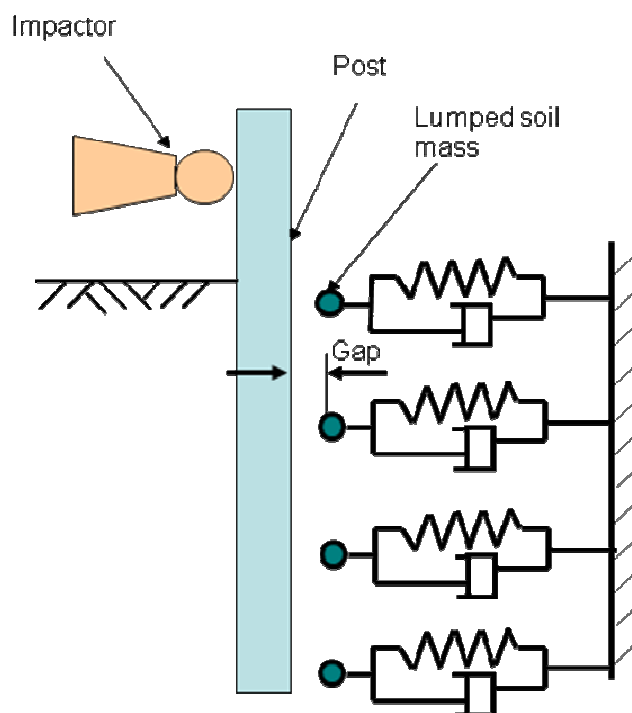


Figure 3.23: Post-soil model with initial interface gap

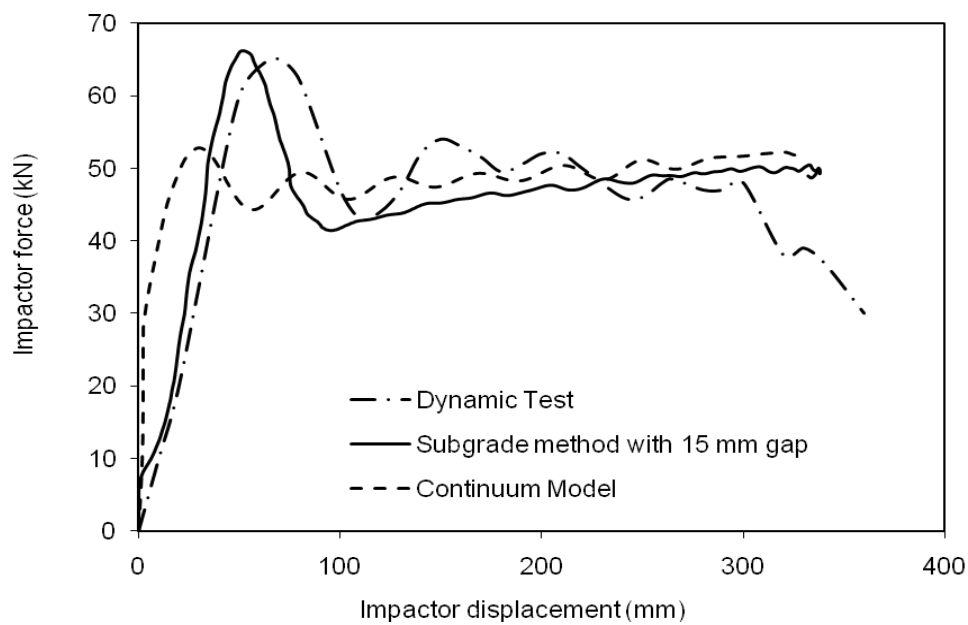


Figure 3.24: Comparison of the dynamic test load deflection curve obtained using the upgraded subgrade method with initial gap

To confirm the assumption that the initial peak seen in the load deflection curve is attributed to the inertial effect, the results of the analysis without the lumped mass are compared with the added mass. Figure 3.25 shows the results for the two simulations. In the case of model with springs and no added mass, the curve filtered at 60 Hz presented a smooth shape with no peak whereas in the case of added mass the load reaches a peak of 63 kN at 7 ms then drops to 34 kN at 14 ms. The two curves, however, seem to be similar after the first 60 ms. These results clearly confirm that the initial peak is affected by the soil inertia. The result also confirms that the proposed approach is able to reproduce the load deflection curve of the impact tests.

Table 3.8 compares the simulation computation time for the continuum method with the spring method and lumped mass for the same run time of 180 ms. The simulation was conducted using the same computer power. The simulation time of the spring method is only 8% of that of the spring method modeled without damper and lumped mass, which indicates that the new subgrade method is computationally efficient. This result is very promising for the simulation of the full guardrail system which involves few posts, and used to suffer from the incapacity of the traditional subgrade method to include the inertia effect and the high computation time of the continuum method.

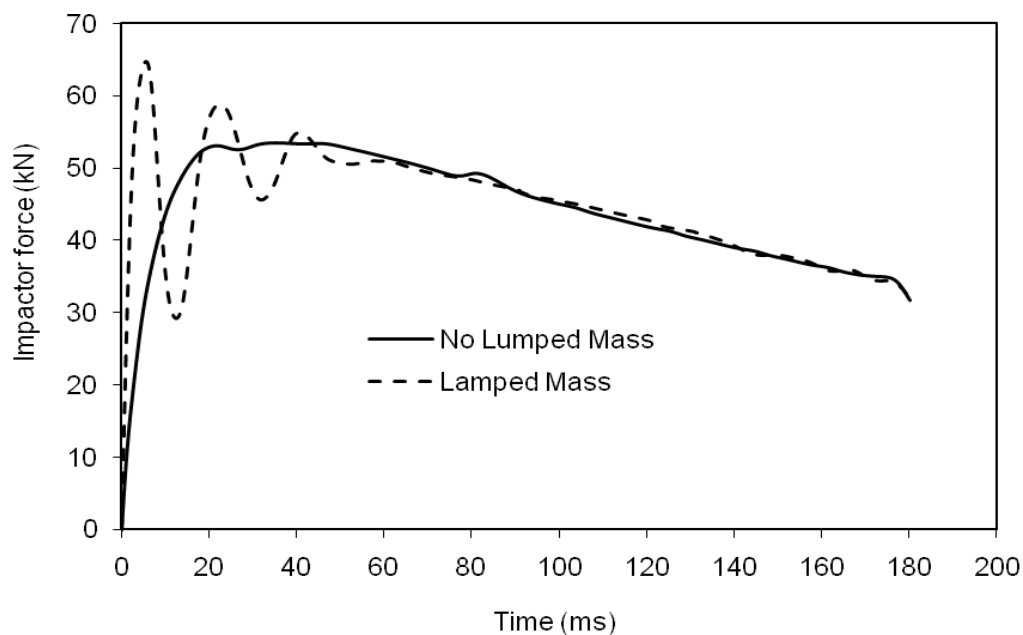


Figure 3.25: Comparison of the impactor force as function of time for the base model and the base with lumped mass approach

Table 3.8: Simulation statistics for simulation of the different models

Model	Continuum Method	Spring model	Spring/Damper
Simulation time (ms)	180	180	180
Run time compared to Spring model	8.49 T	T	1.07 T

3.6. Improved Subgrade Method for Cohesive Soil

The proposed method was extended to the case of cohesive soils. The test conducted by Dewey (1982) is used as a baseline to correlate the simulation with the dynamic test. Dewey conducted a series of static and impact tests to evaluate the load capacity of guardrail posts. The dynamic tests used a cart instrumented with an accelerometer to measure the lateral deceleration during the impact with the post. The cart was very rigid to minimize the energy dissipated in deforming or crushing. The measured displacement of the post was determined by double integration of the deceleration of the cart. A high speed camera (408 frames/second) was used to confirm the displacement and to determine the speed of contact. The displacement of the posts was measured at two locations in the post namely: at the point of load application and the ground surface.

The objective of Dewey's study was to perform a series of dynamic load tests on two types of guardrail posts (steel and wood posts) to determine whether the steel guardrail post can perform satisfactorily without the concrete footing. The post used in the study had a different length and different embedment depths in cohesive and cohesionless soils. The static tests were performed on W6x8.5 (W152x13.4) steel having length of 75 in (1905 mm) with an embedment of 44 in (1117.6 mm). The dynamic tests were conducted with the same steel post having a length of 69 in (1752.6 mm) with an embedment of 38 in (965.2 mm). The dynamic cart used had a weight of 5190 lbs (2353 kg) and impacted the post with an average speed of 24 ft/sec (7.32 m/s). The point of load impact is located at 21 in (533.4 mm) from the ground surface. Figure 3.26 illustrates the test setup. The results of the Finite Element model are compared to the

experimental results for the four tests for the peak load, the average force and travelling distance.

3.6.1 The continuum method

To build the Finite Element model, the material properties, such as the mass density of the soil, the elastic modulus E , Poisson's ratio ν and yield stress σ_y and the steel properties should be determined. Dewey (1982) determined only the cohesion c_u and the friction angle ϕ_u of the clay. The model of the post in the cohesive soil is developed using the same approach explained for the post in sands (section 3.3). The clay could be simulated using Drucker and Prager material law.

The work of Bendidi (2002) was used to determine the remaining properties of the soil and the steel. The soil properties used in the model are those determined by Vickers(1983) and used by Bendidi (2002). The data are summarized in Table 3.9.

Table 3.9:
Soil properties for the cohesive soil used by Bendidi (2002)

Soil Parameters	Value
Young Modulus (GPa)	0.01
Poisson ratio	0.304
a_0	0.0079
a_1	0
a_2	0
a_{\max}	0.0079
P_{\min} Cutoff pressure (MPa)	-0.14

a_0 , a_1 , a_2 are constant defined previously in section 3.3.2.

3.6.2. The subgrade method with the new approach

The soil is simulated as a system of springs-mass-dampers. To get better simulation results, the soil has been divided into layers of 100 mm to represent the variation of the

soil parameters with the depth, the same way as in the cohesionless soil. The soil parameters were assumed to remain constant within each layer.

Calculation of the spring stiffness

The lateral load P of the cohesive soil is calculated according to the method developed by Matlock (1970):

$$P = 0.5 P_u \left(\frac{y}{y_c} \right)^{1/3} \quad (3.26)$$

Where y is the actual lateral displacement, y_c is the lateral displacement at one half of the ultimate resistance and P_u is the ultimate lateral resistance and is defined as:

$$P_u = N_p C_u D \quad (3.27)$$

Where C_u is the undrained shear strength of the clay, D is the width of the post and N_p is a non dimensional coefficient which increases with depth. N_p is bounded between the two values of 3 at the ground and 9 at the critical depth defined by X_r .

$$X_r = \frac{6C_u D}{\gamma' D + I c_u} \quad (3.28)$$

$$N_p = 3 + \frac{\gamma'}{C_u} x + \frac{I}{D} x \quad \text{if } X < X_r \quad (3.29)$$

$$N_p = 9 \quad \text{if } X > X_r \quad (3.30)$$

γ' is the effective unit weight of clay soil. If the soil is not homogenous, γ' is the average effective unit weight from the ground surface to the depth x .

Matlock (1970) defined the value of I experimentally and he found that " I " is 0.5 for soft clay and 0.25 for medium clay. For y_c , the lateral displacement at one half of the ultimate resistance is defined as:

$$y_c = 2.5 \epsilon_c b \quad (3.31)$$

where ε_c is the strain at 50% of the ultimate strength from a laboratory stress–strain curve and is dependant on the consistency of the clay. The typical value used is, in general, equal to 0.01.

Dewey (1982) conducted a geotechnical study and found that the value of undrained shear strength is not constant but varies with the depth as shown in Table 3.10. The curves of the lateral load deflection show that the stiffness at the depth 100 mm is higher than the stiffness at the depth of 200 mm or 400 mm. This fact is due to the over-consolidation of the ground crest which offers a higher undrained shear strength and a higher soil stiffness. Another approach consists of the calculation of the spring stiffness using the average undrained shear strength along the soil depth $C_u \sim 77.56$ kPa.

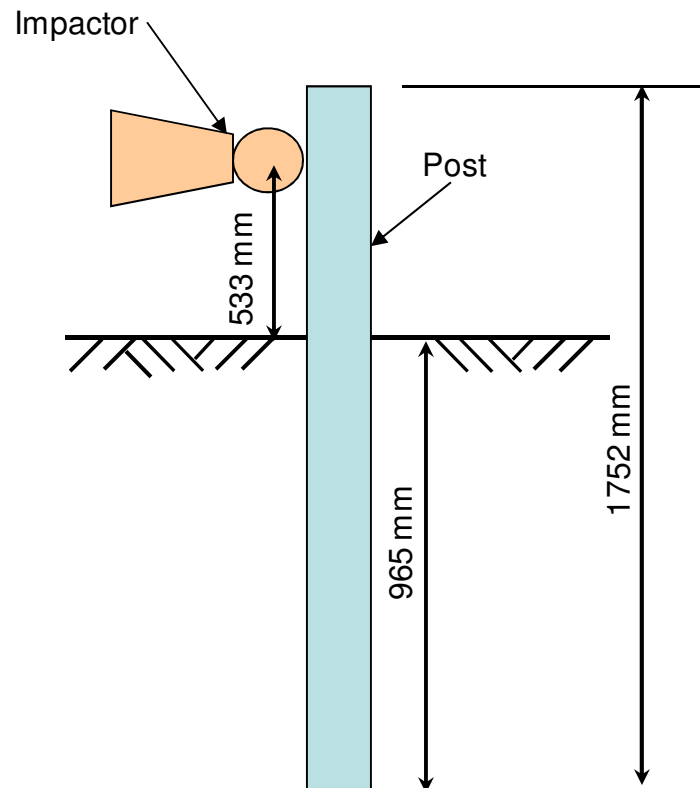


Figure 3.26: Dynamic testing Set-up used by Dewey (1982)

The calculation of the spring stiffness with the current soil properties is more accurate than using an average value of the undrained shear strength C_u .

Table 3.10: Variation of undrained shear strength of the clay as function of the depth for the Dewey's test (1982)

Depth (m)	0.15	0.30	0.46	0.61	0.98
Undrained shear strength C_u (kPa)	95.8	76.6	67.0	71.8	76.6

Evaluation of the lumped mass

As described for the case of cohesionless soil, the results of the continuum model are used to estimate the lumped mass at each spring. The total volume of the soil involved during the impact is divided into layers of 100 mm representing the space between the springs and lumped to the post. The calculation of the lumped mass for each layer and the damping coefficient were calculated with same procedure explained for the cohesionless soil and the results are tabulated in Table 3.11. It can be seen that most of the active mass is located close to the ground surface and the minimum is close to the centre of rotation. Based on the parametric study, the displacement of 1 mm is selected for the criterion retained for the calculation. The curves of the spring stiffness are shown in Figure 3.27.

Evaluation of the damping factor

Adopting the same approach described before in section 3.3.3, a parametric study was conducted to determine the damping factor ξ . The active mass was calculated along the depth Z and a parametric study was conducted to determine the parameter ξ . A value of ξ equal to 10% was found the best results in matching the load deflection curve. The impactor overrides the post for all values of the damping factor.

Table 3.11: Parameters of the springs-mass-dashpot system used to correlate the Dewey (1982) test

Depth	Mass	K	C _c	5% C _c	15% C _c	10% C _c
mm	Kg	kN/mm	N/s			
100	36.08	3.98	23.96	1.20	3.59	2.40
200	27.12	4.35	21.71	1.09	3.26	2.17
300	19.43	4.71	19.14	0.96	2.87	1.91
400	13.02	5.08	16.27	0.81	2.44	1.63
500	7.90	5.45	13.12	0.66	1.97	1.31
600	4.06	5.81	9.71	0.49	1.46	0.97
700	1.49	6.18	6.08	0.30	0.91	0.61
800	0.21	6.55	2.36	0.12	0.35	0.24
900	0.86	6.84	4.85	0.24	0.73	0.49

3.6.3. Analysis and Results for the case of clay

Figures 3.28 and 3.29 show that the current subgrade method captures the effect of soil inertia developed at the early stage of the dynamic impact. The maximum dynamic load registered is around 40 kN at 4ms corresponding to a displacement of approximately 25mm. The simulation and the dynamic test curves show good agreement, especially after the peak load. The peak load of the Finite Element simulation is lower than the dynamic test. The curve reported by Dewey (1982) didn't contain all the data of the curve but just a few points from the test, which does not explain whether the dynamic test data has been filtered. For the current curve, all data has been filtered with SAE 60 filter to eliminate the noise.

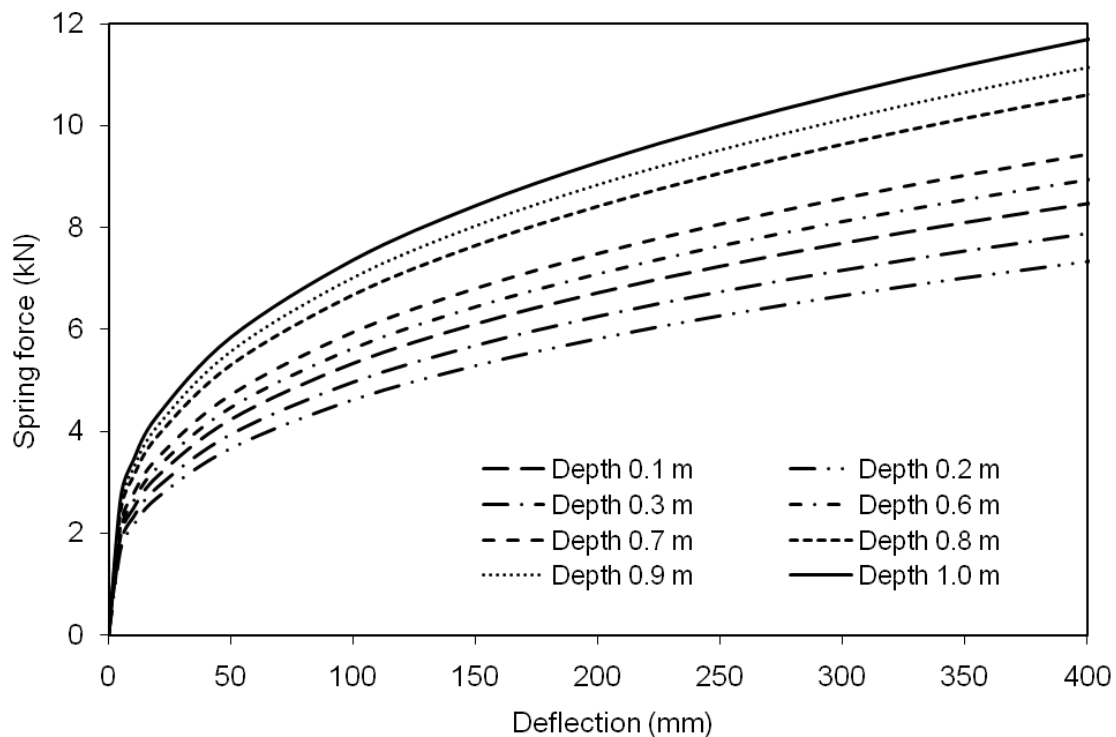


Figure 3.27: Load deflection curves of the unidirectional springs calculated for the test (Dewey, 1982)

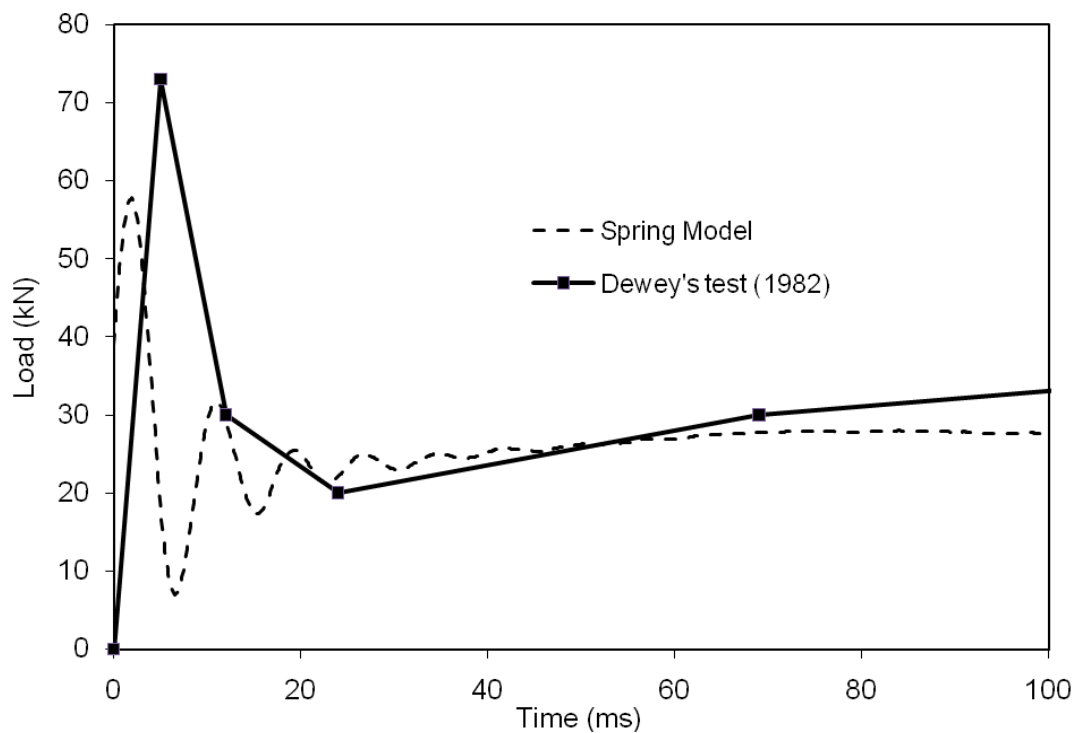


Figure 3.28: Comparison of the Dewey dynamic test load time history with the curve obtained using the improved subgrade method

3.7. Conclusions

An improved subgrade model was developed which includes all relevant soil components such as the soil stiffness, the soil damping and the soil mass involved in the dynamic impact. Two methods for simulating the soil have been compared namely: the continuum method where the soil is modeled as a solid element and the improved method of subgrade approach where the soil is modeled as a mass-spring-damper system. The mass of the soil and the damping effect are being introduced in the subgrade method to simulate more accurately the load deflection curve of the impactor. The traditional study conducted in the field of roadside safety used to simulate the soil reaction only as a simple spring and ignored the effect of its mass and damping.

In the new subgrade method, the spring stiffness is calculated based on the subgrade reaction method. The lumped mass and the damping coefficients are calculated through a simple procedure. The lumped mass is calculated as the active mass involved during the impact and is calculated based on the continuum method where the displacements of 0.01-0.02 B and greater defined the volume of the active mass. The mass is then distributed to the different layers and lumped to the springs. The damping factor is calculated with a parametric study and shows that $\xi = 0.12$ gave the best correlation in this case of cohesionless soil.

The simulation results of the new subgrade method were compared to the dynamic test. The load deflection curve showed a peak comparable to the old subgrade method, which demonstrates that the inertia effect is captured by the new method. The correlation between these models in term of impactor force or displacement is very satisfactory.

The new subgrade method developed here can be a good tool for guiding the design of a new post as well as conducting parametric studies for improving a given vehicle design for road side impact safety. The power of the present new subgrade method is attributed to its accuracy and efficiency since it takes significantly less time than the continuum method

The method developed for the cohesionless soil has been extended to the cohesive soil and shows that it can predict the load deflection curve accurately.

Chapter IV

Parametric Study of the Post Guardrail Embedded in Soil

4.1. Introduction

The analysis of the guardrail system involves very highly nonlinear material behaviour and large deformations caused by the dynamic impact load. This system is too complicated for standard linear-elastic analytical methods and closed-form solutions (Plaxico et al., 1998). To assess the behaviour of the guardrail system and the guardrail post, the finite element analysis method appears to be the best tool that offers full control over all parameters and thus has become an essential tool in guardrail system analysis and the design of roadside safety hardware. These different parameters can be evaluated through an optimization process in order to improve the design of guardrail system to reduce the risk of truck rollover (Tabiei and Wu, 2000). For this purpose, finite element models representing the full-scale crash test or the component testing should be first successfully correlated to physical tests before they can be applied to new design proposals. The finite element analysis effectiveness is confirmed at the end by conducting a dynamic test with the new design. This approach is very reliable and is relatively inexpensive and provides more control over the impact conditions. It also provides detailed information about the mechanics of the impact event (Tabiei and Wu, 2000).

The purpose of this Chapter is to use a finite element model that has been calibrated to study the guardrail post reaction under different design conditions. For cohesionless soil, the resisting shear stress increases with the shear displacement until the failure shear stress is reached. After failure, the residual shear strength decreases (Coon, 1999). Therefore, the soil exhibits a peak stress then it drops to residual pressure that remains the same for the rest of the deformation. The resultant force, which has a direct effect on the force applied to the post, depends on many parameters such as the speed of impact, the embedment of the post and the mass of the impactor.

Sennah et al., (2003) compared the vehicle response impacting guardrail system with different post configuration. The post cross-section and material type were the

parameters of the study. A parametric study was conducted by Elmarakebi et al. (2006) to evaluate the effects of key parameters on the response of the pole embedded in soil when impacted by vehicles. These parameters included soil type (clay and sand), pole material type (steel and aluminum), embedment length of the pole, and vehicle impacting speed. This study highlighted the effect of the different parameters on the vehicle response. However, it considered only the case of small vehicles.

Due to the limited amount of research conducted to evaluate the effects of the different test parameters on the interaction of the post and soil for different test conditions, five different parameters were evaluated and analyzed: impactor speed, impactor mass, the post embedment depth, the blockout crushability and the soil density. A finite element model of a guardrail post impacted by an impactor travelling with an initial velocity was built and used to investigate the effects of the different test parameters on the interaction of the post and soil to compare the load deflection curve for the different parameters with the baseline results. Design guidelines to improve the soil-post interaction for all different conditions and for the full-scale crash test is recommended.

To achieve this goal different parameters have been considered for this study:

- 1- Effect of the sand density
- 2- Effect of the impactor speed
- 3- Effect of the blockout crushability
- 4- Effect of the impactor mass
- 5- Effect of the post depth
- 6- Effect of the clay undrained strength

4.2. Baseline study

The test results reported by Coon et al. (1999) were used as a baseline for the evaluation of the different parameters. As described in Chapter II, a steel post is embedded in sandy soil at a depth of 1118 mm (44 in). Coon et al. (1999) conducted a series of 17 dynamic tests with different post sizes and impactor speeds to evaluate the load capacity of guardrail posts, including steel and wood posts. The cart consisted of a 946 kg rigid nose bogie vehicle, instrumented with an accelerometer to measure the lateral deceleration during the impact. Four tests were conducted with W-section (150×13.5 mm) posts. The tests were conducted with 4.6, 5.4, 5.9 and 8.9 m/s speeds.

The soil density ranged from 1980 to 2240 kg/m³ and the moisture content was kept at zero level for all tests. The impact point of the bogie with the post was located at 550 mm above ground level. The results of the tests showed that for speeds ranging from 4.6 to 5.9 m/s, the impactor rebounds back. However, for the higher speed of 8.9 m/s the impactor slides over the post. As discussed earlier, a finite element model was built to study the guardrail post behaviour. The steel post (W152x13.5), 1830 mm long and 152 mm wide, is modeled by 2020 shell elements and 2142 nodes. The post was meshed with four-nodes using the Radioss QEPH shell formulation. This method was chosen because of its computational efficiency and control of the hourglass (Mecalog 2005). The impactor is modeled as a solid element with added mass distributed to the nodes. The overall mass of the impactor is 948 kg.

4.3. Parametric study

4.3.1. Effect of the impactor speed

In the literature reporting impact test results of the guardrail posts, the impactor speed varied significantly from 4.6 m/s (Coon et al.,1999) to 9.4 m/s (Polivka et al. 2004). To study the effect of the speed on the post guardrail response, a speed range of 3 to 10 m/s was used in the current study. Three dynamic tests conducted by Coon et al. (1999) with different speeds were used to validate the simulation model as explained in Chapter 3. The model simulations have been conducted for a time period of 150 ms and the summary of the results is shown in Table 4.1.

From Figure 4.1, it can be seen that the peak load increases with the increase of the speed. The peak load increases from 43.3 kN at 3.0 m/s to 106.6 kN at 10.0 m/s. The maximum displacement increases from 130.1 mm at 3 m/s to 795.9 at 10.0 m/s as illustrated in Figure 4.2. At speeds higher than 9 m/s the impactor was not stopped by the post reaction and it continued its travel to override the post. The variation of the impactor maximum displacement with the initial impactor speed follows a second degree equation as shown in Figure 4.3. This trend can be modeled as:

$$D_{\max} = 5.2972 V^2 + 25.839 V \quad (4.1)$$

Table 4.1: Summary of the simulation results of impactor hitting the post embedded in the soil with different impact speeds

Speed (m/s)	Peak load (kN)	Maximum displacement (mm)	Average load (kN)	Observation in the post
3	43.3	130.1	35.4	Stopped
4	50.7	191.4	40.4	Stopped
4.6	53.8	233.1	42.9	Stopped
5.4	58.1	294.6	46.2	Stopped
5.9	64.1	336.0	48.1	Stopped
7	77.9	435.6	51.9	Stopped
8	88.7	540.1	55.0	Override
8.9	97.2	645.5	57.3	Override
10	106.6	795.9	59.6	Override

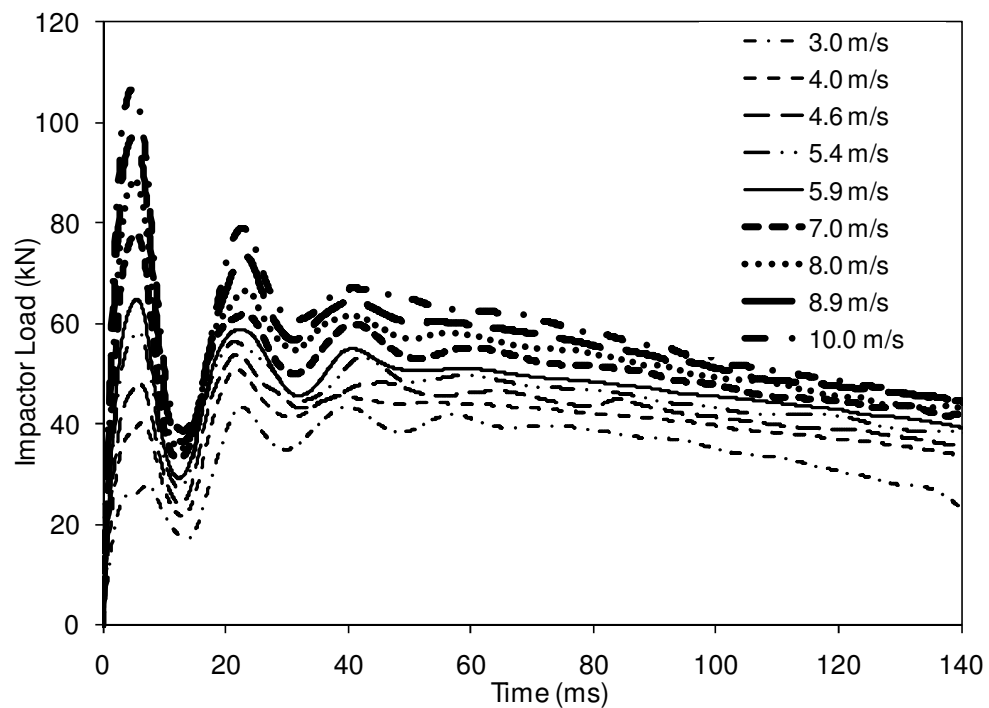


Figure 4.1: Variation of the impactor load as function of time for different speeds

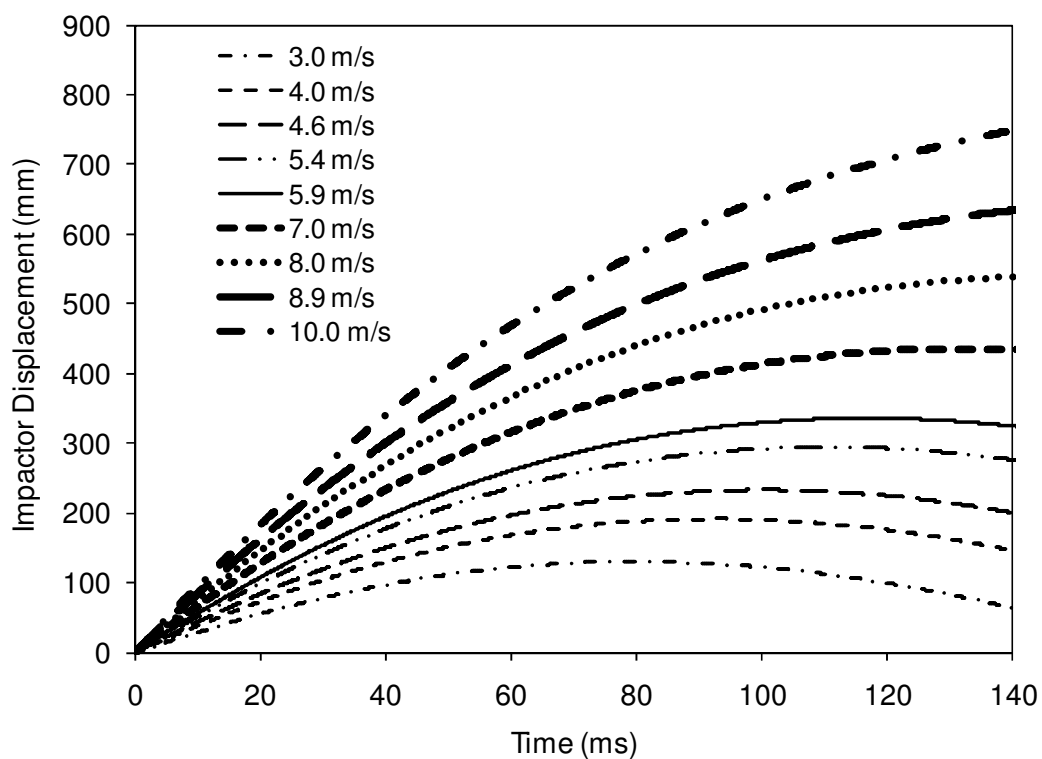


Figure 4.2: Variation of the impactor displacement vs. time for different speed

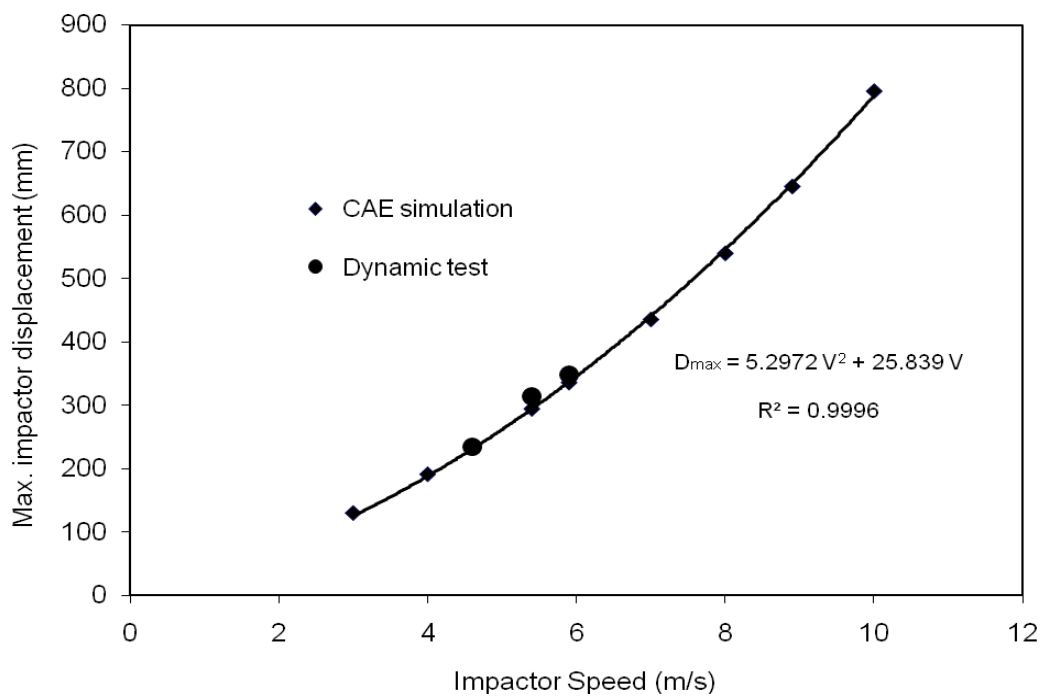


Figure 4.3: Variation of the impactor displacement as function of the speed

For speeds lower than 3 m/s the strain rate effect seems to be limited. The first peak is lower than the maximum load as shown in Figure 4.1 whereas the displacement increases continuously with the speed. If only the first peak load is considered, the maximum load has a linear correlation with the speed defined by:

$$F_{\max} = 10.795 V \quad (4.2)$$

The average load also follows a linear relationship with $a = 3.439$ and $b = 26.863$ as shown in Figure 4.4.

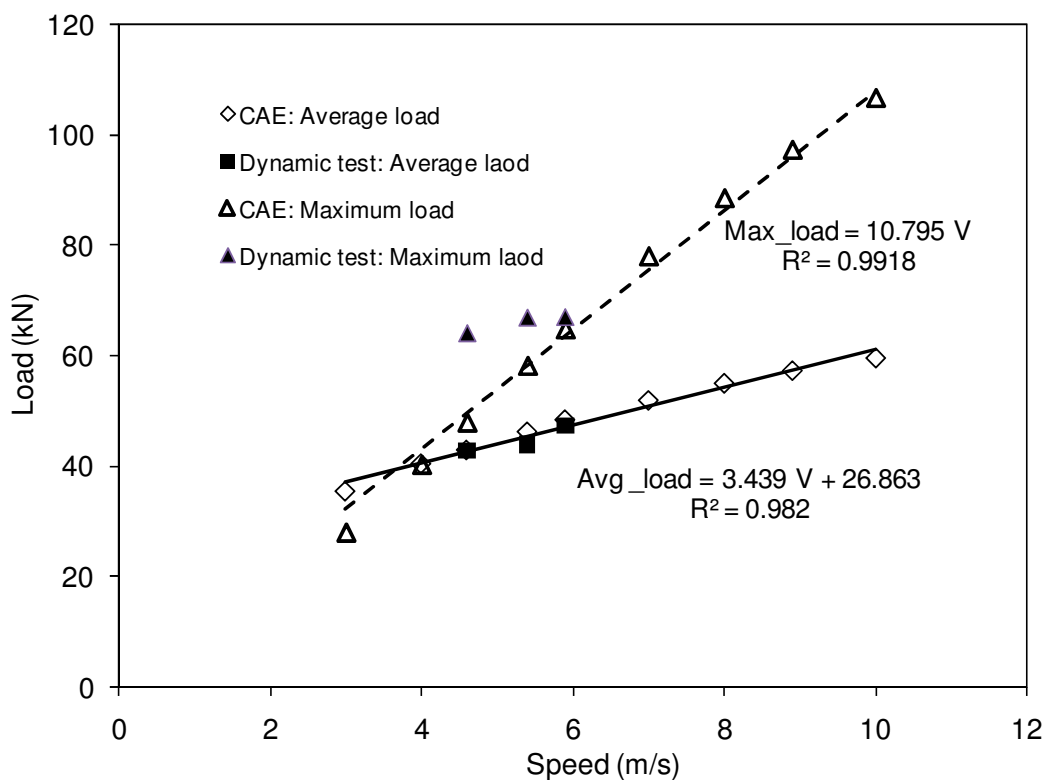


Figure 4.4: Variation of the maximum impactor load and average load as function of the impactor speed

The results show that in all the simulations the post did not bend or develop a plastic hinge and no plastic strain was noticed. Therefore, most of the energy absorbed by the post is elastic as shown in Figure 4.5 and the post sprung back after the test. The post

was continuously pushed in the direction of the loading, developing a rotation centre located around 800 mm under ground level.

The strain rate effect could be attributed to the combination effect of the soil and the steel post. For the soil, the strain rate effect is not homogeneous along the post and the top of the post is experiencing the maximum strain rate effect while the centre of the post is experiencing the minimum effect (Rhode et al., 1996). However, different studies showed that the shear strength parameters of cohesionless soil are not significantly affected by the strain rate. Prakash and Venkatesan (1960) conducted direct shear tests on two different types of sand and reported that the friction angle varied in a narrow range and concluded that the strain rate has no effect on the internal friction angle. Similar results have been reported by Whitman and Healy (1962) who conducted triaxial tests on Ottawa sand. The specimens of dry and saturated sands were strained to failure in duration time ranging from 5 minutes to 5 milliseconds. They used different void ratios to investigate the strain-rate effect on the strength of dry and saturated sands. The peak friction angle of three sand types was found to vary by less than 10% as the failure-time decreased.

The steel post behaviour is, however, influenced by the strain rate effect due, in general, to the rate of dislocation through the crystal structure. The strain rate effect has been defined by the Cowper and Symonds equation (1957):

$$\frac{\sigma'}{\sigma} = \left(1 + \left(\frac{\dot{\epsilon}}{D} \right)^{\frac{1}{q}} \right) \quad (4.3)$$

Where σ and σ' are the quasi-static and dynamic stresses, respectively, and $\dot{\epsilon}$ is the strain rate variable and q , D are estimated to be 5 and 40, respectively (Jones, 1989).

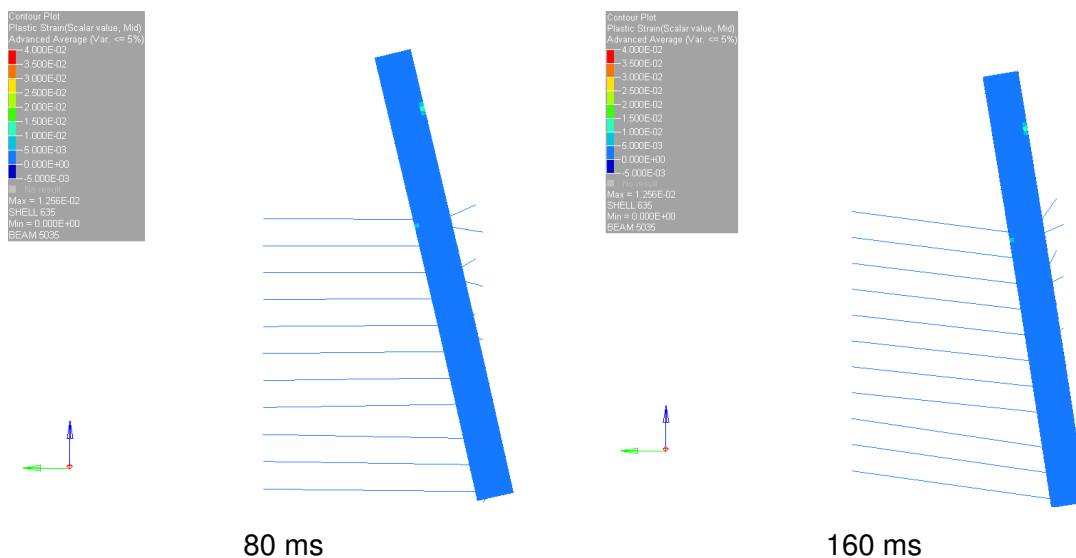


Figure 4.5: Plastic strain of the guardrail post at 80 ms and 160 ms

The use of different impact speed in the component testing raises the question about the appropriate speed to use especially that the results of the tests depend on the speed used. Report 350 (Ross et al. 1993) of NHRCP stated that, in the full-scale testing, the vehicle should be positioned such that the initial impact point for a redirective device should be selected to establish a worst-case testing condition, that is, the critical impact point (CIP) or the point with the greatest potential for causing failure of the test whether by excessive wheel snag, excessive pocketing, or structural failure of the device. According to the NHCRP requirements, the critical impact distance is estimated at 1.3 m for the case of level of service 3-11 where the impact conditions are defined by 100 km/h impact speed, 25° angle of impact and standard $\frac{3}{4}$ -ton pickup trucks as the type of test vehicle. The data of F.E. analysis and the full-scale crash test data showed that the truck speed for this level of service is reduced from 100 km/h to approximately 90 km/h and the impact angle is reduced from 25 deg to 22 deg. These results suggest that it is appropriate to use a speed of 7-9 m/s for the component testing instead of the 11.74 m/s representing the normal component of the speed (100 km/h) applied to the guardrail system by the impactor at the time of contact.

4.3.2. Effect of the embedment depth

Simulations of the post model placed in the soil were conducted to evaluate the effect of the embedment depth on the impactor reaction. The depth range was from 800 mm to 1300 mm. Since the stress applied to the post increases with depth, the study used a W152x23.8 post (W6x16) instead of the W6x9 post to minimize the post yielding and provide a better comparison of the post response with different embedment depths. The two posts, W152x23.8 and W152x13.4, have the same width of 100 mm but the W152x23.8 post has higher cross section parameters as well as web thickness, section area and moment of inertia. This approach has also been used by Kuipers and Reid (2003) who used a higher post (W152x23.8) to determine the dynamic properties of soil-post at various embedment depths under impact loading conditions. They conducted 10 dynamic bogie tests on the embedded steel posts at different depths. The speed for all tests was around 9 m/s and the embedment varies from 864 mm to 1092 mm with a bumper height of 630 mm. For a deeper post, the spring stiffness was calculated for each 100 mm with the same method described earlier. The results of the different simulations are summarized in Table 4.2.

Table 4.2: Summary of the simulations results of the impactor with the post located at different depths of embedment

Depth (mm)	Peak load (kN)	Maximum displacement (mm)	Average load (kN)	Observation in the post
800	35.98	636.4	26.4	Override
900	46.01	486.1	33.7	Override
1000	56.17	400.3	40.7	Stopped
1100	65.1	329.0	48.3	Stopped
1200	70.14	293.1	54.5	Stopped
1300	81.41	259.7	60.9	Stopped

The peak load increases with the depth from 35.9 kN for a depth 800 mm to 81.4 kN for a depth of 1300 mm as shown in Figure 4.6. The relationship between the embedment depth, Z , and the maximum load force, P_{max} , and the average load P_{avg} are illustrated in Figure 4.7 and are defined as:

$$P_{max} = 0.088 Z - 33.347 \quad (4.4)$$

where depth Z is in mm.

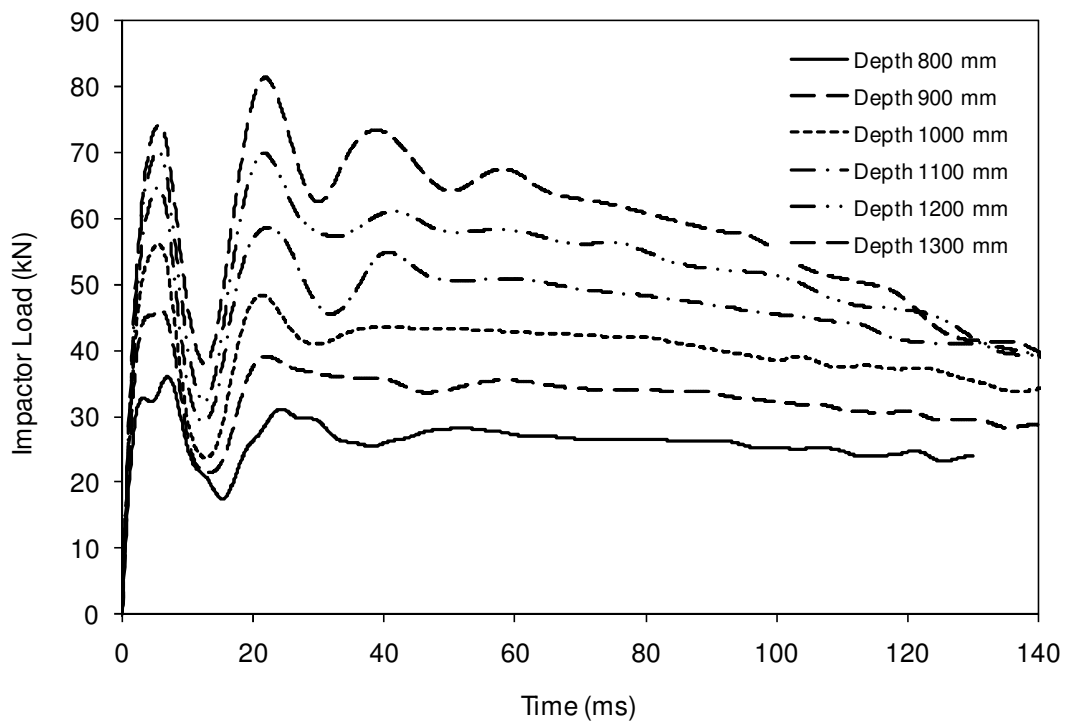


Figure 4.6: Variation of the impactor load vs. time for different depth embedments

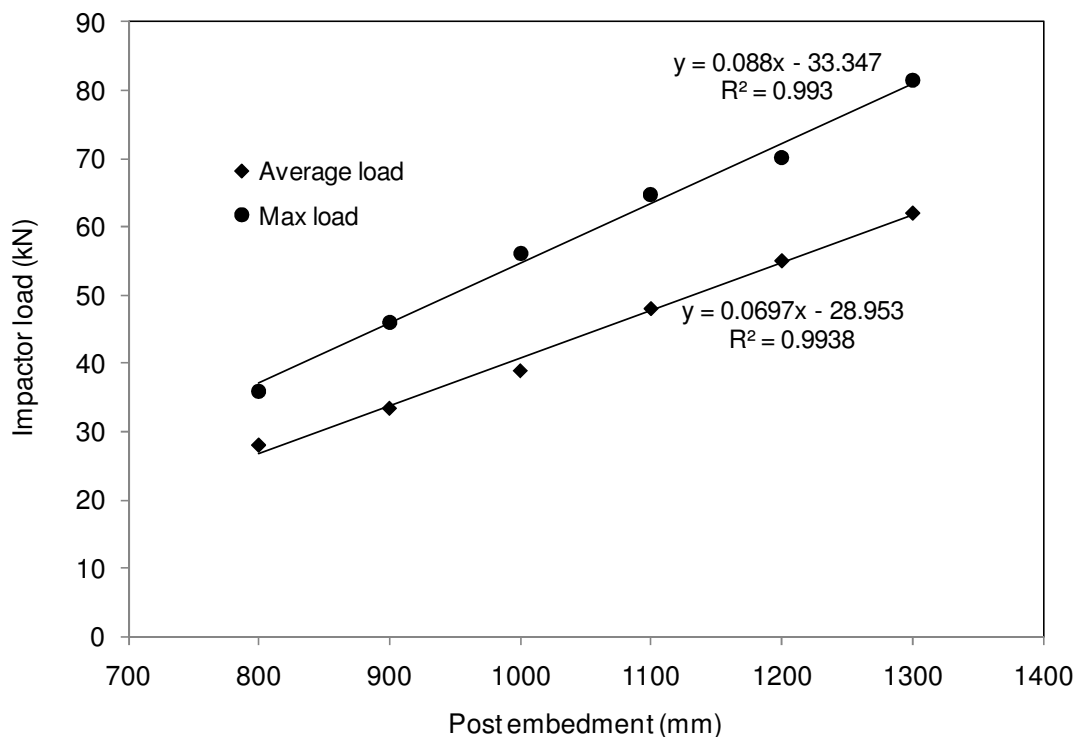


Figure 4.7: Variation of the impactor maximum load vs. post embedment

The curves of the impactor displacement (Figure 4.8) as function of time show that the distance decreases with the depth from 636.4 mm at 800 mm embedment to 259.7 mm at 1300mm. In fact, adding more embedment is equivalent of adding more springs to the post and dissipating more energy in the soil. For embedment depths of 800 and 900 mm, the impactor overrides the post. The latter was pulled out of the ground with no apparent deformation, which concurs with the results of Kuipers and Reid (2003). The post shows a rotation centre around $Z = 644$ mm below ground level for the case of an 800 mm depth. The variation of the maximum impactor displacement vs. the post embedment Z , plotted in Figure 4.9, shows that the relationship follows a power function defined by:

$$D_{\max} = 0.4088 Z^{-1.8332} \quad (4.5)$$

where Z is in m.

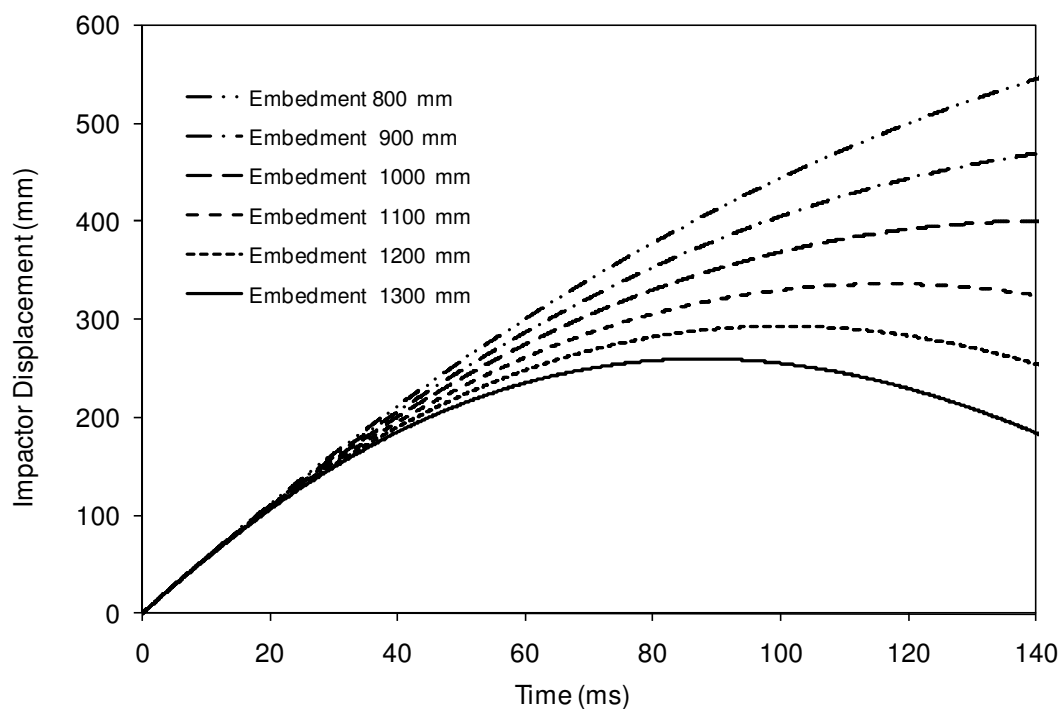


Figure 4.8: Variation of the impactor displacement as function of time for different depth embedment

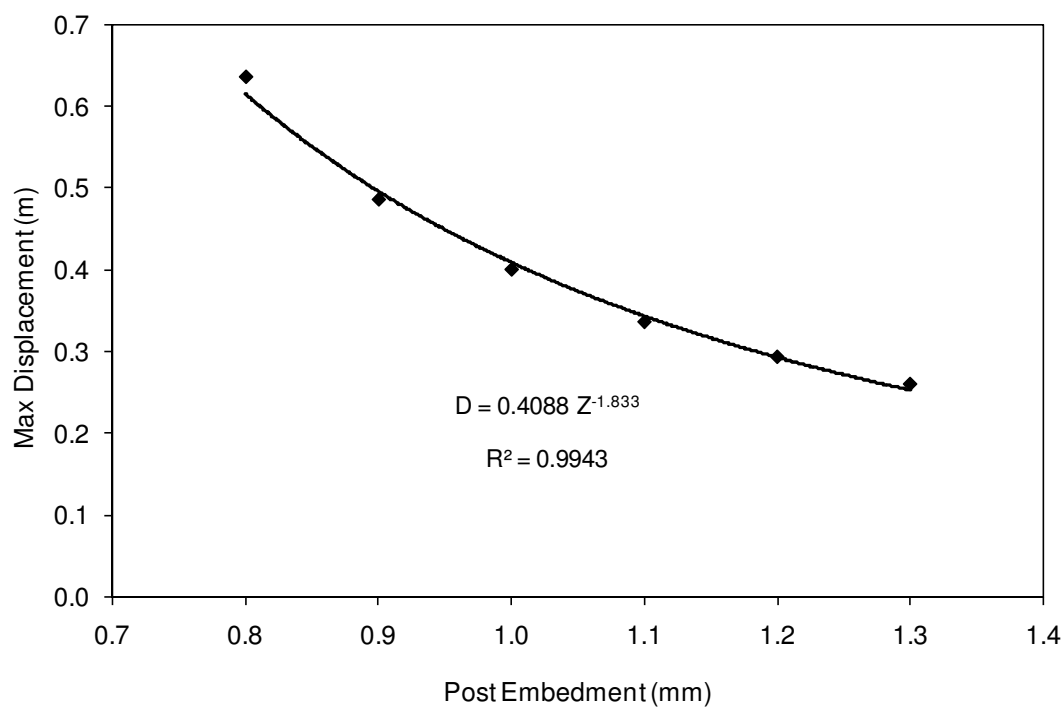


Figure 4.9: Variation of the impactor maximum displacement vs. post embedment

The peak load rose from 64.1 kN for the baseline study to 70.1 kN at a depth of 1200 mm and 81.4 kN for a depth of 1300 mm. This indicates that increasing the embedment depth is not necessarily the right solution in the presence of medium to high density soil since the post reaction becomes very high and exceeds by far the target reaction of 50 kN. A shorter post has less interaction with the soil, which results in the impactor overriding the post and large impactor displacement. For the baseline study where the average force is around 50 kN, the depth of 1100 mm seems to be adequate and this agrees with the conclusion of Kuipers and Reid (2003)

The energy dissipated through the soil, calculated for different embedment shows that the internal energy cumulated in the springs, is constant for the case the impactor is stopped and the energy is higher than for the case where the impactor is being overridden as shown in Figure 4.10.

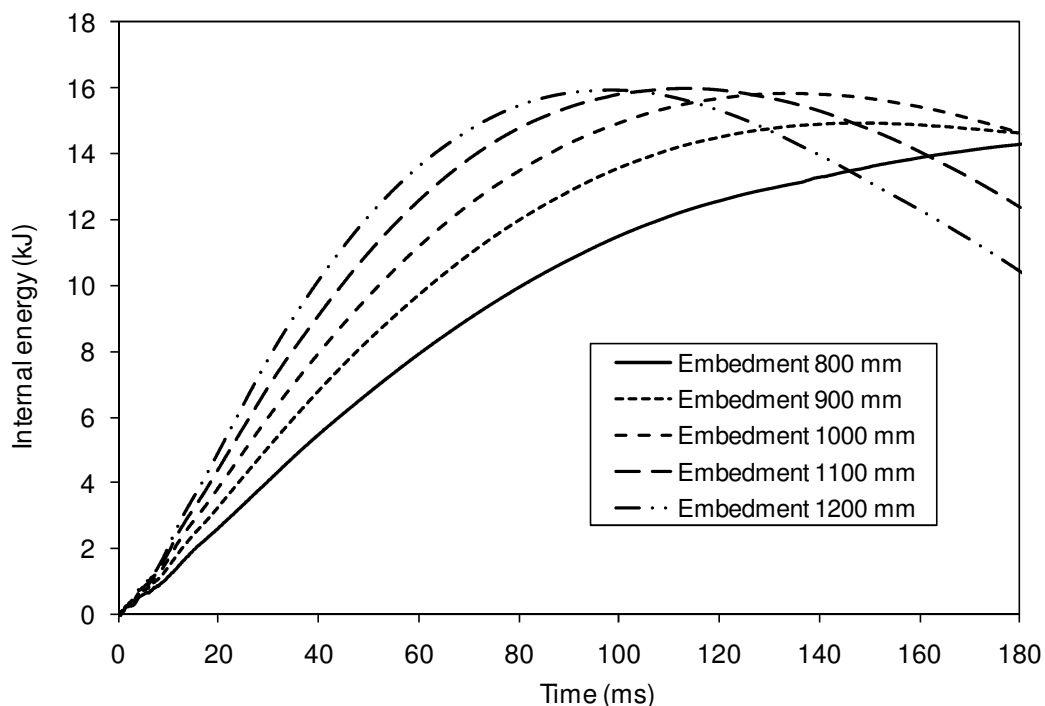


Figure 4.10: Energy dissipation of the guardrail at different embedment

This fact is due to the fact that for the case where the impactor overrides the post, the total energy of the springs is totally mobilized whereas for the case where the impactor is

stopped, a portion of the internal energy is still not dissipated. The rate of energy dissipation rate increases with the depth because more springs are used. The internal energy of the post is constant for all depths where the impactor is stopped. The profile of the force–deflection curves of the test indicates that the forces acting on the post are almost uniform over the duration of the impact. The animation results show that the post had not undergone considerable plastic strain (<3%) as shown previously on Figure 4.5.

The extending of the guardrail post embedment could be a remediation for the case of a poor post-soil interaction in loose sand or for the case of guardrail post implemented close to the embankments where the risk of overriding the barrier can lead to a potential catastrophic accident for the occupants. This countermeasure can be combined with other actions, such as reducing the post spacing and changing the guardrail height, to improve the guardrail reaction.

4.3.3. Effect of sand friction angle

Sand could be classified as loose, medium, dense or very dense depending on its density which typically varies with the friction angle. A typical friction angle range is defined in Table 4.3 in relation to the sand density.

Table 4.3: Typical friction angle for different sand densities

Relative Density	Friction angle (°)
Loose	<30
Medium	31-35
Dense	36-40
Very Dense	>42

The value of the friction angle (ϕ) depends on many factors, such as soil density, gradation, soil compaction and particle angularity. A typical value of the internal friction angle can range from 30° to 35° for poorly graded sand to 40° to 45° for dense sand.

This value is computed from the slope of the straight line drawn through the origin and tangent to the Mohr circle representing the stress at the failure.

The soil reaction increases with the friction angle. If the soil-post interaction is simulated by a nonlinear spring, the stiffness of a spring located at each depth increases with the value of ϕ . Three densities have been considered in this study: loose, medium and dense. In each case of the sand density, the springs of the soil at different depths have been calculated according to the method of Habibagahi and Langer (1984).

The soil with density different than the one defined in the baseline represents, in fact, a new model whose parameters need to be determined, namely the spring stiffness, the damping ratio and the concentrated mass. As a first approximation, the damping ratio and the concentrated mass are assumed to be the same as in the base model. These parameters could be calculated but no data is available to correlate the finite element model. To calculate the spring stiffness, Plaxico et al. (1998) defined a density-dependent modification factor, MF, following a linear relationship with the friction angle:

$$MF = \frac{2}{3}(\phi - 30) + 1 \quad (4.6)$$

The modification factor, MF, adjusts the value of lateral subgrade reaction, k_h , calculated by Habibagahi and Langer (1984) according to the value of the friction angle:

$$A_\phi = A \cdot MF \quad (4.7)$$

where A was defined previously as:

$$A = 15,276 - 14.09 e^{-(0.1245y)} \quad (4.8)$$

y is the lateral deflection of the post.

The lateral bearing capacity, N_q , is related to A by:

$$N_q = A + \sqrt{\frac{z}{B}} \quad (4.9)$$

where B and z are the post width and depth, respectively.

Figures 4.11 and 4.12 for the three different densities show that the peak load reaches values of 88 kN, 64.5 kN and 30 kN for the dense, medium and loose sand, respectively, whereas the maximum displacements were approximately 736 mm, 336 mm and 243 mm. The impactor overrode the post for the case of loose sand and stopped for medium and dense sand. The amount of energy dissipated in the case of the dense sand is higher than in the case of the other densities. Most of this energy is dissipated during the impact as the post pivots in the ground causing the soil to fail.

These results show that the medium density sand offers the best soil interaction as the load level remains around 50 kN. The dense sand shows a high interaction between the soil and the post, which might cause the vehicle impacting the guardrail to rollover. The low density sand shows a poor interaction between the soil and the post which might result in the vehicle overriding the guardrail system.

Figure 4.10 shows that the peak load increases with the friction angle, ϕ . This result is based on the approach used by Plaxico et al. (1998) to adjust the horizontal subgrade method for different densities to account for the effect of the friction angle. The springs, representing the soil stiffness, could be calculated by different methods. Table 4.4 summarizes the values of the horizontal subgrade modulus using different available approaches including Bowles (1982), Terzaghi (1955), Zurabov and Bugayeva (1949), Soletanche (1982), Reese et al. (1974), the NAVFAC (1982) and Plaxico et al. (1998).

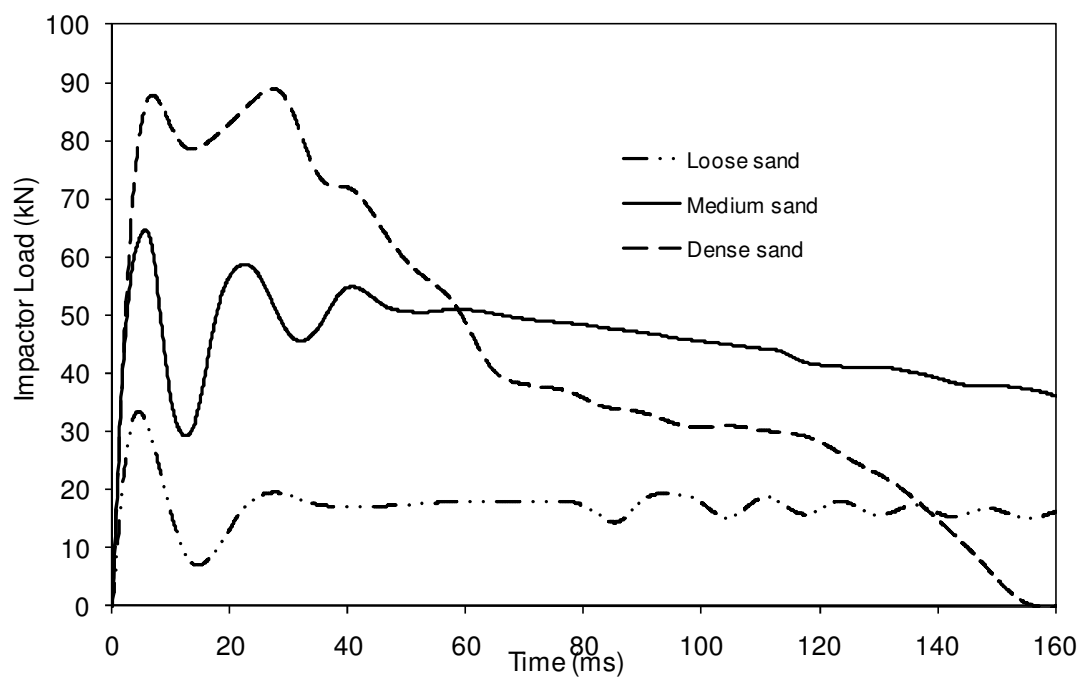


Figure 4.11: Variation of the impactor load as function of time for different sand densities

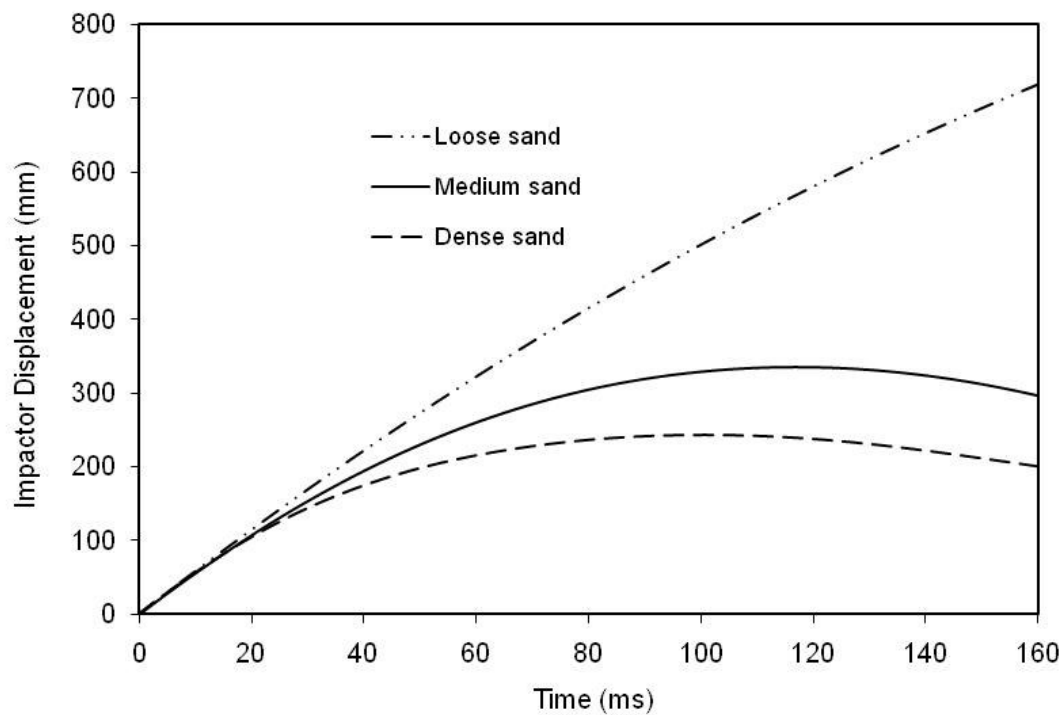


Figure 4.12: Variation of the impactor displacement as function of time for three sands densities of sand

For Terzaghi (1955), Zurabov and Bugaeva (1949), Soletanche (1982), and the NAVFAC (1982), the value of the lateral subgrade reaction is presented as function of the friction angle as shown in Table 4.4. However, for the rest of the references the lateral subgrade reaction is presented for the different densities of the sand and no value of friction angle. A friction angle of 30° for the loose sand, 35° for the medium sand and 40° for the dense sand were assumed when no friction angles were available. All the data consider the sand to be dry and located above the water table level. In order to compare the current approach of the different methods, a modification factor (MF) is defined as the ratio of the lateral subgrade at angle ϕ to lateral subgrade at 30° .

$$MF = \frac{k_{h\phi}}{k_{h(30)}} \quad (4.10)$$

The lateral subgrade modulus is plotted as a function of the friction angle for all the discussed methods. Figure 4.13 shows that all the curves have a similar trend of increasing modification factor with the friction angle. The Figure shows also that Equation (4.6) defined by Plaxico et al. (1998) is very similar to that of the NAVFAC. This result is expected since equation of Plaxico et al. (1998) is derived from the data of the NAVFAC using a pile of an embedment of 500 mm. It can also be seen that while Terzaghi's (1955) curve is the closest to that of Plaxico et al. (1998), the curve of Bowles (1982) is the most different. For a dense sand ($\phi \sim 40^\circ$), the modification factor, MF, could range from 8, calculated by Plaxico et al. to 2 calculated by Bowles. This large difference suggests that equation established by Plaxico et al. (1998) is the most conservative method. As concluded by Plaxico et al. (1998), an extensive study of the post guardrail embedded in different soils is required to develop a more accurate relationship between the value A and the friction angle ϕ .

For most civil engineering problems, the common practice is to tolerate only small strains within the sand mass. For that reason, it is appropriate to use the value of the friction angle based on the peak of the stress-strain curve. However, in the case of guardrail posts, the soil deformation in front of the post can be large. Therefore, it is more appropriate to use the angle under constant volume or residual angle ϕ_{cv} (Lambe and Whitman, 1969).

Table 4.4: Typical values of lateral subgrade modulus for different sand density

Terzaghi (1955)	Friction angle ϕ ($^{\circ}$)	30	34	39	
	k_h	14	42	112	
	MF	1.0	3.0	8.0	
NAVFAC (1982)	Friction angle ϕ ($^{\circ}$)	30	34	39	
	k_h	12	44	80	
	MF	1.0	3.7	6.7	
Soletanche (1982)	Friction angle ϕ ($^{\circ}$)	10	20	30	
	k_h	50	87	168	
	MF	1.0	1.7	1.0	
Zurbov and Bugayeva (1949)	Density	Fine	Medium	Dense	
	Friction angle ϕ ($^{\circ}$)	30	35	40	
	k_h	520-600	520-780	2600-3460	
	Average k_h	550	700	3000	
	MF	1.0	1.3	5.5	
	Density	Fine	Medium	Medium Dense	Dense
Bowles (1982)	Friction angle ϕ ($^{\circ}$)	30	35	40	45
	k_h	500-1200	700-1800	1000-2000	1400-2500
	Average k_h	800	1250	1500	2000
	MF	1.0	1.6	1.9	2.5
	Density	Loose	Medium	Dense	
Reese et al. (1974)	Friction angle ϕ ($^{\circ}$)	30	35	40	
	k_h	35	104	216	
	Average k_h	35	104	216	
	MF	1.0	3.0	6.2	

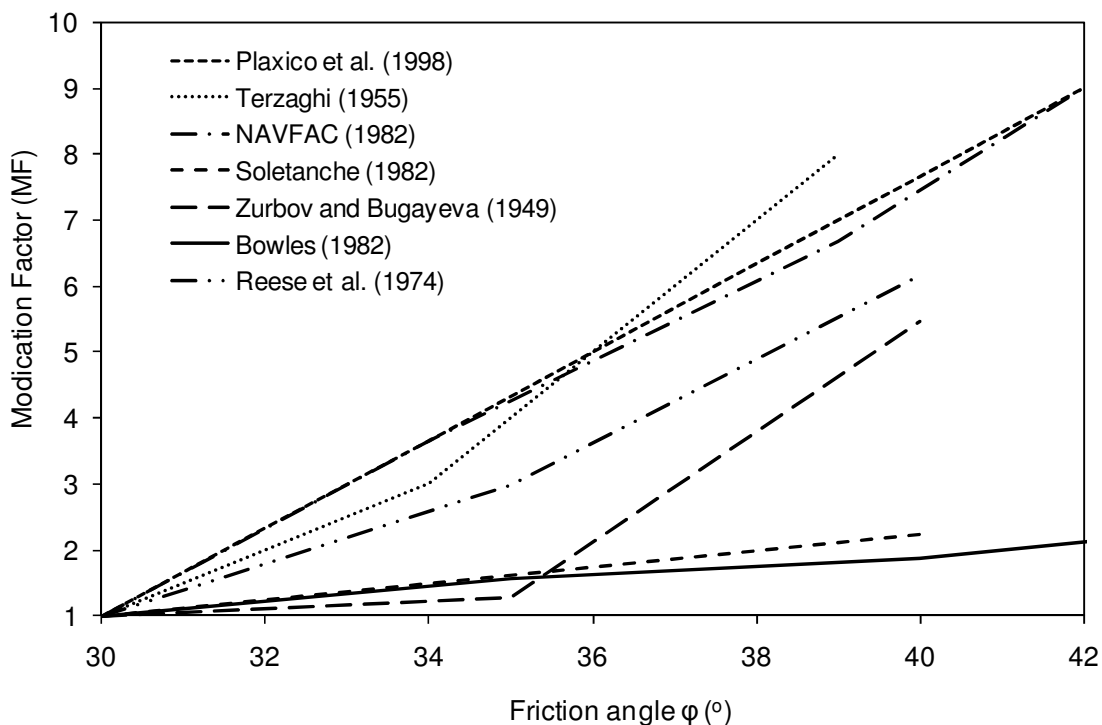


Figure 4.13: Variation of the modification factor (MF) as function of the friction angle by different models

4.3.4. Effect of the impactor mass

The literature review shows that dynamic testing of steel posts embedded in the soil was conducted with different impactor mass to evaluate the post behaviour. Table 4.5 presents a non-exhaustive list of impactors used in the literature. The mass of the impactor could range from 878 to 2324 kg. The impactor consists, in general, of a rigid, thick steel pipe, sometimes filled with concrete, mounted to the front of a bogie vehicle or a pendulum at a given height above ground level.

To assess the effect of the impactor mass, simulations of the guardrail post embedded in the soil and impacted by a cart with different weights were conducted. The baseline model used in this study is the same as the one defined and calibrated by Coon's test (1999), consisting of a cart travelling at 5.9 m/s and having a mass of 946 kg. The spring stiffness representing the soil reaction, the damping coefficient of the soil and the

calculated concentrated masses were assumed to remain constant for all the simulations. The impactor mass varies from 500 to 3000 kg to cover the range of masses used in the literature. Table 4.6 summarizes the results of the conducted simulations.

Table 4.5: Impactor mass used in the literature

Reference	Impactor mass (kg)	Type of impactor
Dewey (1982)	2324	Cart guided on rail
Calcote and Kimball (1978)	1814	Pendulum
Rhode et al. (1996)	1388	Rigid frame bogie vehicle
Polivka et al. (2004)	1014	Rigid frame bogie vehicle
Coon et al. (1999)	946	Rigid frame bogie vehicle
Kennedy et al. (2004)	878	Pendulum

Table 4.6: Results of the energy dissipation with different mass impactor

Mass (kg)	Max energy dissipated(kJ)	peak acceleration (g)
500	8.14	60.7
946	15.39	64.1
1500	23.46	66.4
2000	29.46	67.2
2500	34.43	67.7
3000	37.33	68.0

The load deflection curve of different impactors is shown in Figure 4.14. It can be seen that the post rail undergoes more displacement with the heavier mass than with the lighter mass because of the initial kinetic energy and all curves are following a similar pattern. Figure 4.15 shows that the barrier with a 500 to 1500 kg mass reaches a

maximum displacement then rebounds back, which prove that the barrier was stopped. However, the impactor overrides the post for a mass above 2000 kg. The maximum displacement of the impactor increases linearly with the mass impacting the post following the relation:

$$D = 0.3494 M_{\text{impactor}} \quad (4.11)$$

where D is the maximum displacement of the impactor (mm) and M_{impactor} is the mass of the impactor (kg). The maximum load increases slowly with the impactor mass from 60.7 kN for a mass of 500 kg to 68.0 kN for the heavier impactor (3000 kg). The curves of the dissipated energy for each simulation versus the impactor displacement show that the dissipated energy is highest for the heavier mass and increases linearly with the mass as shown in Figure 4.16. However, the rate of energy dissipation remains the same for all impactor weights, which implies that the post response is independent of the impactor mass.

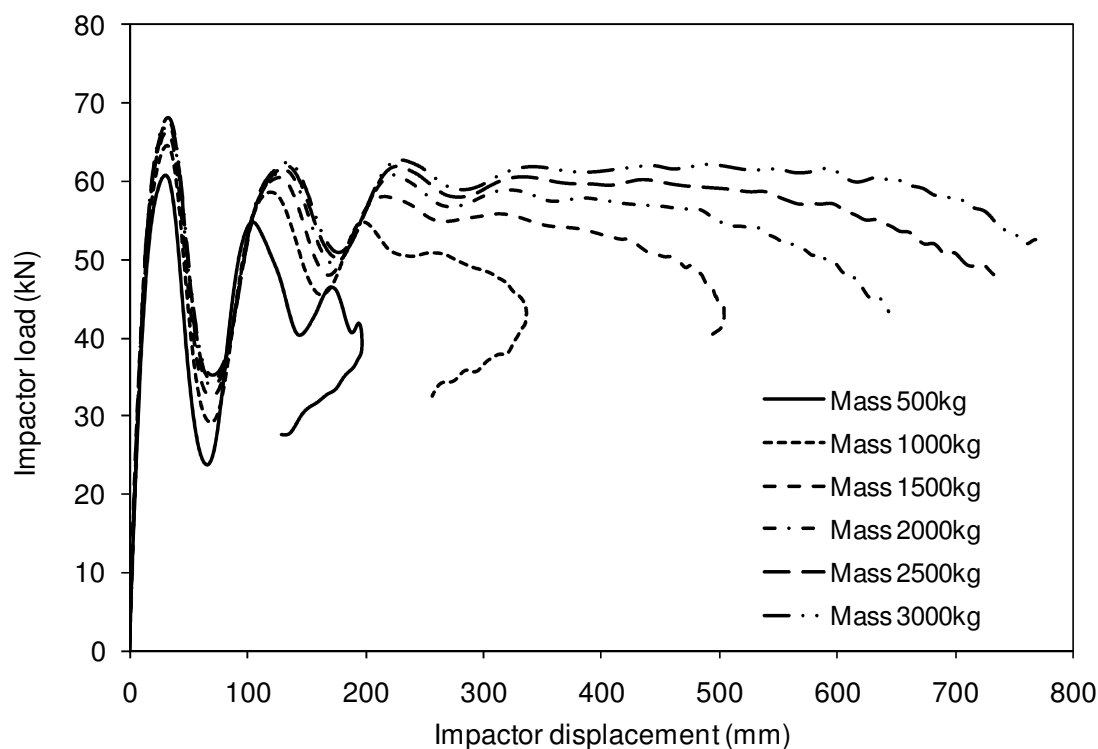


Figure 4.14: Effect of the impactor's mass on the load-deflection the guardrail post

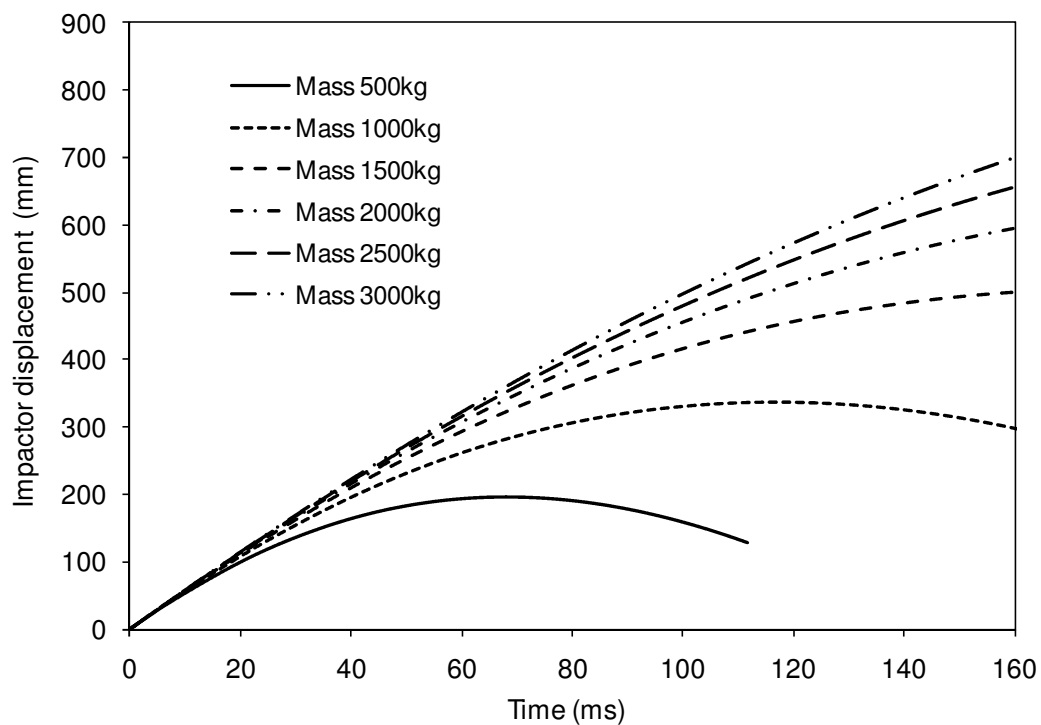


Figure 4.15: Variation of the impactor displacement as function of time for mass impactor

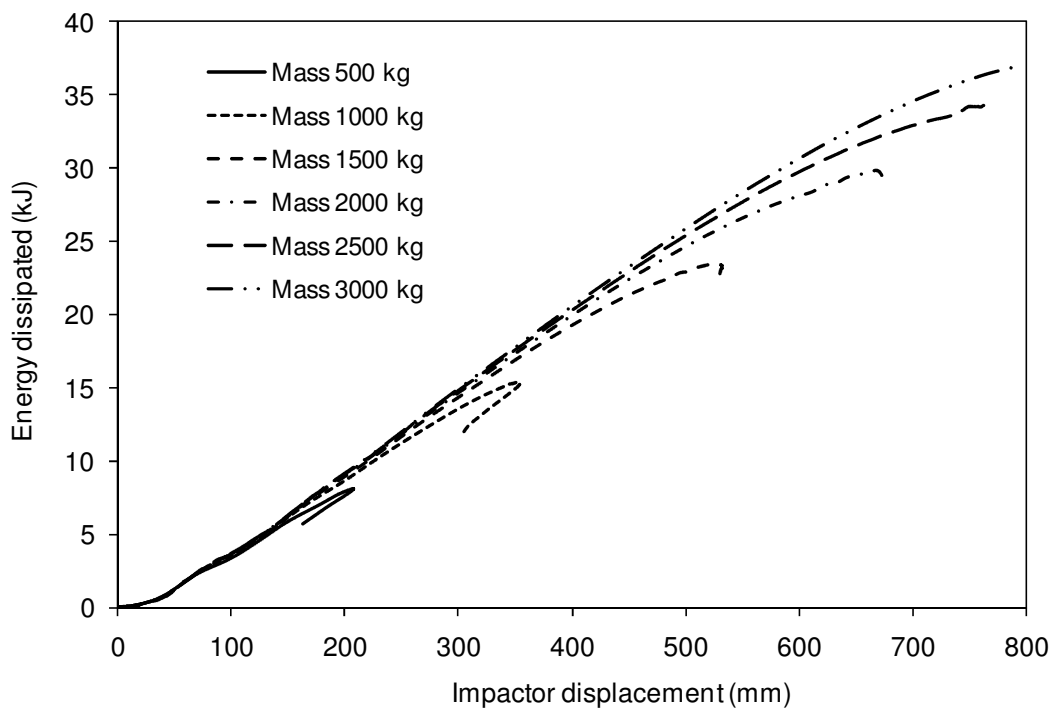


Figure 4.16: Energy dissipation of the guardrail post for different mass impactor

4.3.5. Effect of crushable post blackout

One of the major challenges in road safety is to design the guardrail system with the adequate safety level. To provide the appropriate safety levels for an errant vehicle hitting the guardrail system, the safety barrier should be designed to keep the impact force level lower than 50 kN and to absorb as much energy as possible through the deformation of the soil and guardrail system and maintain the integrity of the system (Ren and Vesenjok, 2005). In order to better control the deceleration of the vehicle, new design of collapsible blackout system is attached to the post. The current blackout consists of a block of rectangular wood posts (200 x 150 x 100) or steel W posts and serves only as a spacer between the post and the impact vehicle with no energy dissipation capacity.

The new shape of the blackout consists of a longitudinal column member that offers the highest degree of energy absorption per unit of mass and guarantees a stable folding pattern during the impact. This approach is inspired from the concept used widely in the automotive crashworthiness where the front rails are designed to absorb the maximum of the frontal impact. Fundamental theoretical research in the area of mechanics of thin-walled structures has been conducted in the past by Wierzbicki and Abramowick (1989), Jones (1983, 1989), Abramowicz and Wierzbicki (1989) and Mahmood and Paluszny (1981). In these references, a simple relation between the wall thickness, the shape geometry and material properties was derived. When a thin-walled column is subjected to uniform axial compression, it develops a state of unstable equilibrium and buckles in a well defined pattern after the column reaches its elastic or inelastic buckling stress. The tube develops buckling waves in the post-collapsing region that are function of the section geometry and material properties. The crash energy of a tube crashed axially are characterized by a folding mechanism and a bending collapse identified by plastic hinges. The structure of a post-blackout should be designed to efficiently absorb part of the kinetic energy in case an errant vehicle hits the guardrail system. The approach of the design has to be such that the post blackout, conventionally in block of wood or W shape, deforms enough to absorb the impact energy and contribute to reduce the vehicle speed and soften the impact against the guardrail.

Five models with different cross sections and thicknesses have been designed and implemented in the baseline guardrail post model as shown in Figure 4.17. The dimensions of these models were selected in such a way that the same space between the post and guardrail is kept, knowing that the increase of the gap between the post and the guardrail should reduce the snagging of the wheel during the full side model impact. Mild steel has been used for all the design scenarios to build the blockout system. The steel properties are presented in Table 4.7. This steel was chosen for its relatively low price while providing material properties that are acceptable for many applications, its relative ductility and its welding capability. To achieve a better performance in controlling the impact load, these models could be optimized in geometry, thickness and material. Only five models have been chosen either because of the simplicity of manufacturing, ease of installation or the expected high energy absorption. Similar approaches have been adopted by Vesenjok and Ren (2007) and Elmarakbi et al. (2005) where different shape of space were studied to improve the vehicle response during the impact with the guardrail system. In both cases, the study was conducted in full scale test and no component study has been conducted.

To minimize the mesh pattern sensitivity on crash simulation results, the same mesh pattern was used. The triggers used in the blockout design were simulated by removing elements from the compressible system. The element size was chosen to be approximately twice that of the sheet thickness (Simunovic et al. 2003), which offers the best trade off between crash simulation and computational efficiency.

Table 4.7: Properties of the Steel Material

Properties	Value
Material	MS
Young modulus E (GPa)	203
Poison coefficient ν	0.30
Yield strength σ_y (MPa)	206
Tensile Strength σ_t (MPa)	330
Elongation (%)	36

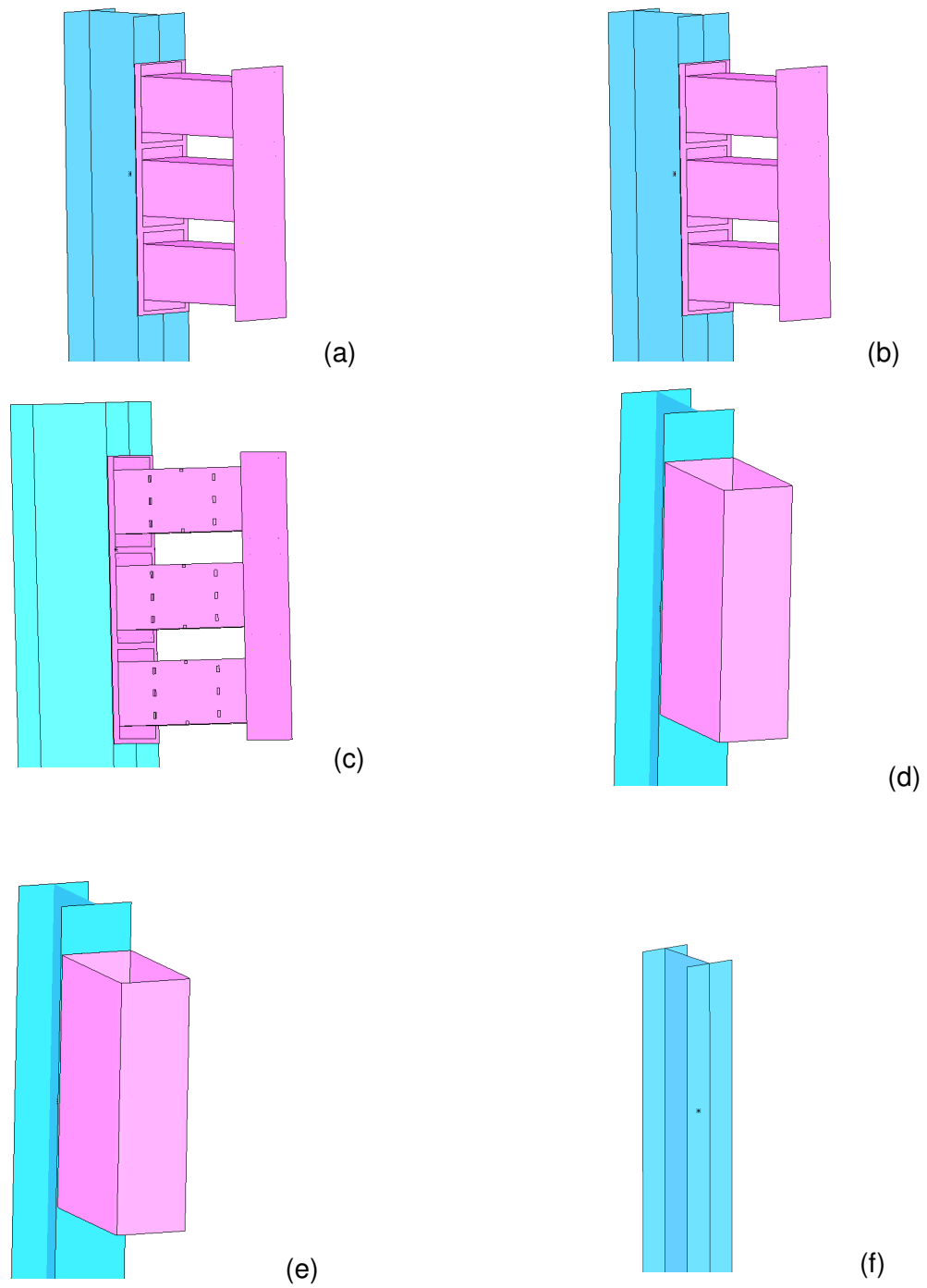


Figure 4.17: Different blockout layout to absorb energy during the impact

The five blackout components considered in this work consisted of a simplified crash box for frontal impact with a square section. Figure 4.17 shows the different considered designs:

Blockout 1 consists of 3 square tubes of 60x60 mm cross section and a wall thickness of 2 mm. The side length of the enclosed square section was 150 mm. The 3 tubes are sandwiched between two metal plates of 2 mm thickness from the same material as the square tube (Figure 4.17a).

Blockout 2 is the same as blackout geometry # 1 but with a wall box thickness of 1.5 mm Figure (4.17b).

Blockout 3's geometry is the same as blackout #1 and #2. To ensure a desirable folding mechanism of the tubes and reduce the peak load of the impactor, the design is pre-triggered symmetrically in both sides of the tube as shown in Figure 4.17 c. The triggers consist of a cut-out material executed on all sides of the tube. The wall thickness of the tube is 1 mm in this case as shown in Figure 4.17c.

Blockout 4 consists of attaching to the post a 100 x 150 x 200 mm rectangular tube (Figure 4.17.e) with a wall thickness of 2.5 mm and the same material as blocks 1-3. The block was attached to the post with 2 bolts simulated as 2 springs with no possibility of failure criteria.

Blockout 5 is similar to blackout #4 with a wall thickness of 3.5 mm

The performances of the different blackout systems are very different as shown in Table 4.8. Blockout #3, consisting of 3 longitudinal tubes and triggered on both sides, absorbs the maximum energy (5.31 kJ) whereas the same design with a 2 mm thickness was reacting very close to the baseline, having a maximum load of 66.8 kN, an average load of 48.4 kN and a maximum displacement of 330 mm. The vertical tube with a thickness of 2.5 mm absorbs 3.6 kJ within the first 50 ms as shown in Figure 4.18, then makes contact with the post, recording a load spike of 80 kN as shown in Figure 4.19. The lowest average load was 38.9 kN. The same design with 3.5 mm absorbs less energy,

0.71 kJ, because only a localized deformation was created at the lower part of the blockout as shown in Figure 4.20. The average load decreases compared to the baseline from 48.4 kN to 47.9 kN and the maximum impactor displacement remains similar to the baseline 336 mm.

Table 4.8: Results of the energy dissipation with different blockout design

Design #	Energy Dissipated (kJ)	Maximum Load (kN)	Average load (kN)	Impactor displacement (mm)
Blockout 1	0.25	66.8	48.4	329.8
Blockout 2	4.44	65.2	48.2	331.6
Blockout 3	5.31	50.3	43.9	378.3
Blockout 4	3.64	80.0	38.9	456.6
Blockout 5	0.71	62.5	47.9	336.3
Baseline	0	64.1	48.1	336.0

As shown in Figure 4.20, the triggers helped initiate a stable asymmetric crushing mode. In fact, the main advantage of a well-designed trigger in the blockout structure is to force the buckling to initiate at the trigger hole locations during crashing. This helped attenuate the first peak load effectively from 64.1 kN to 50.3 kN and reduced the load transferred to the guardrail structure. The triggers control effectively the buckling folding pattern which helped in reducing the crash mode variations and instability due to imperfections originated from material heterogeneity, part geometry or manufacturing processes.

The crushable system was able to reduce the average load to 43.9 kN and to absorb an energy of 5.3 kJ with an impactor displacement of 378.3 mm. This suggests that this crushable blockout can reduce the impactor load transferred to the post during a full crash system of a vehicle hitting the guardrail.

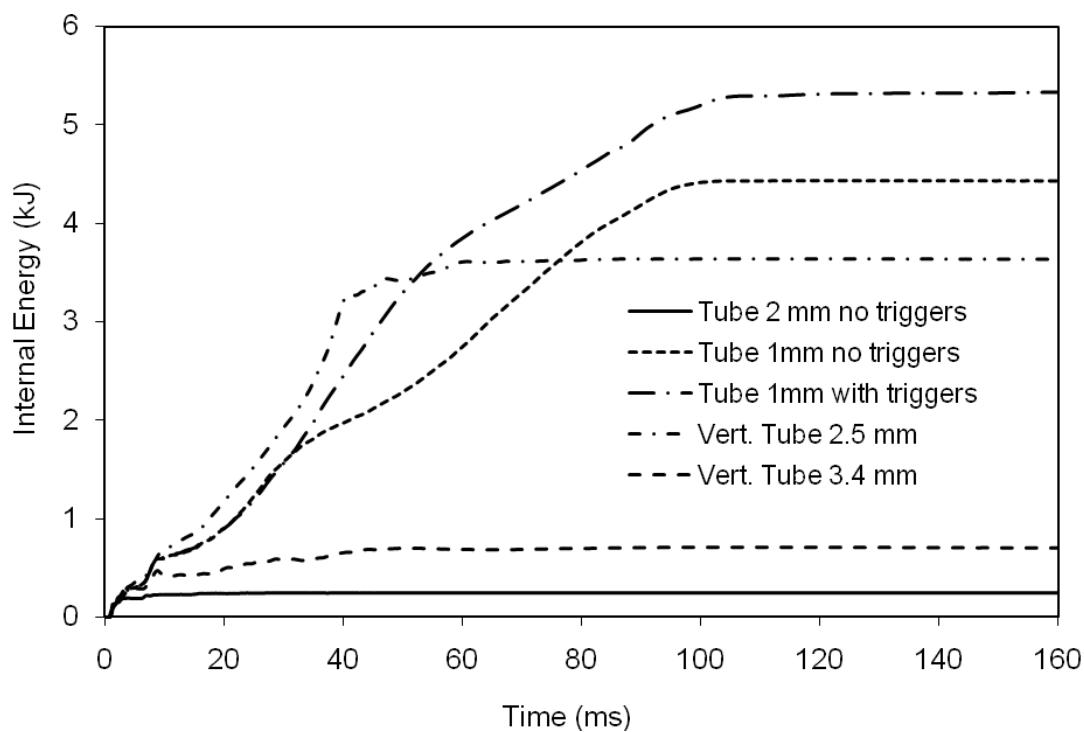


Figure 4.18: Internal energy dissipation as function of time for the blackout design

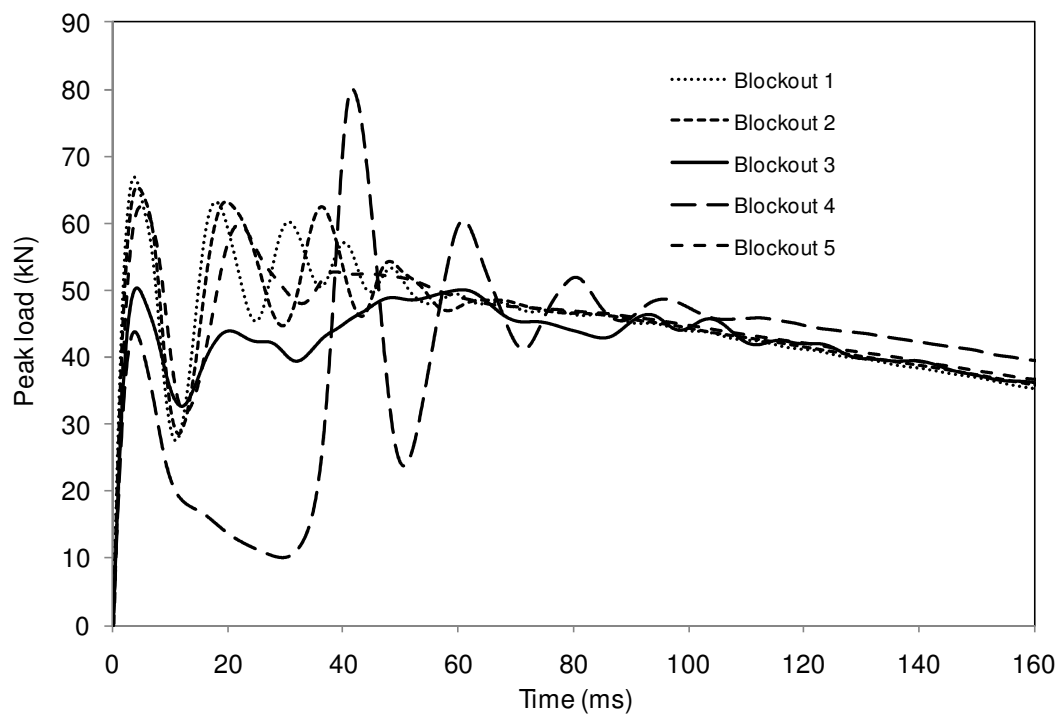
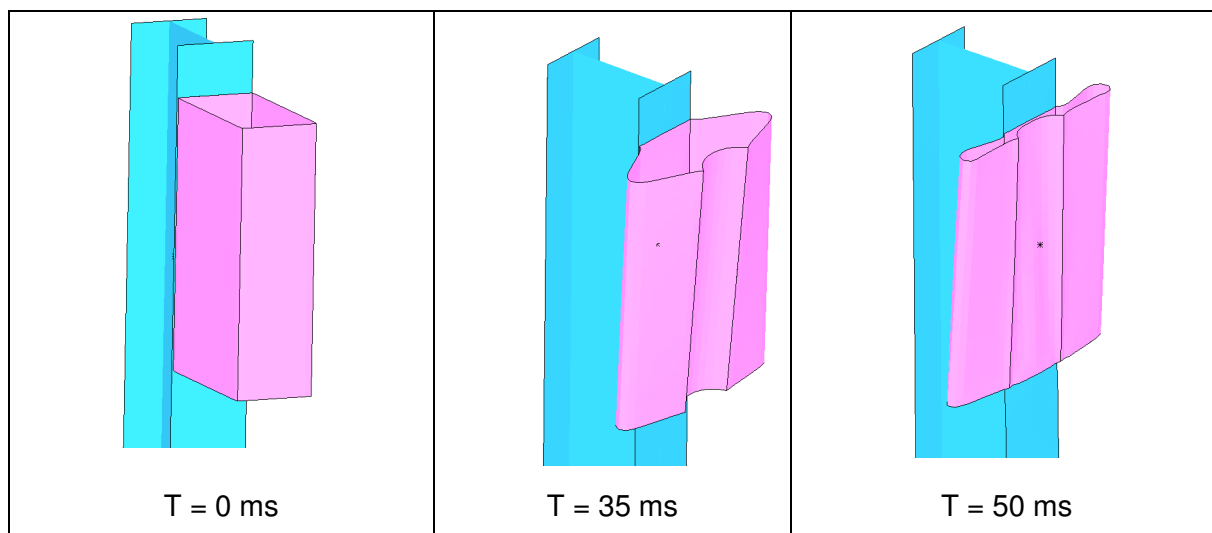
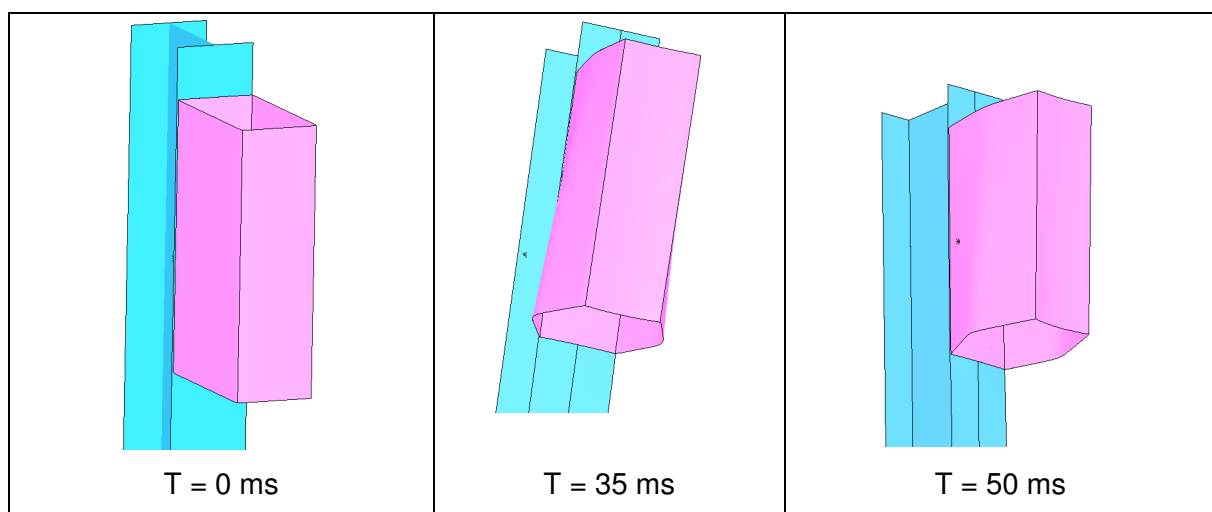


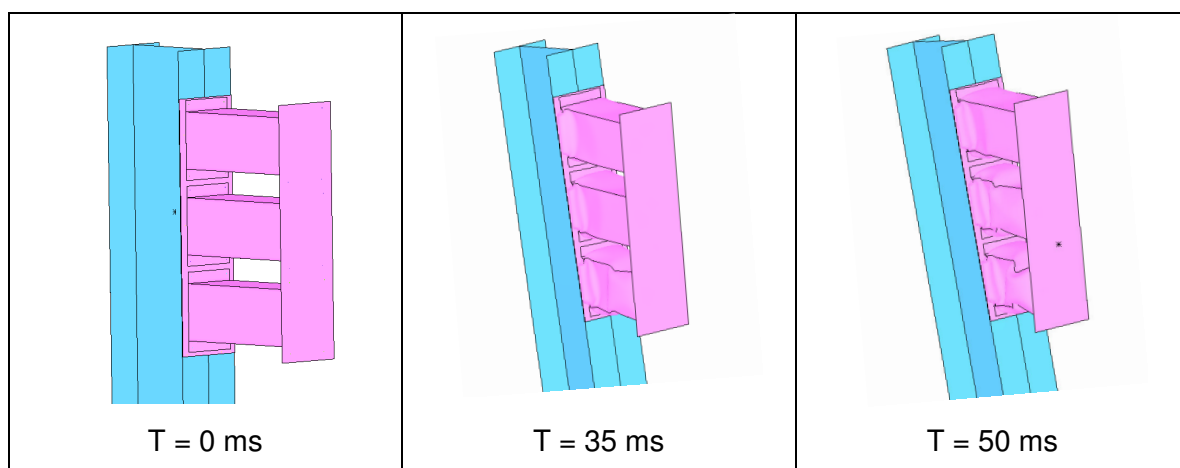
Figure 4.19: Variation of the Impactor load as function of time for different crushable blackout systems



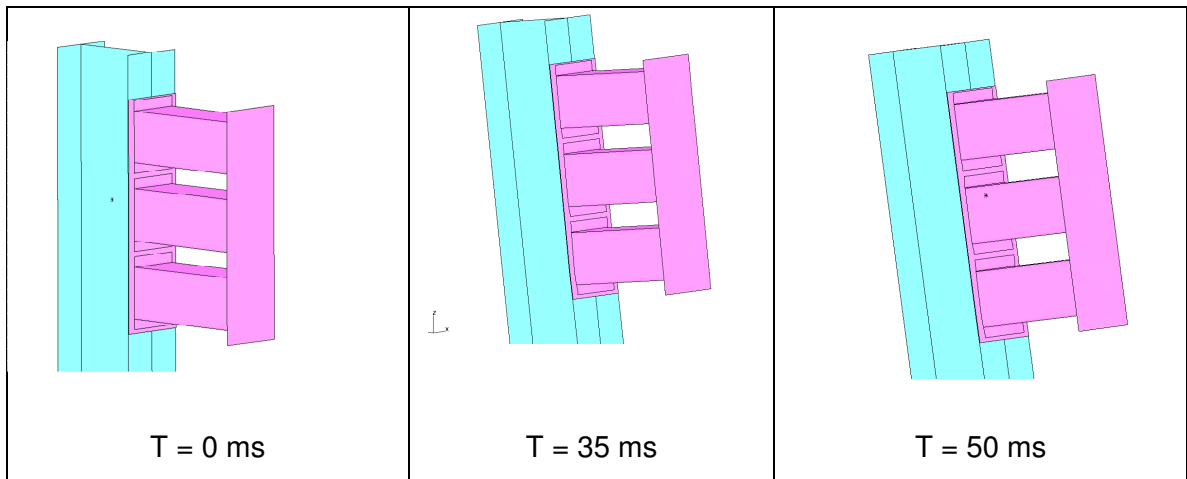
(a)



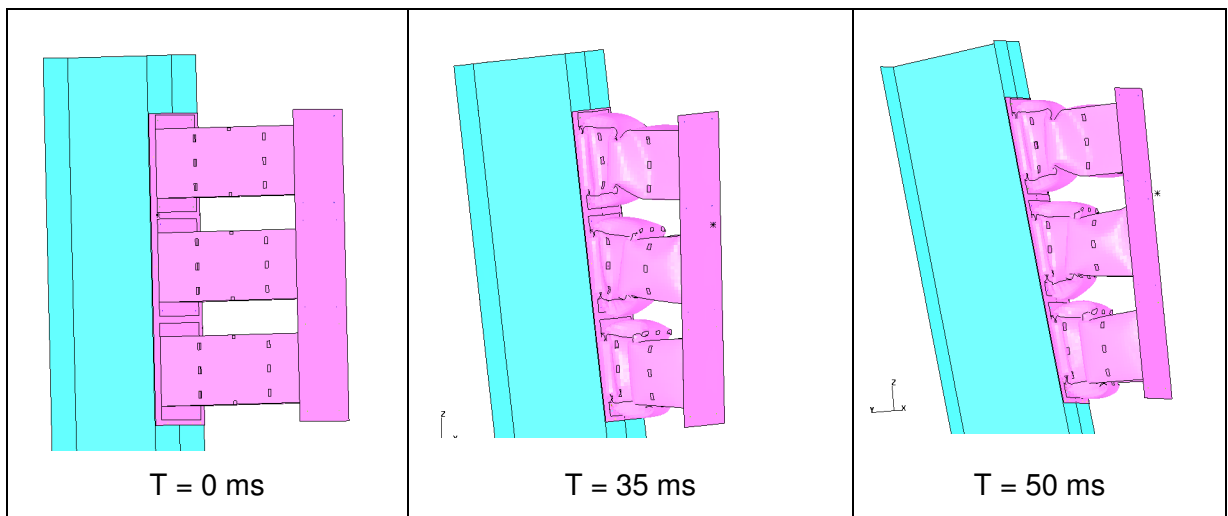
(b)



(c)



(d)



(e)

Figure 4.20: Behaviour of the crushable system as function of time

4.3.6. Effect of the clay undrained shear strength

As noted in chapter 3, the guardrail post could be embedded directly in cohesive soil characterized by the undrained shear strength, C_u , which correlates most of the cohesive soil properties. The method developed by Matlock (1970) is used to calculate the lateral resistance since it is used by many researchers in the area of roadside safety engineering when dealing with cohesive soil. The actual force P of the soil is defined as:

$$P = 0.5 P_u \left(\frac{y}{y_c} \right)^{1/3} \quad (4.12)$$

where y is the lateral actual displacement, y_c is the lateral displacement at one half of the ultimate resistance and P_u is the ultimate lateral resistance.

Fine-grained soils can be classified in relation to the undrained shear strength going from very soft to hard consistency as shown in Table 4.9. From each category of consistency, an average value of undrained shear strength has been chosen in the model to assess the performance of the post during the impact. In practice, an SPT test is conducted in-situ and the consistency is determined based on the number of blows to drive a split spoon 30 cm in depth.

For the present study, the test conducted by Dewey (1982) was used as a baseline to evaluate the effect of the clay consistency on the guardrail post reaction. The average undrained shear strength C_u of the clay was estimated to be 77 kPa and the spring stiffness was determined using this average. The mass and damping properties of the soil were assumed to be constant for all the consistency runs. The results of the finite elements models are shown in Table 4.10.

The peak load and the average load increase with the undrained shear strength following a linear function shown in figure 4.21 and defined as :

$$P_{\max} = a C_u + b \quad (4.13)$$

where $a = 0.19$ and $b = 21$ kN for the case of the peak load and $a = 0.224$ and $b = 7.33$ for the average load. The maximum displacement decreases with the undrained shear strength. The average and the peak load for the hard clay is above 70 kN, indicating high interaction between the post and soil. The behaviour of the hard clay is similar to the cohesionless soil with high density.

Table 4.9: Consistency and undrained shear strength of the cohesive soils

Consistency	Undrained Shear Strength (kPa)	Undrained Shear Strength used in the model (kPa)
Very Soft	<12	10
Soft	12-25	20
Firm	25-50	36
Stiff	50-100	72
Very Stiff	100-200	144
Hard	>200	288

Table 4.10: Summary of the simulations results of the impactor with the post embedded in different cohesive consistency

Undrained shear strength (kPa)	Peak load (kN)	Maximum displacement (mm)	Average load (kN)	Observation in the post
10	23.7	1062	7.2	Over Ride
20	24.5	998	10.4	Over Ride
36	26.4	902	15.5	Over Ride
72	38.2	712	25.1	Over Ride
144	53.4	447	40.6	Stopped
288	76.6	257	71.1	Stopped

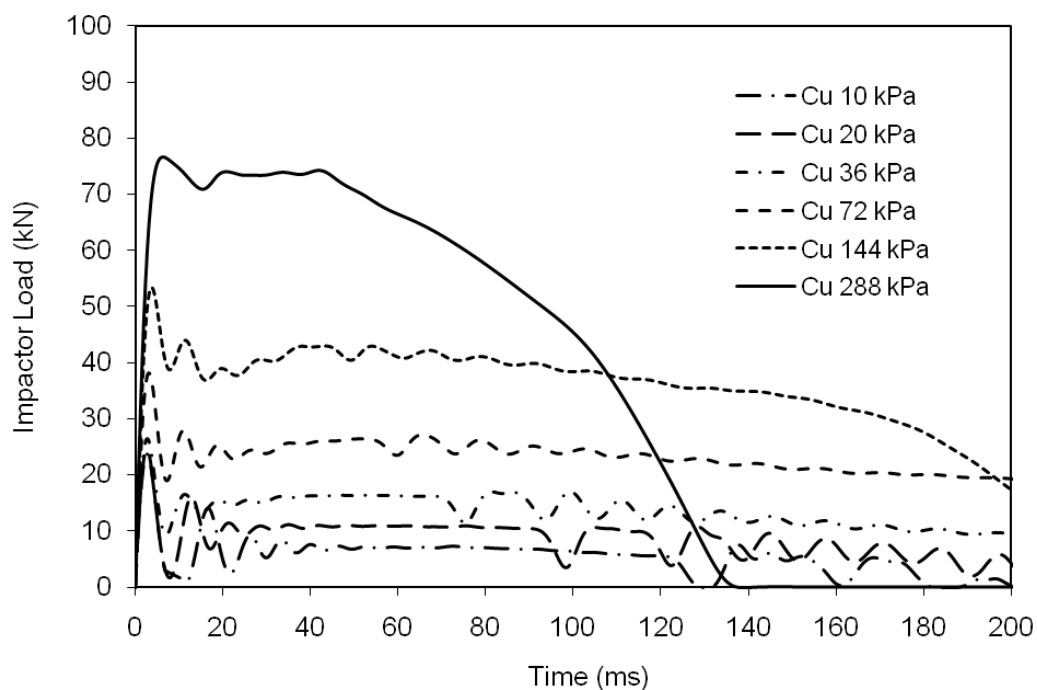


Figure 4.21: Variation of impact load as function of time for different cohesive consistency

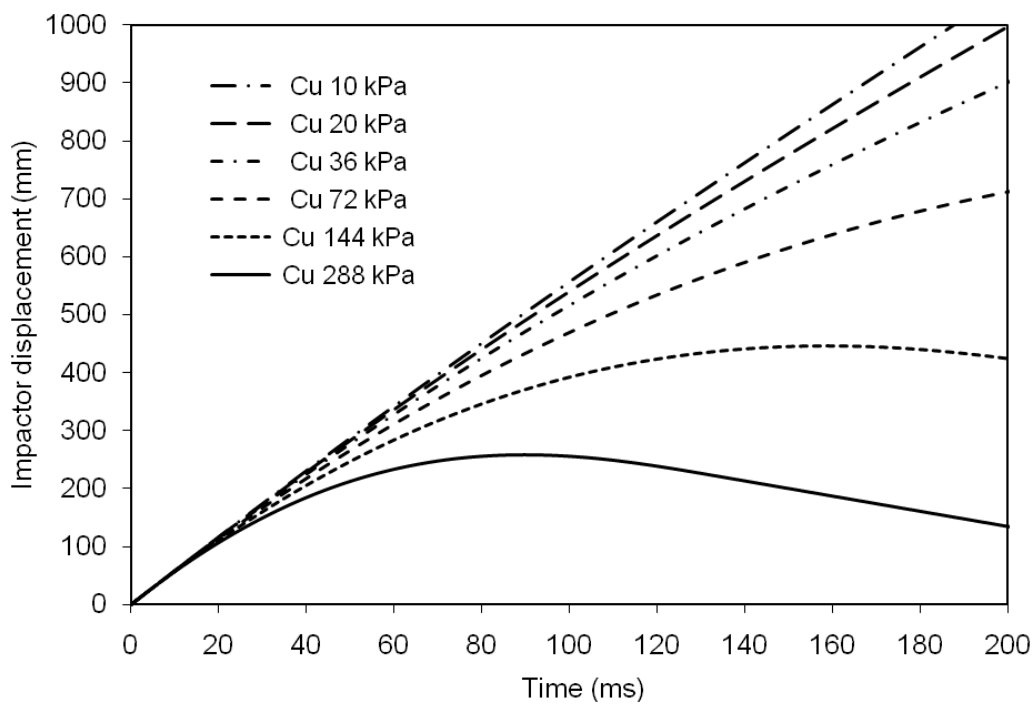


Figure 4.22: Variation of impact displacement as function of the time for different cohesive consistency

4.4. Summary of the Parametric Study

The upgraded mass-spring system of a post embedded in soil was used to conduct an exhaustive parametric finite element study and investigate the effects of the different parameters on the guardrail post reaction. The response of the guardrail post was determined under different loading conditions and the load deflection curve for the different parameters was determined and compared to the baseline. Such parameters include the sand density, the undrained shear strength of the clay, the impactor speed and mass, the post depth and the crushable blockout system were studied and the load and the impactor displacement were calculated for each case.

The study shows that that the peak load and the impactor displacement are increasing with the speed following a linear equation. For high speeds, greater than 9 m/s, the impactor was not stopped by the post reaction whereas for lower speeds, less than 3 m/s, the effect of the strain rate effect seems to be limited.

The results of the simulation with different densities of cohesionless soil and cohesive soils show that the peak load and the impactor displacement increase with the sand density and to undrained shear strength for the cohesive soil. The impactor overrode the post for the loose sand and clay consistency varying from very soft to stiff and was stopped for medium and dense sand and clay consistency higher than stiff. These results show that medium-density sand and hard clay offer the best soil interaction as the load level remains around 50 kN.

The crushable system implemented instead of the conventional rigid blockout system was able to reduce the peak load to 50 kN and the average load to 43.9 kN and absorb an energy of 5.3 kJ with an impactor displacement of 378.3 mm. This suggests that this crushable blockout can reduce the impactor load transferred to the post during a full crash system of a vehicle hitting the guardrail. The triggered design crushed better than simple blockout boxes. The triggers helped initiate a stable asymmetric crushing mode. In fact, the main advantage of well-designed triggers in the blockout structure is to force the buckling to initiate at the trigger hole locations during the crash. This helped attenuate the first peak load effectively and reduced the load transferred to the guardrail structure.

The peak load increases with the depth following a first degree equation whereas the impactor displacement decreases with depth following a power function. For embedment depths less 1000 mm, the impactor overrides the post and for depths higher than 1000 mm, the post did not show any plastic strain higher than 3%.

The post rail undergoes more displacement with the heavier impactor than with the lighter one. However, the maximum load remains quasi constant with a slight increase with the impactor mass. The impactor with mass 500 kg to 1500 kg was stopped but the impactor overrides the post for an impactor mass above 2000 kg. The maximum displacement of the impactor increases linearly with the mass. The rate of energy dissipation remains the same for all impactor weights.

The analyses of guardrail post impacted with an impactor having a speed were limited to a specific type of soil and a W-post (152x13.4). The soil is assumed to be homogenous. However, this assumption is not realistic as the soil is, in general, heterogeneous. The conclusions presented in the parametric study regarding the impactor overriding or stopped by the post were calculated based on the specific case of Coon et al. (1999) impactor displacement curves and speeds. Moreover, the vehicle impacts the guardrail system with an angle. Therefore, the post experiences two components: longitudinal and lateral. For these reasons, the guidelines proposed in the parametric study based solely on the results of those analyses should be taken as directive path and need to be validated with a full crash guardrail system.

4.5. DoE and Taguchi Method Applied to the Problem of Guardrail Post.

Design of Experiments (DoE) is powerful statistical technique for studying multiple variables effect simultaneously. This technique can be used to solve problem whose solution lies in the proper combination of factors or variables rather than a single identifiable cause (Roy 2001).

Design of Experiments (DoE) is a better alternative to the approach of best-guess or one-factor-at-a-time experiments which are not only costly but also not always efficient. The best-guess approach is used in practice by engineers and could work because the

experiments have certain technical, theoretical and practical background of the system under investigation. The best-guess approach has two main disadvantages. The first is that it is time consuming especially if the initial best-guess DoEs not produce the desired results and the second is the necessity of experimental planning especially if the first test produces acceptable results. The one-factor approach is the technique of selecting a baseline set of factors then studying the response of the system by varying each factor over each range with the other factor kept constant. The major disadvantage of this strategy is that it fails to consider any possibility of interaction between the factors (Montgomery 2005).

While, it is essential to have a detailed investigation of the different impact parameters on the guardrail post reaction, it is impractical to optimize all parameters and to establish the best possible conditions by inter-relating all parameters, as this involves numerous experiments to be carried out with all possible combinations. Design of Experiments (DoE) is a better alternative to the approach of best-guess or one-factor-at-a-time experiments which are not only costly but also inefficient for many cases. In fact, DoE, a powerful statistical technique for studying multiple variables simultaneously, will be conducted to investigate the interaction between the different parameters and the contribution of each parameter to the guardrail post reaction. Statistical experimental design methods offer an efficient tool for planning experimentation which involves different control factors simultaneously. These methods can investigate the interactive effects among the control factors and the results could be used to optimize the operational variables. The Taguchi method was selected among the various design-of-experiment (DoE) methods available in practice to study the effects of experimental parameters. This method, extensively applied in industry, has the advantages to optimize many factors and to extract quantitative information by conducting reasonable but enough number of tests.

The Taguchi method involves the establishment of a large (enough) number of experimental situations described as orthogonal arrays (OA) to reduce experimental errors and to enhance the efficiency and reproducibility of laboratory experiments. The result expresses performance in quantitative terms; it alone DoEs not give an understanding of the level of achievement of the objective (Roy 2001). Criteria of result

desirability should be defined. The Quality Characteristic (QC) has three options: Bigger is best, Smaller is best or Nominal is best. Optimization methodology adopted in this study was performed using a modified version of Prakasham et al., 2005 that was divided into four phases (with various steps), viz., planning, conducting, analysis, and validation. The schematic representation of the designed methodology is depicted in Figure 4.23. Each phase has a separate objective, interconnected in sequence to achieve the overall optimization process

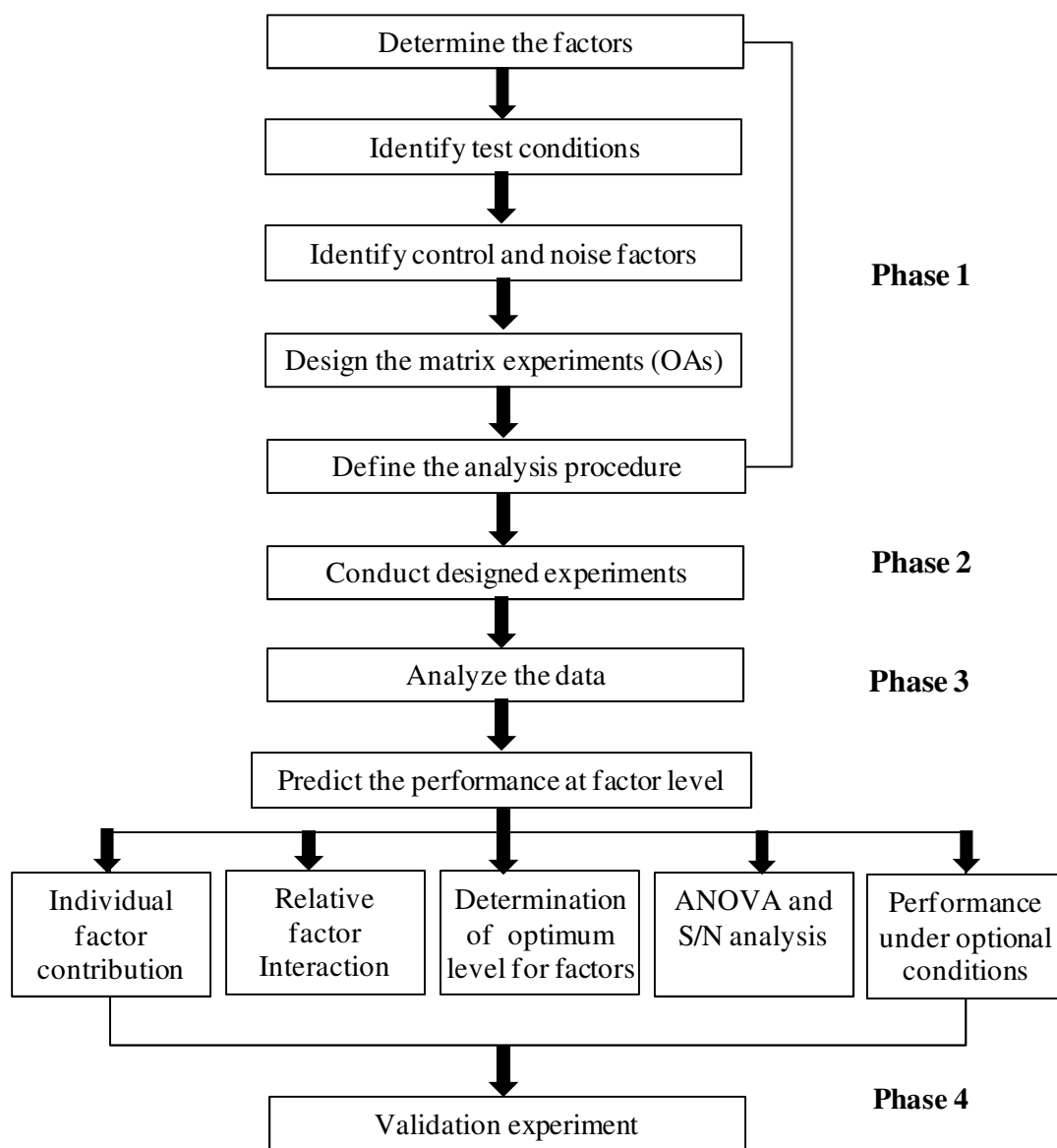


Figure 4.23: Steps involved in the use of Taguchi methodology

4.5.1. Phase 1: Planning of the DoE

The first step in Taguchi DoE approach is the planning. In fact before conducting any experiments, an exhaustive evaluation of all factors that could have any effects the behaviour of the post during the impact was carried out. These factors are divided in two groups: the noise factors and control factors, which could be controlled during the test.

The analysis of the post embedded in soil and impacted by a dynamic cart can be related to many factors suspected to have an influence on the post reaction. The list of potential factors is: the soil type (sand or clay), the soil moisture, the post embedment, the post material, the post geometry, the impactor speed, the impactor mass, the impact height and the impactor head stiffness.

For the current study, only the cohesionless soil was considered and five factors have been selected as shown in the table 4.11. Mass impactor, post embedment, impactor speed, blockout crushability and soil friction angle are retained as the most important factors that affect the guardrail post performance in the cohesionless soil.

Table 4.11: Factors and levels used in DoE layout

Level	1	2	3	4
Soil friction angle	32	37	42	
Mass impactor (kg)	500	1000	1500	2000
Post depth (mm)	900	1000	1100	1200
Crushability	Yes	No		
Speed Impactor (m/s)	4	6	8	10

Four levels have been chosen for the mass impactor ranging from 500 kg to 2000 kg with a step of 500 kg. The impactor speed ranges from 4 m/s to 10 m/s with a step value of 2 m/s. The depth of the post ranges from 900 mm to 1200 mm with a step of 100 mm whereas the friction angle has only three levels: 32°, 37° and 42°. Only two state of crushability have been considered as shown in figure 4.24, the post with rigid blockout which represents the incompressible state and the post with compressible blockout which consists of 3 square tubes of 60x60 mm cross section and a 2 mm wall thickness.

The side length of the enclosed square section was 150 mm. The 3 tubes are sandwiched between two metal plates of 2 mm thickness from the same material as the square tube. To ensure a desirable folding mechanism of the tubes and reduce the peak load of the impactor, the design is pre-triggered symmetrically in both sides of the tube as shown in Figure 4.24. The triggers consist of a cut-out material executed on all sides of the tube.

Factors included in the study have different level and requires a combination design technique to make the arrays compatible with all levels of the factors (Roy 2001). Qualitek-4 software (Nutek Inc., MI) for automatic Design of Experiments using the Taguchi approach was used in the present study to generate an L16 orthogonal distribution array. The automatic design option allows Qualitek-4 to select the array used and assign factors to the appropriate columns.

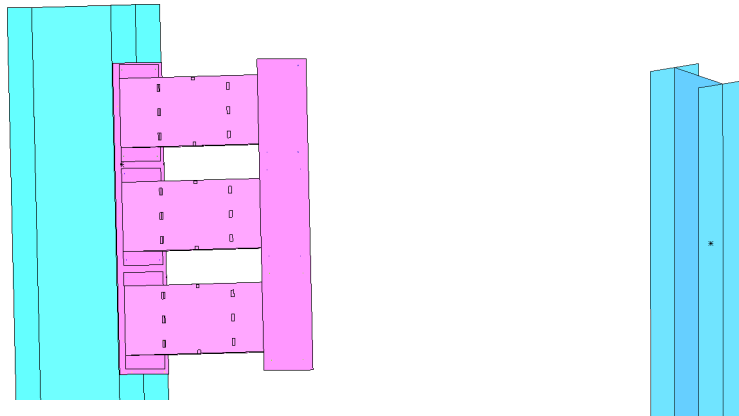


Figure 4.24: crushable and non crushable blackout post

The vertical alignments are called the column of the array and in each column; fraction of all possible combinations involved as shown in Table 4.12. Four levels, three level and the two level parameters have respectively 3 degrees, 2 degrees and one degree of freedom, (No. of levels-1). The total degree of freedom of the (DOF) required was $(3 \times 3 + 2 + 1)$ The most appropriate array in this case L16 OA with offers a maximum of 15 $(16-1)$ DOF defined as the total number of results of all trial minus 1. The L16 array is given in Table 4.12. Column 1 of Table 4.12 contains the three levels of soil friction angle.

Column #2 and 3 are empty, reserved for the interaction study. Column #4, 5, 6 and 7 contain respectively the post embedment, post crushability, the impactor speed and post mass.

Table 4.12: L_{16} Orthogonal array of the current study

	1	2	3	4	5	6	7
Run 1	1	0	0	1	1	1	1
Run 2	1	0	0	2	1	2	2
Run 3	1	0	0	3	2	3	3
Run 4	1	0	0	4	2	4	4
Run 5	2	0	0	1	1	4	3
Run 6	2	0	0	2	1	3	4
Run 7	2	0	0	3	2	2	1
Run 8	2	0	0	4	2	1	2
Run 9	3	0	0	1	2	2	4
Run 10	3	0	0	2	2	1	3
Run 11	3	0	0	3	1	4	2
Run 12	3	0	0	4	1	3	1
Run 13	1	0	0	1	2	3	2
Run 14	1	0	0	2	2	4	1
Run 15	1	0	0	3	1	1	4
Run 16	1	0	0	4	1	2	3

4.5.2. Method of evaluation

The capacity of the guardrail to absorb the vehicle impact is related to the post interaction with soil surrounding the post. A good interaction should generate a load level less than 50 kN, a higher energy absorption and acceptable level of post deflection. Thus, four variables criteria have been selected as design criteria:

Peak load: Peak load of 50 kN was chosen as the first criterion of the DoE results evaluation. The Quality characteristic (QC) is defined for this case as *nominal is better*.

Average load: Average load of 40 kN was chosen as second criterion of the results evaluation. This load corresponds to the value of 50 kN peak load. The Quality characteristic (QC) is defined as *nominal is better*

Energy dissipation: The third criterion of evaluation was the percentage of energy dissipated expressed as:

$$\% \text{ Energy} = \frac{\text{Energy dissipated in the system}}{\text{Initial kinetic energy}}$$

If the total initial kinetic energy of the impactor is dissipated during the impact, the percentage of energy will be equal to 1. The quality characteristic defined for this case is *Nominal is better*.

Post deflection: The last criterion was the post deflection at the point of impact. Even though no requirement is specified in the literature about this value, a value of 600 mm was chosen as a criterion with a QC smaller is better. This value represents the displacement that the impactor will travel freely above the post

4.5.3. Phase II: DoE results

The simulations of different runs were conducted and the results of the peak load, the average load, the maximum deflection and the energy absorbed are presented in Table 4.13.

4.5.4. Analysis of the L16 DoE results:

The influence of the different parameters (Impactor mass, impactor speed, post embedment, blockout crushability and soil friction angle) which highly influence the performance of guardrail post in the cohesionless soil was analyzed using L16 orthogonal array. The performance was analyzed in the form of average load, maximum displacement, peak load, and energy dissipation

Table 4.13: Results of the DoE Study

Runs	Peak load kN	Average load kN	Max displacement mm	Energy dissipated kJ
Run 1	28.71	10.07	322	4.07
Run 2	29.41	17.88	792	15.17
Run 3	80.82	30.62	1043	32.56
Run 4	108.61	43.76	1197	51.75
Run 5	57.70	48.23	890	58.82
Run 6	60.57	52.71	876	59.31
Run 7	63.25	37.01	201	9.02
Run 8	58.50	44.04	177	8.06
Run 9	107.12	86.10	474	35.87
Run 10	108.70	66.51	143	12.11
Run 11	115.40	37.10	850	34.66
Run 12	105.10	68.98	283	15.89
Run 13	69.71	21.36	1013	21.05
Run 14	89.65	21.55	913	22.40
Run 15	30.55	20.99	675	13.48
Run 16	33.39	23.25	938	24.23

Table 4.13 shows the maximum displacement of the post are obtained for runs 3, 4, 13 and 14 and is approximately 1000 - 1200 mm where the friction angle is 32 degrees whereas the minimum displacement are obtained for the runs 7,8 and 10. The maximum peak load is 115.4 kN recorded for Run 11 representing a combination of speed of 10 m/s and a friction angle of 42 degrees. The lowest peak load of 28.71 kN and energy absorbed of 4.07 kJ is obtained for Run 1 which combined a friction angle of 32 degrees with an embedment of 900 mm, a speed of 4 m/s and impactor mass of 500 kg. This represents the run which combined all lowest values of the DoE. Run 6 is the case which absorbed the highest energy level of 59.31 kJ.

ANOVA (Analysis of Variance) of the different parameters has been performed and the results are presented in Tables 4.14, 4.15, 4.16 and 4.17. Table 4.14 shows the

percentage P for the peak load criteria. The value of P, for each factor, is defined as fraction of the net variation of the factor A to total variation (Taguchi 1991). The percentage P calculated in the last column has been collected in unique Table 4.15 where it summarizes the percentage P of each factor in the response of guardrail post with regards to the four quality criteria selected for the study. It can be seen that the speed is the most important factor that has an influence on the post behaviour with a percentage influence of 45.7 % in the energy dissipation, 48.9 % on the post displacement whereas the soil density and the impactor mass have a very close influence factor of approximately 22%. It is interesting to note that the crushability plays little role in the energy dissipation by contributing only 1% as shown in Table 4.15. This factor could be pooled out of the table and the analysis conducted only with the four parameters.

Table 4.16 shows the interaction of the different parameters during the post loading defined by the severity index (SI) calculated for each two factors. Table 4.16 shows that the interaction between the post crushability and the soil friction angle is the highest interaction with an SI ranging from 90.9 % for the peak load to 56.46 % for the energy absorption. The interaction between the post crushability and the post depth is also high with an SI ranging from 61.8 % of the post deflection to 34.03% for the energy absorption. The column number (4) indicated under the column labelled Col represents the column where the interaction effect of the factors was present such as the effect of the interaction of density and the crushability. Table 4.17 shows the optimum condition for different parameters. It can be seen that the optimum condition for the peak load are obtained for friction angle of 32 degrees, a post embedment of 900 mm, a crushable post blockout, an impactor speed of 4m/s and a mass impactor of 1000kg. The optimum post deflection is obtained for a speed of 4m/s, an impactor mass of 500 kg combined with the a friction angle of 42 degrees, a post embedment of 1200 mm and no crushability.

Table 4.14: Analysis of Variation (ANOVA) for post displacement

Column #/Factor	DOF (f)	Sum of Sqrs (S)	Variance (V)	F-Ratio (F)	Pure sum Sq	Percent P (%)
Density	2	581200.039	290600.019	2718000599.928	581200.039	31.695
Depth	3	4058.432	1352.810	40584329.446	4058.432	0.221
Crushability	1	13460.349	13460.349	403810487.502	13460.349	0.734
Speed	3	897362.546	299120.848	2973625464.364	897362.546	48.937
Mass	3	337609.805	112536.601	2376098056.726	337609.805	18.411

Table 4.15: ANOVA of the different criteria for the current DoE

Column #/Factor	Energy dissipation	Max Displacement	Average load	Peak load
Density	22.049	31.695	71.396	50.873
Depth	8.01	0.221	6.054	1.571
Crushability	1.059	0.734	4.908	21.691
Speed	45.769	48.937	2.313	24.788
Mass	22.955	18.411	15.327	1.074

Table 4.16: Results of interaction factors of the different criteria

Interaction Factor pairs	Energy absorbed			Deflection			Average load			Peak load			
	Columns	SI (%)	Col	Opt	SI (%)	Col	Opt	SI (%)	Col	Opt	SI (%)	Col	Opt
Friction angle x crushability	1 x 5	56.46	4	[1,2]	72.5	1	[2,2]	81.98	2	[1,1]	90.95	2	[1,1]
Depth x crushability	4 x 5	34.03	1	[4,2]	61.81	4	[2,2]	34.92	1	[1,1]	58.39	3	[1,1]
Density x Mass	1 x 7	30.88	6	[1,4]	18.24	6	[3,3]	32.09	1	[3,1]	36.69	1	[1,1]
Depth x Mass	4 x 7	30.02	3	[4,4]	38.52	3	[2,3]	20.63	2	[1,2]	34.45	4	[1,1]
Crushability x Mass	5 x 7	22.7	2	[2,4]	39.29	2	[1,1]	18.21	4	[1,1]	14.31	2	[1,3]
Friction angle x Depth	1 x 4	16.44	5	[3,3]	10.76	5	[3,2]	9.83	3	[1,1]	8.01	1	[1,1]
Speed x Mass	6 x 7	16.25	1	[4,4]	34.83	1	[1,3]	8.54	7	[1,1]	5.62	5	[1,1]
Depth x Speed	4 x 6	15.83	2	[4,4]	23.55	2	[2,1]	2.29	6	[1,1]	3.69	6	[1,2]
Friction angle x Speed	1 x 6	7.66	7	[1,3]	18.77	7	[3,1]	1.35	3	[1,1]	1.73	7	[1,1]
Crushability x Speed	5 x 6	7.36	3	[2,3]	10.55	3	[2,1]	0.34	5	[1,1]	0.13	3	[1,1]

Table 4.17: Contribution of the different parameters to the guardrail post response

Column #/Factor	Energy Dissipated			Displacement			Average Load			Peak load		
	Description	Level	Contribution	Description	Level	Contribution	Description	Level	Contribution	Description	Level	Contribution
Density	Low	1	-0.067	High	3	-236.743	Low	1	-15.701	Low	1	-12.844
Depth	1100	3	-0.055	1200	4	-25.309	1100	3	-7.956	900	1	-5.89
Crushability	no	2	-0.015	no	2	-29.005	yes	1	-4.484	yes	1	-14.096
Speed	10	4	-0.136	4	1	-345.153	4	1	-3.984	4	1	-15.085
Mass	1000	2	-0.06	500	1	-244.413	1000	2	-9.29	1000	2	-3.445
Total Contribution From all factors			-0.334	-880.624			-41.415			-51.360		
Current grand Average of performance			-0.143	24.187			4.384			21.699		
Expected results at optimum condition			-0.476	-856.436			-37.031			-29.661		

4.5.5. Conclusion

The L16 OA study shows that the speed and the soil friction angle are individually the most influential parameters of the post behaviour as shown in Table 4.15. When the interaction is taken in account, the post crushability and the soil friction angle show the highest interaction for the different quality parameters. The optimum post deflection is obtained for a speed of 4 m/s an impactor mass of 500 kg combined with the a friction angle of 42 degrees, a post embedment of 1200 mm and no crushability. These conditions causing the minimum post displacement and loads levels represent also the lowest energy input from the impactor to the guardrail system. These conditions do not represent the frequent condition of impact and the DoE study needs to be refined with real impact condition by taking the mass and the speed of the impactor as constant input for the DoE study.

4.6. L9 Orthogonal Array

4.6.1. Phase 1: Planning of the DoE

In the second step of the DoE study, the mass and speed of impactor are kept constant: 1000 kg and the speed 7 m/s. The study is focusing in the evaluation of the different post design parameters during the impact of the post under the same impact energy.. The remaining three factors have been kept from the first DEO study i.e.. the post embedment, the blockout crushability and the soil friction angle. Different levels were chosen in this study for selected three factors as shown in Table 4.18. Three level of crushability have been considered in the current study instead of two used in the previous DoE. An intermediate crushability level has been added. The new level “low crushability”, is assumed through a design similar to level 2 but with a thicker tube of 1.5mm.

It can be seen from Table 4.19, each column contains the same number of 1's 2's and 3's and that these numbers follow certain pattern and not distributed randomly. This balance of the test matrix assure that each level of factor have equal opportunity to influence to the results (Roy, 2001).

Table 4.18: parameters and steps of the current study

Level	1	2	3
Soil friction angle (°)	32	37	42
Post depth (mm)	1000	1100	1200
Crushability	No	High	Low

The three three-level parameters have 2 degrees of freedom, (No. of levels-1), i.e., the total degree of freedom of the (DOF) required was (3x2). The most appropriate array in this case L9 OA which offers a maximum of 8 (9-1) DOF defined as the total number of results of all trial minus 1. The assignment of parameters to the columns of the L9 OA is given in Table 4.19.

Table 4.19: L9 Orthogonal array of the current study

Run #	Factor level		
	1	2	3
Run 1	1	1	1
Run 2	1	2	2
Run 3	1	3	3
Run 4	2	1	2
Run 5	2	2	3
Run 6	2	3	1
Run 7	3	1	3
Run 8	3	2	1
Run 9	3	3	2

4.6.2. DoE results and discussion

The results of the different simulations are presented in Table 4.20.

Table 4.20: Results of the DoE Study

Run #	Peak Load kN	Average load kN	Max Displacement mm	Energy Dissipated kJ
Run 1	60.40	20.50	764	16.94
Run 2	48.01	41.50	432	17.61
Run 3	109.90	53.10	215	14.07
Run 4	75.96	52.50	439	24.70
Run 5	112.10	66.30	193	14.20
Run 6	40.80	26.77	855	22.45
Run 7	116.40	77.10	272	23.05
Run 8	40.70	26.78	777	21.40
Run 9	75.70	54.70	318	16.15

The influence effect of different parameters (embedment, blockout crushability and soil friction angle) which highly influence the performance of guardrail post in the cohesionless soil was analyzed using L9 orthogonal array. The performance was analyzed in the form of average load, maximum displacement, peak load, and energy dissipation

Table 4.20 shows the minimum displacement of the post are obtained for runs 3 and 5 and 7 and is approximately 200 mm where the friction angle is 42 degrees whereas the maximum displacement are obtained for the runs 1, 6, and 8 which corresponds to the low soil friction angle of 32 degrees. The peak load reached the load value of 116 kN and 112 kN for the runs 5 and 7 corresponding also to the highest friction angle of 42 degrees. However, the smaller peak load was 40 kN to runs 6 and 8 corresponding to soil friction angle of 32 degree combined with a low or high degree of crushability of the blockout. The energy dissipated was higher for the Run 4 with total energy dissipation

close to 1 whereas the lowest degree of energy dissipation is obtained for Run 5 where 58% of the energy is dissipated.

The optimum conditions predicted by the analysis of Taguchi L9 experimental design are shown in the Table 4.21. The optimum conditions to target 50 kN are an embedment of 1000 mm with high crushability blockout and small friction angle. The predicted peak load is 35.9 kN (50 kN – 14.1 kN). For the post deflection, the predicted optimum value is 197 mm obtained with high friction angle of the soil, an embedment of 1200 mm with low crushability of the block out. For the average load, the optimum condition is obtained for the combination of an embedment of 1000 mm, low friction angle and low crushability of the blockout. Finally for the energy dissipation, the optimum condition is obtained for an embedment of 1100mm, a low friction angle and no crushable post.

ANOVA (Analysis of Variance) of the different parameters has been performed and the results of the peak loads have been collected in Table 4.22. The percentage P of each factor in the response of guardrail post is summarized for the four quality criteria selected for the study. The analysis based on individual factor L9 experimental design shows that the friction angle plays individually the main role in the guardrail post reaction in respect of peak load, average load and maximum post displacement. In fact the influence factor of these different parameters ranges from 86 % to 99 % as shown in Table 4.22. Similar results were obtained by Plaxico et al. (1998) who conducted a parametric study to determine the role that wood and soil strength play in guardrail system. The rail height deflection at failure of the post was found to be a function of the soil strength parameter, ϕ , for many different post strengths and an increase in the value of the friction angle ϕ leads to an increase in soil strength and a decrease on the post deflection. The post embedment and the post crushability have less impact of the post reaction and their influence remains lower than 6% for peak load and post deflection. This conclusion confirms the test results of Kuipers and Reid (2003) where the initial peak force, the average load and post deflection were similar for two embedments of 1092 mm and 1016 mm. The force level and the energy absorption were reduced only when the embedment depth was reduced to 940 mm. The DoE shows also that the main contribution of the embedment and the blockout crushability appears in the energy

dissipation parameter where their contributions are respectively determined as 42.1 % and 37.3 %.

Table 4.23 summarized the interaction of the different parameters selected for the study. It can be viewed that for the post deflection and average load, the different parameters have very limited interaction and the maximum value of SI is less 15.26. It is interesting to note that, the post crushability have 52.58 % and 54.46% interaction with the depth and the friction angle respectively and the depth have 31.4 5 and 32.05% interaction with the depth and the crushability respectively.

The friction angle as shown in Table 4.22 has influence factor above 86 % which individually seems to play the main role in the guardrail post reaction. In general, with a contribution of less than 5%, one of the common practices of statisticians is to pool the parameter out of the study and conducted a second analysis of variance with the remaining parameters in respect to criteria of evaluation (Roy 2001) of peak load, average load and maximum post displacement.

However, the same factor of the soil friction angle shows an interaction factor with the blockout crushability expressed with a severity index (SI) higher than 54 % for the energy dissipation and 15 % for the average load. For the peak load, the soil friction angle has an interaction with the post depth of 32%. These results are suggesting that these parameters cannot be pulled out of the study even, individually, the parameters seem having minor effect on the results as suggested by the one-at-time method. Friction angle which is influencing the results more than 90% is accomplishing this performance with interaction with the other factors. The crushability of the blockout and the post depth have minor influence in affecting the behavior of the post or getting the optimum condition for the different factors however these are influencing the results by their interaction with the different quality criteria. This study unveils clearly how the factors directly and indirectly influence the final results.

Table 4.21: Contribution of the different parameters in the post reaction

Column #/Factor	Peak Load			Post displacement			Average load			Energy		
	Level Description	Level	Contribution									
Depth	1000	1	-2.783	1200	3	-18.223	1000	1	-8.217	1100	2	0.059
Crushability	High	2	-8.616	Low	3	-11.223	Low	3	-1.727	No	1	0.104
Friction angle	32	1	-28.253	42	3	-247.223	32	1	-21.901	32	1	0.054

Total Contribution From all factors -39.65 -276.7 -31.845 0.216

Current grand Average of performance 25.552 473.89 6.583 0.772

Expected results at optimum condition 14.1 197.22 -25.261 0.989

Table 4.22: ANOVA of the different criteria the post loaded laterally for L9 DoE matrix

Column #/Factor	Energy	Max deflection	Average load	Peak load
Depth	42.126	0.470	11.352	0.513
Crushability	37.374	0.278	1.831	6.174
Friction angle	20.195	99.250	86.816	93.312

Table 4.23: Results of interaction factors of the different criteria for L9 DoE matrix

Interaction Factor pairs	Columns	Post deflection			Energy dissipated			Average Load			Peak load		
		SI (%)	Col	Opt	SI (%)	Col	Opt	SI (%)	Col	Opt	SI (%)	Col	Opt
Depth x Friction angle	1 x 3	6.34	2	[2,3]	6.69	2	[2,2]	4.17	2	[1,1]	31.4	2	[3,1]
Depth x crushability	1 x 2	6.49	3	[2,2]	52.58	3	[2,1]	6.36	3	[1,1]	32.05	3	[3,2]
crushability x Friction angle	2 x 3	1.51	1	[2,3]	54.46	1	[1,2]	15.26	1	[1,1]	5.34	1	[2,1]

Another interesting result, which could be considered using the Qualitek software, is the determination of the optimum post deflection and the identification of the individual influence factor on the post reaction. In Taguchi's method, quality is measured by the deviation of a characteristic from its target value, and a loss function $[L(y)]$ is developed for the deviation as represented by $L(y) = k(y - m)^2$, where k denotes the proportionality constant, m represents the target value and y is the experimental value obtained for each trial. In case of smaller is better QC, the loss function can be written as $L(y) = ky^2$ and the expected loss function can be represented by the results obtained from the data processing shown in Figure 4.25.

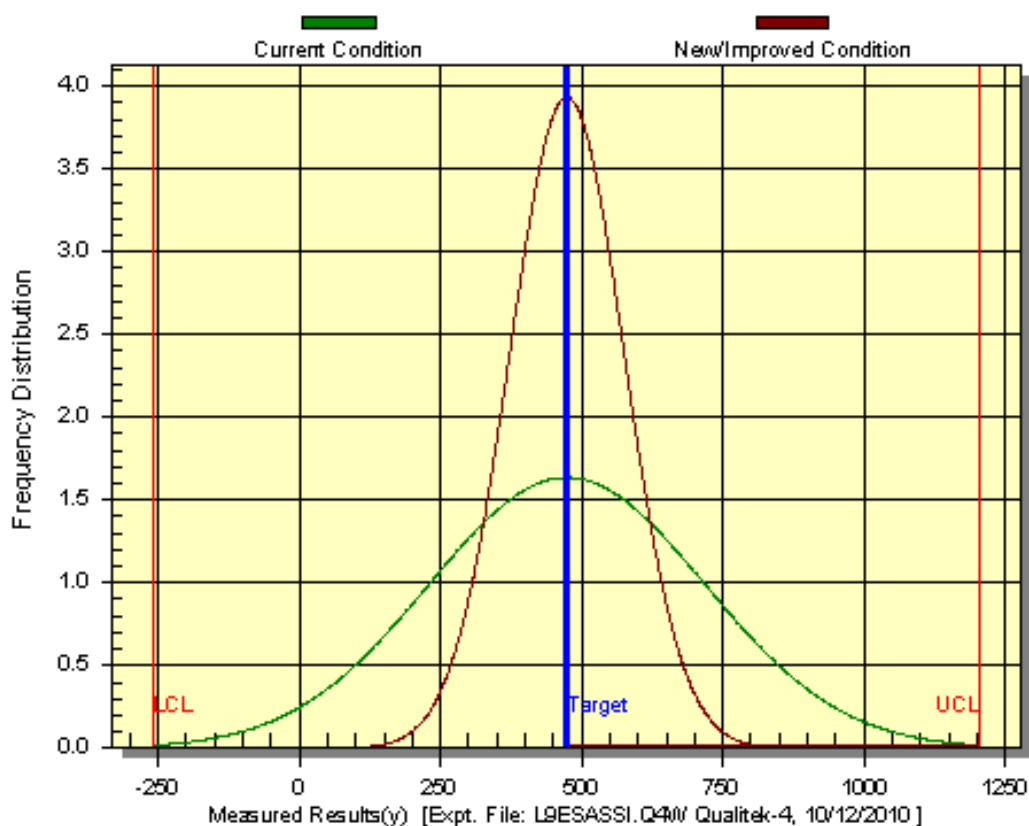


Figure 4.25: Variation reduction plot for smaller post deflection

As shown in Table 4.21, the expected post deflection at the optimum condition is 197.22 mm calculated for a post embedment of 1200 mm in soil with a friction angle of 42 degrees and low compressibility blockout. To accomplish similar performance of post displacement of 200 mm using one-at-time parametric study, a speed of 4 m/s is

required for the baseline condition of loading as shown in Table 4.1 in the parametric study. This speed is low and DoEs not represent a realistic speed of contact. The current speed of 7 m/s applied to the baseline condition yields a 435.6 mm displacement which is two times higher than the one determined by the DoE value. By using Taguchi analysis design, and keeping the conditions of 7 m/s and the impactor of 1000 kg, the post displacement was minimized to 197 mm. This improvement of performance in the post deflection could be viewed in Figure 4.25 which shows that targeted value of 197 mm was achieved at optimum condition predicted from L9 Experimental design.

4.7. Conclusions

The purpose of this chapter is to study the contribution of the different design parameters of the guardrail post to the reaction during lateral dynamic impact using the Taguchi method. The guardrail post depends on the soil to provide the required foundation support. The interaction between the post and the soil depends on many factors such as the soil friction angle, the post depth and the post blockout crushability. Hence, the reaction force recorded is very much related to all conditions implemented in the post design. The L-9 OA design compared to a conventional one-at-a-time-approach has been evaluated in the present investigation. The experimental data depicted the edge in identifying the influence of individual factors and establishing the relationship between variables and operational conditions as well as for the selection of optimal levels for best performance. It can be concluded that:

- The soil friction is the most important factor in guardrail post reaction during the lateral impact and plays a major role with respect to the peak load, average load and maximum post displacement.

- The post embedment and the post crushability seem individually to have less role in the impact of the post reaction and their influence is lower than 6% for peak load and post deflection. However, the interaction of these factors with the soil friction angle is important and can influence the test results.

-The optimum conditions predicted by the analysis of Taguchi L9 experimental design shows that the crushability of the blockout post is an important factor to achieve an optimal condition.

Chapter V

Full-Scale Finite Element Model Development and Analysis

5.1. Introduction

Most of the roadside hardware evaluation has been achieved by conducting destructive full-scale crash testing to evaluate performance of roadside safety devices. The result and the analysis of the test is used to identify potential safety problems. However full-scale testing suffers from many shortcomings, as many parameters are not controlled efficiently and the test is costly. The need for full crash testing evolved from the requirement to meet the NCHRP Report 230 (Michie, 1981) to NHCRP 350 (Ross et al., 1993). One major change was the replacement of the 2044 kg passenger car by a 2000 kg pickup truck under NCHRP Report 350 guidelines (Ross et al., 1993). The C1500 pickup truck has been the main test vehicle for the majority of roadside hardware evaluation and certification crash tests (Marzoughi et al., 2004).

As computer processing power has increased and finite element analyses become more accessible and affordable, these analyses play a major role for the design of roadside hardware. Computer simulations reduce the development cost by optimizing different design alternatives prior to any full-scale destructive crash testing. However, the accuracy of simulation depends upon the development of reliable models of each distinct component of the guardrail system as well as the integration of all these parts in the same global model (Plaxico, 2002). On the other hand, the accuracy of the finite element models should not penalize the full model in terms of time computation. For example, most of the bolt connections should be modeled as springs in lieu of dense mesh of the geometry details.

In order to implement the results of the parametric study, finite element model of a full-scale crash test is built representing the impact of a pickup truck travelling at 100 km/h and impacting the guardrail with an angle of 25° as required by NCHRP Report 350. The model is used to study the interaction of the posts with the vehicle during the full-scale crash test and compare the results with those obtained from the component crash model. The model serves also to review the vehicle behaviour and the post reaction

under different blockout designs, crushable and non-crushable, and compare it to the baseline vehicle reaction. The modeling of each component of the guardrail system is presented with validation.

5.2. Finite Element Modeling

5.2.1. Guardrail modeling

The W-beam guardrail model used in this study consists of corrugated sheet steel beams as shown in Figure 5.1. The cross section is 312 mm height and 83 mm width and 2.66 mm thickness. Details of the guardrail section are presented in Figure 5.1. The model consisted of guardrail beams of 3820 mm length each overlapped over 320 mm between each two adjacent beams. The guardrails located at the central portion and subjected directly to the impact of the vehicle are meshed with fine mesh since the deformations are expected to be significant while the guardrail beams located at the two ends of the guardrail and subjected only to pure tension, and they are meshed with a coarse mesh to balance adequately the simulation response of the beam guardrail and the computation time consuming.

The W-beam rail material is classified as AASHTO M-180 Class A Type II (ASSHTO, 2000). The material is defined as linear elasto-plastic with kinematic strain hardening, material type 36 in Radioss. The material properties of the guardrail needed for the finite element model are determined from the tests conducted by Hamilton (1999) who performed a series of three tensile tests on steel coupons taken from guardrail posts. The material properties used are summarized in Table 5.1. These properties are similar to those properties presented by Wright and Ray (1996).

The guardrail was meshed with four-node, as illustrated in Figure 5.2, using Quadrilateral Elasto Plastic Hourglass Control shell formulation known as QEPH shell elements (Mecalog 2005) which is one Gauss point of quadrature numerical integration. The under-integration formulation can reduce the computation time but have the risk that it can lead to zero-energy hourglass modes depending on the mesh and the geometry. A review of the hourglass energy was conducted after each finite element simulation to ensure that no numerical instabilities are created and the percentage of hourglass energy is kept under an acceptable level of the total energy. From the automotive best

practice, 2% is chosen as criterion for acceptable level. The shell element has five integration points through the thickness of the element.

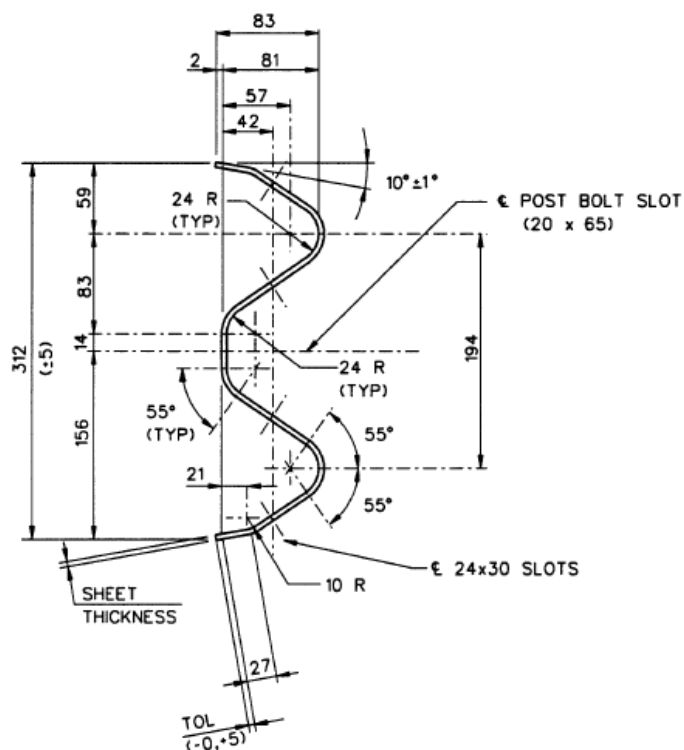


Figure 5.1: Guardrail cross-section of the W beam after AAHTSO (2000)

Table 5.1: Material properties for modeling guardrail steel (Plaxico, 2002)

Material Property	Value							
Material Type	AASHTO M-180							
Density kg/m ³	7890							
Poisson's ratio	0.30							
Yield Stress (MPa)	415							
Strain (%)	0	0.02	0.08	0.165	0.330	0.495	0.66	1.00
Stress (MPa)	0.0	415	548	585	591	595	600	600

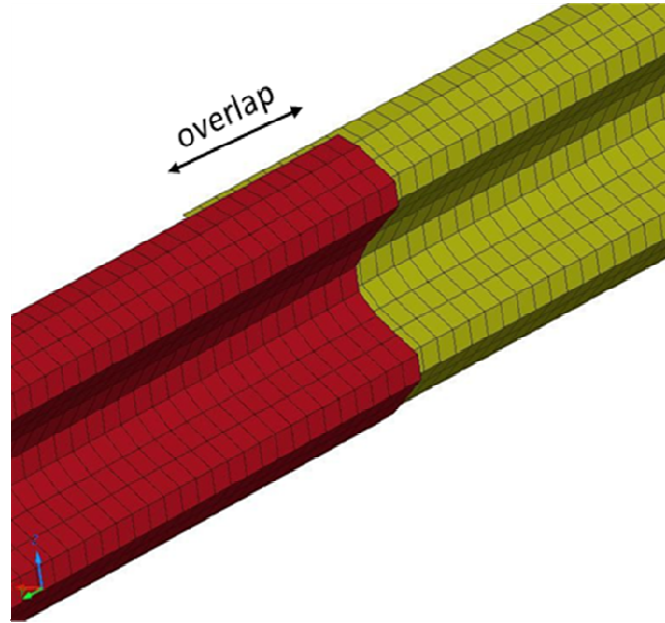


Figure 5.2: Finite element meshing of the W-beam

It is acknowledged that the strain rate effect has a significant influence on the dynamic impact behaviour of the steel. The yield criterion which governs the plastic flow in the structural problem is dependent of the rate of stain (Jones 1989). The post is modeled using an elasto-plastic material with strain rate effect. The strain rate effect has been defined by Cowper and Symonds equation (1957):

$$\frac{\sigma'}{\sigma} = 1 + \left(\frac{\dot{\epsilon}}{D} \right)^{\frac{1}{q}} \quad (5.1)$$

σ and σ' are the quasi-static and dynamic stresses and $\dot{\epsilon}$ is the strain rate and q , D are the Cowper and Symonds coefficients, for the steel, q and D are estimated to be 5 and 40 as mentioned previously in Chapter 3.

5.2.2. Guardrail post modeling

The posts used in the guardrail system model are W150x13.5 beam where the cross section was described earlier in Chapter 3 (Section 3.2). The steel post is 1.8 m long and has two symmetric holes located 178 mm from the top of the post to attach the blockout with a M16 bolt. In the current study, these holes were filled since the bolt was

modeled as spring. A Detail of the finite element model of the post is shown in Figure 5.3.

Following the same strategy of balancing the computational time and the results accuracy, two finite element models of the post were developed. The first model consisted of a coarse mesh and used for the non-impact zone located close to the two ends of the guardrails and the second with a fine mesh for the impacted zone. The fine model for the W150×13.5 (W6×9) steel post consists of 2020 elements and 2142 nodes whereas the coarse model consists of 819 elements and 896 nodes. As stated by Plaxico (2002) the W150x13.5 posts are weak in torsion and tend to twist during impact, which consequently reduces the lateral bending stiffness of the posts so the fine mesh was necessary in the impact region due to the large deformations of those posts during impact.

The post was meshed with four-node QEPH shell elements. This type of element uses one Gauss quadrature numerical integration and five integration points through the element thickness. The material properties are illustrated in Table 5.2.

Table 5.2: Material properties for modeling guardrail post steel
(Wright, A. and Ray, M.H. 1996)

Material Properties	Value							
Density kg/m ³	7890							
Young modulus (GPa)	200							
Poisson's ratio	0.29							
Yield Stress (MPa)	336							
Strain (%)	0	0.024	0.042	0.057	0.141	0.213	0.250	1.00
Stress (MPa)	0.0	336	401	434	527	589	675	677

Plaxico (2002) recommended using more than three integration points through the thickness for the guardrail post to capture the stress profile through the thickness of the

elements. In fact, when a shell element is subjected to pure tension or compression, the stress and strain calculated at the point is uniform through the thickness of the element and the number of integration points is not important. On the other hand if a shell element is subjected to bending and might develop plastic strains, the number of integration points through the thickness plays a significant role in the accuracy of the results. If the number of integration points is reduced to three, the entire section might become plastic too early and the deflection will be overestimated (Plaxico 2002).

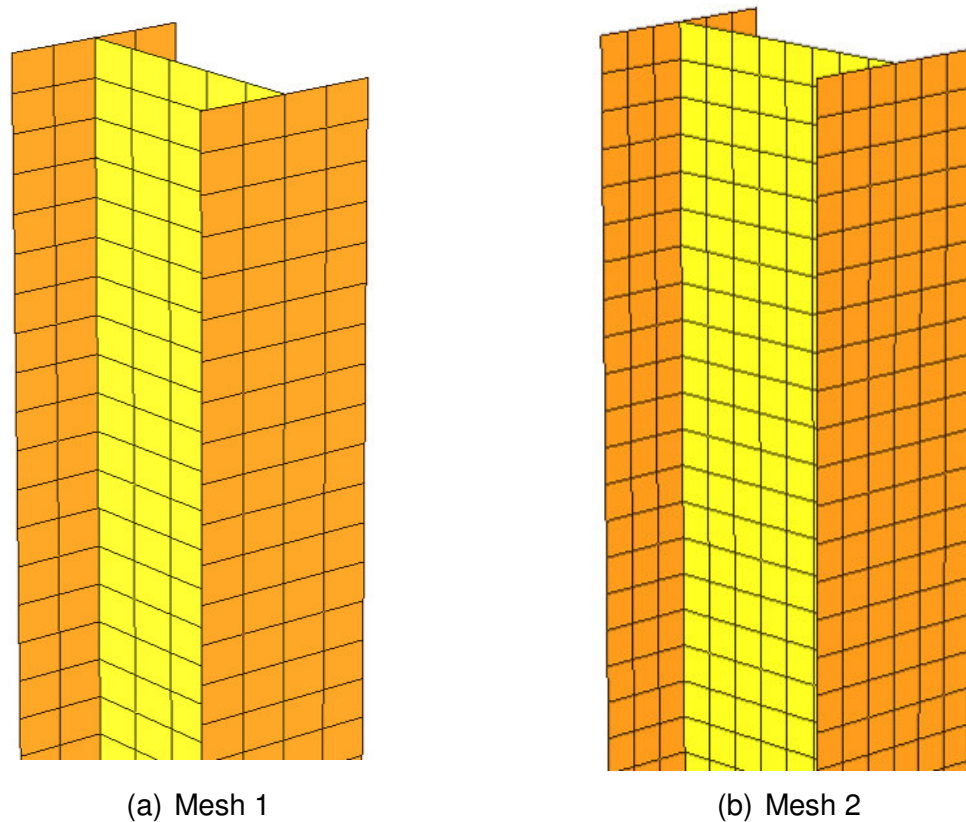


Figure 5.3: Finite Element meshing of the post guardrail

5.2.3. Soil-post interaction

The simulation of the soil-post interaction is very critical to assess the response of the guardrail and the vehicle during a lateral impact event. For the finite element analysis of the full guardrail model, two approaches are utilized as described in Chapter 3: the continuum finite element approach where the soil is modeled as solid elements; and the subgrade reaction approach where the post is attached to an array of springs representing the soil resistance. For the current study, the soil reaction was modeled as

a system of springs and dampers attached to concentrated masses using the subgrade method developed in section 3. In this approach, the soil is modeled as an array of unidirectional uncoupled nonlinear springs acting on both cross sections of each post at 100 mm. The stiffness of the springs is determined by the method proposed by Habibagaha and Langer (1984). The proposed approach accounts for the damping effect of the soil and the inertial effect generated by the soil mass which were ignored in previous studies. The soil mass surrounding the post was added as lumped mass and attached to the post to simulate the effect of the soil inertia. This approach ignores the torsional moment induced by the impactor about the axis of the post (about Z-direction). The torsional moment is the result of the non-coincidence of the centre of mass and the centre of rigidity because of the asymmetry of structure elements or uneven mass distribution (Canadian Geotechnical Society, 2006).

The post-soil interaction was validated with the dynamic impact test conducted by Coon et al. (1999) for test speeds of 4.6 m/s, 5.4 m/s, 5.9 m/s and 8.9 m/s. The soil density ranged from 1980 kg/m³ to 2240 kg/m³ and the length of the post was 1830 mm with an embedment of 1100mm. The point of impact of the bogie with the post was located at 550 mm above the ground level. Figure 5.4 illustrates the modelling of the post-soil interaction as discussed previously in Chapter III.

5.2.4. W beam rail to the post connections

The post guardrail is fastened to a W-beam with a M16 bolt going through the blackout and a slotted hole in the beam. The shear of the bolt and the loss of connection with the blackout were observed in many dynamic tests due to the high forces applied on the bolt. This behaviour is very important to simulate accurately the kinematics of the vehicle impacting the barrier and the post. In fact, if the connections between the post and the W-beam are too strong, the W-beam is most likely to follow the post during the impact and be pulled to the ground with the post which results in the errant vehicle overriding the guardrail. On the other hand, if these connections are too weak, the rail can be pulled away from the post under relative low force very early causing the separation of the post from the guardrail which allows the rail to drop and the vehicle to penetrate the system (Plaxico, 2002). Following Tabiei and Wu (2000) and Plaxico (2002), a spring with nonlinear load-deflection constitutive law is used to simulate the behaviour of the connection.

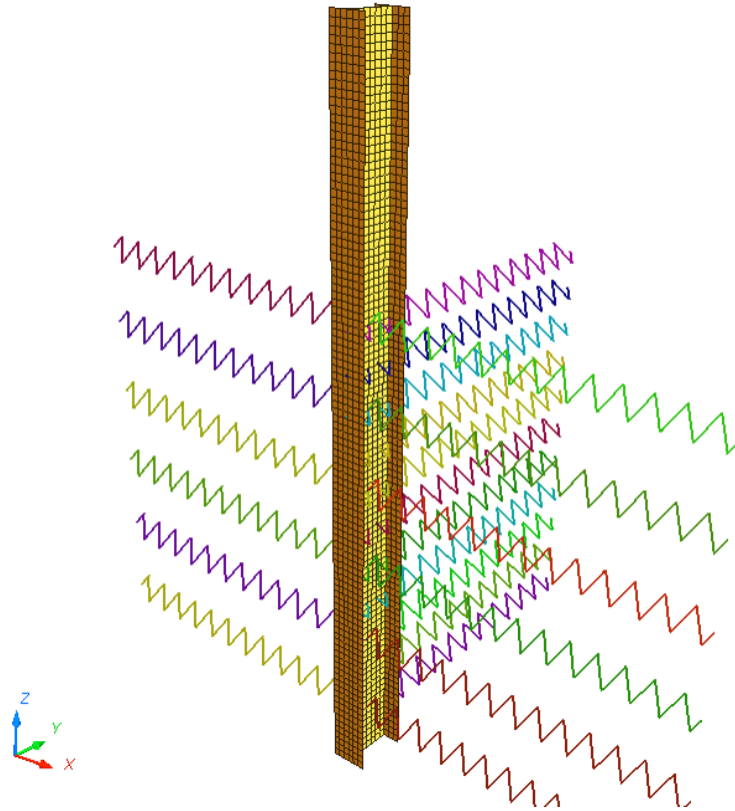


Figure 5.4: Subgrade modelling of the post-soil interaction

To determine the behaviour of the connection, Tabiei and Wu (2000) considered two cases of the bolt location. In the first case the bolt was located at the centre of the slot of the W-beam and in the second case the bolt was located at the edge of the slot. The test results from finite element simulations showed that the maximum forces required to pull the bolt through the beam was around 30 kN and 80 kN for the bolt at the centre and the edge respectively. Plaxico (2002) conducted quasi-static laboratory tests to estimate the beam/bolt connection using a 1780 kN capacity Tinius Olsen axial load testing machine. Four cases of loading were investigated:

- One layer of W-beam with the bolt positioned in the center of the slot in the W-beam.
- One layer of W-beam with the bolt positioned at the edge of the slot in the W-beam.
- Two layers of W-beams with the bolt positioned at the center of the slots in both sections.

- Two layers of W-beams with the bolt positioned at the edge of the slots in both sections.

The test results showed that the minimum pull-out force required to break the connection in case 1 has an average value of 18 kN whereas the maximum pull-through force in cases 2,3 and 4 has an average value of 28.7 kN, 41.0 kN and 64.7 kN which are close to the value determined by Tabiei and Wu (2000). For the current study, the nonlinear springs is the best approach to simulate the bolt connection and the force-deflection characteristics in the full finite element model are the obtained through component testing of Plaxico (2002) with no failure criteria.

5.2.5. Blockout modeling

The blockout could be made of solid block of wood or steel W-beam. For the case of wood, the blockout consists of parallelepiped with rectangular cross section (150 x 200 mm, height 360), modeled using 8-node hexahedron. To optimize the computing time, the blockout located in the area of impact were selected to have a Corotational formulation with eight integration points whereas the remaining blockout located in the non-impact zone close to the two ends of the guardrails, are modeled with a Corotational formulation with one point of integration. For the case of crushable blockout, similar formation as defined in Chapter IV is used.

5.2.6. Vehicle model development

A finite element model of the Chevrolet C-1500 pickup truck available from National Crash Analysis Center (NCAC) was used in this study representing the 2000P pickup truck. The model was developed to offer a simplified version of the detailed model to reduce time computation (Marzoughi et al., 2004). Although most of the parts of the reduced model were crudely modeled, it has been extensively used by many researchers; to list a few Bendidi (2002) Whitworth et al. (2004), Plaxico et al. (2002), Plaxico (2002) and Atahan (2002). The truck model contained approximately 62,300 nodes and 56,000 elements. In order to improve the quality of the truck model and to capture better kinematics of the interaction guardrail post with the truck, several modifications were implemented in this study:

- The quality of the model has been improved by cleaning the model from most of the penetration and the intersection.
- The four tires were re-meshed and the volume between the tires and the rim has been defined as monitored volume with a net internal pressure of 35 psi. This will improve the interaction of the tire with the ground.
- The front suspensions were upgraded to improve the response of the vehicle's dynamic behaviour during impact with barrier. Tiso (2002) showed that the implementation of the suspension to the C1500 Pickup Truck Finite Element Model gave more realistic vehicle kinematics. A detailed component of the front suspension has been integrated to the pickup model as shown in Figure 5.5.
- The impact side of the truck, directly in contact with the W-rail and the posts, was re-meshed with a finer mesh as shown in Figure 5.5.
- The element formulation of many parts has been changed and 5 integration points through the thickness were chosen.
- The overall weight of the truck was 2023, by adding 211 kg distributed over the model.

All these modifications were necessary to increase the accuracy of the finite element model in capturing the actual crash test performance of the guardrail system.

The model's accuracy has been improved by Zaouk et al. (1997) where several coupons from parts such as the engine cradle, fender, hood, bumper, rails, door and door frame were tested to obtain their properties. The pickup truck is regular-cab with a wheelbase of 334 cm, an overall length of 543.5 cm a weight of 2000 kg, close enough to the recommended properties of the 2000P truck as recommended in the NCHRP Report as shown in Table 5.3.

The available original model developed in LS-DYNA (Hallquist, 2006) model was converted to Radioss format. The conversion was done using Hypercrash software which is able keep the geometry, the thickness, the rigid bodies, and to convert the material properties defined as piecewise elastic-plastic (LAW24) in LS-DYNA to the equivalent material (LAW36) in Radioss. A review of the different parts (connectivity, mass, gravity, added mass) is necessary to assure that the finite element model is accurate and representative to the vehicle. The shell formulation was converted to the

default shell formulation in Radioss so it has changed to QEPH formulation as stated before due to its computation efficiency and control of the hourglass energy.

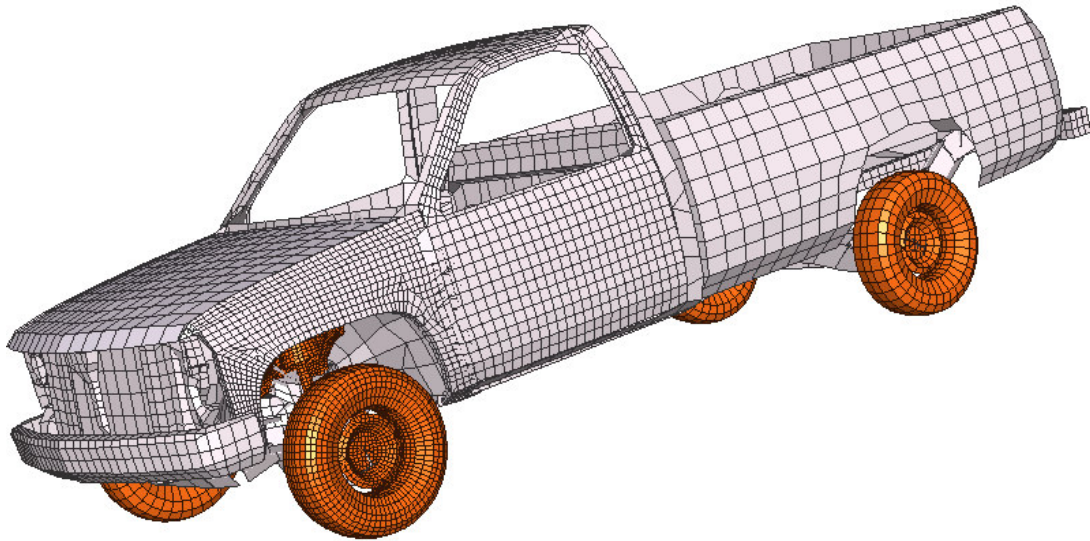


Figure 5.5: Detailed finite element model of pickup C1500

Table 5.3: Comparison of the C1500 between the NHTSA test and simulation model

Parameters	Finite Element Model	NHTSA test
Overall weight (kg)	2023	2023
Wheelbase (mm)	3382	3340
Total length of the vehicle at CL (mm)	5428	5428
Ride height measured at wheel house		825/888
CG in the X direction (mm)	1430	1557
Engine Type	V6 4.3 L	V6 4.3 L
Weight split Front (%)		53.4

5.3. Validation of the Pickup Truck Model

5.3.1 Full frontal crash testing

To validate the truck model, a full front test vehicle conducted by NHTSA (National Highway Traffic Safety Administration) on Chevrolet C1500 pickup was used. The vehicle was equipped with a 4.3 litre inline engine, an automatic transmission, power steering and power brakes. The 56 km/h frontal barrier impact test is part of the New Car Assessment Program (NCAP) conducted for the National Highway Traffic Safety Administration (NHTSA) in August 1992. The test was conducted under contract No DTNH22-90-22121. The test consists of hitting the vehicle against a rigid barrier and recording the dummies' injury data parameters on the driver and passenger sides. The vehicle's test weight was 2023 kg and the Vehicle impact speed was 55.8 kph. The vehicle was instrumented with 9 accelerometers located in different strategic points in the vehicle to measure the vehicle longitudinal axis accelerations. The accelerometers located at the rear seat cross members was used to calculate the vehicle response.

The response of the occupant is related to the vehicle kinematics and structure response, commonly referred to as the crash pulse. The crash pulse could be defined as the basic characteristic of a vehicle response in crash testing simulation (Huang 2002). The pulse is identified by installing an accelerometer on the rocker at the B-Pillar or by calculating the load applied on the rigid wall. The data recorded by the accelerometers and the load cells, referred to as wideband data were filtered through digital filtering technique to remove the noise recorded and obtain useful signals.

Figure 5.6 shows the force applied by the pickup truck on the rigid wall for the test conducted by NHTSA compared to the finite element simulation. The rigid wall of NHTSA test was instrumented by a set of loadcells covering the area of the impact and the test force was calculated by adding the force recorded the loadcells. For the simulation, the impact force is recorded as an input of the rigid wall. A good agreement could be noticed between the two pulses indicating that the model is capturing the kinematics and the reaction of the vehicle accurately in the frontal crash of the truck against a rigid barrier. The two curves show similar behaviour. The first peak represents the load applied by the two rails which reached a load of approximately 400 kN for the two cases. The second peak represents the impact of the engine against the wall which

results in a spike of the engine deceleration time history and force recorded by the front barrier. The two peaks occurred at a similar time 15 ms and 50 ms indicating a good agreement between the simulation and the NHTSA test results.

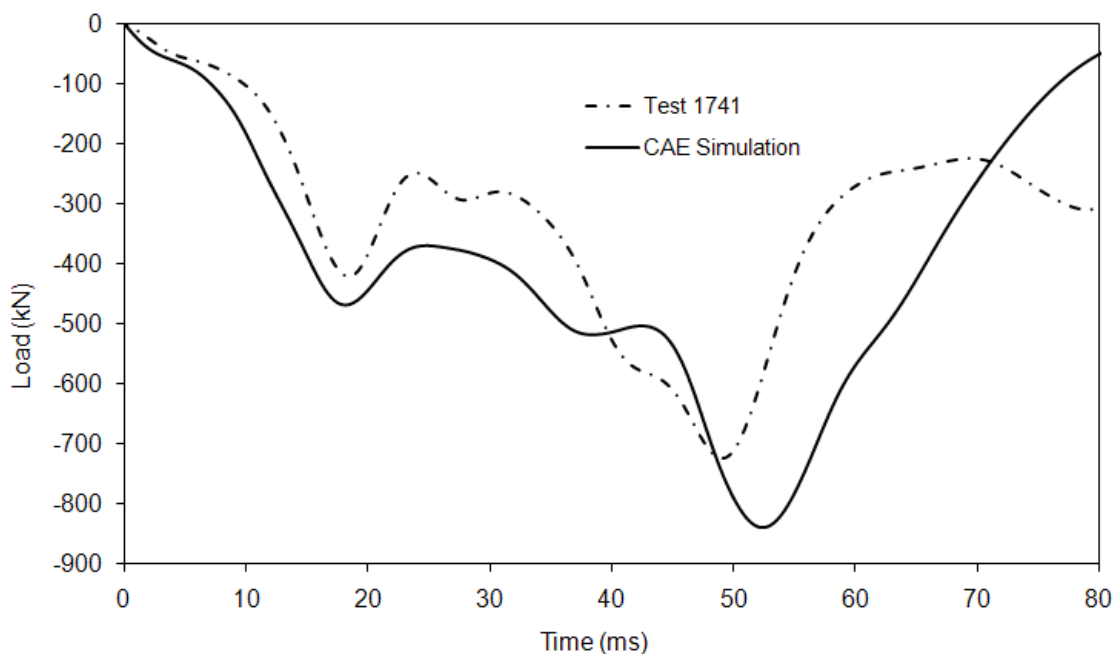


Figure 5.6: Load cell force time histories at front barrier of the NHTSA test and the Finite element simulation

Another useful datum to compare is the engine deceleration time history. In fact, during the full front crash, the engine block running initially with the same speed of the vehicle 56 km/h get stopped against the wall resulting in high peak in the deceleration time history curve. The C1500 truck NHTSA test was instrumented with two accelerometers at the top and bottom of the engine block. The experimental deceleration curves were compared to the finite element simulation results and shown in Figure 5.7.

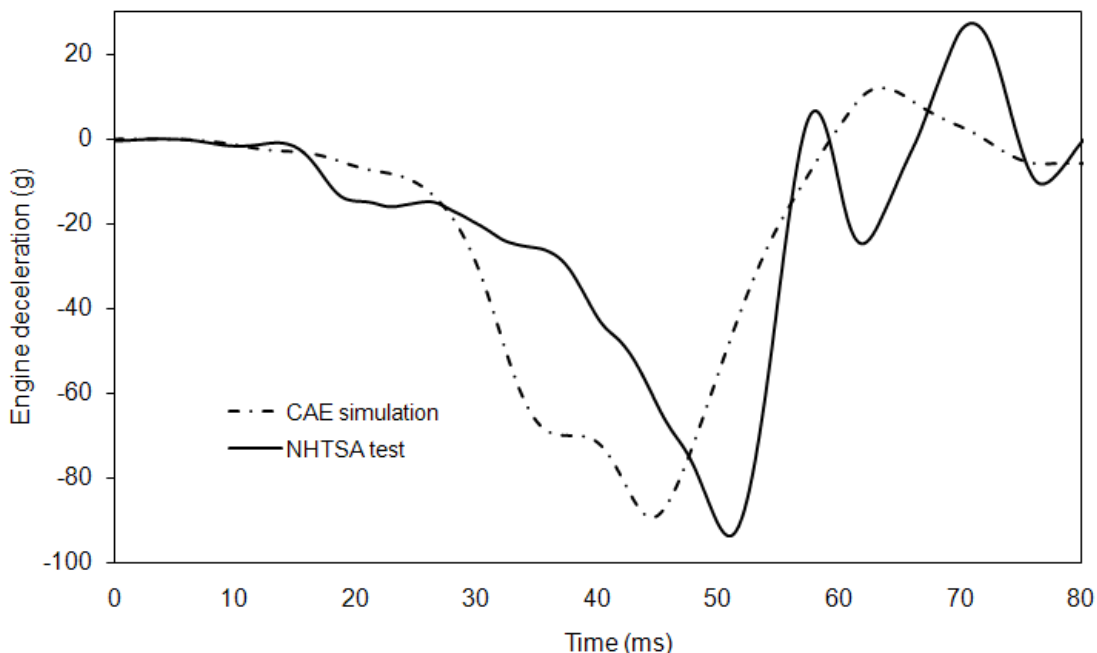


Figure 5.7: Engine deceleration time histories for NHTSA test and the finite element simulation

Figure 5.8 illustrates an overview comparison of the vehicle post crash between the finite element simulation and the dynamic test. No video is available in the NHTSA website to compare the crash test during the impact and have a better qualitative comparison. Thus, we are limited to the post crash pictures. The two tests show that the frame of the underbody structure bends in the two cases and the vehicle exhibits a similar pitch and drops. The hood buckles and the lateral crush lines have similar shapes. The post crash visual inspection shows an acceptable agreement between the finite element simulation and the NHTSA crash test.

5.3.2 Validation of the truck model in side crash

A side angular test was conducted on a Chevrolet pickup C1500 travelling with a speed of 100 km/h and an angle of 25 degrees against a 107 cm (42 inches) vertical block of New Jersey Concrete barrier. Since the dynamic test was conducted with C2500 pickup truck instead of C1500 pickup truck used in the simulation, an adjustment of 300 kg has been adopted in the simulation model to reflect the weight difference between the V8 5.7 L and V6 4.3 L. Table 5.4 summarizes the test data.

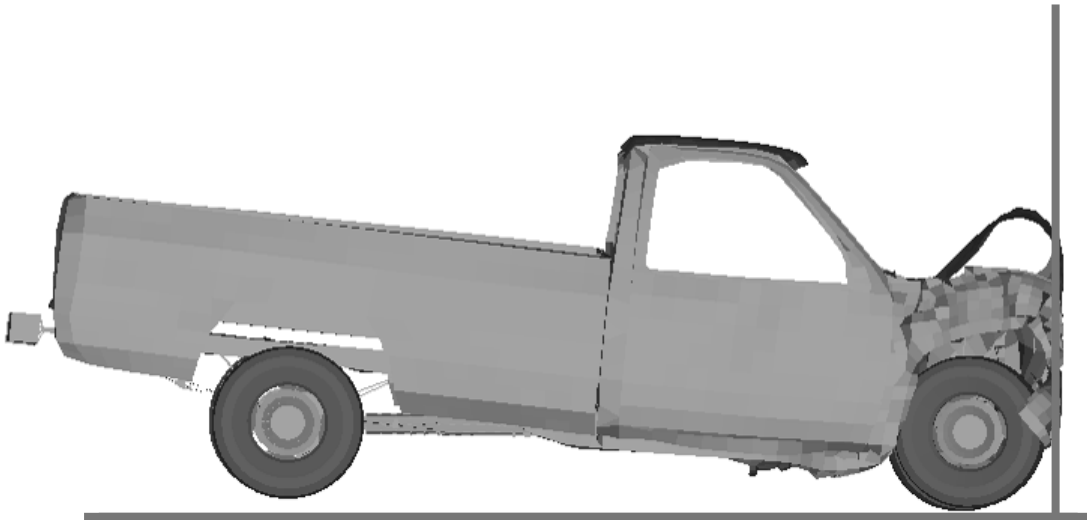
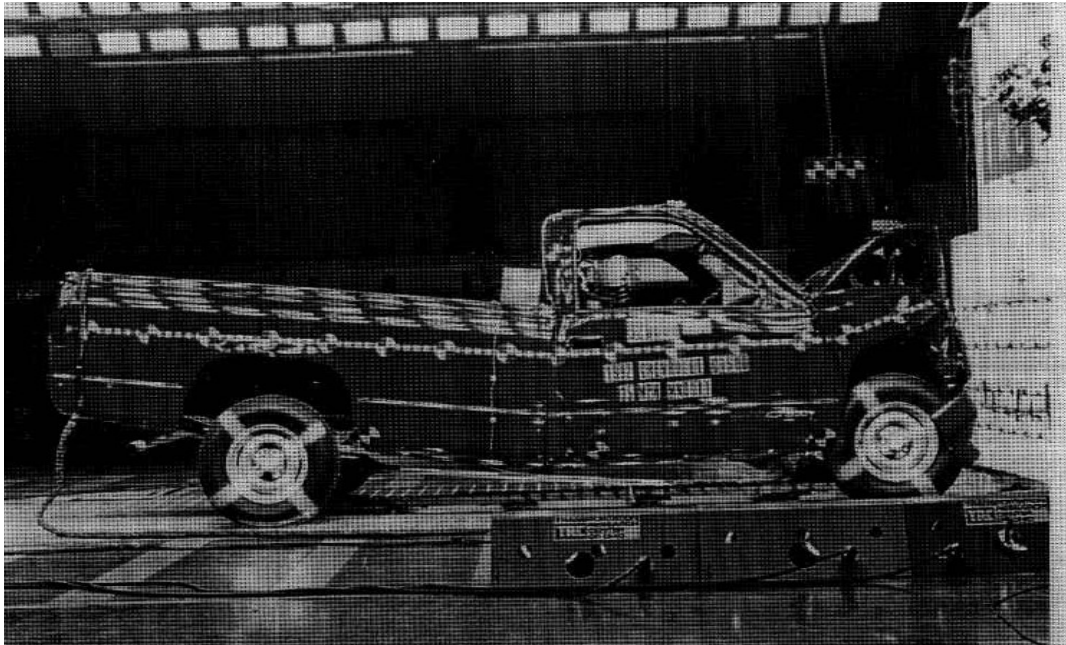


Figure 5.8: Comparison of the vehicle C1500 after crash for the NHTSA test and the finite element simulation.

Table 5.4: Description of the impact of C2500 truck against the barrier concrete

Test Number	DTFH61-95-C00136
Test date	October 19, 1995
Vehicle type	Chevrolet C2500
Engine type	V8 capacity 5.7 L
Transmission Type	Automatic
Vehicle speed	100 km/h
Angle of impact	25°

Figure 5.9 and Figure 5.10 show four snapshots from the sequences of the impact test taken from two views: a top view taken from a camera attached to a pillar mounted on the truck and the second is a front view captured by a camera on the ground and aligned with the concrete barrier. The sequences of the view covered a range of time from initial state to time where the truck was stopped. Figure 5.9 shows that the vehicle impacted the concrete barrier at $t=0$ then the right corner of the front bumper hits the barrier and the right front tire starts to climb the lower part of the barrier. At time $t = 120$ ms, the dynamic test and the simulation show that the pickup truck angle of impact starts to be reduced and the truck is aligned parallel to the barrier at 225 ms.

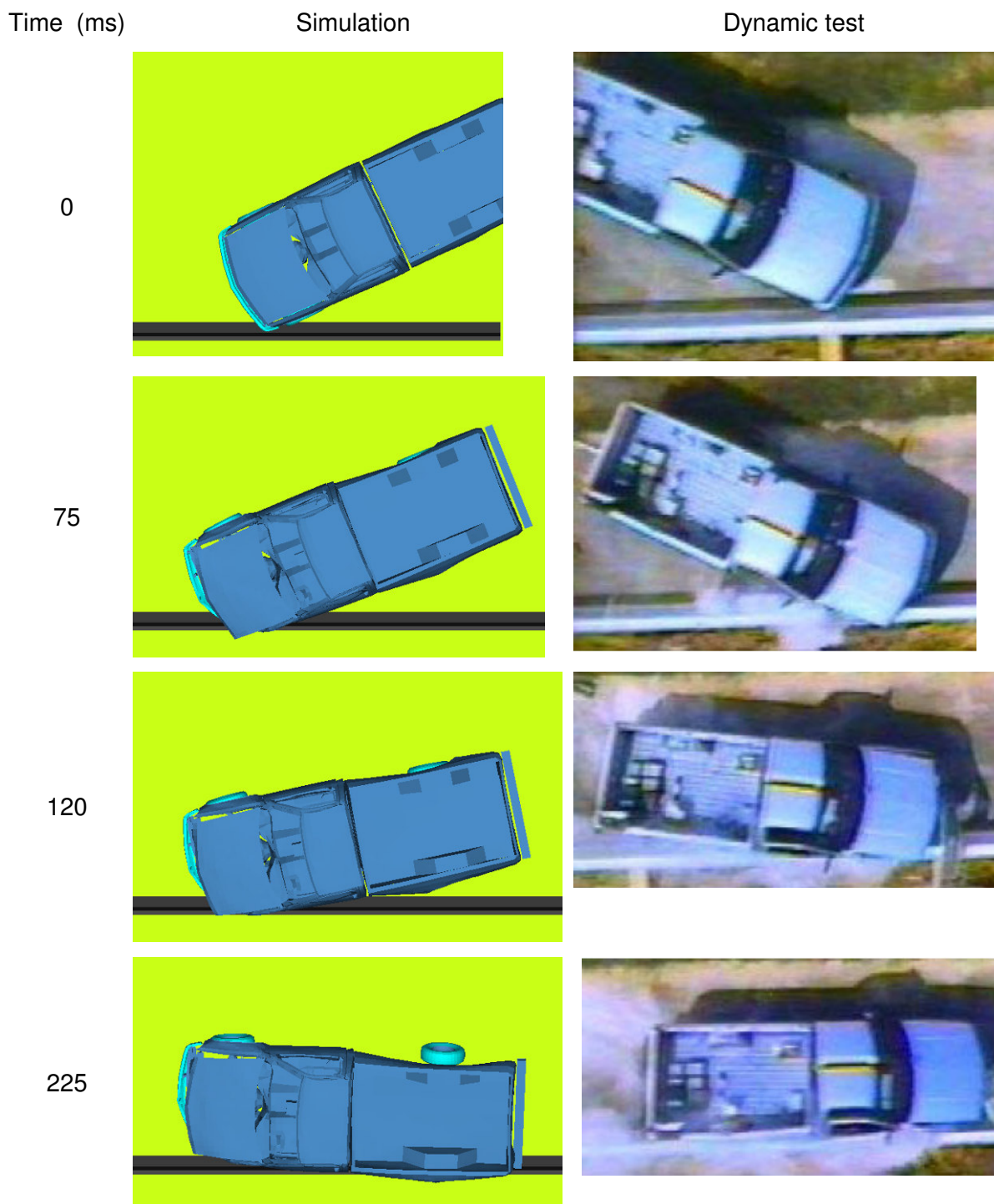


Figure 5.9: Sequential overhead of impact event of NHTSA test and finite element simulation

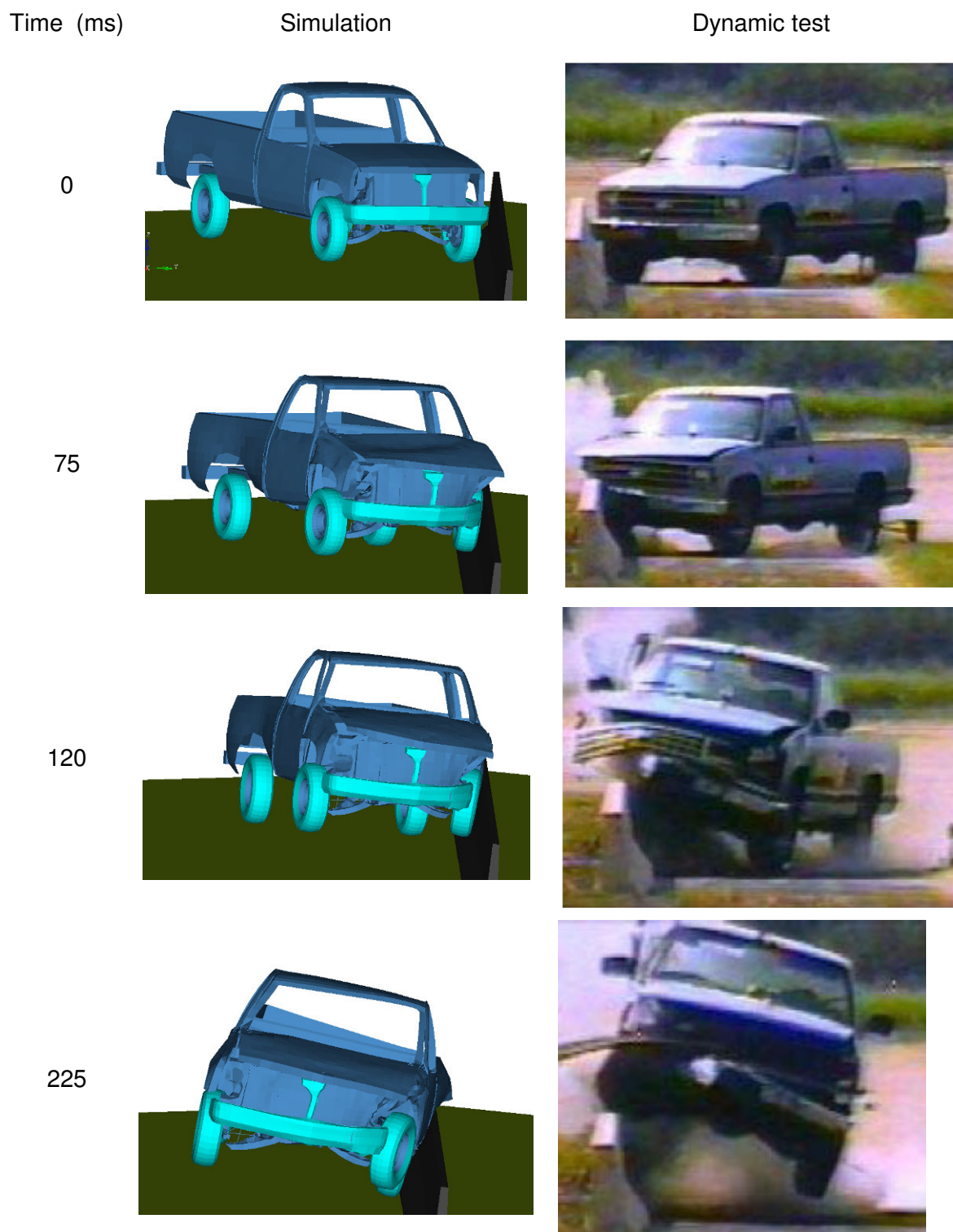
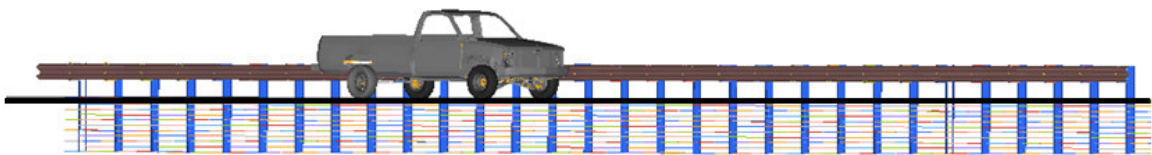


Figure 5.10: Sequential frontal view of impact event of NHTSA test and finite element simulation

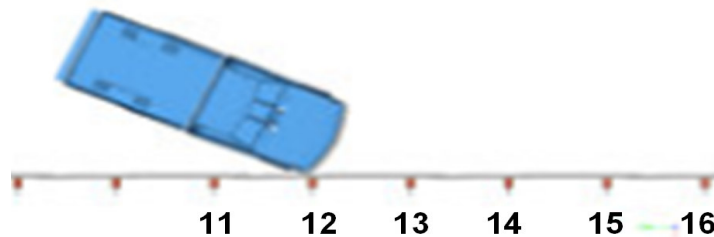
5.4. Impact of the Pickup with the Guardrail System: Baseline Model

5.4.1 Full Scale finite element model

A finite element model consisting of a guardrail system with wood blockouts and impacted by Chevrolet pickup truck C1500 was developed using the methodology illustrated in section 5.3. The model consists of 30 posts spaced at 1.905 m embedded at a depth of 1.100 m and connected to guardrail W-beams of a length of 3.810 m. The post is connected to a series of springs to simulate the soil reaction. The guardrail rails are joined with bolts simulated as rigid connections since no failure occurred between the rails. Figure 5.11 illustrated the position of the pickup truck with regards to the guardrail system.



(a)



(b)

Figure 5.11: Finite element model of pickup truck impacting the guardrail system (a) Side view, (b) top view.

The impact of the pickup created a lateral load which is carried in part by the tension in the guardrail. This tension force pulled the guardrails at its ends therefore an accurate

modeling of the end constraints of the rail is required. The response of a guardrail system to impact is sensitive to end constraints of the rail and the stiffness of the ends could serve as parameter data to calibrate the full-scale test. For the current case, the ends consisted of Modified Eccentric Loader Terminal (MELT) ends where the displacements Subgrade modelling of the post-soil interaction are in general very limited. The MELT Terminals are designed to prevent the end rail spearing an errant vehicle. The end of the MELT is curved away from the traffic face and a buffered end section is installed to prevent spearing, the rails were selected to be constrained in displacement at the two ends.

The truck was positioned at the post # 14 and let to impact the guardrail beam at an angle of 25° . The parameters of the soil used in the study replicate the test conditions of the test conducted by the Texas Transportation Institute (TTI) on November 16, 1995 (Test 405421-1). The test consisted of a guardrail with a total length of 53.3 m and impacted at the post# 12 with a Chevrolet pickup traveling at a speed of 101 km/h and an angle of 25.5° . The guardrail has a central portion 30.5 m long with W-beam guardrail system and two, 11.4 m long MELT terminals at both ends. The finite element test was conducted over 800 ms duration.

5.4.2 Comparison between finite element simulation and full-scale crash test

In order to compare the performance of the finite element simulation with the full-scale dynamic test conducted by TTI, the speed of the truck during the impact, the roll, yaw and the pitch angles are calculated and the pictures at different time instances have been taken.

Figure 5.12 shows a comparison of the speed time history of the simulations and the dynamic tests. It can be noticed that the two curves present a small plateau for the first 20 ms then decrease almost linearly from the speed of 101 km/h to 60 km/h at 300 ms. The simulation shows that the pickup truck is exiting the guardrail system with slightly higher speed than in dynamic test. Overall, the simulation is capturing accurately the deceleration of the pickup.

Figure 5.13 shows the roll angle of the vehicle traced over the centre of the gravity. The roll angle is defined as the angle measured from the horizontal axis (x axis) of the vehicle which could be visualized as the difference in level between the tires of the same axle. The roll angle is calculated at the centre of the vehicle and compared to the dynamic test. Figure 5.13 shows that the finite element simulation captures the kinematics of the vehicle and have similar behaviour especially after 250 ms. The roll angle of the simulation and the full-scale test presents two humps where the first occurred between 0 to 280 ms and the second from 280 ms to 600 ms. The maximum roll angle for both cases was approximately 11° occurring at 500 ms.

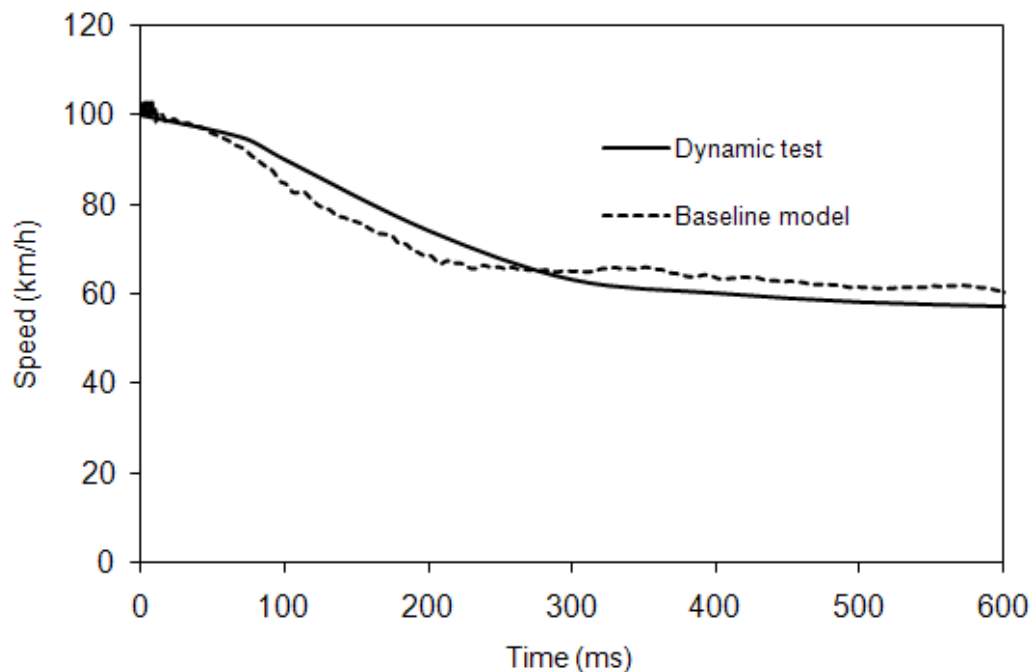


Figure 5.12: Velocity-time history at the C.G. of the vehicle for the dynamic test and the finite element analysis

Figures 5.14 and 5.15 show a sequential view of the impact for the finite element and the dynamic test taken from different angle: frontal, side and overhead. From these views, the finite element shows a good agreement with the dynamic test in terms of vehicle position with regards to the guardrail and interaction with the barrier.

The Finite element simulation shows the pickup located in the front of the guardrail barrier at time 0 ms. The vehicle impacted the guardrail at the speed of 101 km/h and angle of 25.5° . The front bumper is the first component that impacted the guardrail and started to deform at 40 ms. The left tire contacted the post # 13 at 90 ms and the post # 14 at 180 ms. The tire started to deform and the left fender shows severe deformation after 170 ms. The vehicle became totally aligned with the guardrail with a intrusion of 525 mm at time of 250 ms. The speed is reduced to 60.5 km/h and the roll angle to 8.5° . At 360 ms the pickup started exiting with a constant speed of 60 km/h and an exit angle of 18° .

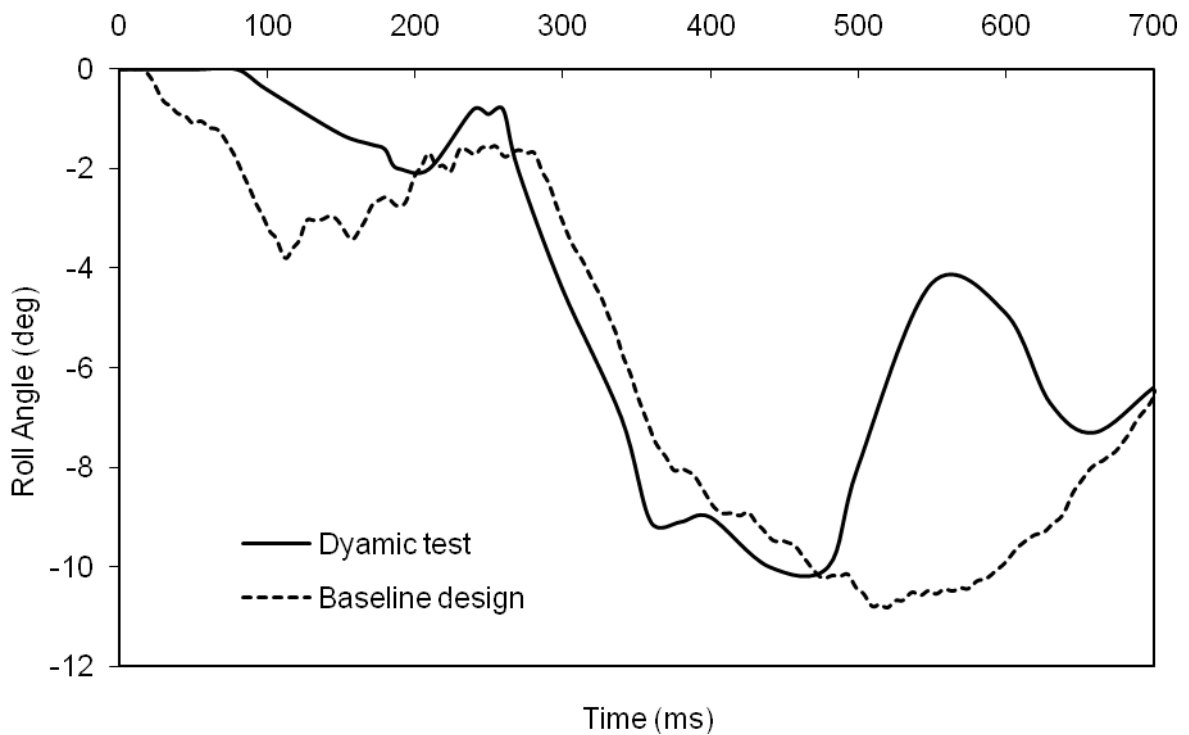


Figure 5.13: Roll angle displacement-time history at the C.G of the vehicle for the dynamic test and the finite element analysis

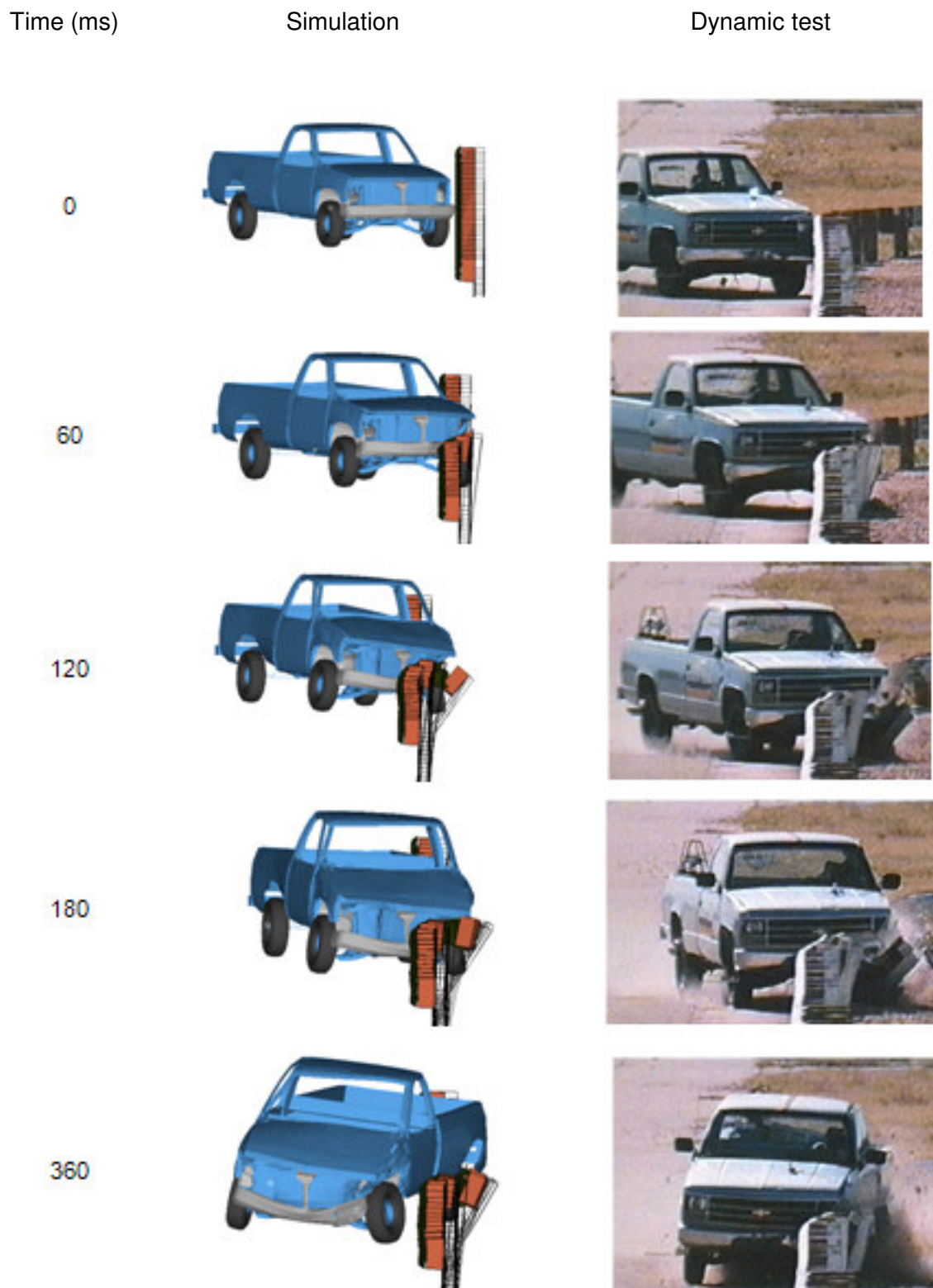


Figure 5.14 Sequential frontal view of impact event of NHTSA test and finite element simulation

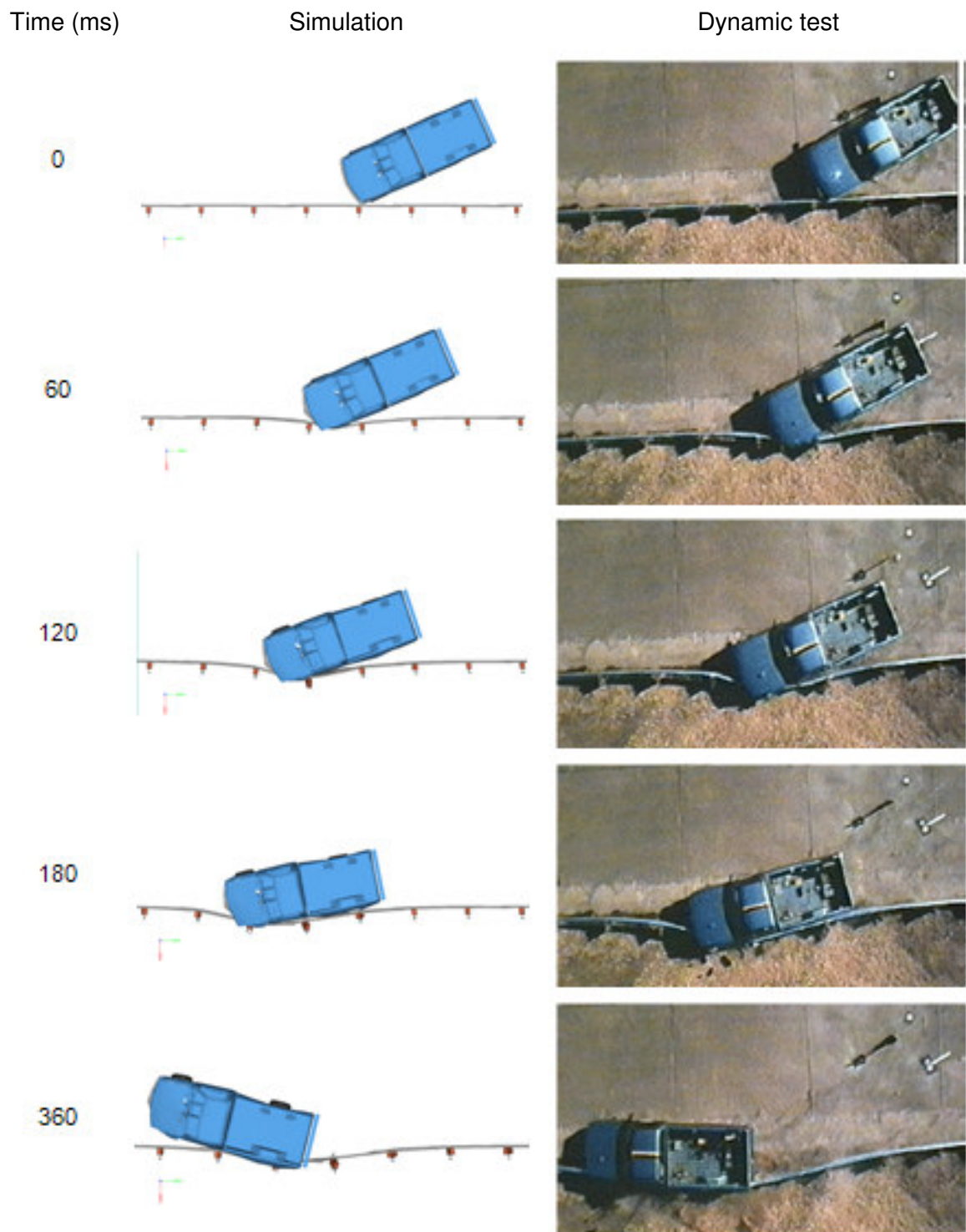


Figure 5.15 Sequential overhead of impact event of dynamic test and finite element simulation

5.4.3 Results of the base model and analysis

The pickup impacted the guardrail with an initial angle of 25° . During the impact the angle of the pickup and the guardrail was reduced to reach approximately zero at 250 ms where the vehicle became parallel to the guardrail. The component of the force perpendicular to guardrail beam is created by the impact force of the truck and by the friction of the vehicle against the guardrail. This force acts on the guardrail and induces the post deflections in the longitudinal and transversal direction are plotted in Figure 5.16 and 5.17. Only for the posts involved in the crash event, post # 11 to post # 16, are considered the main posts responsible for the guardrail system reaction. The curves show that post # 11 and post # 16 deflections are lower than 50 mm whereas post # 12 and post # 15 are more involved and the maximum post deflection is about 160 mm. The major reaction of the posts came mainly from post # 13 and post # 14 located in front of the truck where the deflections in the longitudinal direction were 650 mm and 620 mm in the longitudinal (X) direction respectively.

The speeds of the impact in the longitudinal and transversal direction of post #13 and #14 are plotted in Figure 5.18. It can be seen that the post # 13 reaches a speed value of 16.8 m/s and 16.6 m/s in the x and y directions and the post # 14 reaches a peak value of 8.8 m/s and 10.6 m/s in the X (longitudinal) and Y (Transversal) directions. These speeds are found to be higher than the speed used in the component testing where the speed remains in general under 10 m/s as discussed in section 4.3.1. Figure 5.16 shows that post # 13 deflected about 200 mm at the time of 80 ms, time of contact with the left tire and Figure 5.19 shows that the blockout and the cross section of the post didn't remain normal to the x direction as in the initial state and as in the component testing which is suggesting that speed is not representative of the component testing.

The initial speed of 100 km/h of full-scale testing could be decomposed in two components: the normal component to the guardrail is equal to 42 km/h (11.6 m/s) and the tangential component of 91 km/h (25.2 m/s). At time of contact with post #13, the speed was reduced to 90 km/h as shown in Figure 5.12 and the angle of impact is reduced from 25° to 20° . These new conditions of loading could be decomposed in two components: one normal component of 31.4 km/h (8.7 m/s) and a tangential component of 86.4 km/h (24.0 m/s). These conditions are not reproduced when compared to the test

of a single post with an impactor which seems unable to reflect the condition of the full-scale testing in terms of speed and boundary conditions.

The force generated at the interface of the post guardrail is plotted in Figure 5.20. Post #12 shows that the force level reaches 120 kN whereas the other posts are barely loaded. This level of force is approximately two times greater than the force recorded in the test. This level of force is due to the rotation of the blockout before the impact with the pickup.

The predicted roll angle when compared to the full-scale test results shows overall good agreement with some discrepancies at the beginning of the test (0-100 ms) and between (500-600 ms) as shown in Figure 5.13. It is important to mention that the mesh truck model study is coarse and many important parts are not included. At the same time, if two identical full-scale tests are conducted with the same test conditions, it is very unlikely that the results in term of crash pulse or structure response or occupant injury values be identical. This variability in testing is due to the existence of many uncontrollable variables

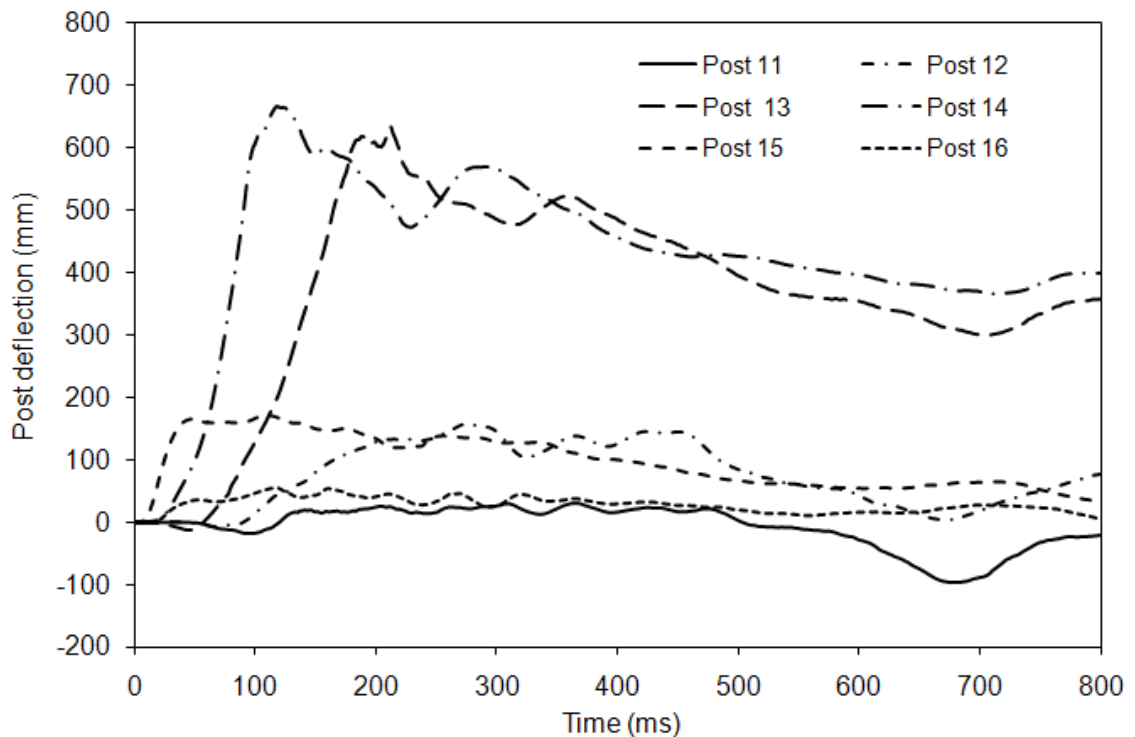


Figure 5.16: Post deflections of the guardrail system in the longitudinal axis (X) during the pickup impact

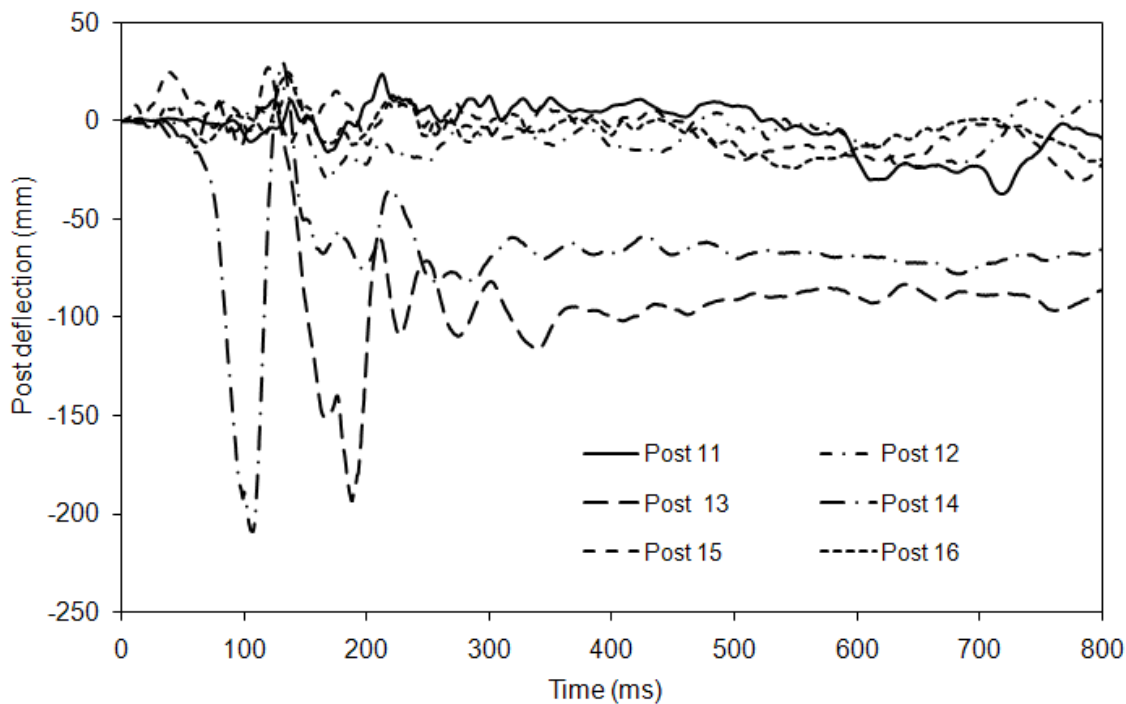


Figure 5.17: Post deflections of the guardrail system in the transversal axis (Y) during the pickup impact

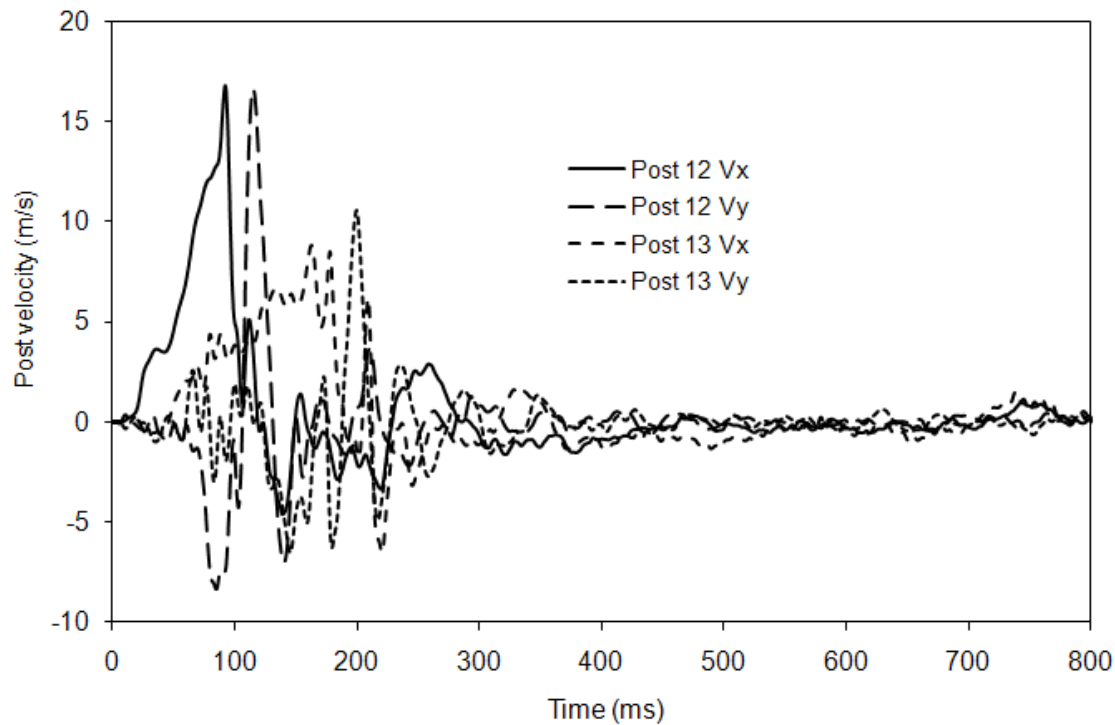


Figure 5.18: Speed of the posts in the longitudinal and transversal axis during the pickup impact

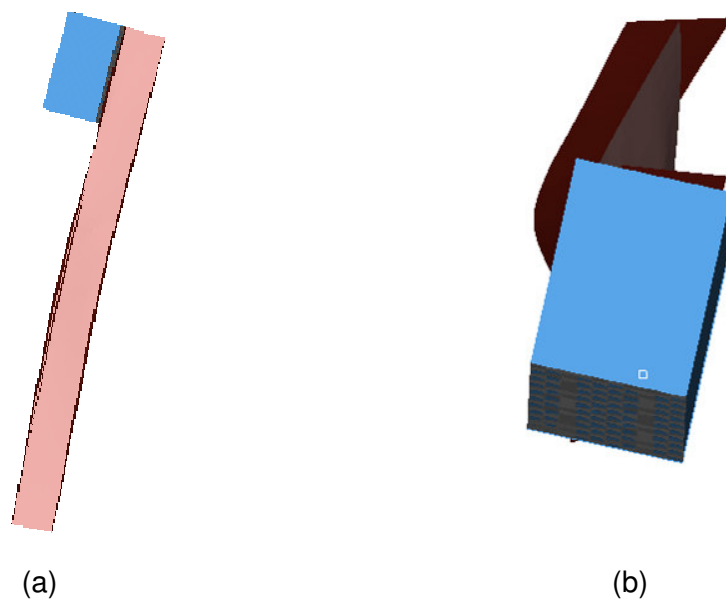


Figure 5.19: a) Side view of post # 13 at 80 ms. b) Top view of the post #13 at 80 ms

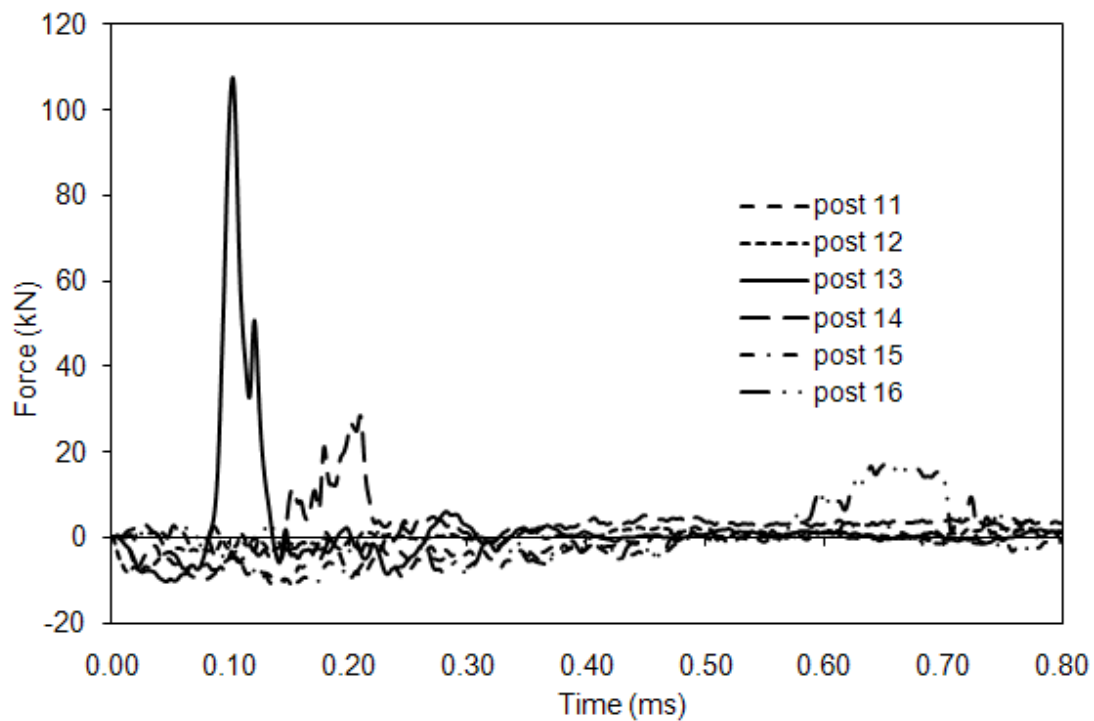


Figure 5.20: Force applied on the posts during the crash event of the full scale crush test

5.4.4 Results of the base model with crushable blackout

The full-scale model was built by implementing a crushable blackout on the posts. Only six posts located at the vicinity to the pickup truck and judged to be involved in the impact have the blackout replaced while the other posts remain with the same configuration because the effect of the impact on them is marginal. The crushable system, as described earlier in Chapter 4, consists of 3 square tubes of 60x60 mm cross section and a wall thickness of 2 mm. The side length of the enclosed square section was 150 mm as illustrated in Figure 4.17. The pickup truck impacted the guardrail with speed of 100 km/h and an initial impact angle of 25° at the same location of the base model and the impact was conducted up to 800 ms.

As it can be noticed from Figure 5.21, the pickup was redirected safely for the guardrail system with the crushable blackout and exited the guardrail at 370 ms traveling at a speed of 53.3 km/h at an angle of 16.6 degrees. Figure 5.22 shows a comparison of the pickup speed obtained by finite element model including the compressible system and the base model. It can be seen that the speed of the pickup is reduced for the case of the compressible blackout from 61.4 km/h to 53.5 km/h. The roll angular displacement time history of the vehicle model is plotted as in Figure 5.23. The roll angle is reduced from a maximum of 10° for the base model to 5° for the crushable system, which represents a net improvement for the safety and stability of the truck. This improvement in the truck stability is due mainly to the energy absorbed by the guardrail system which has become more compliant with the implementation of the compressible blackout. Similar results were obtained by Elmarakbi et al. (2005) who conducted a finite-element to evaluate a circular and hexagonal distance spacers made of steel and aluminum materials. It was found that the hexagonal spacers made of aluminum material absorbed more energy than other proposed designs which would reduce the deformation of the vehicle and enhanced vehicle occupant. Vasenjek and Ren (2007) found that the hexagonal distance space provided the highest level of the crash energy absorption because of its geometry which assures him a controllable deformation.

Figure 5.24 shows the blackout of posts # 12 to #15. It can be concluded that post #12 was not loaded and the blackout kept its integrity. The blockouts of post # 13 to post #14 are completely crushed following the folds initiated by the triggers in the tubes. Since more crushing was developed in the guardrail system, more intrusion of the pickup truck

into the barrier was developed as the vehicle was able to be more in contact with the post. The benefit of reducing the speed and the roll angle has been counterbalanced by the danger of the wheel snagging noticed in posts # 12, 13 and post 14 whereas the problem snagging was limited to only the post #13 for the case of the baseline simulation. The displacements in the X (longitudinal) and Y (transversal) directions are plotted for the post #13 and 14 compared to the baseline model and shown in Figure 5.25 and Figure 5.26.

It can be seen that the post # 13 for the case of the crushable blockout shows more longitudinal and lateral deflections than the baseline model. Post # 14 shows more deflection in the Y direction due to the impact with the front tire. In order to check the development of tearing in the guardrail, the plastic strain is calculated for both models with and without crushable system. Plastic strain is used as an indicator of failure of the guardrail since it is a measure of the cumulative material damage to the material (Engstrand 2000). Radioss software can include the plastic strain as failure condition for the element of the model. When the effective plastic strain of the element reaches a certain value, the stress is set to be null and the element is removed from the part. For the current full-scale study, no failure condition was included to be able to monitor the area of stress concentration and identify the location of a possible tear.

The analysis of the finite element baseline model shows that the maximum plastic strain reaches 18.0 % for element 82651 located close to post # 13 as shown in Figure 5.27. The high strain occurred when the guardrail is dragged up against the sharp edge of the blockout. Similar observation was reported by Engstrand (2000) who found that during the full-scale test and the simulation, a tear at the lower edge of the rail is developed. The full-scale simulation revealed that the nick was created when the rail was dragged up against the post over the sharp flange of the top of the twisted post.

The simulation of the full-scale with crushable blockout shows that the maximum plastic strain didn't exceed 10.56% recorded at element 83156, as illustrated in Figure 5.28, located close to the post # 13. This result is showing that the guardrail with the crushable blockout is more protected against the tearing and offer better performance than the baseline model. This improvement is due to the energy dissipation through the blockout that reduces the energy absorbed by the guardrail and the severity of the impact.

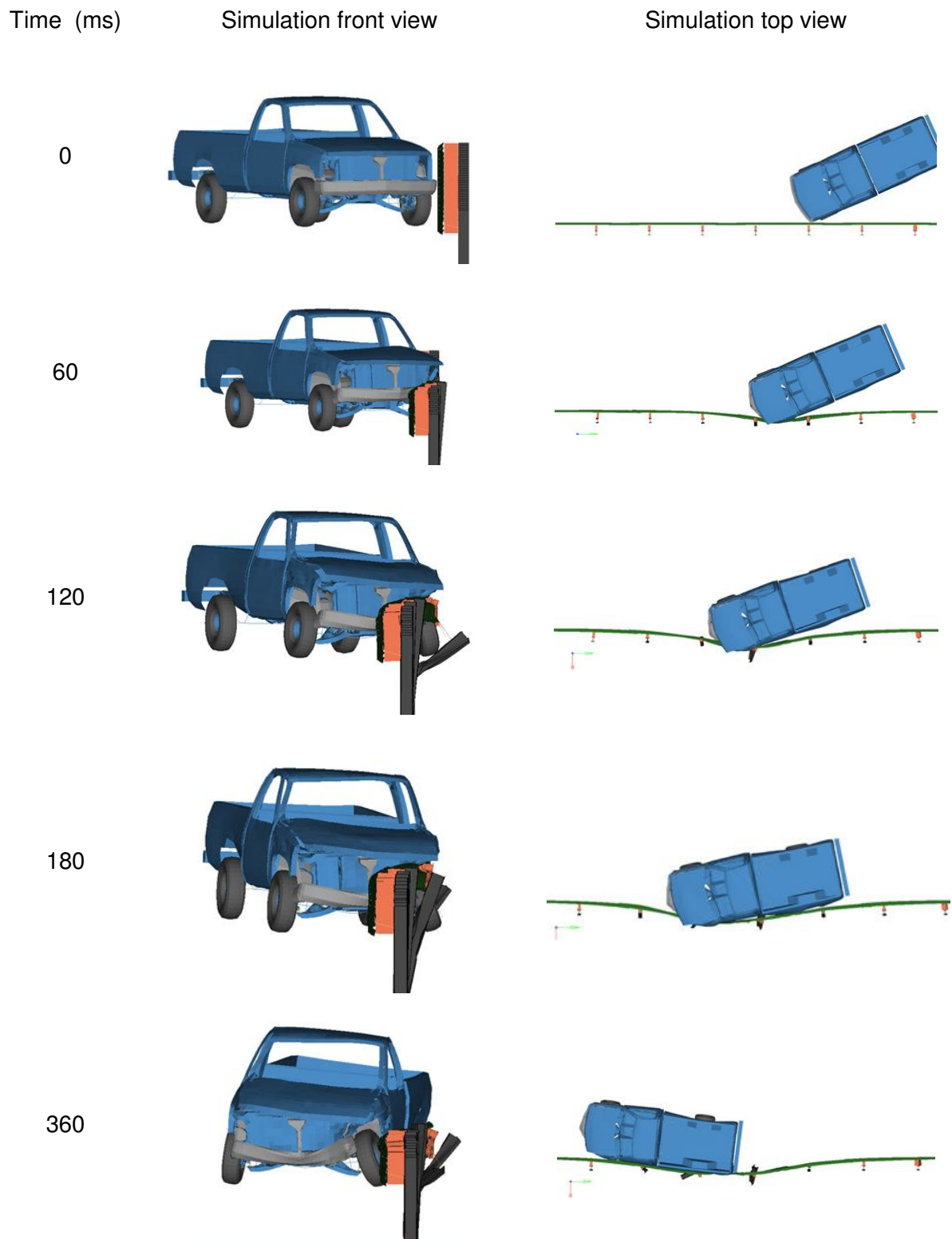


Figure 5.21: Sequential frontal and side views of the finite element simulation of the C1500 impacting the guardrail system with crushable blockout

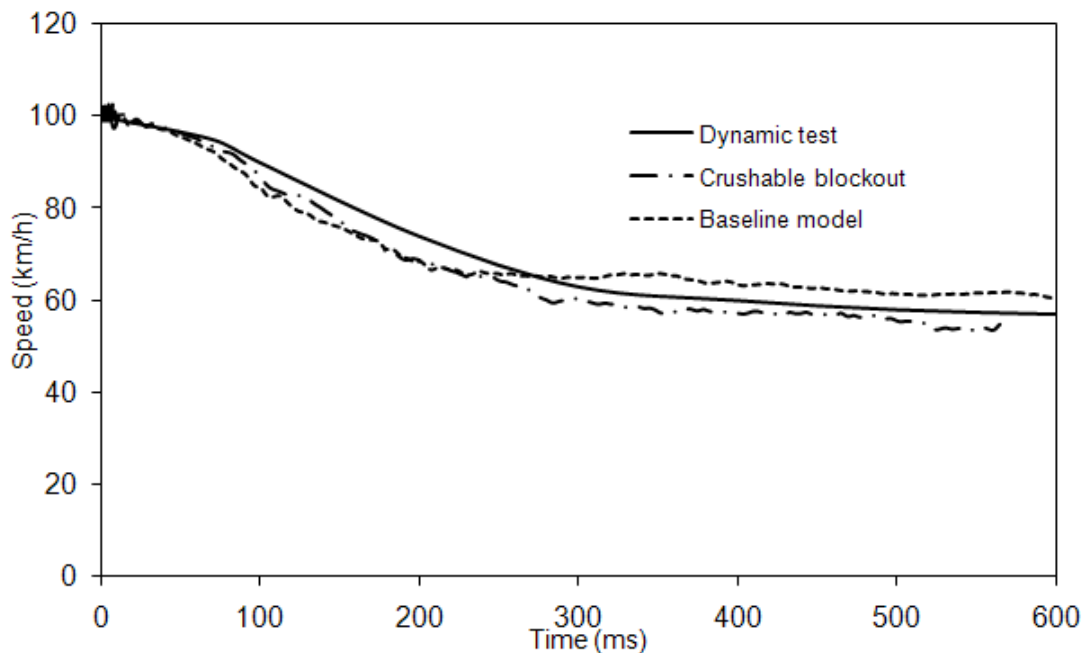


Figure 5.22: Velocity time-history at the C.G. of the vehicle for the dynamic test and the finite element analysis for crushable un-crushable blackout

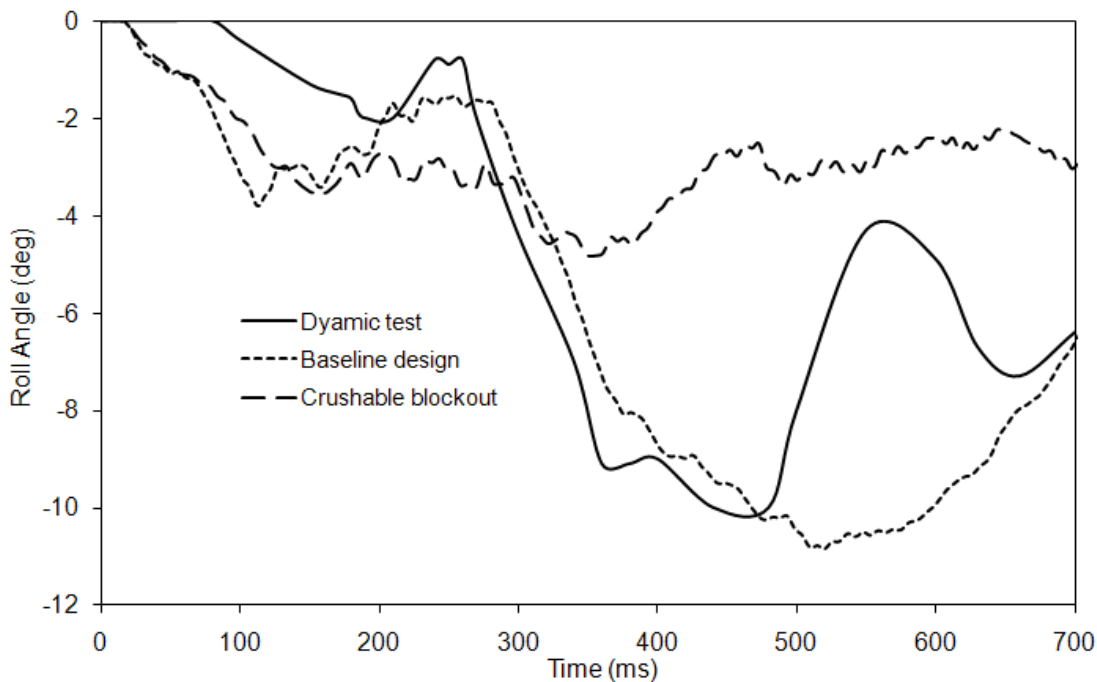


Figure 5.23: Roll angle as function of time history at the C.G of the vehicle for the dynamic test and the finite element analysis for crushable and non-crushable blackout

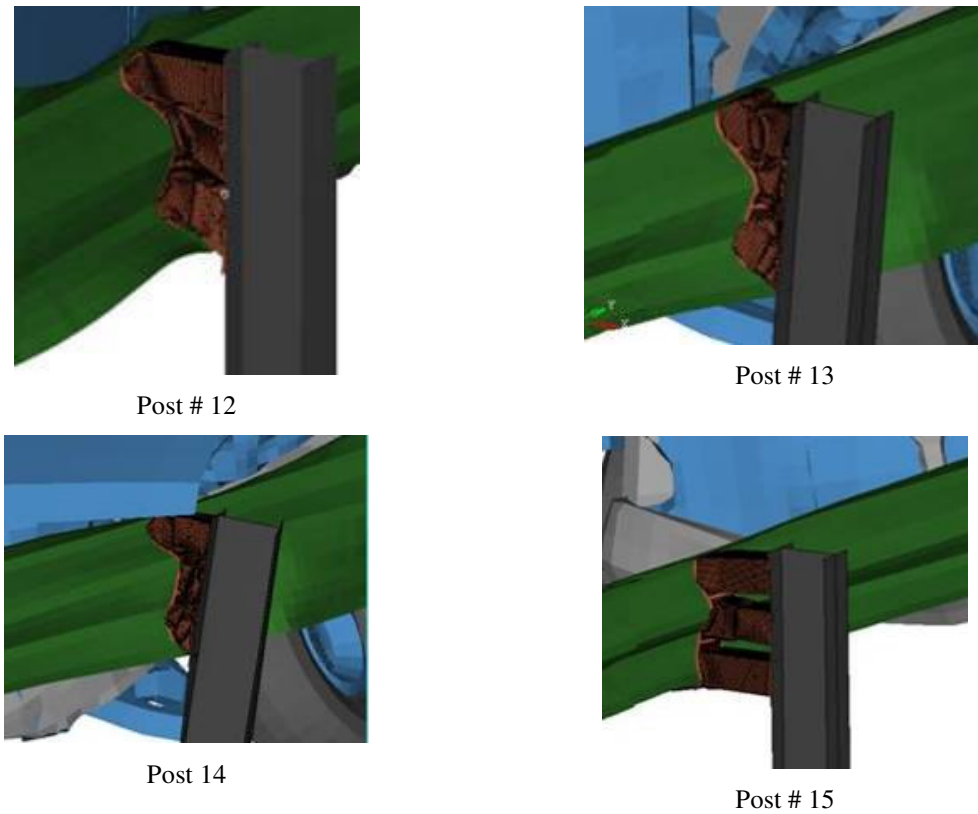


Figure 5.24: Crushable blockout of the post 12 to 15 during the impact

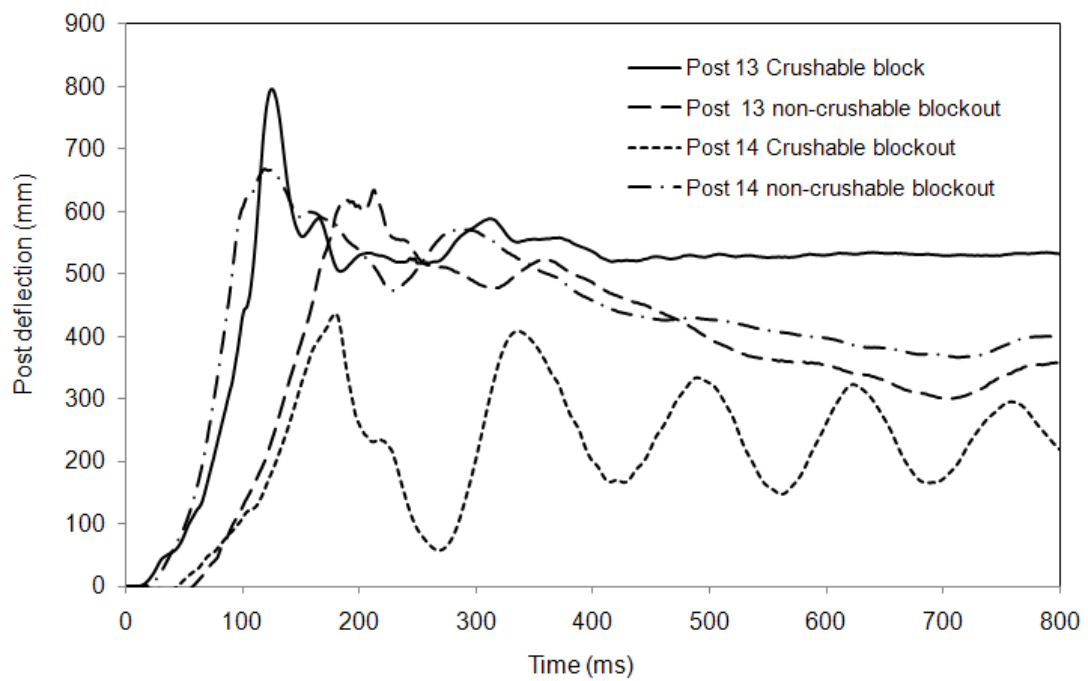


Figure 5.25: Deflection of the Posts 13 and 14 in the transversal axis (X) during the pickup impact for base and the crushable models

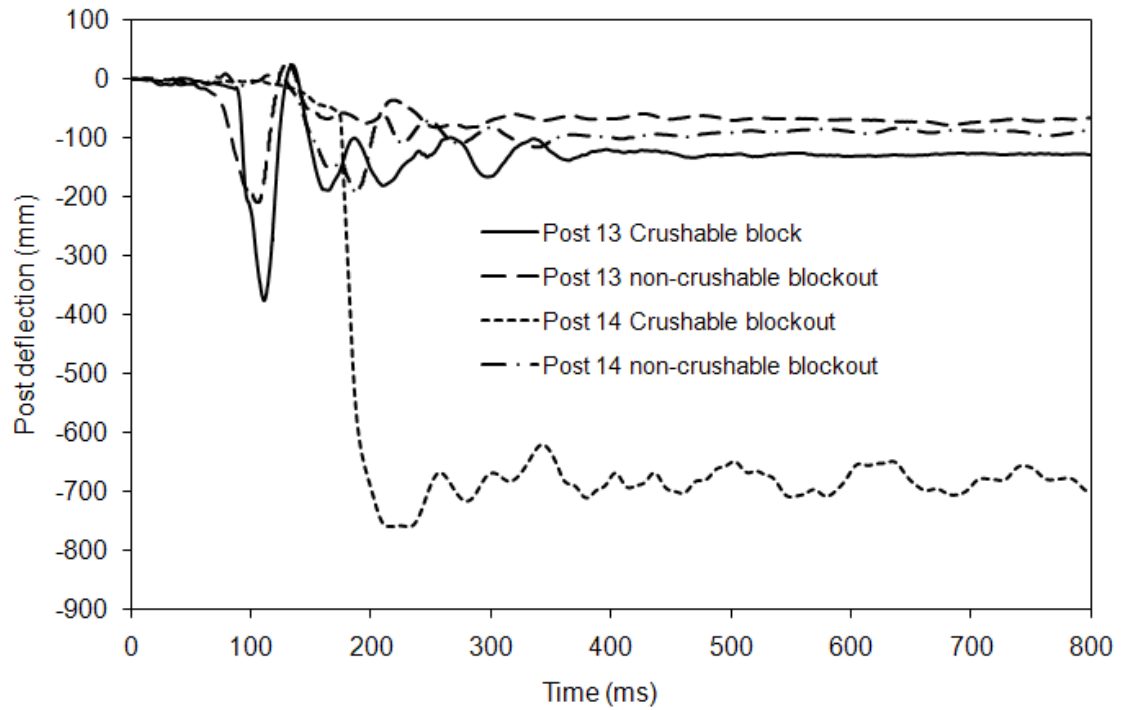


Figure 5.26: Deflection of posts 13 and 14 in the transversal axis (Y) during the pickup impact base and the crushable models

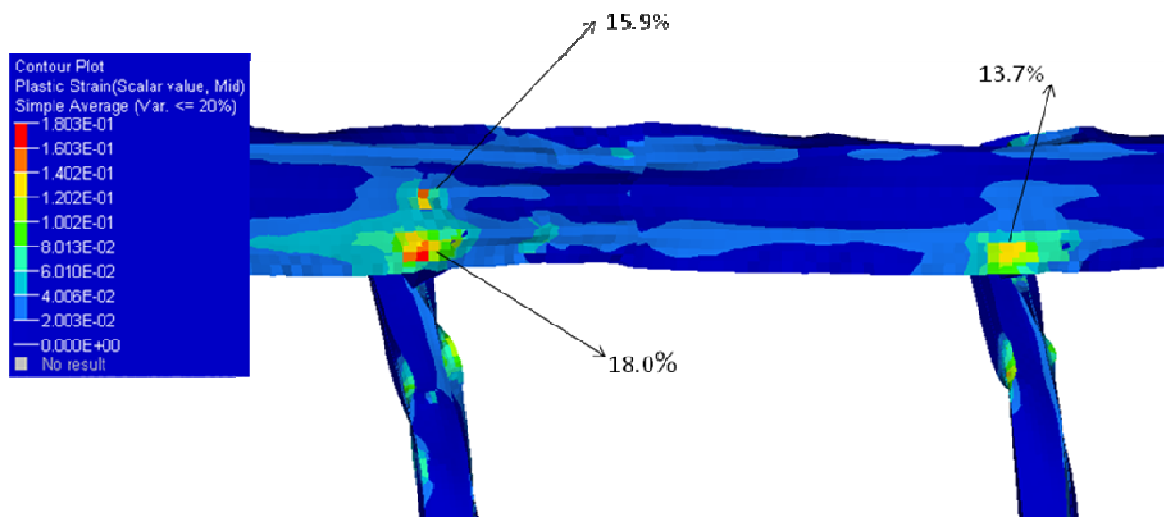


Figure 5.27: Plastic strain of the guardrail at 100 ms for the baseline model

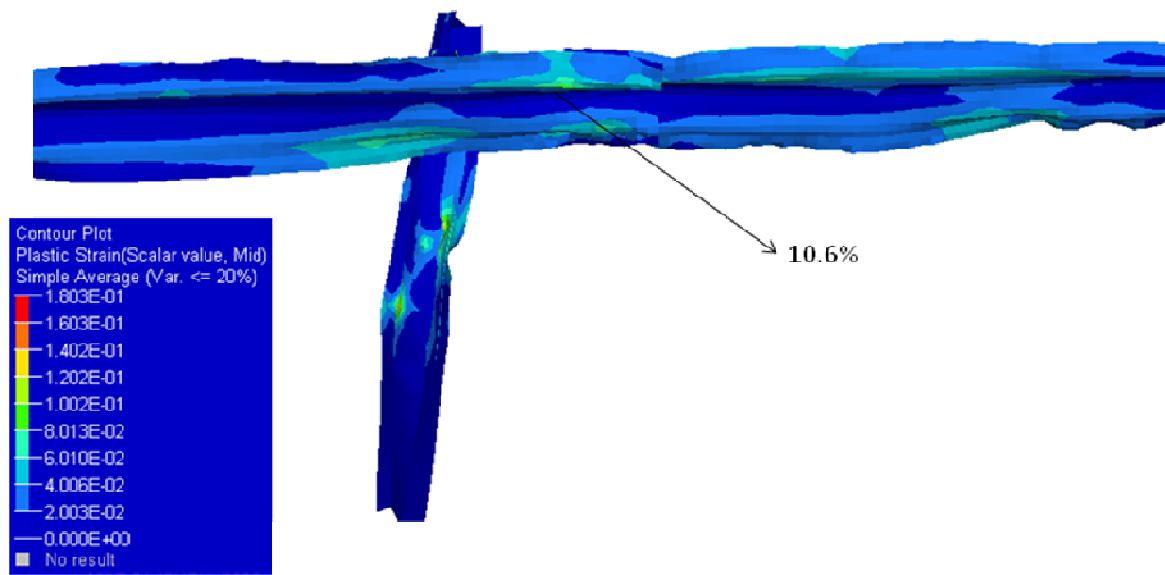


Figure 5.28: Plastic strain of the guardrail at 100 ms for the baseline with crushable blockout

5.5. Conclusions

The present chapter discussed the finite element modeling of C1500 vehicle impacting guardrail posts and the posts interaction with the soil during the impact event using the nonlinear finite element program Radioss. The post-soil interaction was modeled using the subgrade reaction approach which involves an array of nonlinear springs attached along the post. The interaction has considerable influence upon the response of the system and these components must be modeled accurately to capture the kinematics of the vehicle and the post. The finite element model of C1500 2000-kg pickup truck was validated in two different modes: Full front crash test and side crash. The full front test vehicle was conducted by NHTSA (National Highway Traffic Safety Administration). The test consists of hitting the vehicle against a rigid barrier with an impact speed was 55.8 kph. The side angular test was conducted on a Chevrolet pickup C1500 travelling with a speed of 100 km/h and an angle of 25 degrees against a 107cm vertical block of New Jersey Concrete barrier. The simulations results show good agreement between the

crash test and the finite element simulation with respect to velocity histories, event timing and exit conditions.

The full-scale baseline model was used to investigate the effect of replacing the incompressible blockout by crushable blockout which consists of 3 square tubes of 60x60 mm cross section and a wall thickness of 2 mm. The side length of the enclosed square section was 150 mm. The pickup truck impacted the guardrail with speed of 100 km/h and an initial impact angle of 25° at the same location of the base model and the impact was conducted up to 800 ms. The results of the finite element simulation show that the pickup was redirected safely for the guardrail system with reduced speed and roll angle than the baseline.

The simulation shows that Figure 5.24 shows the blockouts involved in the crash are completely crushed following the folds initiated by the triggers in the tubes whereas the remaining blockout kept their integrity. The results show that the maximum plastic strain with the crushable system is lower than the baseline model which shows that the compressible blockout offers more protection against the tearing and offer better performance than the baseline model.

Chapter VI

Conclusions and Recommendations

5.6. Introduction

The current dissertation research dealt with the study of the interaction between the guardrail post and the soil under different loading conditions using the finite element method. Finite Element Analysis has rapidly become a fundamental tool in the analysis and design of roadside safety hardware systems instead of the traditional method of the destructive full-scale crash testing. The method is not only reliable but also relatively inexpensive and can provide valuable information during the impact event, such as the stress in the barrier and the vehicle, the strain and the energy dissipated during the crash. The behaviour of the guardrail post embedded in cohesionless soil was analyzed for two cases: a single post impacted by an impactor cart and a guardrail system formed by a set of posts impacted by a pickup truck. The study was conducted in order to analyze the effect of the different loading parameters on the post behaviour and to propose design guidelines to improve vehicle safety in highways. The recommended design proposals are based on the results of the Design of Experiments (DoE) approach and on full-scale crash test simulations.

5.7. Summary of the Research

The interaction of a single post in the cohesionless soil has been reviewed using different available methods in the geotechnical field. These methods have been used to determine the ultimate lateral resistance of statically loaded, rigid vertical posts. The predicted lateral load was compared to data collected from the field. Based on a simplified lateral earth pressure distribution along the post length, an analytical model was developed to analyze the guardrail post subjected to lateral load. The new model, based on the Rankine passive earth pressure, takes into account the three-dimensional (3D) effect, which is important for the case of the guardrail posts embedded in soils. The results of the new model are compared to data collected from the literature and show a good agreement. To simplify the modeling behaviour of an embedded post subjected to impact forces, it is proposed to calibrate the finite element model using static analysis. The maximum forces obtained from a static analysis were compared with the results of

simulation of the dynamic loading. A parametric analysis showed that a calibration factor of 2.4 can be used to estimate the dynamic force from the static analysis.

To develop the finite element method, two methods for simulating the soil have been evaluated namely: (i) the continuum method where the soil is modeled as solid elements and (ii) an improved subgrade method which includes all relevant soil components such as the soil stiffness, soil damping and soil mass involved in the dynamic impact. The mass of the soil and the damping effect are being introduced in the improved subgrade method to simulate accurately the post reaction during the impact. Previous conventional studies used to ignore the effect of the soil mass and damping and account only for the soil stiffness. The lumped mass and the damping coefficients of the masses are calculated using a simple procedure. The simulation results of the improved subgrade method were compared to the dynamic test and the load deflection response showed a good agreement between the experimental and simulation results, especially in the early stage of loading, which demonstrates that the inertia effect is captured properly by the improved subgrade method. The correlation between these models in terms of impactor force or displacement is found to be satisfactory. The improved method has been extended to cohesive soils and the results were also in good agreements with the experimental findings.

The results of the improved subgrade method have been used to conduct an extensive parametric finite element study where the effects of the different parameters on the guardrail post reaction have been investigated. These parameters include the sand density, the impactor speed and mass, the post depth and the crushable blockout system and the undrained shear strength of the clay. The study showed that the peak load, the average load and the post deflection increase with the speed of the impactor, the friction angle and the embedment depth. However, the effect of the mass impactor was marginal. The crushable system implemented instead of the conventional rigid blockout system was able to reduce the peak load by approximately 21% and the average load by 10%.

A DoE was conducted to evaluate the contribution of the different design parameters of the guardrail post on the reaction during lateral dynamic impact using the Taguchi method. An L_9 Orthogonal Array design compared to a conventional one-at-a-time-

approach has been evaluated in the present investigation. The experimental data identify the influence of individual factors and establish the relationship between variables and operational conditions as well as the selection of optimal levels for best performance. The results showed that the soil friction is the most important factor in guardrail post reaction during a lateral impact and plays a major role with respect to the peak load, average load and maximum post displacement. The results showed that the crushability of the blockout post is an important factor to achieve the optimal condition by interacting with the other different parameters: the soil friction angle and the embedment depth.

Recommendations based on the parametric and the design of experiment studies were implemented to build a full-crash test model of a vehicle travelling at 100 km/h and impacting the guardrail with an angle of 25° as defined by NCHRP Report 350. A finite element model of the C1500 Chevrolet pickup truck was built and correlated to dynamic frontal crash test conducted by NHTSA. The full-scale baseline model was used to investigate the effect of replacing the incompressible blockout by crushable blockout. The results of the finite element simulation show that the crushable blockout redirected the pickup truck safely by reducing the speed and roll angle than the baseline.

5.8. Future Work

As of January, 2011, all new highway hardware testing must be evaluated using MASH 08, Manual for Assessing Safety Hardware (AASHTO 2009), crash test criteria for use on the National Highway System (NHS). MASH 09 (AASHTO 2009) is the new state of the practice for the crash testing which updates and supersedes NCHRP Report 350. (Ross et al., 1993)

The need for updated crash test criteria was motivated primarily by the changes in the vehicle fleet. Most of the new pickup trucks and passenger vehicles in the market have increased in size and the new trucks have raised the bumper heights since 1993, when the NCHRP Report 350 criteria were adopted. The Insurance Institute for the Highway Safety (IIHS) noticed that the bumper height of the new light trucks is higher than those of the old trucks and decided to include this fact into their side crash testing protocol. The deformable barrier used by IIHS is 1,676 mm wide and has a height of 759 mm and

a ground clearance of 379 mm when mounted on the test cart compared to 330 mm of ground clearance used by NHTSA.

The implementation plan for MASH 08 required that all highway safety hardware accepted prior to its adoption – using criteria contained in NCHRP Report 350 – may remain in place and may continue to be manufactured and installed. In addition, highway safety hardware accepted using NCHRP Report 350 (Ross et al. 2009) criteria is not required to be retested using MASH criteria (AASHTO 2009). However, new highway safety hardware must use MASH criteria for testing and evaluating. The major change with regards to the current study was to upgrade the weight of the light trucks and small cars from 2000 kg and 820 kg to 2270 kg to 2000 kg, respectively. The impact angle remains 25° for the light trucks and increased for the small cars from 20° to 25°. The speed remains 100 km/h even though some highways post speed limits above 110 km/h (65 mph) because the speeds are in general reduced due to the pre-crash application of brakes. These new requirements need a new pickup truck model that should be validated and correlated to crash tests. The component tests will remain valid. However, a very important step is to build a suitable full-scale model and more work is still required to understand the interaction of the post statically and dynamically. For all these reasons, the following is a list of urgent topics that need to be addressed:

- Extend the approach developed to predict the peak load during the static loading condition to cohesive soils characterised by the undrained shear strength. The relationship should include the undrained shear strength, the value of the passive earth pressure determined in the tridimensional assumption and the embedment of the post in the soil.
- Conduct component dynamic tests with cohesionless soil by varying the different test parameters such as the impactor speed, the impactor mass and the soil friction angle. These dynamic tests will serve to establish a relationship between the lumped mass and the damping ratio with the different parameters. This study will improve the finite element model calibration and contribute to a better prediction of the dynamic loads.
- Conduct component dynamic tests with baseline design consisting of a post with the conventional blockout, embedded at 1100 mm in sand and a dynamic test with the

parameters defined from the DoE consisting of a post embedded in dense soil at a depth of 1200 mm with a crushable blockout. This study will be used to verify the DoE results.

- For the full-scale testing, the first step should consist of building more sophisticated truck finite element models that replace the crude one used up-to-date in the roadside safety area. The model should reflect the actual bumper and door stiffness by including all the door hardware in the model such as the door inner sheet metal, the glass mechanism and the door beams. The model should reflect also the new regulation defined in MASH 08 (AASHTO 2009). The second step would be to conduct a full-scale dynamic test implementing the crushable blockout to check the energy dissipation capability.

- The complete model could serve to assess the response of occupants during the impact and the severity of the injury. Different anthropomorphic test device (ATD) could be investigated such as ES2 dummy, SID2s or Child.

REFERENCES

AASHTO (1990) "AAHSTO M187-65 Materials for Aggregate and Soil-Aggregate Subbase, Base and Surface Courses." American Association of State Highway and Transportation Officials, Washington, D.C.

AAHSTO (1998) "AASHTO M183, Standard specification for structural steel." American Association of State Highway and Transportation Officials, Washington, D.C.

AASHTO (2000) "AAHSTO M180 Corrugated Sheet Steel Beams for Highway Guardrail." American Association of State Highway and Transportation Officials, Washington, D.C.

AAHSTO (2009) "Manual for Assessing Safety Hardware." American Association of State Highway and Transportation Officials.

Abramowicz, W. and Wierzbicki, T. (1989) "Axial Crushing of multicorner sheet metal columns." *Journal of Applied Mechanics* 56, pp. 113–120.

Ashour, M. and Norris, G. (2000) "Modeling lateral soil-pile response based on soil-pile interaction." *Journal of Geotechnical and Geoenvironmental Engineering*, 126 (5), pp. 420–428.

Atahan, A. O. (2002) "Finite element simulation of a strong-post W-Beam guardrail system." *SIMULATION*, Vol. 78, Issue 10, pp. 587-599.

Atahan, A.O. and Cansiz, O.F. (2005) "Impact analysis of a vertical flared back bridge rail-to-guardrail transition structure using simulation" *Finite Elements in Analysis and Design*, 41, pp. 371–396.

Baker LC, Krueger A.B. (1992) "Medical costs in workers' compensation insurance." *Journal of Health Economics*, vol. 14, pp. 531-550.

Barber, E.S. (1953) "Discussion to paper by S. M. Glesser" *ASTM*, STP 154, pp. 96-99.

Bendidi, R. (2002) "Finite element analysis of the crash performance of W-Beam guardrail systems." Ph.D. Dissertation, Mechanical Department, Howard University, Washington DC.

Bentley, K. J and El Naggar, M. H. (2000) "Numerical analysis of kinematic response of single piles." Canadian Geotechnical Journal 37, pp. 1368–1382.

Bierman, M. G. (1995) "Behavior of guardrail posts to lateral impact loads." Master dissertation, University of Nebraska, Lincoln, Nebraska.

Bligh R.P., Seckinger N. R, Abu-Odeh A Y., Roschke, P N., Menges W L, and Haug R. R. (2004) "Dynamic response of guardrail systems encased in pavement mow strips." Texas Transportation Institute, Report 0-4162-2.

Blum, H. (1932) "Wirtschaftliche Dalbenformen und deren Berechnung." Bautechnik, 10(5), pp. 122–135 [In German.].

Bowles J.E. (1982) "Foundation analysis and design." McGraw Hill, New York, 1982.

Broms, B.B. (1964) "Lateral resistance of piles in cohesionless soils." ASCE Journal of the soil Mechanics and Foundations Division, 90 (SM3), pp. 123-156.

Bronstad, M. E., and Burket, R. B. (1971) "Evaluation of timber weak-post guardrail systems." Highway research record 343, Transportation Research Board, Washington D.C.

Bronstad, M. E., Calcote, L. R., Ray, M. H. and Mayer, J. B. (1988) "Guardrail-bridge rail transition designs." Report FHWA-RD-86-178, FHWA, US Department of Transportation.

Bronstad, M. E., and Michie, J. D. (1974) "Recommended Procedures for Vehicle Crash Testing of Highway Appurtenances." NCHRP Report 153, Transportation Research Board, National Research Council, Washington, D. C.

Calcote L.R. and Kimball C.E. (1978) "Properties of guardrail posts for various soil types." Transportation Research Record 679, National Research Council, Washington, D.C., pp. 22-25.

Canadian Geotechnical Society (2006) "The Canadian foundation engineering manual" Fourth edition.

Canadian Institute of Steel Construction (1991) "Handbook of steel construction." Universal Offset Limited, Markham, Ontario.

Coon, B. A. (1999) "Dynamic impact testing and simulation of guardrail posts embedded in soil." Master thesis, University of Nebraska.

Coon, B. A., Reid, J. D. and Rhode, J. R. (1999) "Dynamic Impact testing of guardrail posts embedded in soil." Research Report No. TRP-03-77-98, Midwest Roadside Safety Facility, University of Nebraska-Lincoln, Lincoln, Nebraska.

Cowper, G. R. and Symonds, P. S. (1957) "Strain hardening and strain rate effects in the impact loading of cantilever beams." Report N° 28, Brown University Division of Applied Mathematics.

Dewey, J. F. (1982) "A Study of the soil-structure interaction behavior of highway guardrail posts." Master thesis, Texas Transport Institute, Texas A&M University.

Eggers, D. W. and Hirsch T. J. (1986) "The effects of embedment depth, soil properties and soil type on the performance of highway guardrail post." Texas transportation Institute, Report FHWA/TX-86/64 405-1.

Elmarakbi, A., Vesenjaj, M. and Sennah, K. (2005) "Finite-element simulation of an improved traffic W-shape guardrail system in vehicle collision." Proceedings, Canadian Multidisciplinary Road Safety Conference CMRSC-XV, Fredericton, NB, pp. 1-8.

Elmarakbi, A., Sennah, K., Siriya, P. And Emam, A. (2006) " Parametric effects on the performance of traffic light poles in vehicle crashes" International Journal of Crashworthiness, 11:3, 217 - 230

El Naggar M. H. and Bentley K. J. (2000). "Dynamic analysis for laterally loaded piles and dynamic p-y curves." Canadian Geotechnical Journal, Vol. 37, No. 6, pp. 1166-1183.

El Naggar M. H. and Novak, M. (1995) "Nonlinear lateral Interaction in pile dynamics" Soil Dynamics and Earthquake Engineering, Volume 14, Elsevier Science Limited, pp. 141-157.

El Naggar M. H. and Novak, M. (1996) "Nonlinear analysis for dynamic lateral pile response." Soil Dynamics and Earthquake Engineering, Volume 15, Elsevier Science Limited, pp. 233-244.

Elvik, R. (1995) "The safety value of guardrails and crash cushions: a meta-analysis of evidence from evaluation studies." Accident Analysis and Prevention, 27, pp. 523-549.

Engstrand, K.E. (2000) "Improvements to the weak-post W-beam guardrail." Master of Science, Civil Engineering, Worcester Polytechnic Institute.

Faller, R. K, Polivka, K. A., Kuipers, B. D, Bielenberg, R. W, Reid, J.D, Rohde J. R, Sicking, D. L. (2004) "Midwest guardrail system for standard and special applications." Transportation research record, Washington DC, National Research Council, pp. 19–33.

Gabauer, D. J., Kusano, K. D., Marzougui, D., Opiela, K., Hargrave, M. and Gabler, H. C. (2010) "Pendulum testing as a means of assessing the crash performance of longitudinal barrier with minor damage." International Journal of Impact Engineering Volume 37, Issue 11, pp. 1121-1137.

Habibagahi, K. and. Langer J. A. (1984) "Horizontal subgrade modulus of granular soils." Laterally Loaded Deep Foundations, ASTM Special Technical Publication 835, Langer, Mosely, and Thompson, editors. American Society for Testing Materials, pp. 21-34.

Hallquist, J. O. (2006) "LS-DYNA Theoretical Manual, version 971." Livermore Software Technology Corporation, Livermore, CA, 2006.

Hamilton, M. E. (1999) "Simulation of the T-6 bridge rail using LS-DYNA." MS thesis, Texas A&M University, College Station, Texas.

Hetenyi M. (1967) "Beams on elastic foundations." 8th printing, Ann Arbor Michigan., University Of Michigan Press.

Highway Research Circular 482 (1962) "Proposed full-scale testing procedures for guardrails." Committee on Guardrail and Guide Posts, Highway Research Board, Washington, D.C.

Holloway, J. C., Bierman, M. G., Pfeifer, B. G., Sicking, D. L., and Rosson, B. T. (1996) "Performance evaluation of KDOT W-beam systems." Vols I and II, Final Report to the Kansas Department of Transportation, Project SPR-3(017), Report No. TRP-03-39-96.

Horn, A. (1972) "Résistance et déplacements de culées de ponts charges latéralement." European Conference on Soil mechanics and foundations engineering, Vol.2, pp. 143-145, Madrid.

Huang, M. (2002) "Vehicle crash mechanics" CRC Press Inc.

Ivey, D. L., Robertson, R. and Buth, C. E. (1986) "Test and evaluation of W-beam and thriebeam guardrails." Report FHWA/RD-82/071, Texas Transportation Institute, Texas, A&M University, College Station.

Jones, N. (1989) "Structural impact." Cambridge University Press.

Jones, N. (1983) "Several phenomena in structural impact and structural crashworthiness." *European journal of mechanics and solids*, 22, no. 5 pp. 693-707.

Karl, L., Haegemana W. and Degrandeb, G. (2006) "Determination of the material damping ratio and the shear wave velocity with the Seismic Cone Penetration Test." *Soil Dynamics and Earthquake Engineering* 26, pp. 1111–1126.

Karlsson, J.E. (2000) "Design of a non-snagging guardrail post." Master of Science, Civil Engineering, Worcester Polytechnic Institute.

Kennedy, J. C., Plaxico, C. A. and Miele C. R. (2004) "Design development and qualification of new guardrail post." *Transportation Research Record*, paper No. 04-2936.

Kilareski, W. P., El-Gindy, M., St. John, B. D. and Peacheux, B. (1999) "Type 2 Weak-Post Guardrail Testing." Pennsylvania Transportation Institute, Pennsylvania State University, State College, PA.

Kokusho, T. (1980) "Cyclic triaxial test of dynamic soil properties for wide strain range." *Soils and Foundations*, Japanese Geotechnical Society, 20(2), 45-60, 1980-06-15.

Krieg, R.D. (1972) "A simple constitutive description for cellular concrete." Sandia National Laboratories, Albuquerque, NM, Report Sc-DR-72-0883.

Kuipers, B. D. and Reid, J. D. (2003) "Testing of W152x23.8 (W6x16) Steel posts-Soil embedment depth study for the Midwest guardrail system (Non-propriety guardrail system) MwRSF." Research Report No.TRP-03-136-03, Final report to the Midwest States' Regional Pooled Fund Program, Midwest Roadside Safety Facility, University of Nebraska-Lincoln, Lincoln, Nebraska.

Lambe, T. W. and Whitman, R. V. (1969) "Soil Mechanics." Series in Soil Engineering, Wiley, 1st edition.

Lochner R. H. and Matar, J. E. (1990) "Design for quality: an introduction to the best of Taguchi and western methods of statistical experimental design." Quality Resources and ASQC Quality Press, Milwaukee.

Mahmood, H. F. and Paluszny, A. (1981) "Design of thin walled columns for crash energy management-Their strength and mode of collapse." SAE 811302, pp. 7-18.

Mak, K. K. and Menges, W. C. (1994) "Crash testing and evaluation of strong-post, W-beam guardrail system." Texas Transportation Institute, Texas A&M University, College Station.

Marzoughi D., Meczowski L., Taylor, H. and Bedewi N. (2001) "Sign support height analysis using finite element simulation." International Journal of Crashworthiness, Volume 6, Issue 1 2001 , pp. 33 – 42.

Marzougui D., Zink M., Zaouk A., Kan C.D., and Bedewi N.E. (2004) "Development and validation of a vehicle suspension finite element model for use in crash simulations." International Journal of Crashworthiness, Vol. 9, No. 6, pp. 565-576.

Matlock, H. (1970) "Correlations for design of laterally loaded piles in soft clay." Offshore Technology Conference, Houston, Texas, vol. I, pp. 577-594.

McCelland, B. and Focht, J. A. (1958) "Soil modulus for laterally loaded piles." Transactions, American Society of Civil Engineers, Volume 123, pp. 1049-1086.

Mecalog (2005) "Radioss starter manual, Radioss user's manual." France.

Menard, L. (1962) "Comportement d'une fondation profonde soumise à des efforts de renversement." Sols-Soils, No 3, pp. 9-12.

Meyerhof G. G., Mathur S. K. and Valsankar, A. J. (1981) "Lateral resistance and deflection of rigid walls and piles in layered soils." Canadian Geotechnical Journal, Volume 18, pp. 150-170.

Michie, J. D. (1981) "Recommended Procedures for the Safety Performance Evaluation of Highway Appurtenances." NCHRP Report 230, Transportation Research Board, National Research Council, Washington, D.C.

Mohan, P., Marzougui, D., Meczowski, L. and Bedewi, N. (2005) "Finite element modeling and validation of a 3-strand cable guardrail system." International Journal of Crashworthiness, 10:3, pp. 267 – 273.

Montgomery, D. (2005) "Design and analysis of experiment." John Wiley & Sons Inc, sixth edition, 2005.

Mosher, R. L. and Dawkins, W. P. (2000) "Theoretical manual for pile foundations." U.S. Army Engineer Research and Development Center, Information Technology Laboratory, 3909 Halls Ferry Road, Vicksburg, MS 39180-6199, Oklahoma State University, Stillwater, OK 74074.

Mostafa, Y. E. and El Nagggar M. H. (2002) "Dynamic analysis of laterally loaded pile groups in sand and clay.", Canadian Geotechnical Journal, Vol. 39, pp. 1358-1383.

Mouazen, A. and Neményi, M. (1999) "Tillage tool design by the finite element method: part1. Finite element modeling of soil plastic behavior." Journal agricultural engineering research, Volume 72, Issue 1, pp. 37-51.

NAVFAC (1982) "Foundations and earth structures." Department of the Navy, Naval Facilities Engineering Command, Alexandria, VA.

Novak, M. (1974) "Dynamic stiffness and damping of piles." Canadian Geotechnical Journal, Volume 13, No. 4, pp. 271-285.

Novak, M. and Sheta, M. (1980) "Approximate approach to contact problems of piles." ASCE National Convention, Florida, pp. 53-79.

Pacheco-Crosetti, G. (2007) "Dynamic lateral response of single piles considering soil inertia contribution." PhD dissertation, Civil Engineering, University Of Puerto Rico, Mayaguez Campus.

Palmer, L.A. and Thompson, J.B. (1948) "The earth pressure and deflection along the embedded lengths of piles subjected to lateral thrusts." Proceeding 2nd International conference Soil Mechanics and Foundation Engineering., Rotterdam, vol. 5, pp. 156-161.

Patzner, G. S., Plaxico, C. A. and Ray, M.H. (1999) "Effect of post and soil strength on the performance of the modified eccentric loader breakaway cable terminal." Transportation Research Record, Paper No. 990046, Transportation Research, Board, Washington, D.C.

Pernetti, M. and Scalera, S. (2007) "Development of validated finite-element model of a rigid truck suitable to simulate collisions against road safety barriers." 6th European LS-DYNA User's Conference.

Pfister, P., Evers, G., Guillaud, M. and Davidson, R. (1982) "Permanent ground anchors: Soletanche design Criteria." Final report No. FHWA/RD81/150, US Department of Transportation, Federal Highway Administration, pp. 18-22.

Plaxico C. A. (2002) "Design guidelines for the use of curbs and curb/guardrail combinations along high-speed roadways." Ph.D. dissertation, Civil Engineering, Worcester Polytechnic Institute.

Plaxico, C. A., Patzner, G. S. and Ray, M. H. (1998) "Finite-element modeling of guardrail timber posts and soil-post interaction." Transportation Research Record No. 1647, Transportation Research Board, Washington, D.C.

Polivka, K. A., Faller, R. K., Sicking, D. L., Reid, J. D., Rohde, J. R., Holloway, J. C., Bielenber, B. W., Kuipers, B. D. (2004) "Development of the Midwest guardrail system (MGS) for standard and reduced post spacing and in combination with curbs." MwRSF, Final Report 1999-2004, Research Report No. TRP-03-139-04.

Poulos, H.G. (1971) "Behavior of laterally loaded piles." ASCE Journal of the Soil Mechanics and Foundations Division, 97 (SM5), pp. 711-751.

Poulos H.G. (1974) "Elastic solutions for soil and rock mechanics." John Wiley & Sons Inc.

Poulos H.G. and Davis E. H. (1980) "Pile foundation analysis and design." John Wiley & Sons, New York, NY.

Prakash, S. and Venkatesan, S. (1960) "Characteristics of dense sand at different rates of strains." Journal, Scientific and Industrial Research, Vol. 19A, 5, pp. 219-223.

Prakasham, R. S., Subba R. C., Sreenivas R. R. and Sarma, P. N. (2005) "Alkaline protease production by an isolated bacillus circulans under solid-state fermentation using agroindustrial waste." Process Parameters Optimization. Biotechnol. Prog., 21, pp. 1380-1388.

Prasad, Y. V. and Chari, T. R. (1999) "Lateral capacity of model rigid piles in cohesionless soils." Soils foundations, Vol. 39, No.2, pp. 21-39.

Ray, M. H. and McGinnis, R. G. (1997) "Guardrail and median barrier crashworthiness." Synthesis No. 244, Transportation Research Board, National Academy of Sciences, Washington, D.C.

Reese, L. C., Cox, W. R. and Koop, F.D. (1974) "Analysis of laterally loaded piles in sand." Proceedings of the 6th annual offshore technology conference, Houston, Texas.

Reese, L. C., and Matlock, H. (1956) "Non-dimensional solutions for laterally loaded piles with soil modulus assumed proportional to depth." Proceeding 8th Texas conference Soil Mechanics and Foundation Engineering, special publication No. 29, Bureau of Engineering Research, University of Texas, Austin, Texas.

Reid, J. D. (1999) "A new breakaway mailbox designed using nonlinear finite element analysis." Finite Elements in Analysis and Design, Volume 32, Issue 1, 15, pp. 37-49.

Reid, J. D., Hascall, J. A., Sicking, D L and Faller, R. K. (2009) "Inertial effects during impact testing." Transportation Research Record: Journal of the Transportation Research Board, Volume 2120 / 2009, pp. 39-46.

- Reid, J. D., Sicking, D. L. Faller R.K. and Pfeifer, B.G. (1997)** "Development of a new guardrail system." Transport Research Record, 1599, TRB, National Research Council, Washington, D.C. 1997, pp. 72-80.
- Ren, Z. and Vesenjaj, M. (2005)** "Computational and experimental crash analysis of the road safety barrier." Engineering failure Analysis Journal, volume N.12, p963-973, 2005.
- Rhode, J. R., Rosson, B. T., and Smith R. (1996)** "Instrumentation for determination of guardrail-soil interaction." Transport Research Record, 1528, TRB, National Research Council, Washington, D.C., pp. 109-115.
- Ross, H. E., Sicking, D. L. and Ferrara, H. S. (1993)** "Recommended Procedures for the safety performance evaluation of highway appurtenances." National Cooperative Highway Research Program Report No. 350, National Academy of Sciences, Washington, D.C.
- Rosson, T. B., Bierman G. M., Rohde, R. J. (1996)** "Assessment of guardrail-strengthening techniques." Transportation Research Record 1528, Washington, D. C., pp. 69-77.
- Roy, K. R. (2001)** "Design of Experiments using Taguchi approach 16 steps to product and process improvement." John Wiley & Sons, Inc.
- Sassi, A., Ghrib, F., and Battachargee, S. (2010)** "An improved an improved subgrade model for the crash analysis of guardrail posts." CSCE 2010 General Conference, Winnipeg, Manitoba.
- Sennah, K., Samaan, M. and Elmarakbi. A. (2003)** "Impact performance of flexible guardrail systems using LS-DYNA." Proceedings of the 4th European LS-DYNA Conference, Ulm, Germany, pp. 1-9.
- Seo, T., Ando, K., Fukuya, T., Kaji, S. (1995)** "Development of guardrails for high-speed collisions." Transportation Research Record 1500, Washington, D. C., pp. 52-58.
- Shukla, S. (1997)** "Simulation of quasi-static tension test for roadside hardware material using LS-DYNA3D." 5th International LS-DYNA Users Conference.
- Simunovic, S., Kumar,V., Nukala, P., Fekete, J., Meuleman, D. and Milititsky, M. (2003)** "Modeling of strain rate effects in automotive impact." SAE paper, 2003-01-1383.
- Škrabl S. and Macuh B. (2005)** "Upper-bound solutions of three-dimensional passive earth pressures." Canadian Geotechnical Journal, volume 42, No. 5, pp. 1449–1460.

- Soletanche (1982)** "Permanent ground anchors." Final report N° FHWA/RD-81/150, U.S. Department of Transportation, Federal Highway Administration, pp. 18-22.
- Soubra, A. H., and Regenass, P. (2000)** "Three-dimensional passive earth pressure by kinematical approach." *Journal of Geotechnical and Geoenvironmental Engineering*, ASCE, 126(11), pp. 969–978.
- Tabiei, A., and Wu, J. (2000)** "Roadmap for crashworthiness finite element simulation of roadside safety structures." *International Journal Finite Elements in Analysis and Design*, Vol. 34, No. 2, pp. 145-157.
- Taciroglu, E., Rha, C. and Wallace, J. W. (2006)** "A Robust Macroelement Model for Soil–Pile Interaction under cyclic loads." *Journal of Geotechnical and Geoenvironmental Engineering*, ASCE, 132(10), pp. 1304-1314.
- Taguchi, G. (1991)** "Taguchi methods: research and development." *Quality Engineering Series*, Vol. 1, ASI Press, Dearborn, MI.
- Taguchi, G. (1987)** "System of experimental design. Engineering methods to optimize quality and minimize costs". Kraus International, White Plains, NY.
- Taguchi, G. (1999)** "System of experimental design Engineering: methods to optimize quality and minimize costs." Volume one, Quality resources, White Plains, New York, 1991.
- Terzaghi, K. (1955)** "Evaluation of coefficients of subgrade reaction." *Geotechnique*, Volume 5, No 4, pp. 297-326.
- Tiso, P. (2001)** "Improvements to the suspension of the NCAC C2500 Pickup truck finite element mode." Master Thesis, Worcester Polytechnic Institute, Worcester, MA.
- Transport Canada (2001)** "Trends in Motor Vehicle Traffic Collision Statistics 1988 – 1997" TP 13743 E.
- Transport Canada (2006)** "2005 Annual report on road safety vision 2010" TP13347 E, TC 1002086, Catalogue No. T45-1/2005E-PDF.
- Transport Canada (2010)** "2007 Canadian Motor Vehicle Traffic Collision Statistics." TC-1003618, TP 3322, Catalogue No. T45-3/2007.
- U.S. Army Corps of Engineers (1991)** " Engineer manual: design of pile foundations." Washington, DC 20314-1000, 1110-2-2906.

Vesenjak, M., Borovinsek, M. and Ren, Z. (2007) "Computational simulations of road safety barriers using LSDYNA." 6th European LS-DYNA User's Conference, Anwenderforum, Frankenthal.

Vickers, B. (1983) "Laboratory work in soil mechanics." 2nd edition, Granada Publishing.

Vodden, K., Smith, D., Eaton, F., and Mayhem, D. (2007) "Analysis and estimation of the social cost of motor vehicle collisions in Ontario." Transport Canada, TP 14800F, N0779, 2007.

Whitman, R. V. and Healy, K. A. (1962) "Shear strength of sands during rapid loading." Journal of Soil Mechanics and Foundations Division, ASCE, Vol. 88, No. SM2, pp. 99-132.

Whitworth, H.A., Bendidi, R., Marzoughi, D. and Reiss, R. (2004) "Finite element modeling of the crash performance of roadside barriers." International Journal of Crashworthiness, volume 9, Issue 1, pp. 35-43.

Wierzbicki T. and Abramowicz W. (1989) "The mechanics of deep plastic collapse of thin-walled structures." Wierzbicki T, Jones N, editors Structural failure. New York: John Wiley, pp. 281-329.

Wright, A. and Ray, M.H. (1996) "Characterizing Roadside hardware Materials for LSDYNA Simulations." Report No. FHWA-RD-96-108, Federal Highway Administration.

Wu, J. (2000) "Crashworthiness simulation of roadside safety structures with development of material model and 3-D fracture procedure." Ph.D. dissertation, Aerospace engineering, University of Cincinnati.

Wu, W and Thomson, R. (2007) "A study of the interaction between a guardrail post and soil during quasi-static and dynamic loading." International Journal of Impact Engineering" Volume 34, Issue 5, pp. 883-898.

Zaouk, A. K., Bedewi, N. E., Kan, C. D., and Marzougui, D. (1997) "Development and evaluation of a C-1500 pickup truck model for roadside hardware impact simulation" Report Number FHWA-RD-96- 212, FHWA Vehicle Crash Analysis, Federal Highway Administration, Washington, D.C.

Zurabov G.G. and Bugaeva O. A. (1949) "High Pile Grillages of Bridge" (in Russian) Dorizdat (1949).

VITA AUCTORIS

Abdelmonaam Sassi was born in 1964 in Sousse (Tunisia). He graduated from El-Mansourah High School in Kairouan (Tunisia) in 1982. From there he went on to Ecole Nationale des Ingénieurs de Tunis (National School of Engineers in Tunis) where he obtained a B.Sc. in Civil Engineering in 1989. In 1990, He started a Master degree in Ecole Polytechnique de Montreal, Montreal, Quebec (Canada) where he graduated in 1992. He is currently a candidate for the Ph.D. degree in Civil Engineering at the University of Windsor and hopes to graduate in Fall 2011.